

Ultrafast Charge Transfer and Relaxation Dynamics in Metal Chalcogenide Based p-n Semiconductor Heterojunctions

Arshdeep Kaur

*A thesis submitted for the partial fulfillment of
the degree of Doctor of Philosophy*



Institute of Nano Science and Technology

Knowledge City, Sector 81, SAS Nagar, Manauli PO, Mohali
140306, Punjab, India.

Indian Institute of Science Education and Research Mohali

Knowledge City, Sector 81, SAS Nagar, Manauli PO, Mohali
140306, Punjab, India.

February 2024

DEDICATIONS

*To my Family, Teachers, Friends
and well wishers*

Declaration

The work presented in this thesis has been carried out by me under the guidance of Prof. Hirendra N. Ghosh and Dr. Ramendra S. Dey at the Institute of Nano Science and Technology Mohali. This work has not been submitted in part or in full for a degree, a diploma, or a fellowship to any other university or institute. Whenever contributions of others are involved, every effort is made to indicate this clearly, with due acknowledgment of collaborative research and discussions. This thesis is a bona fide record of original work done by me and all sources listed within have been detailed in the bibliography.

Arshdeep Kaur

In my capacity as the supervisor of the candidate's thesis work, I certify that the above statements by the candidate are true to the best of my knowledge.



Prof. Hirendra N. Ghosh
(Co-Supervisor)

Dr. Ramendra S. Dey
(Supervisor)

Acknowledgments

“If I have seen further, it is by standing on the shoulders of giants.”

- *Isaac Newton*

*“First and foremost, I bow down to **The Lord Almighty**, the Eternal Source of Wisdom and Strength for giving me the courage, patience, and whose infinite grace and blessings have lit my way and led me with constant assurance through every complex step of this deep and transformational journey.*

The triumph of the thesis work is evidence of the outcome of collective efforts and persistent support from many individuals and I owe a debt of gratitude and appreciation to all those who stood by me and supported me in my peaks and valleys during my Ph.D. journey.

*First, I would like to extend my heartfelt gratitude to my co-supervisor **Prof. Hirendra N. Ghosh**, for his unwavering guidance, insightful feedback, and continuous encouragement in shaping the course of this thesis. I always get inspired by his tireless hard work, clear vision, devotion to research, and positive and energetic attitude. I consider myself extremely lucky to have Prof. Hirendra N. Ghosh as my advisor. His positive outlook is very remarkable, and it helped me to stay strong and focused even during difficult times. He is the epitome of resilience, never faltering in his resolve. Prof. Ghosh consistently has faith and trust in his students. His firm faith always gives me a tremendous sense of confidence that enables me to take on obstacles head-on. His mentoring serves as a source of inspiration, showing us that any challenge can be surmounted with the correct attitude. In addition to his scientific expertise, I found him to be a trustworthy and helpful person in real life. His profound understanding, clear vision, remarkable knowledge, and exciting ideas benefited me tremendously. Apart from science, he also taught me how to be a strong and bold person. Anytime I am feeling low, all it takes is one conversation with him to get me motivated again. Thank you so much sir for everything. I have learned so many things from you. You have provided me with a lot of strength. Throughout my life, I will be grateful to you and I wish you good health and success in all your future endeavours. I will always remember your advice and guidance.*

*I would like to thank my supervisor **Dr. Ramendra S. Dey** for his continuous support, precious time and help as a supervisor after Prof. H. N. Ghosh rejoined BARC. He*

always helped me out with tasks associated with the PhD documentation. Dr. Dey's subject-knowledge is incredible and he has been a great resource to me. He possesses a dynamic and approachable personality. I found him very helpful and supportive person. Thank you, sir, for your countless help and support.

*Furthermore, I am grateful to my Ph.D. monitoring committee members, **Dr. Kiran Shankar Hazra, Prof. Dipankar Mandal, Prof. Abir De Sarkar and Dr. Tapasi Sen** for yearly assessments, insightful ideas, valuable time, and interesting suggestions to improve my research work. I also want to thank **Prof. Kamal P. Singh** for evaluating my SRF presentation.*

*I would like to thank **Prof. Deepa Ghosh, Prof. Debabrata Patra and Prof. Suvankar Chakravarty** for always backing us whenever needed.*

*I want to express my deepest gratitude to **INST Mohali** for providing the financial instrument facilities and to **IISER Mohali** for the Ph.D. registration. I would like to thank the great administrative staff of both INST and IISER Mohali for doing timely and smooth work.*

*I gratefully acknowledge and thank the Department of Science and Technology (**DST-INSPIRE, New Delhi**), Government of India for providing a research fellowship.*

*I would also like to acknowledge **the Advanced Materials Research Centre (AMRC), Kamand Campus Indian Institute of Technology Mandi, Himachal Pradesh** for XPS measurements when this instrument was not available in INST.*

*I would like to take this opportunity to thank **Prof. Anindya Datta** for upconversion studies.*

*I want to express my sincere gratitude to our laser engineers- **Arun Kumar (Laser Science Services (I) Pvt. Ltd.) and Rajneesh sir** for their prompt assistance in operation of our laser systems.*

*I am grateful to engineer **Anoop Srivastava (Hing High Vacuum Company)** for patiently and thoroughly teaching me thermal evaporation and sputtering systems. Thank you for answering all my questions.*

*I would like to thank our alumni **Dr. Sachin R. Rondiya (my collaborator also)** for his invaluable guidance and for patiently addressing every question that arose in my mind, whether it was related to science or beyond. I also want to thank **Dr. Palwinder Singh, Dr. Dharmendra Yadav, Dr. Sourav Maity, Dr. Samaresh Samanta** for their guidance.*

*I bow a debt of gratitude and would like to thank my lab, “**Ultrafast Territory.**” They are like my family. During research life lab mates play an important role in helping out with experiments, managing time, scientific discussions, and all other non-scientific bits and pieces that made the time a memorable experience. Therefore, I take this chance to thank all my lab mates for their extraordinary support. I greatly thank all lab members **Dr. K. Justice Babu, Nandan Ghorai, Tanmay Goswami, Ayushi Shukla, Himanshu Bhatt, Manvi Sachdeva, Nitika Kharbanda and Vikas Nain** for their consistent support and help. Each member is unique and I have learnt a lot of things from them. I will always cherish the time spent with you people in the lab and outside. I wish to express my heartfelt thanks to my seniors **Dr. Nandan, Dr. Tanmay and Dr. Gurpreet** for their constant guidance and support. Their helping attitude, research attitude and commitment to work always inspired me. I have learnt a lot of things from them both professionally and personally. I have always been inspired by the professional and personal management skills of **Tanmay sir** and thank him for his great help and assistance in my work. I would like to thank **Gurpreet di** for always being there and for her support. I thank **Ayushi (we joined the lab together)** for providing support and care at the beginning of my Ph.D. journey. I will remember our talks and long phone calls during the COVID period. I am grateful to my juniors **Himanshu, Manvi, Nitika and Vikas** for providing a great support and help. I would like to give special thanks to **Dr. K. Justice Babu** for his help, and the motivational lectures and stories that he shared whenever I was tired and felt low. He is a very supportive person and I have learnt a lot of things from him, particularly synthesis. Thank you, sir, for giving life lessons and motivational books. I will cherish the South Indian food, ginger tea, and black coffee that he prepared for us. He was always there to support me when I needed him. I would also like to thank **Ramchandra Saha (RCS), Mohammed Patel and Anil.***

*I would like to thank TEM operators: **Ashwinder Singh, Neha Kumari and Baljeet Kaur** for their help.*

*I am thankful to **Hemant** for doing PL measurements during my paper revision time.*

*I owe a lot to my friends from high school and Panjab University. Thank you: **Gurwinder, Manpreet, Ritu, Jaspreet, Deesha and Kiran,** for always staying in touch and making time in your busy schedules to meet and speak which always lifted my spirits.*

*I want to give special thanks to my INST friends **Harri, Varun, Himadri, Silky, Akshay, Archna, Anamika, Liza, Parry, Arsh, Ritika, Manish, Ashmita, Sakshi, Chinmayee, Charan, Manpreet and Arushi** who have helped and supported me during my Ph.D. journey. I would also like to acknowledge everyone who provided me assistance whether directly or indirectly while working at INST.*

*I want to sincerely bow my gratitude to my **family** for their unconditional love, care, and support, which always helped me to lead my journey fully-fledged. Their patience and sacrifices motivated me all the way throughout my Ph.D. journey to complete my task potentially. I don't have enough words to thank my parents, **my father** and **my mother** who have their unwavering belief in me and have been my constant pillars of support and encouragement throughout this journey. Whatever I am today is because of their blessings. They always offered me emotional support during my tough times and supported me to pursue higher studies. I would like to give my heartfelt credit to my **brother** for his care, unwavering support and encouragement that have been a constant source of strength and inspiration for me. I wish to express my heartfelt appreciation to my beloved **sister-in-law** and friend for her care and love. A special credit goes to my cousin sister **Charanjeet Kaur** for her motivational talks. Now, I would like to owe my heartiest gratitude to the pillar of my strength, **my life partner, Mr. Harmanpreet Singh Sohal** who supported me in every aspect to achieve the successive goals of my life. He consistently celebrates my achievements and offers a listening ear during my tough times. I thank him from the core of my heart for being with me and appreciate his impact on my personal and professional growth. My sincere thanks to my supportive **in-law family**, especially my **father-in-law** and **mother-in-law**, for their cooperation and trust in me and the encouragement they always give me. I would like to thank my **brother-in-law** for his support and care. Also, I would also like to thank my **grandparents** for their love, care, and support.*

This work is a combination of ideas, suggestions, reviews, contributions, and efforts of many and never the work of an individual. I wish to express my gratitude to all those, with whom I have worked, interacted, and whose thoughts and insights helped me in furthering my knowledge and understanding of the subject.

Date:

Arshdeep Kaur

Abstract

Metal chalcogenides are emerging solar energy materials and are blessed with unique properties such as high abundance and absorption coefficient (10^4 - 10^5 cm^{-1}), tunable bandgap, low cost, and high stability, etc. Recently, metal chalcogenide-based p-n heterostructures have indeed gained tremendous attention in the field of solar energy conversion due to their potential for high efficiency. The p-n junctions are the fundamental and elementary building blocks of many electronic and energy storage devices, gas sensing devices, photovoltaics, photocatalysis viz. solar cells, diodes, light emitting diodes (LEDs), etc. They are the main active sites, where the efficient charge transfer processes take place. They offer fast separation and migration of the photoinduced charge carriers due to the presence of the built-in electric field. The efficient separation and longer lifetime of photoinduced charge carriers are crucial for any device. As the efficiency of any device is highly dependent on the dynamics of photoexcited charge carriers at the heterointerface, thus we must investigate excited state photophysical processes like charge transfer and recombination dynamics at the interface to fabricate efficient optical devices. Since these events are ultrafast in nature, we have utilized transient absorption spectroscopy (TAS) in my thesis work to track the interfacial charge transfer and relaxation events that occur over time scales of a few femtoseconds (fs) to nanoseconds (ns) in different heterojunction systems. To design cost effective devices, it is vital to comprehend the dynamics of these materials in their excited states. My first work deals with the synthesis of $\text{Cu}_2\text{ZnSnS}_4$ (CZTS) nanoparticles and CdS quantum dots (QDs) using the hot-injection method followed by fabrication of CZTS, CdS, and CZTS/CdS heterojunction thin films with the help of a spin-coating technique. Steady state and time-resolved photoluminescence studies confirm the hole transfer from photoexcited CdS to CZTS and the hole transfer rate constant was calculated to be 0.366×10^9 sec^{-1} . The ultrafast studies clearly suggest electron transfer from the CZTS domain to the CdS domain with a time constant of 0.14 ps, establishing the charge transfer efficiency in the heterointerface. Thus, our results demonstrate the fast charge separation in CZTS/CdS heterojunction film. The next work is designed to explore the underlying hot carrier relaxation and transfer strategies within the SnSe/CdSe p-n heterostructure. SnSe/CdSe heterostructure is synthesized by hot injection followed by the cation exchange method. The epitaxial growth of the (400) plane of SnSe along the (111) plane of CdSe has been confirmed through HRTEM analysis. Transient absorption

(TA) studies demonstrate a drastic enhancement of the CdSe biexciton signal which points toward the hot carrier transfer from SnSe to CdSe in a short time scale. Afterward, these carriers are transferred back to SnSe. The observed delocalization of carriers in these two systems is crucial for an optoelectronic device. Further, we examine the ultrafast excited-state dynamics at the junction between Sb_2Se_3 and CdSe QDs in the $\text{Sb}_2\text{Se}_3/\text{CdSe}$ p-n heterostructure system. The enhanced intensity of the CdSe hot excitonic (1P) bleach in the heterostructure system confirmed the hot electron transfer, instead of getting trapped in the defect states present in Sb_2Se_3 , migrate from Sb_2Se_3 to the CdSe system. Further, both the 1S and 1P signals are dynamically very slow in the heterosystem, validating this charge migration phenomenon. Interestingly, recovery of the 1P signal is much slower than that of 1S which indicates the robustness of hot electron transfer in this unique heterojunction, that helps in increasing the carrier lifetime in the hot state. My next work is based on studying the interfacial charge transfer processes at the p-n junction of the 1D/0D SnS@CdS p-n heterostructure system. The structural and morphological properties presented that CdS QDs are uniformly anchored on the surface of SnS NRs resulting in an intimate contact between two components. The steady state and time resolved photoluminescence analysis demonstrated the transfer of photoexcited holes from CdS QDs to SnS NRs which was further confirmed by transient absorption studies. Moreover, the transient studies reveal the delocalization of electrons between the conduction band of SnS NRs and CdS QDs in the SnS@CdS heterostructure, resulting in efficient charge separation across the p-n hetero-junction. Finally, we have explored the charge transfer and recombination dynamics in $\text{Sb}_2\text{Se}_3/\text{CdS}$ thin film p-n heterojunction. The $\text{Sb}_2\text{Se}_3/\text{CdS}$ heterojunction film was fabricated using the thermal evaporation technique. The ultrafast studies reveal the electron transfer from Sb_2Se_3 to CdS thin film and spatial charge separation at the $\text{Sb}_2\text{Se}_3/\text{CdS}$ p-n junction. Moreover, the photocurrent response of $\text{Sb}_2\text{Se}_3/\text{CdS}$ heterojunction was greatly enhanced as compared to bare Sb_2Se_3 and CdS films under light illumination owing to improved separation rate of photogenerated charge carriers in heterojunction system, which correlates with our transient investigations, and are crucial factors for the fabrication of solar energy-based devices. In conclusion, we have investigated the intrinsic photophysical processes at the interface of some very prominent metal chalcogenides, which will open a new route for the fabrication of extremely effective photovoltaic and photocatalytic devices.

Table of Contents

Content	Page No.
<i>Dedication</i>	<i>iii</i>
<i>Declaration</i>	<i>v</i>
<i>Acknowledgements</i>	<i>vii-x</i>
<i>Abstract</i>	<i>xi-xii</i>
<i>List of Figures</i>	<i>xvii-xxvi</i>
<i>List of Tables</i>	<i>xxvii-xxviii</i>
<i>List of Schemes</i>	<i>xxix</i>
<i>List of Abbreviations</i>	<i>xxxi</i>
<i>List of Symbols</i>	<i>xxxv</i>
Chapter 1: Introduction	1-38
1.1. General Introduction.....	3
1.2. Metal chalcogenides	4
1.3. Nanocrystals and Quantum dots	4
1.3.1. Confinement effect in NCs	5
1.3.2. Particle-in-a sphere model	6
1.3.3. Effective mass approximation theory	7
1.3.4. Effect of dimensionality of material on the density of states	10
1.3.5. Charge separation in quantum dots	12
1.4. Semiconductor heterojunctions and their various types	12
1.5. Importance of p-n heterojunction	13
1.5.1. Theory of p-n heterojunctions	15
1.6. Marcus's theory of electron transfer	16
1.7. Different photophysical processes in semiconductor nanocrystals	17
1.7.1. Hot carrier relaxation dynamics in QDs	18
1.7.2. Phonon bottleneck	19
1.7.3. Auger recombination	19
1.7.4. Multiple Exciton generation (MEG)	20
1.7.5. Effect of carrier trapping on optical properties of QDs.....	21
1.7.6. Hot charge carrier extraction from semiconductor QDs	22
1.7.7. Charge transfer processes in p-n heterojunction.....	24

1.8. Overview and scope of the thesis	24
1.9. References	27
Chapter 2: Synthesis and Characterization Techniques.....	39-86
2.1. Synthesis techniques	43
2.1.1. Colloidal Synthesis: Hot injection method.....	43
2.1.2. Synthesis of colloidal p-n semiconductor heterostructures: Cation exchange	44
2.2. Fabrication of thin films	45
2.2.1. Spin Coating Method.....	45
2.2.2. Thermal evaporation technique	46
2.3. Synthesis procedures.....	47
2.3.1. Materials used.....	47
2.3.2. Synthesis of CZTS NPs	48
2.3.3. Synthesis of CdS QDs	48
2.3.4. Fabrication of CZTS/CdS heterojunction	48
2.3.5. Synthesis of SnSe NSs.....	49
2.3.6. Synthesis of CdSe QDs	49
2.3.7. Synthesis of SnSe/CdSe heterostructure	50
2.3.8. Synthesis of Sb ₂ Se ₃ /CdSe heterostructure.....	50
2.3.9. Synthesis of Sb ₂ Se ₃ QDs	50
2.3.10. Synthesis of SnS NRs	51
2.3.11. Synthesis of CdS QDs stock solution.....	51
2.3.12. Synthesis of SnS@CdS p-n heterojunction	51
2.3.13. Deposition of Sb ₂ Se ₃ film	52
2.3.14. Deposition of CdS film	52
2.3.15. Deposition of Sb ₂ Se ₃ /CdS thin film p-n heterojunction	52
2.4. Characterization Techniques	53
2.4.1. X-ray diffraction (XRD).....	53
2.4.2. X-ray Photoelectron Spectroscopy (XPS).....	55
2.4.3. Scanning Electron Microscopy (SEM).....	57
2.4.4. Transmission Electron Microscopy (TEM).....	58
2.4.5. Mott Schottky (MS) plots	63
2.5. Steady-state optical studies.....	63
2.5.1. Steady-state absorption spectroscopy (UV-Vis)	63
2.5.2. Photoluminescence spectroscopy	64

2.6.	Techniques to Monitor Ultrafast Processes in Semiconductor NCs	67
2.6.1.	Time-Correlated Single Photon Counting (TCSPC)	67
2.6.2.	Pump-Probe Transient Absorption (TA) spectroscopy	68
2.6.3.	Principle and origin of various signals in TA data	69
2.6.4.	Instrumentation of femtosecond transient absorption spectroscopy setup.....	71
2.6.4.1.	Ti-sapphire oscillator/seed laser: ultra-short pulse generation...	71
2.6.4.2.	Ti-Sapphire amplifier	73
2.6.4.3.	Pulse stretcher	73
2.6.4.4.	Pulse picker	74
2.6.4.5.	Pump laser	74
2.6.4.6.	Ti-sapphire amplifier: Regenerative amplifier	74
2.6.4.7.	Pulse compressor	75
2.7.	Optical Parametric Amplifier (OPA).....	76
2.8.	Transient Absorption Spectrometer.....	78
2.9.	Surface Xplorer _{TM} software.....	79
2.10.	References	79
Chapter 3: Probing Ultrafast Charge Separation in CZTS/CdS Heterojunctions through Femtosecond Transient Absorption Spectroscopy.....		87-110
3.1.	Introduction	91
3.2.	Results and Discussions	92
3.2.1.	Structural characterization	92
3.2.2.	Optical studies	94
3.2.3.	Ultrafast transient absorption studies	96
3.3.	Conclusion.....	104
3.4.	References	105
Chapter 4: Enhanced Charge Carrier Separation and Improved Bi-exciton Yield at the p-n Junction of SnSe/CdSe Heterostructures		111-142
4.1.	Introduction	115
4.2.	Results and discussion.....	118
4.2.1.	Synthesis and structural characterization of materials	118
4.2.2.	Optical studies	122
4.2.3.	Cyclic voltammetric and band edge measurements	124
4.2.4.	Transient absorption studies	128
4.3.	Conclusion.....	135
4.4.	References	136

Chapter 5: Efficient Hot Electron Transfer and Extended Separation of Charge Carriers at the 1P Hot State in Sb₂Se₃/CdSe p-n Heterojunction	143-170
5.1. Introduction	147
5.2. Results and discussion	148
5.2.1. Synthesis and characterizations	148
5.2.2. Optical studies	153
5.2.3. Transient absorption studies	156
5.3. Conclusion	163
5.4. References	164
Chapter 6: Ultrafast Hole Migration at the p-n Heterojunction of One Dimensional SnS Nanorods and Zero Dimensional CdS Quantum Dots ...	171-202
6.1. Introduction	175
6.2. Results and discussion	176
6.2.1. Structural and morphological characterizations	176
6.2.2. Optical Studies	183
6.2.3. Femtosecond transient absorption spectroscopy	188
6.3. Conclusion	195
6.4. References	195
Chapter 7: Ultrafast Electron Transfer and Efficient Charge Separation in Sb₂Se₃/CdS Thin Film p-n Heterojunction.....	203-226
7.1. Introduction	207
7.2. Results and Discussion	208
7.2.1. Structural and compositional studies	208
7.2.2. Optical studies	213
7.2.3. Transient absorption studies	213
7.3. Conclusion	220
7.4. References	221
Chapter 8: Conclusions and Future Perspective.....	227-232
8.1. Conclusions	229
8.2. Future perspective	231
List of Publications	233-236
List of Conferences	237
Permissions from Journals for reuse of content in thesis.....	239
Conference Certificates	247
Vita	257

List of Figures

Figure No.	Captions	Page No.
1.1	Schematic illustration of quantum confinement effect in semiconducting NCs or QDs	6
1.2	Energy band diagram (“E” vs “k”) for (A) direct and (B) indirect bandgap semiconductors	9
1.3	Schematic illustration of the variation of density of states with increasing quantum confinement	11
1.4	Schematic representation of charge carrier localization regions for different types of heterojunctions	13
1.5	Schematic illustration of the electron-hole separation under the influence of the internal electric field in a p–n heterojunction photocatalyst under light irradiation	14
1.6	Electrostatic potential from negative acceptor (-) and positive donor (+) ions near the junction	15
1.7	Potential energy versus nuclear coordinate plot in electron transfer reaction	16
1.8	A plot of electron transfer rate versus change in Gibb’s free energy, depicting three different regions of electron transfer reactions	17
1.9	Different photophysical processes in a semiconducting system, after photoexcitation	18
1.10	Schematic diagram of hot carrier relaxation through (A) phonon emission, (B) phonon bottleneck	19
1.11	Schematic of (A) MEG (biexciton) and (B) Augur process	20
1.12	Different trapping mediated recombination processes: (A) electron trapping, (B) hole trapping and (C) both electron and hole trapping	21
1.13	Absorption of an incident photon with energy higher than the bandgap energy (E_g) of a semiconductor. Excited electrons and holes are collectively called hot carriers, whose excess energy is ΔE_e and ΔE_h for hot electrons and hot holes, respectively. Upon de-excitation, the excess energy is converted to heat through the emission of phonons	23

1.14	Various photophysical processes in a semiconducting heterojunction system, after photoexcitation	24
2.1	(A) Classic La Mer mechanism for nucleation and growth for synthesis of monodisperse colloidal particle. (B) Typical hot injection synthesis setup for the synthesis of metal chalcogenide nanoparticles	43
2.2	Schematic of cation exchange reaction	45
2.3	Schematic diagram for thin film deposition via spin coating technique	46
2.4	(A) Picture of the instrumental set-up for thermal and magnetron sputtering system, and (B) Basic layout of the evaporation process	47
2.5	Diffraction of incident X-rays by a crystal and Bragg's law	54
2.6	The basic layout of powder X-ray diffractometer	54
2.7	The basic principle of XPS	55
2.8	Outline of an XPS setup	56
2.9	The basic layout of Scanning Electron Microscope showing the various parts of the instrument	57
2.10	The different signals generated when a high-energy electron beam interacts with the thin specimen	60
2.11	The basic layout of Transmission Electron Microscope showing the various parts of the instrument	61
2.12	Basic optical setup of steady state absorption spectrometer, showing different parts of the instrument	64
2.13	Optical layout of photoluminescence spectrofluorometer	66
2.14	Schematic of the TCSPC spectrophotometer	68
2.15	(A) Different types of TA signals; Bleach, SE, and PIA. (B) origin of signals	70
2.16	A Schematic diagram of transient absorption setup	70
2.17	The basic layout of femtosecond Ti-sapphire oscillator for generation of ultrashort laser pulses	72
2.18	Schematic illustration of femtosecond pulse stretcher	73
2.19	Schematic representation of Ti-sapphire amplifier	75

2.20	Optical layout of pulse compressor	76
2.21	The basic outline of an OPERA-SOLO setup	76
2.22	Optical layout of the Helios Fire transient absorption spectrometer	79
3.1	XRD patterns of (A) CZTS NPs, JCPDS lines show tetragonal structure of kesterite CZTS; (B) CdS QDs, JCPDS lines show zinc blend structure of CdS; (C) HR-TEM images of (a-c) CZTS NPs and (d) SAED pattern of corresponding CZTS NPs and (D) HRTEM images (a-c) of CdS QDs and (d) SAED pattern of corresponding CdS QDs.	93
3.2	(A) Steady-state optical absorption spectra of (a) CZTS NPs and tauc plot (inset), (B) Steady-state (b) optical absorption, and (c) corresponding photoluminescence (PL) spectra of CdS QD, (d) Time-resolved PL decay trace of CdS QD after exciting sample at 402 nm and monitoring at 445 nm (inset).	94
3.3	(A) Steady-state optical absorption spectra of (a) CZTS film (b) CdS film (c) CZTS/CdS film, (B) Photoluminescence (PL) spectra of (d) CdS film (e) CZTS/CdS film; Inset: Time-resolved PL decay trace of (f) CdS film and (g) CZTS/CdS film after monitoring at 455 nm and exciting at 402 nm.	95
3.4	(A) Transient absorption spectra of CZTS thin film at different probe delays following photo-excitation of 350 nm laser pulse with $200 \mu\text{J}/\text{cm}^2$ laser fluence; and (B) Transient decay kinetics of photo-induced absorption signal, monitored at 580nm (I: Ultrafast trapping of photo-excited carriers, II and III: Trap mediated slow recombination).	96
3.5	Fluence-dependent transient absorption kinetics of CZTS thin film on glass substrate after probing at wavelength 580 nm and exciting at 350 nm laser light. Laser power varied from $100 \mu\text{J}/\text{cm}^2 - 700 \mu\text{J}/\text{cm}^2$.	98
3.6	(A) Transient absorption spectra of CdS thin film at different probe delays, following photo-excitation of 350 nm laser pulse with $200 \mu\text{J}/\text{cm}^2$ laser fluence, and (B) Transient decay kinetics at (a) 432 nm (Band edge exciton) and (b) 457 nm (Bi-exciton).	99

- 3.7** Second order derivative of steady-state absorption of **(A)** CdS thin film **(B)** CZTS/CdS hetero-junction film. Early time TA spectra of **(C)** CdS (120 fs) thin film and of **(D)** CZTS-CdS hetero-junction (100 fs), which match well with the second order derivative of steady state optical absorption spectra (A and B) respectively. This observation clearly indicates the presence of a biexciton-induced stark effect in the TA spectra. **100**
- 3.8** **(A)** Transient absorption spectra of CZTS/CdS heterojunction film, following 350 nm photo-excitation, with $200 \mu\text{J}/\text{cm}^2$ laser fluence; (inset: Enlarged photoinduced absorption signature of CZTS in the red region of the spectra in heterojunction film); **(B)** Transient decay profiles of CZTS photoinduced absorption signal in absence and presence of CdS; **(C)** Formation and recovery dynamics of band edge bleach signal for CdS thin film and CZTS/CdS thin film probing at 432 and 434 nm respectively; Dotted lines represent enhancement of CdS exciton growth time in presence of CZTS in the hetero-junction film; and **(D)** Bi-exciton dynamics in pure CdS and CZTS/CdS, normalizing with respect to their excitonic bleach intensity. **101**
- 4.1** **(A) Left Panel:** Schematic illustration for the synthesis of SnSe/CdSe HS. *Right panel:* photographic image of prepared materials **(B)** Powder X-ray diffraction pattern of **(a)** SnSe NSs **(b)** CdSe QDs **(c)** SnSe/CdSe HS; JCPDS lines are also indicated **(C)** AFM image of SnSe NSs on the silicon substrate (**inset:** corresponding height profile). **119**
- 4.2** TEM and HRTEM images of **(a-d)** SnSe NSs, **(e-h)** CdSe QDs, and **(i-l)** SnSe/CdSe HS. Inset of **(k)** and **(l)** shows HRTEM images indicating the retained morphology of particles after cation exchange and the interface between the (111) plane of cubic CdSe and (400) plane of orthorhombic SnSe, respectively. **120**
- 4.3** Particle size distribution and SAED pattern of **(A, C)** SnSe NSs, and **(B, D)** CdSe QDs. **121**
- 4.4** EDX spectrum of SnSe/CdSe HS. **121**

4.5	Steady-state optical absorption spectrum of (A) (a) SnSe NSs, and τ_{auc} plot (inset); (B) Steady-state optical absorption of (b) CdSe QDs and (c) SnSe/CdSe HS; (C) Steady-state PL spectra of (d) CdSe QDs and (e) SnSe/CdSe HS; (inset: PL of SnSe NSs) dispersed in toluene and (D) Time-resolved PL decay trace of (f) CdSe QDs and (g) SnSe/CdSe HS after exciting the sample at 402 nm and monitoring at 569 nm.	123
4.6	Cyclic Voltammogram recorded for the SnSe NSs, CdSe QDs, and SnSe/CdSe HS. The dotted line in Figure (A) , (A(a)) , (B) represents the controlled CV in TBAP-DCM without the NCs sample and red solid lines for (A) SnSe, (A, a) CdSe and (B) SnSe/CdSe HS. The inset of Figure 4B shows the enlarged view of the anodic and cathodic peaks. Figure 4 (C, D, E) scan rate dependant current response for the CVs recorded for (C) SnSe, (D) CdSe, and (E) SnSe/CdSe HS. The inset of Figure 4 (C, D, E) shows the linear regression fitting for current values as a function of under square root of the scan rate. (F) Schematic energy band diagram of SnSe/CdSe HS, with small band offset (0.72 eV) at the interface.	126
4.7	TA spectra of the SnSe NSs at (A) early time scale and (B) longer time scale following photoexcitation of a 350 nm laser pulse with 200 $\mu\text{J}/\text{cm}^2$ laser fluence. Corresponding kinetic profiles monitoring at (C) 460 nm and (D) 590 nm.	129
4.8	(A) Transient absorption spectra of CdSe QDs following photoexcitation of 350 nm laser pulse with 200 $\mu\text{J}/\text{cm}^2$ laser fluence. (B) Transient dynamic profiles of 1S, 1P exciton, and band edge bi-exciton signals monitoring at 560, 459, and 605 nm.	130
4.9	Transient absorption spectra of the (A) SnSe/CdSe HS at different probe delays. (B) Comparative transient spectra of CdSe, SnSe, and the HS at 1 ps probe delay time. Comparative dynamic profiles of CdSe and SnSe/CdSe HS for (C) 1S exciton and (D) band edge bi-exciton. The experiments were carried out after exciting at 350 nm.	132
4.10	Transient absorption spectra of the (A) SnSe/CdSe HS at different probe delays. (B) Comparative transient spectra of CdSe, and SnSe/CdSe HS at 1 ps probe delay time. Comparative dynamic profiles of CdSe and SnSe/CdSe HS for (C) 1S exciton and (D) band edge bi-exciton. The experiments were carried out after exciting at 400 nm laser pulse.	134

5.1	Schematic diagram illustrating the synthetic process of $\text{Sb}_2\text{Se}_3/\text{CdSe}$ heterostructure and Sb_2Se_3 from CdSe QDs.	149
5.2	TEM and HRTEM images of bare CdSe QDs (A, D); Sb_2Se_3 QDs (B, E); $\text{Sb}_2\text{Se}_3/\text{CdSe}$ heterostructure (C, F); inset of Figure 5.2F: enlarged view of $\text{Sb}_2\text{Se}_3/\text{CdSe}$ heterostructure. XPS analysis of $\text{Sb}_2\text{Se}_3/\text{CdSe}$ heterostructure: high-resolution scan of (G) Sb $3d_{5/2}$, $3d_{3/2}$ (H) Cd $3d_{5/2}$, $3d_{3/2}$, (I) Se $3d_{5/2}$, Se $3d_{3/2}$ signals.	150
5.3	Particle size distribution of (A) CdSe QDs, (B) Sb_2Se_3 QDs, and (C) $\text{Sb}_2\text{Se}_3/\text{CdSe}$ heterostructure.	151
5.4	(A) XPS survey spectra and high resolution XPS spectra of (B) Cd $3d_{5/2}$, $3d_{3/2}$ (C) Se 3p signals for CdSe sample.	151
5.5	XPS survey spectra of (A) Sb_2Se_3 QDs, high-resolution XPS scan of (B) Sb 3d, and (C) Se 3d, signals for Sb_2Se_3 QDs.	152
5.6	Energy dispersive X-ray spectrum of $\text{Sb}_2\text{Se}_3/\text{CdSe}$ heterostructure. Inset: Observed atomic percentage of Sb, Cd, and Se.	153
5.7	(A) Powder X-ray diffraction pattern of (a) CdSe QDs, (b) Sb_2Se_3 QDs, and (c) $\text{Sb}_2\text{Se}_3/\text{CdSe}$ heterostructure; JCPDS lines are also specified; (B) Steady-state optical absorption spectrum of (a) CdSe QDs, (b) Sb_2Se_3 QDs, and (c) $\text{Sb}_2\text{Se}_3/\text{CdSe}$ heterostructure; Inset : tauc plot of Sb_2Se_3 ; (C) Steady-state PL spectra of (a) CdSe QDs, (b) Sb_2Se_3 QDs, and (c) $\text{Sb}_2\text{Se}_3/\text{CdSe}$ heterostructure, upon 400 nm photoexcitation; (D) Energy level positions of Sb_2Se_3 QDs and CdSe QDs as calculated from both the XPS spectra and the Tauc plot.	154
5.8	Time-resolved photoluminescence (PL) measurements for CdSe and $\text{Sb}_2\text{Se}_3/\text{CdSe}$ heterostructure after exciting the samples at 402 nm and lifetime is monitored at 587 nm and 601 nm for CdSe QDs and $\text{Sb}_2\text{Se}_3/\text{CdSe}$ heterostructure, respectively.	154
5.9	Determination of valance band positions of (A) Sb_2Se_3 QDs and (B) CdSe QDs from the XPS valence band spectra.	156

5.10	Transient absorption spectra of (A) Sb ₂ Se ₃ QDs, (B) CdSe QDs, and (C) Sb ₂ Se ₃ /CdSe hetero-structure at different probe delay following photoexcitation of a 410 nm. laser pulse with 200 μJ/cm ² laser fluence; (D) Transient decay kinetics of photo-induced absorption signal of Sb ₂ Se ₃ QDs monitored at 605 nm; (E) Bleach recovery kinetics of 1P excitonic bleach at 470 and 490 nm for CdSe QDs and Sb ₂ Se ₃ /CdSe heterostructure respectively; and (F) Bleach recovery kinetics of 1S excitonic bleach at 563 and 587 nm for CdSe QDs and Sb ₂ Se ₃ /CdSe heterostructure respectively.	158
5.11	(A) Transient absorption spectra of the Sb ₂ Se ₃ /CdSe heterostructure at different probe delays following photoexcitation with 750 nm laser pulse; and (B) Transient decay kinetics of negative bleach signal probed at 587 nm.	161
6.1	Schematic illustration for the preparation of 1D/0D SnS@CdS p-n heterojunction.	177
6.2	(A, D) TEM, (B, E) HR-TEM images and (C, F) XRD pattern of SnS NRs and CdS QDs, respectively (JCPDS data of (C) orthorhombic phase of SnS and (F) zinc-blende phase of CdS marked under the bottom).	178
6.3	(A, B) HR-TEM images of SnS@CdS HS, dotted green and yellow lines indicated SnS NRs and CdS QDs, respectively. and (C) XRD pattern of newly synthesized SnS@CdS HS (JCPDS values also marked under the bottom for the orthorhombic phase of SnS and top for the zinc-blende phase of CdS) and (D) Atomic model showing the interface between SnS NRs and CdS QDs viewed along the c direction (we have omitted some of the CdS QDs attached to SnS NRs for clarity).	179
6.4	(A, B) Mapping and (C) EDX spectrum of SnS NRs indicating the homogenous distribution of Sn and S elements. (Inset: Observed atomic percentage of Sn and S). (D, E) Mapping and (F) EDX spectrum indicating the homogenous distribution of Cd and S elements in the CdS QD. (Inset: atomic percentage of Cd and S).	180

6.5	EDX Mapping images of 1D/0D SnS@CdS HS, indicating the coexistence and homogenous distribution of (A) Sn, (B) Cd, and (C) S elements in the SnS@CdS HS, (D) EDX spectrum of SnS@CdS HS. Inset: Observed atomic percentage of Sn, Cd, and S.	181
6.6	XPS analysis of SnS NRs, CdS QDs, and SnS@CdS p-n heterojunction: (A) survey scan of (a) SnS NRs.; (b) CdS QDs, (c) SnS@CdS p-n heterojunction. High-resolution XPS spectra of (B) Cd 3d in (a) pristine CdS QDs and (b) SnS@CdS HS; (C) Sn 3d in bare (a) SnS and (b) SnS@CdS; and (D) S 2p in (a) pristine SnS NRs and (b) CdS QDs as well as in (c) SnS@CdS HS.	182
6.7	Mott Schottky plots of (A) SnS NRs and (B) CdS QDs measured at the frequency of 1kHz.	183
6.8	(A) Steady-state optical absorption spectra of CdS QDs, SnS NRs, and SnS@CdS HS (B) Tauc plot of SnS NRs (C) PL spectra for pristine CdS QDs, pristine SnS NRs and SnS@CdS HS in hexane upon 400 nm photoexcitation. (Inset: enlarged PL spectrum SnS@CdS HS) and (D) Time-resolved PL studies of bare CdS QDs and SnS@CdS HS after exciting the samples at 402 nm and the decay trace monitored at 462 nm.	184
6.9	XPS valence band spectra of (A) SnS NRs and (B) CdS QDs.	186
6.10	Band alignment of SnS@CdS p-n heterojunction calculated from XPS analysis.	186
6.11	(A) Photoluminescence up-conversion trace of CdS QDs and SnS@CdS HS; (B) Normalized photoluminescence up-conversion decay of CdS QDs and SnS@CdS HS dispersed in hexane monitored at 462 nm (bandedge emission) after exciting samples at 400 nm.	187
6.12	Transient absorption spectra of the (A) SnS NRs; (C) CdS QDs; (B) Transient PIA kinetics of SnS NRs probed at 607 nm. (D) Transient decay profiles of CdS QDs at 1S exciton and bandedge biexciton positions. The experiments were carried out after photo-excitation with a 350 nm laser pulse with 200 $\mu\text{J}/\text{cm}^2$ laser fluence.	189
6.13	Linear dependence of ΔA^{-2} vs. early probe delay time for SnS NRs at 350 nm pump excitation.	190

6.14	Transient absorption spectra of the (A) SnS@CdS HS at different probe delay. Inset: enlarged PIA signature in the red region of the spectra in the heterostructure system. Transient kinetics of CdS QDs and the SnS@CdS HS for the (B) 1S bleach and (C) band edge biexciton signal. (D) PIA signal of SnS NRs and SnS@CdS HS at 607 nm probe wavelength, all the experiments were carried out following 350 nm laser pulse with a 200 $\mu\text{J}/\text{cm}^2$ laser fluence.	191
6.15	Normalized kinetics of (A) bandedge bleach of CdS QDs and SnS@CdS HS, and (B) PIA of SnS NRs and SnS@CdS HS monitored at 607 nm probe wavelength, after photo excitation with 350 nm laser pulse.	192
6.16	(A) TA spectra of SnS@CdS HS at pump fluence of 200 $\mu\text{J}/\text{cm}^2$. Transient kinetics of (B) 1S bleach, (C) biexciton, and (D) PIA signal in SnS@CdS HS system upon 350 nm pump excitation at different pump fluences (100 $\mu\text{J}/\text{cm}^2$, 200 $\mu\text{J}/\text{cm}^2$ and 500 $\mu\text{J}/\text{cm}^2$).	194
7.1	Schematic of (A) film deposition by thermal evaporation technique and (B) picture of Sb ₂ Se ₃ /CdS thin film heterojunction.	209
7.2	(A) XRD pattern of (a) Sb ₂ Se ₃ , (b) CdS and (c) Sb ₂ Se ₃ /CdS film heterojunction; (B) XPS spectra of Sb ₂ Se ₃ /CdS film; High-resolution XPS of (C) Cd, (D) Sb, (E) S, and (F) Se elements.	209
7.3	XPS of Sb ₂ Se ₃ and CdS films (A) XPS spectrum of CdS film along with high-resolution XPS spectra of (B) Cd 3d, (C) S 2p. (D) XPS spectrum Sb ₂ Se ₃ film along with high-resolution XPS of (E) Sb 3d, (F) Se 3d elements.	210
7.4	(A) FESEM image of Sb ₂ Se ₃ @CdS film. (B) EDX Mapping images of Sb ₂ Se ₃ @CdS heterojunction, indicating the co-existence and homogenous distribution of (C) Sb, (D) Cd, (E) S, and (F) Se elements.	211
7.5	Energy dispersive X-ray spectrum of Sb ₂ Se ₃ /CdS thin film heterojunction. Inset: Observed atomic percentage of Sb, Cd, S, and Se elements.	211
7.6	Determination of valance band positions of (A) Sb ₂ Se ₃ and (B) CdS films from the XPS valence band spectra. (C) Band alignment of Sb ₂ Se ₃ /CdS heterojunction.	212

7.7	(A) Steady-state optical absorption spectrum of pristine Sb ₂ Se ₃ , CdS films, and Sb ₂ Se ₃ /CdS heterojunction. (B) Tauc plot for Sb ₂ Se ₃ film.	213
7.8	TA spectra of (A) Sb ₂ Se ₃ film, (B, C) formation and decay dynamics of Sb ₂ Se ₃ film monitored at 579 and 681 nm probe wavelengths. (D) Schematic diagram showing the different trapping and recombination dynamics of charge carriers in Sb ₂ Se ₃ film after the photoexcitation with a 410 nm laser pulse.	214
7.9	TA spectra of (A) CdS film, and (B) Sb ₂ Se ₃ /CdS heterojunction at different probe delays following photoexcitation of a 410 nm laser pulse with 200 μJ/cm ² laser fluence. (C) Bleach recovery kinetics of 1S excitonic bleach at 504 and 509 nm for CdS and Sb ₂ Se ₃ /CdS heterojunction, respectively. (D) Transient kinetics of the PIA signal of Sb ₂ Se ₃ and Sb ₂ Se ₃ /CdS heterojunction monitored at 681 and 650 nm, respectively.	216
7.10	(A) TA spectra of the Sb ₂ Se ₃ /CdS heterojunction at different probe delays following photoexcitation with 650 nm laser pulse. (B) Transient decay kinetics of bleach signal probed at 503 nm.	219
7.11	(A) I-V characteristics of the Sb ₂ Se ₃ /CdS heterojunction. (B) Transient photocurrent response of pristine Sb ₂ Se ₃ , CdS films and Sb ₂ Se ₃ /CdS heterojunction film with the periodic (25 s) under solar light illumination of 1 sun power density.	220

List of Tables

Table No.	Captions	Page No.
3.1	Kinetics fitting parameters at different key wavelengths for CZTS, CdS thin films, and CZTS/CdS heterojunction after exciting the samples at 350 nm.	103
3.2	Kinetics fitting parameters at different key wavelengths for CZTS, CdS thin films, and CZTS/CdS p-n heterojunction at 350 nm photo-excitation with different laser intensity. Laser Intensity was kept at 100 $\mu\text{J}/\text{cm}^2$, 200 $\mu\text{J}/\text{cm}^2$, 300 $\mu\text{J}/\text{cm}^2$, 500 $\mu\text{J}/\text{cm}^2$ and 700 $\mu\text{J}/\text{cm}^2$.	104
4.1	The various key structural parameters such as lattice parameters (hkl), interplanar spacing d_{hkl} (nm), strain (ϵ), and dislocation density (ρ_d) for SnSe NSs, CdSe QDs and SnSe/CdSe HS system.	123
4.2	Quantum yield calculation.	124
4.3	Summarized data for the electrochemical measurements (CV), the band structure parameters (VB vs. NHE, CB vs. NHE, VB vs. Vacuum (Vac), CB vs. Vac and Electrochemical (Eg) band gap)	127
4.4	Kinetic fitting parameters for SnSe NSs solution under 350 nm pump excitation with 200 $\mu\text{J}/\text{cm}^2$ laser fluence.	131
4.5	Kinetic fitting parameters at excitonic bleach and biexciton position for CdSe QDs and SnSe/CdSe HS system under 350 nm pump excitation with 200 $\mu\text{J}/\text{cm}^2$ laser fluence.	132
4.6	Kinetic fitting parameters at excitonic bleach and biexciton position for CdSe QDs and SnSe/CdSe HS system under 400 nm pump excitation with 200 $\mu\text{J}/\text{cm}^2$ laser fluence.	134
5.1	Fitting components of time-resolved luminescence for CdSe QDs and $\text{Sb}_2\text{Se}_3/\text{CdSe}$ heterostructure monitored at 587 nm and 601 nm, respectively upon 402 nm excitation.	155
5.2	Summarized data for XPS valence band spectra and the band structure parameters (VB vs NHE, CB vs NHE, VB vs Vacuum (Vac), CB vs Vac, and (Eg) Bandgap).	155

5.3	Kinetic fitting parameters of PIA signal of Sb ₂ Se ₃ QDs, excitonic bleach, and bi-excitonic position for CdSe QDs and Sb ₂ Se ₃ /CdSe heterostructure system upon 410 nm pump excitation with 200μJ/cm ² laser fluence.	159
5.4	Kinetic fitting parameters at excitonic bleach position in Sb ₂ Se ₃ /CdSe heterostructure system under 750 nm pump excitation.	162
6.1	Quantum yield calculation	185
6.2	Fitting components of time resolved photoluminescence for CdS QDs and SnS@CdS HS monitored at 462 nm upon 402 nm excitation.	187
6.3	Fluorescence up-conversion time constants of CdS QDs and SnS@CdS HS at 462 nm wavelength after exciting the samples at 400 nm (λ_{ex}). Parentheses indicate the weight percentage of the respective components.	188
6.4	Kinetic fitting parameters at excitonic bleach, biexciton position, and PIA signal for bare CdS QDs, SnS NRs and SnS@CdS HS system upon 350 nm pump excitation with 200μJ/cm ² laser fluence.	194
7.1	Fitted parameters for transient kinetic traces of the Sb ₂ Se ₃ film upon photoexcitation with 410 nm pump wavelength.	215
7.2	Kinetic fitting parameters at different key wavelengths for Sb ₂ Se ₃ , CdS thin films, and Sb ₂ Se ₃ /CdS heterojunction after photoexcitation of the samples with 410 nm pump wavelength.	218

List of Schemes

Scheme No.	Captions	Page No.
3.1	Simplified schematic illustrations of the relaxation pathway of photo-excited charge carriers in CZTS/CdS heterojunction after 350 nm pump irradiation.	102
4.1	Schematic Illustration of the different processes taking place in SnSe/CdSe heterostructure system upon (A) 350 nm and (B) 400 nm pump excitation. Here (a) corresponds to the transfer of hot carriers (both electrons and holes) from SnSe to the CdSe system and (b) implies the back transfer of band edge electrons and holes from CdSe to SnSe which is a thermodynamically viable process.	133
5.1	Simple Schematic representing the electron and hole transfer at the interface of Sb ₂ Se ₃ /CdSe heterostructure, for high energy (3.0 eV) pump excitation.	162
5.2	Schematic Illustration of the different processes taking place in Sb ₂ Se ₃ /CdSe heterostructure system upon 750 nm pump excitation.	162
6.1	Schematic illustration of different photophysical processes occurring at the interface of SnS@CdS p-n heterojunction.	193
7.1	Simple scheme representing charge transfer dynamics at the interface of Sb ₂ Se ₃ /CdS heterojunction for high-energy (3.0 eV) pump excitation.	217
7.2	Schematic Illustration of charge transfer processes taking place in Sb ₂ Se ₃ /CdS heterojunction system upon 650 nm pump excitation.	219

List of abbreviations

XRD	X-ray Diffraction
XPS	X-ray Photoelectron Spectroscopy
UV	Ultraviolet
PL	Photoluminescence
TCSPC	Time-Correlated Single Photon Counting
CB	Conduction Band
VB	Valance Band
E_g	Energy bandgap
QD	Quantum Dot
ODE	Octadecene
OA	Oleic Acid
OLM	Oleylamine
N₂	Nitrogen
TA	Transient Absorption
CV	Cyclic voltammetry
MS	Mott Schottky
fs	femtosecond
ns	nanosecond
ps	picosecond
NIR	Near Infrared
PIA	Photoinduced absorption
GSB	Ground State Bleach
QY	Quantum Yield
SEM	Scanning Electron Microscopy
TEM	Transmission Electron Microscopy
SAED	Selected Area Electron Diffraction
SHG	Second Harmonic Generation
TRPL	Time Resolved Photoluminescence
1D	One-Dimensional

2D	Two-Dimensional
3D	Three-Dimensional
SnS	Tin Sulfide
YAG	Yttrium Aluminum Garnet
nm	Nanometre
CdS	Cadmium Sulfide
CdSe	Cadmium Selenide
JCPDS	Joint Committee on Powder Diffraction Standards
MEG	Multiple Exciton Generation
OPA	Optical Parametric Amplifier
CZTS	Copper Zinc Tin Sulfide
SnSe	Tin Selenide
FWHM	Full Width Half Maxima
EDS	Energy Dispersive X-ray Spectroscopy
CBO	Conduction Band Offset
VBO	Valence Band Offset
HRTEM	High Resolution Transmission Electron Microscopy
FESEM	Field Emission Scanning Electron Microscopy
Sb₂Se₃	Antimony Selenide
W	Tungsten
LaB₆	Lanthanum Hexaboride
CW	Continuous Wave
SDG	Synchronization and Delay Generator
GVD	Group Velocity Dispersion
SFG	Sum Frequency Generation
NPs	Nanoparticles
DFG	Difference Frequency Generation
HC	Hot carrier
PCE	Photo Conversion Efficiency
NC	Nanocrystal

RBF	Round Bottom Flask
HMDS	Hexamethyldisilazane
TOP	Trioctylphosphine
DDT	Dodecanethiol
LED	Light Emitting Diode
HS	Heterostructure
HJ	Heterojunction
eV	Electron Volt
NHE	Normal Hydrogen Electrode
TBAP	Tetrabutylammonium Perchlorate
DI	Deionized
Ti	Titanium
TA	Transient Absorption
CBM	Conduction Band Maximum
VBM	Valence Band Minimum
EMA	Effective Mass Approximation
PLQY	Photoluminescence Quantum Yield

List of symbols

T	Temperature
k_B	Boltzmann constant
λ	Wavelength
μ	Reduced mass
$^\circ$	Degree
τ_{avg}	Average lifetime
θ	Angle
ϕ	Work function
t	Time
V	Potential
τ	Time constant
I	Current
q	Charge
h	Planck constant
a_B	Bohr radius
ϵ	Dielectric constant

CHAPTER 1

Introduction

1.1. General Introduction

The energy crisis and environmental difficulties are now major worldwide challenges due to the quick expansion of modern industry and the rise in population.¹⁻⁴ Thus, it is highly encouraged to develop better alternative systems that are low-cost, renewable, earth-abundant, and have the potential to replace silicon in the electronic industry. Metal chalcogenide-based semiconductor materials have attracted immense attention in the research field. They are the best alternative materials for harvesting light as they possess unique electronic and optical properties such as, high absorption coefficient (10^4 - 10^5 cm⁻¹), tunable bandgap, high stability, low cost, and earth-abundant elements.⁵⁻⁷ The flexibility in bandgap engineering makes metal chalcogenides a promising candidate for next-generation semiconductor devices. However, the performance of these materials is limited by the fast recombination of photogenerated electron and hole pairs and inadequate band edge potentials.⁸ Thus, various strategies have been encountered to efficiently separate the electron-hole pairs including doping, metal loading, and engineering the heterojunctions. Among them, the engineering of p-n heterojunctions has indeed been considered one of the most promising strategies for the fabrication of reliable and efficient photovoltaic and photocatalytic devices.⁹⁻¹³ Due to the synergic absorption of two semiconductors with distinct bandgaps, the wide light response range of heterostructures expands to the entire solar spectrum, thus increasing their solar energy utilization efficiency. Moreover p-n heterojunctions offer bandgap tunability and spatial separation of electron-hole pairs owing to the presence of the built-in electric field.¹⁴⁻¹⁷ The p-n junctions are the fundamental and elementary building blocks of many electronic and energy storage devices, gas sensing devices, photovoltaics, photocatalysis viz. solar cells, light emitting diodes (LEDs), etc.¹⁸⁻²⁰ They are the primary active sites where the efficient charge transfer processes take place.²¹ The efficiency of any device is highly dependent on the dynamics of photoexcited charge carriers at the interface of heterojunctions. The fate of quasi-particles, excitons, and biexcitons including their relaxation, transfer, and recombination pathways directly impacts the overall efficiency of the photovoltaic devices. Therefore, an in-depth understanding of these photophysical processes is essential to repudiate processes that limit performance and to design efficient optical devices.^{22,23} Since these processes are ultrafast, therefore we have utilized transient absorption spectroscopy (TAS) to observe them. TAS can

examine ultrashort events that take place in a very short time scale viz picoseconds (ps- 10^{-12} s) and femtoseconds (fs- 10^{-15} s). In this thesis, we have used the femtosecond transient absorption (TA) technique to study charge transfer and relaxation dynamics at the p-n junction of different heterostructures. In some cases, we have also established a direct connection between photocurrent response and excited state charge carrier dynamics.

This chapter briefly introduces metal chalcogenide nanocrystals (NCs), quantum dots (QDs) and their fascinating optical properties, the effect of quantum confinement on the size and properties of QDs, different types of heterojunctions, p-n heterojunctions, and Marcus theory of electron transfer. The chapter further addresses the numerous photophysical processes that occur in semiconductor QDs as well as interfacial charge transfer processes that take place in semiconductor heterojunction upon photoexcitation

1.2. Metal chalcogenides

Metal chalcogenide nanocrystals (NCs) are nanoscale semiconductor materials composed of metal cations and chalcogen anions such as sulfur (S), selenium (Se), or tellurium (Te). Binary metal chalcogenide NCs consist of single anionic chalcogen and single cation, belonging to I₂-VI groups, II-VI groups, and IV-VI group compounds. Widely used II-VI group NCs are CdS, CdSe, CdTe, ZnS, ZnSe, etc. IV-VI group consists of SnS, SnSe, PbS, PbSe, etc. Alloyed metal chalcogenide QDs consist of either a single anionic chalcogen and more than one cation or more than one anionic chalcogen and cations. Alloyed metal chalcogenide nanoparticles are mainly focused on quaternary alloyed QDs I₂-II-IV-VI₄ such as CZTS, CZTSe, etc.²⁴ They have unique optical and electronic properties making them attractive for various applications, including optoelectronics, photocatalysis, photovoltaics, and biomedicine. In my thesis, we have worked on binary and quaternary metal chalcogenides.

1.3. Nanocrystals and Quantum dots

Recently, semiconductor NCs or QDs have emerged as a new category of materials and exhibit unique optical and electronic properties.^{25,26} Consequently, QDs provide a unique platform for the fast development of technologies like photocatalysis,

photovoltaics, and light-emitting devices.²⁷⁻³⁰ In semiconductor materials, the motion of charge carriers (electrons and holes) is restricted when the dimension of the material is less than the de-Broglie wavelength of carriers. Based on the confinement of charge carriers, the nanomaterial can be defined into three categories:

1. Two-dimensional (2D) – In two-dimensional materials, the charge carriers are confined in only one direction. For example, quantum wells or thin films.
2. One-dimensional (1D) – In one-dimensional material, the charge carriers are confined in two directions. For example, quantum wires.
3. Zero-dimensional (0D) – In zero-dimensional material, the charge carriers are confined in all three directions. For example, in quantum dots.

In general, quantum confinement causes an increase in the bandgap of the semiconductor while the size of the QDs decreases as shown in **Figure 1.1**. The QDs are semiconductor NCs where the motion of charge carriers (electrons and holes) is constrained in all three dimensions.^{31,32} They have properties intermediate to bulk materials and single molecules. Material properties depend on size, shape, and surface area to volume ratio when the crystal lattice size reduces to the nanometre level. The quantum confinement phenomenon in QDs enables us to modify optical characteristics such as absorbance and photoluminescence (PL) throughout the broad range of the optical spectrum by only maintaining the composition of the material constant while varying the size of the material. These materials provide numerous fundamental interesting aspects and different potential applications in biomedical,^{33,34} solar light harvesting,^{35,36} and light emitting devices³⁷ owing to their exciting properties including higher absorption coefficient, large dipole moments, optical tunability, etc.³³⁻³⁶

1.3.1. Confinement effect in semiconductor NCs

When light shines on a material, an electron is excited from the valence band (VB) to the conduction band (CB), creating an exciton or electron-hole pair. If m_h and m_e are the effective masses of holes and electrons, respectively, the exciton Bohr radius can be expressed by the following equation:

$$a_B = \epsilon \frac{m}{\mu} a_H$$

where ϵ is the dielectric constant of the material, a_H is the Bohr radius of the hydrogen atom (0.0052 nm), m is the rest mass of an electron, and μ is the reduced mass of the exciton (electron-hole reduced mass).

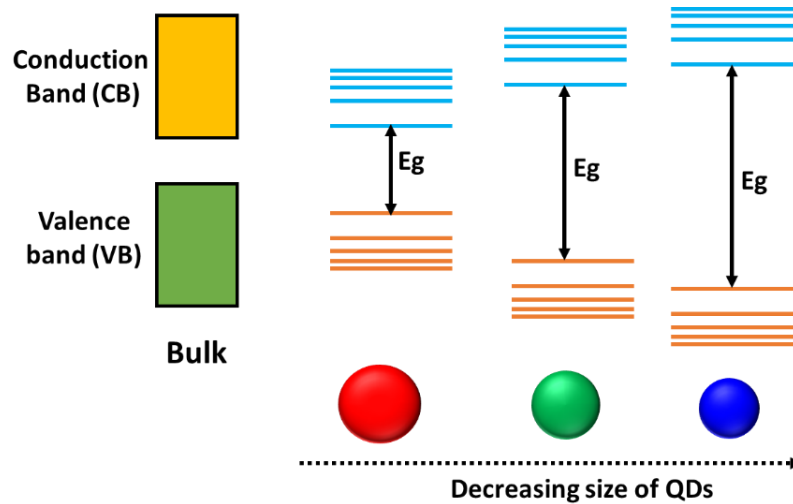


Figure 1.1. Schematic illustration of quantum confinement effect in semiconducting NCs or QDs.

The NCs display several types of confinement depending on the size of the NCs. If the size of NC (r) is less than the Bohr radius of electron, hole, and exciton ($r < a_e, a_h, a_e$), it shows a strong confinement regime. On the other hand, in the weak confinement region, the NC radius is smaller than the electron and hole but is larger than the exciton Bohr radius. If the radius is bigger than either electron (or hole) but smaller than the exciton Bohr radius, it will result in an intermediate confinement zone. Lowering the particle size results in greater confinement and more distinct energy levels.^{38,39}

1.3.2. Particle-in-a sphere model

The particle in a three-dimensional box is the most basic model to explain the quantum confinement phenomenon in semiconductor QDs. In QDs, as we discussed earlier, the electron and hole pairs are confined in all three directions which results in size quantization. The particle-in-a-sphere model has been employed to describe size quantization in terms of quantum mechanics. When a particle of mass “ m ” is confined in a sphere of radius “ a ” with the conditions for potential energy following the below equation⁴⁰:

$$V(r) = 0, \text{ for } r < a$$

$$V(r) = \infty, \text{ for } r > a$$

Where $V(r)$ is the potential energy of the particle. The wavefunction obtained by solving the Schrodinger equation has the form:

$$\Phi_{n,l,m}(r, \theta, \varphi) = C \frac{j_l(k_{n,l}r)Y_l^m(\theta, \varphi)}{r}$$

Here, C is the normalization constant, $j_l(k_{n,l}r)$ is the spherical Bessel function of l^{th} order and $Y_l^m(\theta, \varphi)$ is the spherical harmonics.

From this, the particle energy can be calculated from the eigenvalue of the Schrodinger equation

$$E_{n,l} = \frac{\hbar^2 k_{n,l}^2}{2m} \quad \text{where, } k_{n,l} = \frac{\alpha_{n,l}}{a}$$

$$E_{n,l} = \frac{\hbar^2 \alpha_{n,l}^2}{2ma^2}$$

According to Schrödinger's wave theory, there is no potential energy inside the sphere. Thus, the only source of energy that contributes to the total is the electron's kinetic energy which is highly dependent on the size of the QDs. The quantized state may be characterized by distinct quantum numbers like n (1, 2, 3...), l (s, p, d...), and m since the eigenfunctions are analogous to atoms. This model gives an approximate solution for the size dependent electronic structure of quantum confined particles. According to this model, the sphere is empty and the particle within has been liberated from all forms of perturbation. But in a crystal, the semiconductor is made up of several atoms. After considering effective mass approximation theory, this restriction can be eliminated.

1.3.3. Effective mass approximation theory

In contrast to what the particle-in-a-sphere model predicts, the semiconductor NCs are composed of atoms. Therefore, effective mass approximation (EMA) is used to realistically depict the photo-excited carriers inside a sphere.⁴¹ Here, the valence and conduction bands in bulk semiconductors are represented by parabolic isotropic

bands. According to the block theorem, the wavefunction of bulk semiconductors can be presented as

$$\psi_{nk}(r) = u_{nk}(r) \exp(ik \cdot r)$$

Where " $u_{nk}(r)$ " is the function of the crystal lattice's periodicity, "n" stands for the band index label (n = c for the conduction band and n = v for the valence band), and "k" is the wave vector. The "E" vs. "k" plot energy level of the wave function is shown in **Figure 1.2**. The bands are taken to be parabolic for simplicity in the effective mass approximation. In general, this approximation classifies semiconductors into two types: direct band gap and indirect band gap semiconductors. In the case of a direct band gap semiconductor, the maxima of the VB and minima of the CB both lie at k=0, whereas in the case of an indirect band gap semiconductor, the conduction band minimum is apart from k=0. As a result, to follow the Frank-Condon principle, electronic transitions from the VB to the CB require phonons for indirect bandgap semiconductors.

According to effective mass approximation the energy of valence and conduction band can be written a

$$E_k^c = \frac{\hbar^2 k^2}{2m_{eff}^c} + E_g$$

$$E_k^v = - \frac{\hbar^2 k^2}{2m_{eff}^v}$$

Where E_g represents the band gap of bulk semiconductor and the superscript "c" and "v" stand for valence and conduction bands, respectively. The m_{eff}^c and m_{eff}^v are the effective mass of the electron in the conduction band and the hole in the valence band, respectively. In this approximation, the charge carriers are considered as a free particle with effective mass m_{eff} . The scope of this approximation, however, is restricted to bulk semiconductors when the parabolic nature of the valence and conduction bands is assumed.

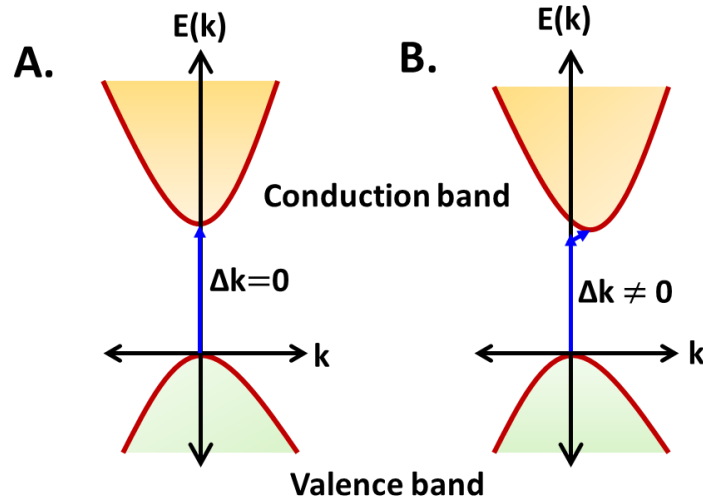


Figure 1.2. Energy band diagram (“E” vs “k”) for (A) direct and (B) indirect bandgap semiconductors.

For single particle systems like electrons, holes and exciton, this model has been modified using envelop function approximation. According to this theorem, the wavefunction of a single particle is given as:

$$\psi_{sp}(r) = \sum_i^k C_{nk} u_{nk}(r) \exp(ik \cdot r)$$

where C_{nk} is the expansion coefficient that satisfies the spherical boundary conditions.

Upon considering the weak dependence of $u_{nk}(r)$ on k, the wavefunction equation can be simplified as:

$$\psi_{sp}(r) = u_{n0}(r) \sum_k C_{nk} \exp(ik \cdot r) = u_{n0}(r) f_{sp}(r)$$

Here, $f_{sp}(r)$ is referred to as a single-particle wave function. Index “n” denotes the conduction and valence band for electron and hole, respectively. Thus, the exciton envelop wavefunction can be written as the combination of electron and hole envelop function. The exciton or electron-hole pair (ehp) energy can be expressed by the following equation⁴²:

$$E_{ehp} = E_g + \hbar^2 \left(\frac{k^2}{2m_{eff}^c} + \frac{k^2}{2m_{eff}^v} \right)$$

$$E_{ehp} = E_g + \frac{\hbar^2}{2a^2} \left(\frac{\alpha^2}{2m_{eff}^c} + \frac{\alpha^2}{2m_{eff}^v} \right)$$

In exciton, the electron and hole pair experience strong coulombic interactions. The coulomb energy varies inversely with particle radius. So, the overall energy of exciton in QD can be written as:

$$E_{ehp} = E_g + \frac{\hbar^2 \pi^2}{2m_{eh} a^2} \left(\frac{\alpha^2}{2m_{eff}^c} + \frac{\alpha^2}{2m_{eff}^v} \right) - \frac{1.8 e^2}{\epsilon a}$$

Where, m_{eh} is the reduced mass of the electron and hole pair.

Hence, the final energy of the exciton depends on three parameters: the material's band gap (E_g), confinement energy, coulomb energy, and radius (a) of the QD. On a decrease in the size of the nanoparticle i.e., in a strong confinement regime, the confinement energy term becomes more dominant than the coulomb energy term. Thus, the EMA theory successfully describes the discrete nature of the energy levels and enhancement in the band gap upon reducing particle size. In this thesis, we have synthesized CdX (X= S, Se) QDs and their heterostructures for charge transfer investigation.

1.3.4. Effect of dimensionality of material on the density of states

The density of states describes the distribution of allowed energy states in any material. It is defined as the number of available energy states per unit volume per unit energy interval and is denoted by $g(E)$. It is an important parameter that influences the optical properties and charge carrier dynamics processes in a material.^{43,44}

Let us assume that the particle is confined in a potential barrier with boundary conditions given below:

$$k_x = \frac{2\pi}{L} n_x, \quad k_y = \frac{2\pi}{L} n_y, \quad k_z = \frac{2\pi}{L} n_z$$

Here, "k" and "n" are the wave vector and real value, respectively.

The density of states for electrons is expressed as:

$$N = 2 \times \frac{4\pi}{3} \times k_f^3 \times \frac{V}{8\pi^3}$$

Where "V" is the volume per state and the factor "2" comes due to the presence of two spin states.

The density of states can be written as

$$g(E) = \frac{1}{V} \frac{\partial N}{\partial E}$$

For bulk (3D) semiconductor

$$g(E)^{3D} = \frac{\sqrt{2Em^3}}{\pi^2 \hbar^3}$$

Thus, for bulk or 3D materials, the density of states is continuous and is proportional to the square root of energy.

In the case of quantum well or 2D materials,

$$g(E)^{2D} = \frac{m}{\pi \hbar^2}$$

For 2D materials, the density of states is independent of energy.

For quantum wire or 1D materials, density of states is expressed as,

$$g(E)^{1D} = \frac{m}{\pi \hbar} \sqrt{\frac{2m}{E}}$$

So, for 1D material, the density of the state is inversely proportional to the square root of the energy.

Since the charge carriers are restricted in all three special directions for QDs or 0D systems, the energy states are discrete and the density of states may be represented as a delta function. The variation of density of states with increasing carrier confinement is shown in **Figure 1.3**.

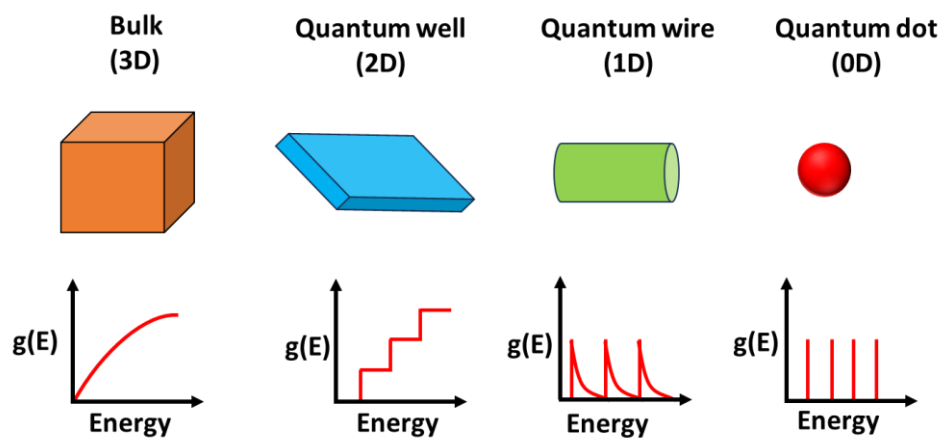


Figure 1.3. Schematic illustration of the variation of density of states with increasing quantum confinement.

1.3.5. Charge separation in quantum dots

A large surface-to-volume ratio in QDs causes the ions on the surface to trap the charge carriers, which results in charge carrier loss. Additionally, the strong columbic interaction inside the charge carrier promoted recombination due to confinement in a relatively tiny volume. These prohibit such QDs from being used in any device applications. However, the fast recombination of charge carriers may be avoided and electrons and holes can be separated by creating heterostructures, as will be covered below.

1.4. Semiconductor heterojunctions and their various types

When light falls on a semiconductor material electron and hole pairs are generated. As a result, it is highly challenging to separate photogenerated electron-hole pairs which is crucial for device applications. Despite being a highly challenging task, avoiding electron-hole recombination can be achieved with the right photocatalyst design. Many different techniques, such as doping, metal loading, and making heterojunctions, have been suggested to effectively separate the photogenerated electron-hole pairs in semiconductor photocatalysts. Among them engineering heterojunctions in photocatalysts has emerged as one of the most promising methods for the creation of advanced photocatalysts owing to its effectiveness and feasibility for the spatial separation of electron-hole pairs. A heterojunction is an interface between two different semiconductor materials within a device or a structure. Depending upon the CB and VB offset between different semiconductor materials, different possibilities can be identified as shown in **Figure 1.4**. In Type-I or straddling gap heterojunctions, the conduction band minimum (CBM) and the valence band maximum (VBM) of one material lie within the CBM and VBM of the other material, respectively. This alignment results in the confinement of both electrons and holes in one of the semiconductor materials, leading to strong carrier localization.^{45,46} Thus, the electron-hole pairs cannot be successfully separated because both electrons and holes accumulate on the same semiconductor. In Type-II or staggered gap heterojunctions, the CBM and VBM of the second semiconductor lie below the CBM and VBM of the first semiconductor, respectively. As the lowest energy state of electron and hole reside in distinct semiconductors, the energy gradient at the interfaces tends to

spatially separate them on different sides of the heterojunction. This spatial separation is useful for applications such as photodetectors and solar cells.⁴⁷⁻⁵⁰ Similar to the type-II heterojunctions, the type-III or broken gap heterojunctions have a staggered gap that is so severe that the bandgaps do not overlap. Because of this, type-III heterojunctions cannot allow for electron-hole migration or separation between the two semiconductors, making them unsuitable for improving electron-hole pair separation.

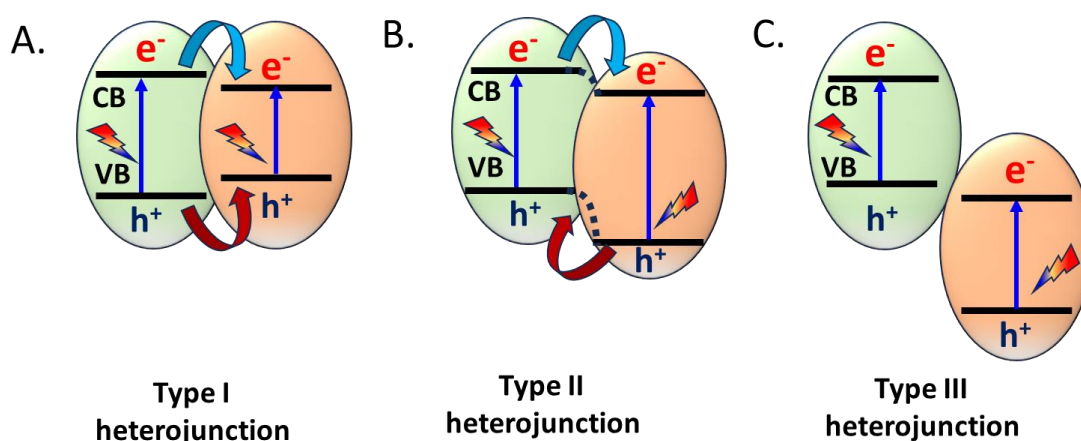


Figure 1.4. Schematic representation of charge carrier localization regions for different types of heterojunctions.

1.5. Importance of p-n heterojunction

Although the type-II heterojunction can separate electron-hole pairs in space but the boost in electron-hole separation that has been obtained across a type-II heterojunction is insufficient to stop the ultrafast electron-hole recombination on the semiconductor. Thus, to overcome these limitations, p-n semiconductor heterojunctions were proposed. The goal is to accelerate the migration of electron-hole pairs across the heterojunction, thereby enhancing photocatalytic performance.⁵¹ William Shockley made important contributions to the p-n junction hypothesis. He developed Shockley diode equation. A semiconductor diode's current-voltage characteristics are described by the Shockley diode equation. This equation served as the basis for understanding other semiconductor devices like p-n junctions.⁵² Semiconductor p-n heterojunction is fabricated by combining p-type and n-type semiconductors (**Figure 1.5**). Before light irradiation, there is a diffusion of electrons from the n-type semiconductor to the p-type semiconductor, leaving positively

charged ions and holes from the p-to-n-type semiconductor, leaving negatively charged ions. When the p-type and n-type semiconductors are exposed to light with energy equal to or higher than their bandgap value, both types of semiconductors get excited and generate electron-hole pairs. The photogenerated electrons and holes in the p-type and n-type semiconductors migrate under the influence of the internal electric field to the CB of the n-type semiconductor and the VB of the p-type semiconductor, respectively. This spatial separation of electron-hole pairs contributes to the improved photocatalytic performance. The electron-hole separation process is thermodynamically feasible because the CB and the VB of the p-type semiconductor are normally located higher than those of the n-type semiconductor in a p-n heterojunction photocatalyst. The electron-hole separation efficiency in p-n heterojunction photocatalysts is faster than that of type-II heterojunction photocatalysts due to the synergy between the internal electric field and the band alignment.⁵³ In my thesis work, we have synthesized p-n heterojunctions employing CZTS, SnS, SnSe and Sb₂Se₃ semiconductors as a p-type material and CdX (X=S, Se) as n-type semiconductor material.

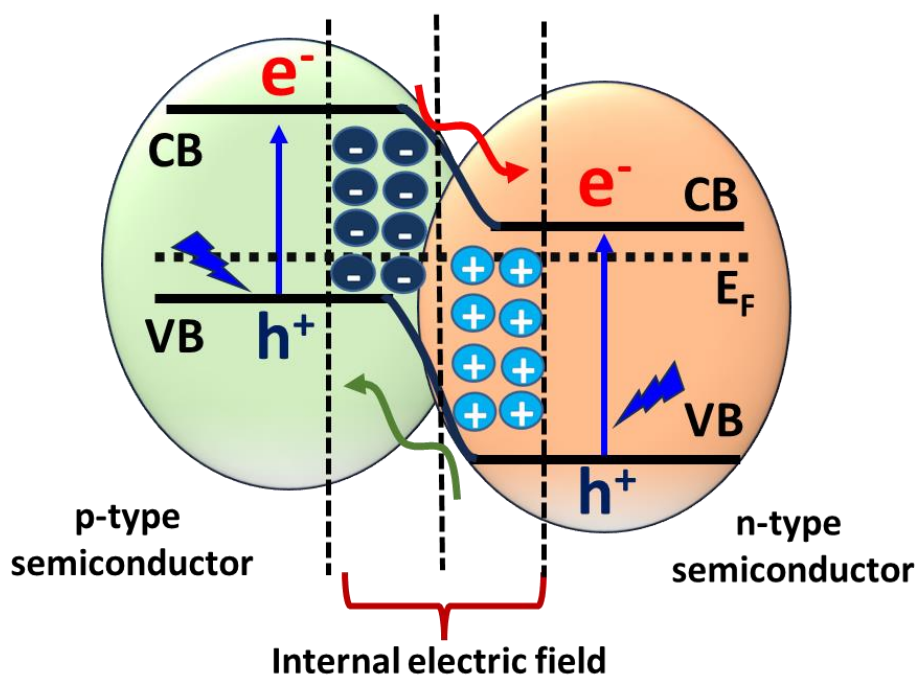


Figure 1.5. Schematic illustration of the electron-hole separation under the influence of the internal electric field in a p-n heterojunction photocatalyst under light irradiation.

1.5.1 Theory of p-n heterojunctions

A small charge transfer by diffusion leaves behind on the p-side an excess of negative (-) ionized acceptors and on the n-side an excess of positive (+) ionized donors. This charge double layer creates an electric field directed from n to p that inhibits diffusion and thereby maintains the separation of the two carrier types. Because of this double layer, the electrostatic potential in the crystal takes a jump in passing through the region of the junction as represented in **Figure 1.6**.

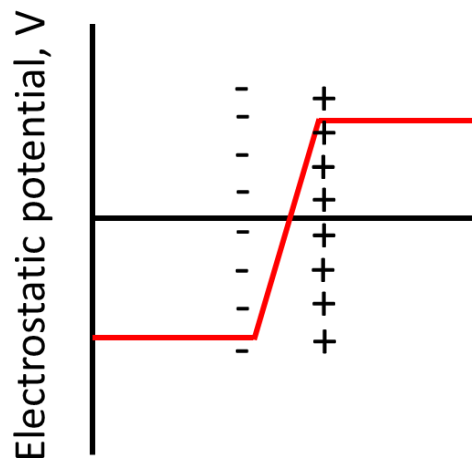


Figure 1.6. Electrostatic potential from negative acceptor (-) and positive donor (+) ions near the junction.

The potential gradient inhibits diffusion of holes from the p-side to the n-side, and it inhibits diffusion of electrons from the n-side to the p-side. The electric field in the junction region is called the built-in electric field.

The electric currents of holes and electrons are additive so that the total forward electric current is given by the following equation.

$$I_D = I_s [\exp (qV/k_B T)-1]$$

where I_D is the diode current, I_s the reverse bias saturation current, V is voltage, k_B is the Boltzmann constant, q represents the elementary charge and T is absolute temperature. This equation is well satisfied for p-n junctions and is called Shockley ideal diode equation.

1.6. Marcus's theory of electron transfer

The Marcus theory explains the complete mechanism of the electron or charge transfer process. According to electron transfer (Marcus) theory, the rate of electron transfer can be expressed by the following equation,^{54,55}

$$k_{ET} = k \frac{k_B T}{h} \exp\left(-\frac{\Delta G_{ET}^\ddagger}{k_B T}\right)$$

$$\text{here, } \Delta G_{ET}^\ddagger = \left(\frac{\Delta G_{ET}^0 + \lambda}{4\lambda}\right)^2$$

where, k is the adiabaticity parameter ($k=1$ for adiabatic reaction, and $k<1$ for non-adiabatic reaction). λ is the reorganization energy which is the energy required to reorganize the reactants and their surrounding solvent from the product without the transfer of electrons. ΔG_{ET}^\ddagger is the activation energy for electron transfer, ΔG_{ET}^0 is the difference in free energy of the reactant and product, also called the driving force for the reaction, k_B is the Boltzmann constant, h is the Planck constant and T is for absolute temperature. Thus, the rate of electron transfer depends on the change in free energy (ΔG_{ET}^0) and reorganization energy (λ) parameter. **Figure 1.7** shows the plot of potential energy of reactant (R) and product (P).

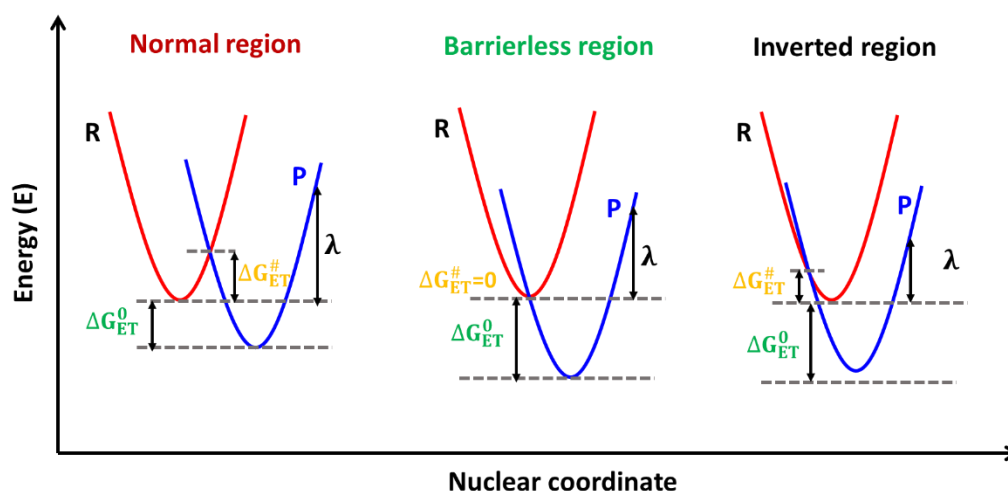


Figure 1.7. Potential energy versus nuclear coordinate plot in electron transfer reaction.

According to the values of ΔG_{ET}^0 and λ . Three Marcus regions can be constructed for a non-adiabatic case (**Figures 1.8**).⁵⁶

- a) **Normal region:** The region is referred to as a normal region when $-\Delta G_{ET}^0 < \lambda$. Here, the rate of electron transfer increases with an increase in the value of free energy difference.
- b) **Barrierless region:** When, $-\Delta G_{ET}^0 = \lambda$. In this situation the activation energy for electron transfer $\Delta G_{ET}^0 = 0$
- c) **Inverted region:** When $-\Delta G_{ET}^0 > \lambda$. In this case, the rate of electron transfer decreases with increasing the value of free energy difference.

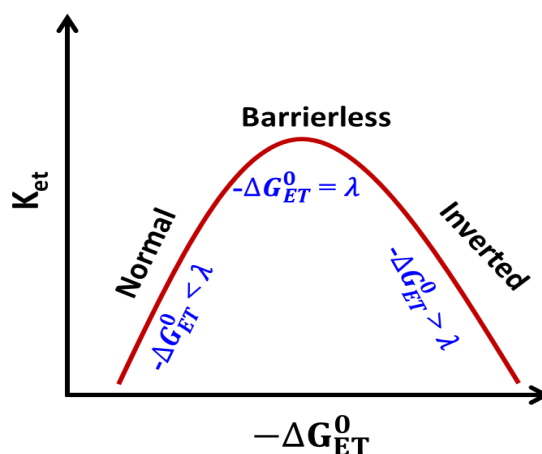


Figure 1.8. A plot of electron transfer rate versus change in Gibb's free energy, depicting three different regions of electron transfer reactions.

The Marcus-Hush equation has been used instead of the Marcus equation in an adiabatic situation which is expressed below

$$k_{ET} = \frac{2\pi}{\hbar} |H_{DA}^2| \frac{1}{\sqrt{4\pi\lambda k_B T}} \exp\left(-\frac{(\lambda + \Delta G_{ET}^0)^2}{4\lambda k_B T}\right)$$

Here, H_{DA}^2 represents the electron coupling between donor and acceptor wavefunction. For adiabatic reaction, $|H_{DA}| \gg k_B T$ whereas $|H_{DA}| < k_B T$ for non-adiabatic reaction.

1.7. Different photophysical processes in semiconductor nanocrystals

When semiconducting material is excited with energy (process 1) greater than the bandgap of material, it results in the formation of hot electron and hole pairs in the high energy states. The hot charge carriers relax to the lowest energy state or bandedge (process 2). Once the electron and hole are in the lowest energy state, they

can recombine radiatively to give photoluminescence (process 3). However, the hot as well as thermalized electron or hole can get trapped (process 4). In the presence of suitable molecules or other nanoparticles having favourable energy states both the hot and thermalized electron (and hole) can be transferred or extracted (processes 5 and 6) as depicted in **Figure 1.9**. In my work, I have fabricated different heterojunctions to extract the charge carriers. This process is very important for photovoltaic and photocatalytic applications.

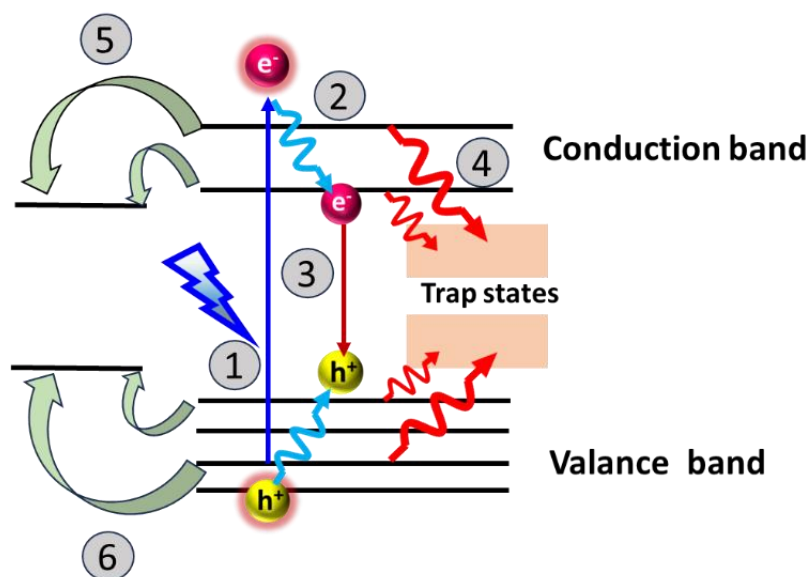


Figure 1.9. Different photophysical processes that take place in a semiconducting system, after photoexcitation.

1.7.1. Hot carrier relaxation dynamics in QDs

When a photon with energy higher than the band gap energy of semiconductor QD is absorbed, hot exciton (electron-hole pairs) is generated. The hot carriers both hot electrons and hot holes can relax to the corresponding bandedge through different relaxation pathways. Since the energy spacing between intrabands in a bulk semiconductor is smaller than thermal energy, therefore, the carrier relaxation (cooling) occurs via phonon emission.⁵⁷⁻⁵⁹ However, in quantum dots the energy gap between two intraband states is higher than thermal energy, therefore, the hot carrier relaxes in a variety of ways, including Auger recombination, phonon bottleneck, and electron-hole energy transfer.⁶⁰⁻⁶²

1.7.2. Phonon bottleneck

In semiconductor QDs, the relaxation of hot excitons to their lowest electronic state is impeded by a phenomenon known as phonon bottleneck.^{63,64} The electronic states are separated by large energies (fractions of eV) in QDs compared to the phonon energies of tens of meV. Therefore, the relaxation of hot electrons through transferring excess energy to phonon requires multiple phonon emissions which is a very slow process. The expected slow cooling of hot electrons in QDs is known as *phonon bottleneck* (**Figure 1.10**).⁶⁵⁻⁶⁷ Such multi-phonon relaxation time can be estimated by⁶⁸

$$\tau = \frac{1}{\omega_{LO}} \exp\left(\frac{\Delta E}{k_B T}\right)$$

Where ΔE is the energy spacing between the intraband states of the CB and ω_{LO} is the frequency of the longitudinal optical phonon. $k_B T$ is the thermal energy where k_B is Boltzmann constant and T is the absolute temperature. Thus, carrier relaxation is mediated by interaction between the electron and longitudinal optical phonon which increases the cooling time of the NCs while decreasing the size of NCs due to restrictions imposed by momentum and energy conservation.

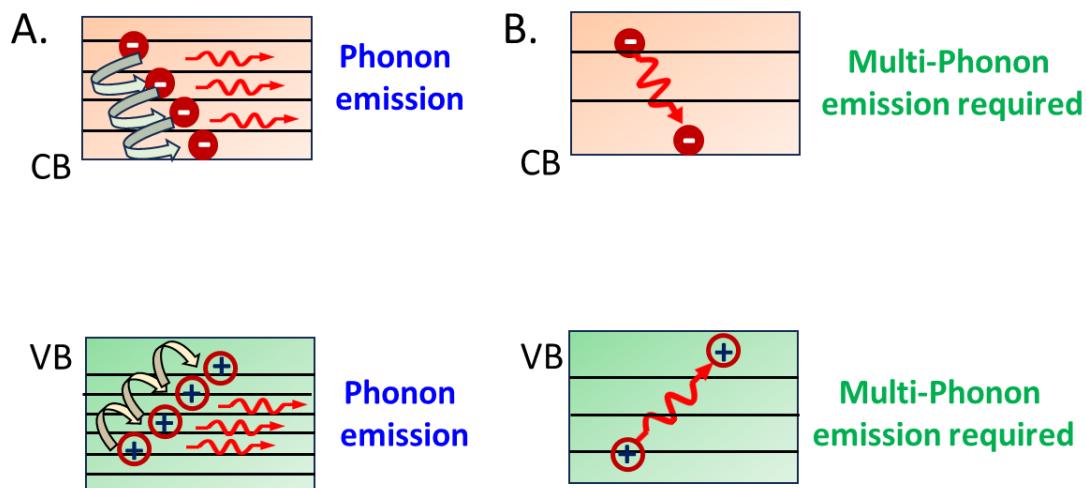


Figure 1.10. Schematic diagram of hot carrier relaxation through (A) phonon emission, (B) phonon bottleneck.

1.7.3. Auger recombination

It has been observed experimentally that the hot electron relaxation rate increases for QDs (CdSe) on decreasing the size which suggests the involvement of other relaxation channels.⁶⁹⁻⁷³ One major mechanism is the Auger-assisted relaxation process. It is a non-radiative process which require three particles to take place. Either

two electrons and one hole or two holes and one electron. In this process, the hot electron transfers its energy to the valence band hole as in the smaller size regime due to large coulomb attraction, the electron-hole become coupled to each other strongly. Due to the higher effective mass of holes ($m_h/m_e=6$ in CdSe) than electrons in II-VI semiconductors, holes are more easily able to relax through phonon emission. When the electron is decoupled from the hole the electron cooling becomes slower.

1.7.4. Multi Exciton Generation (MEG)

In a particular semiconductor when the excitation energy of a photon has energy at least two times or more than the band gap of the semiconductor ($h\nu \gg E_g$), then during relaxation of hot exciton, the excess energy can generate another exciton within the semiconductor leading to biexciton. Depending on the photon energy sometimes more than two excitons can be generated which is more efficient for lower band gap materials such as PbS, PbSe, CdTe, etc. Such a process is commonly known as multi-exciton generation.⁷⁴⁻⁷⁶ Sometimes the process is also referred as impact ionization. The Augur process is reverse to the MEG phenomenon (**Figure 1.11**). The MEG process is beneficial for improving the efficiency of solar cells.⁷⁷ In this mechanism, the semiconductor having more than one exciton, can transfer energy to another exciton as a result hot exciton is created. The hot exciton can undergo relaxation in many different pathways. The hot exciton produced by the pump and the band-edge exciton produced by the probe beam interact Coulombically to form the biexciton. In my thesis work, we have noticed that CdSe biexciton signal intensity becomes much higher in SnSe/CdSe heterostructure when photoexcited with 350 nm laser pulse.⁶⁸

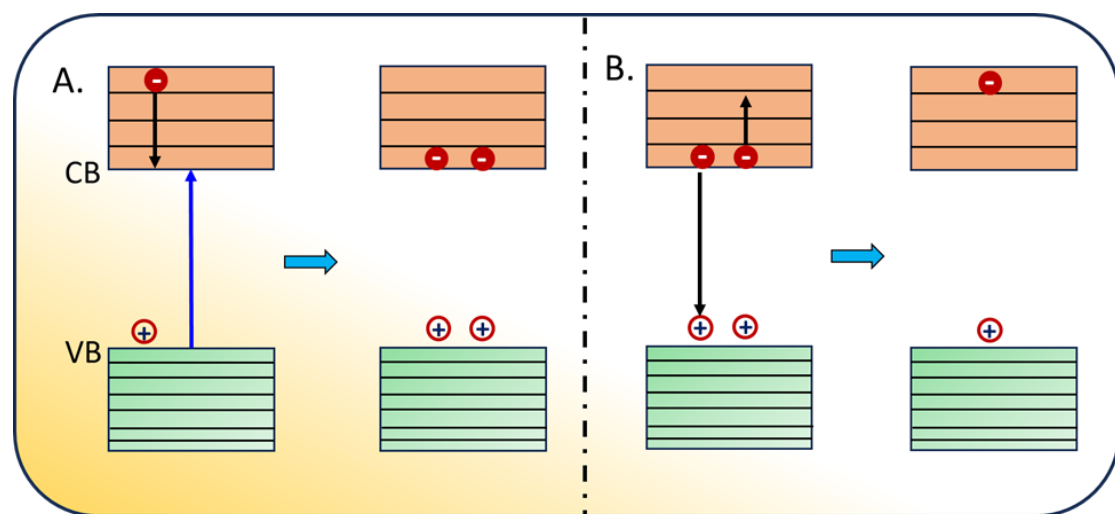


Figure 1.11. Schematic of (A) MEG (biexciton) and (B) Augur process.

1.7.5. Effect of carrier trapping on optical properties of QDs

The surface of quantum dots has a significant impact on their optical characteristics.⁷⁸⁻⁸⁰ With a decrease in particle size, the surface-to-volume ratio increases which results in more atoms at the surface. When compared to the atoms inside the QDs, these surface-located atoms are different. In contrast to atoms at the surface, those inside are totally bound and have completed their valency. In the band gap of QDs, these unfilled valency sites of the atoms at the surface lead to non-bonded energy states. These are referred to as dangling bonds or defects and are seen in picture and play a significant role in nanomaterials (**Figure 1.12**). Defects play an important role in nanomaterials. The optical characteristics are significantly influenced by the surface structure. Surface dangling bonds are created as a result of the atoms on the surface being under coordinated control, acting as localized states generating shallow or deep trap states in the energy band structure of the material. These trap centers act as a sink for the photoexcited charge carriers. Trapping of electron and hole pairs enhance the probability of non-radiative recombination and is a detrimental process which decrease the photoluminescence quantum yield.^{81,82} Charge trapping is usually a very fast process and it can accelerate the hot carrier cooling and the subsequent recombination processes.

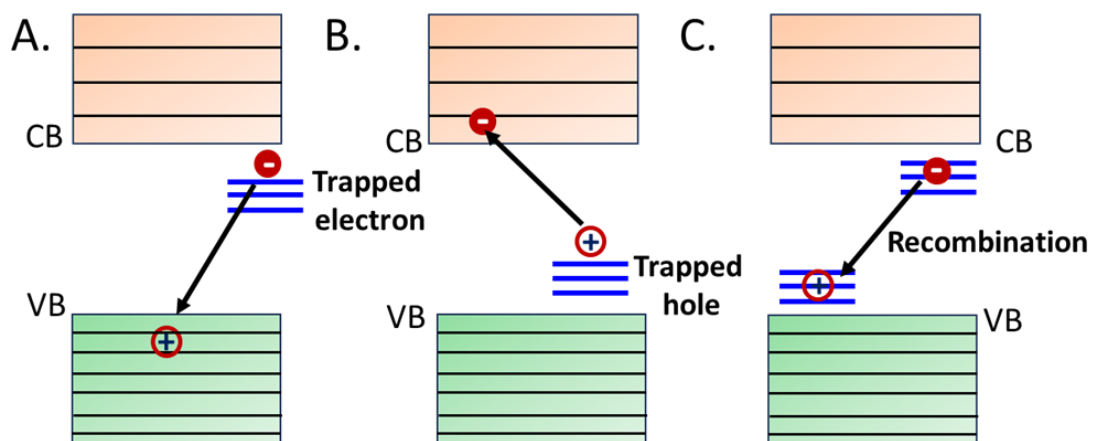


Figure 1.12. Different trapping mediated recombination processes: (A) electron trapping, (B) hole trapping and (C) both electron and hole trapping.

The trapping of charge carriers can be reduced by transfer or extracting these carriers to another material before trapping which can be efficiently done by making heterojunctions.⁸³ In my thesis work, we found that instead of trapping in the defect

states present in Sb_2Se_3 QDs, the hot electrons get transferred from photoexcited states of Sb_2Se_3 to the hot state of CdSe which increased the spatial separation of charge carriers in a hot excitonic state.⁸⁴

1.7.6. Hot charge carrier extraction from semiconductor QDs

Any photon with energy above the bandgap that strikes a semiconductor material produces electron and hole (e-h) pairs with extra kinetic energy equal to the energy difference between the incident photon energy and the bandgap energy of the material. These e-h pairs are referred to as hot charge carriers (**Figure 1.13**). In conventional solar cells, the excess energy of photons over the bandgap is wasted as heat. The hot carrier transfers their extra energy to heat upon deexcitation. The following equations illustrate how the extra energy is distributed among the hot carrier⁵⁸

$$\Delta E_e = (h\nu - E_g) \left[1 + \frac{m_e^*}{m_h^*} \right]^{-1}$$

$$\Delta E_h = (h\nu - E_g) - \Delta E_e$$

where m_e^* and m_h^* are the effective masses of electrons and holes, respectively. ΔE_e and ΔE_h are the excess energy of hot electrons and holes, respectively. ΔE_h is the difference in energy between VB and initial energy of photogenerated holes, whereas ΔE_e denotes the energy difference between the initial energy of photogenerated electrons and the CB. Since the photogenerated charge carriers formed by the absorption of photons larger than the bandgap are out of equilibrium, these excess energies manifest as kinetic energy in the corresponding charge carriers (holes and electrons). The hot carriers cool down to bandedge through carrier-carrier and carrier-phonon scattering. It continues until the energy of hot carrier is below the energy of longitudinal optical phonon. Hot carriers show a great potential in devices such as solar cells allowing to break the 33% Shockley Queisser limit thereby increasing the efficiency of light harvesting materials.⁸⁵ The effective utilization of such excess energy can be achieved by two alternative processes, namely (i) by-extracting the hot carriers before their rapid cooling, or (ii) by producing one or two more e-h pairs through impact ionization. The first process refers to the hot-carrier solar cell and the

second one is known as multiple exciton generation (MEG) or carrier multiplication.^{86,87} Hot carrier extraction is an unconventional and innovative approach to overcoming the unavoidable energy losses in solar cells.⁸⁸⁻⁹² As a result, hot carriers enable boosting the power conversion efficiency (PCE) beyond Shockley–Queisser (S–Q) limit. The concept is based on the thermal isolation of hot carriers and phonons (so that they may stay at different temperature regimes), followed by their selective extraction to the external circuit through efficient energy-selective contacts. Studies on hot carriers have been also extended to various significant applications such as photocatalysis,⁹³⁻⁹⁸ photodetection,^{99,100} and light emission.^{101,102}

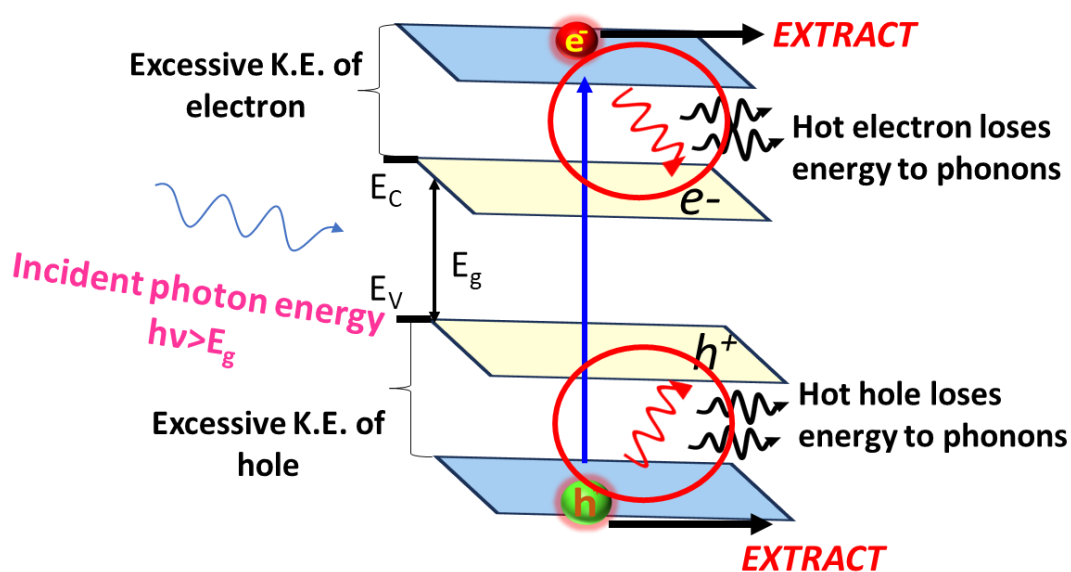


Figure 1.13. Absorption of an incident photon with energy higher than the bandgap energy (E_g) of a semiconductor. Excited electrons and holes are collectively called hot carriers, whose excess energy is ΔE_e and ΔE_h for hot electrons and hot holes, respectively. Upon de-excitation, the excess energy is converted to heat through the emission of phonons.

So, in order to extract these hot carriers in a material, it is extremely important to make its heterostructure with other suitable bandgap semiconductor material. In my thesis work, I have studied the charge transfer dynamics in various heterojunction systems using transient absorption spectroscopy.

1.7.7. Charge transfer processes in p-n heterojunction

Heterostructures consist of two or more different semiconductor materials and they exhibit a wide range of photophysical processes owing to the interaction between two constituent materials (**Figure 1.14**). These processes can be harnessed for various applications in optoelectronics, photovoltaics, and photonics.¹⁰³ When different materials are in close proximity, excitons can transfer their energy from one material to another which can be utilized in light harvesting in fluorescence resonance energy transfer-based sensors. P-n heterostructures provide built-in electric fields that facilitate charge carrier separation, which is essential for generating photocurrent. In some cases, for high-carrier density in narrow-bandgap materials, Auger recombination becomes significant. In heterojunctions, energy band alignment can be engineered to enhance or reduce Auger recombination rates. We have found that the Auger recombination rate in SnS@CdS p-n heterostructure gets reduced as compared to bare SnS NRs and CdS QDs due to significant hole transfer from CdS QDs to SnS NRs.⁹⁸

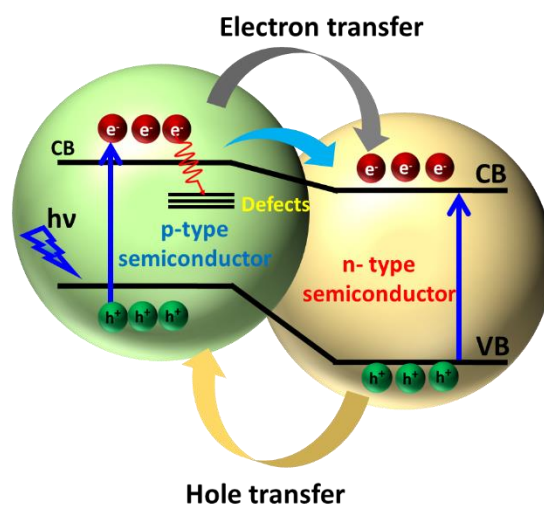


Figure 1.14. Various relaxation pathways in a semiconductor p-n heterojunction system, after photoexcitation.

1.8. Overview and scope of the thesis

The goal of the current thesis is to better understand the fundamental photophysics involved at the interface of p-n heterojunctions. Revealing the carrier cooling, trapping, and recombination processes is extremely important to understand the working mechanism and design of highly efficient optoelectronic devices. The present

dissertation focuses on exploring the interfacial charge transfer, trapping and relaxation dynamics in p-n semiconductor heterojunction systems using the femtosecond TA spectroscopy. The processes of charge separation and transport must be thoroughly understood to build highly effective devices.

The thesis has been organized as follows:

Chapter 1: This chapter describes the fundamentals of metal chalcogenides and different types of heterojunction systems. The effect of quantum confinement and band structure in semiconductor QDs, different types of heterojunctions, importance of p-n heterojunctions and Marcus's theory of electron transfer also has been explained. A brief description of the numerous ultrafast carrier relaxation processes that take place in nanomaterials and at the interface of heterostructures after photoexcitation has been addressed.

Chapter 2: This chapter deals with the synthesis techniques used to fabricate nanocrystals and their heterostructures along with the different experimental techniques employed for characterization, detailing the theory behind each approach and the comprehensive overview of the precise experimental setups used. The as-synthesized materials and their heterostructures were characterized using many different techniques, like X-ray diffraction (XRD), X-ray photoelectron spectroscopy (XPS) and Transmission electron microscopy (TEM). XRD give information of the crystal structure of materials. TEM and High-resolution TEM (HRTEM) provide information about the size and morphology of these materials, and for establishing the existence of any intimate contact between two systems in a heterojunction. The ground-state optical properties were monitored using steady-state optical absorption and photoluminescence (PL) spectroscopy. Time-correlated single photon counting (TCSPC) was utilized to determine the average PL lifetime of the synthesized materials. Finally, a detailed exploration of ultrafast charge transfer and relaxation dynamics was monitored through ultrafast transient absorption spectroscopy.

Chapter 3: The third chapter deals with the synthesis of $\text{Cu}_2\text{ZnSnS}_4$ (CZTS) nanoparticles and CdS quantum dots (QDs) using the hot-injection method followed by fabrication of CZTS, CdS, and CZTS/CdS heterojunction thin films with the help of a spin-coating strategy. Steady state and time-resolved photoluminescence studies

confirm the hole transfer from photoexcited CdS to CZTS and the hole transfer rate constant was found to be $0.366 \times 10^9 \text{ sec}^{-1}$. The ultrafast studies clearly suggest electron transfer from the CZTS to the CdS domain with a time constant of 0.14 ps, establishing the charge transfer efficiency in the heterointerface. Thus, our results demonstrate the fast charge separation in CZTS/CdS heterojunction film.

Chapter 4: This chapter reveals the underlying hot carrier relaxation and transfer strategies within the SnSe/CdSe p-n heterostructure. SnSe/CdSe heterostructure is synthesized by hot injection followed by the cation exchange of Cd^{2+} with Sn^{2+} ions. The epitaxial growth of the (400) plane of SnSe along the (111) plane of CdSe has been confirmed through HRTEM analysis. Transient absorption (TA) studies demonstrate a drastic enhancement of the CdSe biexciton signal which points toward the hot carrier transfer from SnSe to CdSe in a short time scale. Afterward, these carriers are transferred back to SnSe. The observed delocalization of carriers in these two systems is crucial for an optoelectronic device.

Chapter 5: Further, we examined the ultrafast excited-state dynamics at the junction between Sb_2Se_3 and CdSe QDs in the $\text{Sb}_2\text{Se}_3/\text{CdSe}$ p-n heterostructure system in this chapter. The enhanced intensity of the CdSe hot excitonic (1P) bleach in the heterostructure system confirmed that instead of getting trapped in the inter bandgap defect states present in Sb_2Se_3 , the hot electron transfer from Sb_2Se_3 to CdSe system. Further, both the 1S and 1P signals are dynamically very slow in the heterosystem as compared to bare CdSe validating the charge migration phenomenon. Interestingly, recovery of the 1P signal is much slower than that of 1S which indicates the robustness of hot electron transfer in this unique heterojunction, which helps in increasing the carrier lifetime in the hot state. This slower decay of hot energy excitons provides us a unique opportunity to extract these hot carriers for the betterment of an optical device.

Chapter 6: This chapter is based on studying hole transfer process at the p-n junction of 1D/0D SnS@CdS p-n heterojunction system. The structural and morphological properties confirm that CdS QDs are uniformly anchored on the surface of SnS NRs resulting in an intimate contact between SnS NRs and CdS QDs. The steady state and time resolved photoluminescence analysis demonstrated the transfer of photoexcited holes from CdS QDs to SnS NRs which was further confirmed by transient absorption

studies. Moreover, the transient studies reveal delocalization of electrons between the conduction band of SnS NRs and CdS QDs in SnS@CdS heterostructure. Furthermore, pump fluence studies proved that hole migration, rather than Auger recombination, is effectively occurring in SnS@CdS HS. These results will provide new insight into designing low cost and better energy storage devices.

Chapter 7: Finally, in this chapter, we have explored the charge transfer and recombination processes in Sb₂Se₃/CdS thin film p-n heterojunction. The Sb₂Se₃/CdS heterojunction film was fabricated using the thermal evaporation deposition technique. The ultrafast studies reveal the electron transfer from Sb₂Se₃ to CdS thin film and spatial charge separation at the interface of Sb₂Se₃/CdS heterojunction. Moreover, the photocurrent response of Sb₂Se₃/CdS heterojunction was greatly enhanced as compared to bare Sb₂Se₃ and CdS films under solar light illumination owing to improved separation rate of photogenerated charge carriers in heterojunction system, which correlates with our transient investigations, and are crucial factors for the fabrication of highly efficient solar energy-based devices. This ultrafast charge transfer process faster than the trapping process is crucial in optimizing the Sb₂Se₃ based heterostructures in photovoltaic applications.

The final chapter, **Chapter 8**, deals with the summarized discussion of all these results and future perspectives. These findings would help in the development of better solar cells, photo-detector, and photocatalytic devices.

1.9. References

- (1) Lewis, N. S. Toward Cost-Effective Solar Energy Use. *Science* **2007**, *315*, 798-801.
- (2) Zhao, G.; Rui, K.; Dou, S. X.; Sun, W. Heterostructures for Electrochemical Hydrogen Evolution Reaction: A Review. *Adv. Funct. Mater.* **2018**, *28*, 1803291.
- (3) Wang, Y.; Wang, Q.; Zhan, X.; Wang, F.; Safdar, M.; He, J. Visible Light Driven Type II Heterostructures and their Enhanced Photocatalysis Properties: A Review. *Nanoscale* **2013**, *5*, 8326-8339.

- (4) Khalate, S. A.; Kate, R. S.; Deokate, R. J. A Review on Energy Economics and The Recent Research and Development in Energy and the $\text{Cu}_2\text{ZnSnS}_4$ (CZTS) Solar Cells: A focus towards efficiency. *Sol Energy*. **2018**, *169*, 616-633.
- (5) Zhang, Y.; Zhou, Q.; Zhu, J.; Yan, Q.; Dou, S. X.; Sun, W. Nanostructured Metal Chalcogenides for Energy Storage and Electrocatalysis. *Adv. Funct. Mater.* **2017**, *27*, 1702317.
- (6) Selinsky, R. S.; Ding, Q.; Faber, M. S.; Wright, J. C.; Jin, S. Quantum Dot Nanoscale Heterostructures for Solar Energy Conversion. *Chem. Soc. Rev.* **2013**, *42*, 2963-2985.
- (7) Courel, M.; Andrade-Arvizu, J. A.; Vigil-Galán, O. Towards a $\text{CdS}/\text{Cu}_2\text{ZnSnS}_4$ Solar Cell Efficiency Improvement: A Theoretical Approach. *Appl. Phys. Lett.* **2014**, *105*, 233501.
- (8) Rao, V. N.; Ravi, P.; Sathish, M.; Vijayakumar, M.; Sakar, M.; Karthik, M.; Balakumar, S.; Reddy, K. R.; Shetti, N. P.; Aminabhavi, T. M.; Shankar, M. V. Metal Chalcogenide-Based Core/Shell Photocatalysts for Solar Hydrogen Production: Recent Advances, Properties and Technology Challenges. *J. Hazard. Mater.* **2021**, *415*, 125588.
- (9) Tiwari, K. J.; Neuschitzer, M.; Espíndola-Rodríguez, M.; Sanchez, Y.; Jehl, Z.; Vidal-Fuentes, P.; Saucedo, E.; Malar, P. Efficient $\text{Sb}_2\text{Se}_3/\text{CdS}$ Planar Heterojunction Solar Cells in Substrate Configuration with (hk0) Oriented Sb_2Se_3 Thin Films *Sol. Energy Mater. Sol. Cells* **2020**, *215*, 110603.
- (10) Calow, J. T.; Deasley, P. J.; Owen, S. J. T.; Webb, P. W. A Review of Semiconductor Heterojunctions. *J. Mater. Sci.* **1967**, *2*, 88-96.
- (11) Wang, H.; Zhang, L.; Chen, Z.; Hu, J.; Li, S.; Wang, Z.; Liu, J.; Wang, X. Semiconductor Heterojunction Photocatalysts: Design, Construction, and Photocatalytic Performances. *Chem. Soc. Rev.* **2014**, *43*, 5234-5244.
- (12) Di Liberto, G.; Cipriano, L. A.; Tosoni, S.; Pacchioni, G. Rational Design of Semiconductor Heterojunctions for Photocatalysis. *Chem. Eur. J.* **2021**, *27*, 13306-13317.

- (13) He, M.; Sun, K.; Suryawanshi, M. P.; Li, J.; Hao, X. Interface Engineering of pn Heterojunction for Kesterite Photovoltaics: A Progress Review. *J. Energy Chem.* **2021**, *60*, 1-8.
- (14) Wang, L.; Karuturi, S. K.; Zan, L. SnS₂-In₂S₃ pn heterostructures with enhanced Cr⁶⁺ reduction under visible-light irradiation. *Appl. Surf. Sci.* **2021**, *537*, 148063.
- (15) Yu, X.; Liu, J.; Genç, A.; Ibanez, M.; Luo, Z.; Shavel, A.; Arbiol, J.; Zhang, G.; Zhang, Y.; Cabot, A. Cu₂ZnSnS₄-Ag₂S Nanoscale p-n Heterostructures as Sensitizers for Photoelectrochemical Water Splitting. *Langmuir* **2015**, *31*, 10555-10561.
- (16) Bengas, R.; Lahmar, H.; Redha, K. M.; Mentar, L.; Azizi, A.; Schmerber, G.; Dinia, A. Electrochemical Synthesis of n-Type ZnS Layers on p-Cu₂O/n-ZnO Heterojunctions with Different Deposition Temperatures. *RSC Adv.* **2019**, *9*, 29056-29069.
- (17) Zhang, L.; Li, Y.; Li, C.; Chen, Q.; Zhen, Z.; Jiang, X.; Zhong, M.; Zhang, F.; Zhu, H. Scalable Low-Band-gap Sb₂Se₃ Thin-Film Photocathodes for Efficient Visible-Near-Infrared Solar Hydrogen Evolution. *ACS nano* **2017**, *11*, 12753-12763.
- (18) Li, H.; Zhou, Y.; Tu, W.; Ye, J.; Zou, Z. State-of-the-Art Progress in Diverse Heterostructured Photocatalysts Toward Promoting Photocatalytic Performance. *Adv. Funct. Mater.* **2015**, *25*, 998-1013.
- (19) Mathew, M.; Shinde, P. V.; Samal, R.; Rout, C. S. A. Review on Mechanisms and Recent Developments in pn Heterojunctions of 2D Materials for Gas Sensing Applications. *J. Mater. Sci.* **2021**, *56*, 9575-9604.
- (20) Kershaw, S. V.; Susha, A. S.; Rogach, A. L. Narrow Bandgap Colloidal Metal Chalcogenide Quantum Dots: Synthetic Methods, Heterostructures, Assemblies, Electronic and Infrared Optical Properties. *Chem. Soc. Rev.* **2013**, *42*, 3033-3087.

- (21) Liu, M.; Verma, S. D.; Zhang, Z.; Sung, J.; Rao, A. Nonequilibrium Carrier Transport in Quantum Dot Heterostructures. *Nano Lett.* **2021**, *21*, 8945-8951.
- (22) Kaur, A.; Goswami, T.; Babu, K. J.; Ghorai, N.; Kaur, G.; Shukla, A.; Rondiya, S.R.; Ghosh, H. N. Probing Ultrafast Charge Separation in CZTS/CdS Heterojunctions through Femtosecond Transient Absorption Spectroscopy. *J. Phys. Chem. C* **2020**, *124*, 19476-19483.
- (23) Zhong, Y.; Zi, J.; Wu, F.; Li, Z.; Luan, X.; Gao, F.; Lian, Z. Defect-Mediated Electron Transfer in Pt-CuInS₂/CdS Heterostructured Nanocrystals for Enhanced Photocatalytic H₂ Evolution. *ACS Appl. Nano Mater.* **2022**, *5*, 7704-7713.
- (24) Kottayi, R.; Maurya, D. K.; Sittaramane, R.; Angaiah, S. Recent Developments in Metal Chalcogenides Based Quantum Dot Sensitized Solar Cells. *ES energy environ.* **2022**, *18*, 1-40.
- (25) García de Arquer, F. P.; Talapin, D. V.; Klimov, V. I.; Arakawa, Y.; Bayer, M.; Sargent, E. H. Semiconductor Quantum Dots: Technological Progress and Future Challenges. *Science* **2021**, *373*, 8541.
- (26) Bera, D.; Qian, L.; Tseng, T. K.; Holloway, P. H. Quantum dots and Their Multimodal Applications: a review. *Mater.* **2010**, *3*, 2260-2345.
- (27) Nozik, A. J.; Beard, M. C.; Luther, J. M.; Law, M.; Ellingson, R. J.; Johnson, J. C. Semiconductor Quantum Dots and Quantum Dot Arrays and Applications of Multiple Exciton Generation to Third-Generation Photovoltaic Solar Cells. *Chem. Rev.* **2010**, *110*, 6873-6890.
- (28) Green, M. A. Third generation photovoltaics: Ultra-High Conversion Efficiency at Low Cost. *Prog. Photovolt.: Res. Appl.* **2001**, *9*, 123-135.
- (29) Vasudevan, D.; Gaddam, R. R.; Trinchì, A.; Cole, I. Core-Shell Quantum Dots: Properties and Applications. *J. Alloys Compd.* **2015**, *636*, 395-404.
- (30) Henglein, A.; Small-Particle Research: Physicochemical Properties of Extremely Small Colloidal Metal and Semiconductor Particles. *Chem. Rev.* **1989**, *89*, 1861-1873.

- (31) Rogach, A. L. *Semiconductor Nanocrystal Quantum Dots Synthesis, Assembly, Spectroscopy and Applications*; Springer Wien, New York, **2008**.
- (32) Alivisatos, A. P. Perspectives on the Physical Chemistry of Semiconductor Nanocrystals. *J. Phys. Chem.* **1996**, 13226–13239.
- (33) Algar, W. R.; Susumu, K.; Delehanty, J. B.; Medintz, I. L. Semiconductor Quantum Dots in Bioanalysis: Crossing the Valley of Death. *Anal. Chem.* **2011**, 83, 8826–8837.
- (34) Michalet, X.; Pinaud, F. F.; Bentolila, L. A.; Tsay, J. M.; Doose, S.; Li, J. J.; Sundaresan, G.; Wu, A. M.; Gambhir, S. S.; Weiss, S. Quantum Dots for Live Cells, in Vivo Imaging, and Diagnostics. *Science* **2005**, 38–544.
- (35) Cao, A.; Liu, Z.; Chu, S.; Wu, M.; Ye, Z.; Cai, Z.; Chang, Y.; Wang, S.; Gong, Q.; Liu, Y. A Facile One-Step Method to Produce Craphene-CdS Quantum Dot Nanocomposites as Promising Optoelectronic Materials. *Adv. Mater.* **2010**, 22, 103–106.
- (36) Semonin, O. E.; Luther, J. M.; Choi, S.; Chen, H. Y.; Gao, J.; Nozik, A. J.; Beard, M. C. Peak External Photocurrent Quantum Efficiency Exceeding 100% via MEG in a Quantum Dot Solar Cell. *Science*, **2011**, 334, 1530–1533.
- (37) Colvin, V. L.; Schlamp, M. C.; Alivisatos, A. P. Light-Emitting Diodes Made from Cadmium Selenide Nanocrystals and a Semiconducting Polymer. *Nature* **1994**, 370, 354–357.
- (38) Neeleshwar, S.; Chen, C. L.; Tsai, C. B.; Chen, Y. Y.; Chen, C. C.; Shyu, S. G.; Seehra, M. S. Size-dependent properties of CdSe quantum dots. *Phys. Rev. B.* **2005**, 71, 201307.
- (39) Wu, W. Y.; Schulman, J. N.; Hsu, T. Y.; Efron, U. Effect of Size Nonuniformity on The Absorption Spectrum of a Semiconductor Quantum Dot System. *Appl. Phys. Lett.* **1987**, 51, 710-712.
- (40) Brus, L. E. A Simple Model for the Ionization Potential, Electron Affinity, and Aqueous Redox Potentials of Small Semiconductor Crystallites. *J. Chem. Phys.* **1983**, 79, 5566-5571.

- (41) Efros, A. L. Luminescence Polarization of CdSe Microcrystals. *Phys. Rev. B* **1992**, *46*, 7448.
- (42) Thambidurai, M.; Murugan, N; Muthukumarasamy, N.; Agilan, S.; Vasantha, S.; Balasundaraprabhu, R. Influence of the Cd/S Molar Ratio on the Optical and Structural Properties of Nanocrystalline CdS Thin Films. *J. mater. sci. technol.* **2010**, *26*, 193-199.
- (43) Brennan, F. K. *The Physics of Semiconductors*, Cambridge University Press, New York, NY, 1997.
- (44) Lee, S. J.; Shin, N. H.; Ko, J. J.; Park, M. J.; Kummel, R. Density of States of Quantum Dots and Crossover from 3D to Q0D Electron Gas. *Semicond. Sci. Technol.* **1992**, *7*, 1072.
- (45) Ivanov, S. A.; Piryatinski, A.; Nanda, J.; Tretiak, S.; Zavadil, K. R.; Wallace, W. O.; Werder, D. Klimov, V. I. Type-II core/shell CdS/ZnSe nanocrystals: Synthesis, Electronic Structures, and Spectroscopic Properties. *J. Am. Chem. Soc.* **2007**, *129*, 1708-11719.
- (46) Cheng, Z.; Wang, F.; Shifa, T. A.; Jiang, C.; Liu, Q.; He, J. Efficient Photocatalytic Hydrogen Evolution via Band Alignment Tailoring: Controllable Transition from Type-I to Type-II. *Small* **2017**, *13*, 1702163.
- (47) Huang, S.; Wang, Z.; Von Lim, Y.; Wang, Y.; Li, Y.; Zhang, D.; Yang, H. Y. Recent Advances in Heterostructure Engineering for Lithium–Sulfur Batteries. *Adv. Energy Mater.* **2021**, *11*, 2003689.
- (48) Xiong, R., Song, Y., Li, K., Xiao, Y., Cheng, B. and Lei, S. A Novel 1D/2D Core/Shell CdS@SnS₂ Heterostructure for Efficient Piezocatalytic Hydrogen Evolution and Pollutant Degradation. *J. Mater. Chem. A* **2023**, *11*, 18398-18408.
- (49) Agostini, G.; Lamberti, C. eds.; *Characterization of semiconductor heterostructures and nanostructures*. Elsevier, 2011.
- (50) Zhang, L.; Jaroniec, M. Toward Designing Semiconductor-Semiconductor Heterojunctions for Photocatalytic Applications. *Appl. Surf. Sci.* **2018**, *430*, 2-17.

- (51) He, M.; Sun, K.; Suryawanshi, M. P.; Li, J.; Hao, X. Interface Engineering of pn Heterojunction for Kesterite Photovoltaics: A Progress Review. *J. Energy Chem.* **2021**, *60*, 1-8.
- (52) Alferov, Z. I. The History and Future of Semiconductor Heterostructures. *Semiconductors* **1998**, *32*, 1-14.
- (53) Low, J.; Yu, J.; Jaroniec, M.; Wageh, S.; Al-Ghamdi, A. A. Heterojunction photocatalysts. *Adv. Mater.* **2017**, *29*, 1601694.
- (54) Marcus, R. A.; Sutin, N. Electron Transfers in Chemistry and Biology. *Biochimica et Biophysica Acta* **1985**, *811*, 265-322.
- (55) Marcus, R.A.; Relation Between Charge Transfer Absorption and Fluorescence Spectra and the Inverted Region. *J. Phys. Chem.* **1989**, *93*, 3078-3086.
- (56) Yan, S. G.; Prieskorn, J. S.; Kim, Y.; Hupp, J. T. In Search of the Inverted Region: Chromophore-Based Driving Force Dependence of Interfacial Electron Transfer Reactivity at the Nanocrystalline Titanium Dioxide Semiconductor/Solution Interface. *J. Phys. Chem. B* **2000**, *104*, 10871-10877.
- (57) Kambhampati, P. Hot Exciton Relaxation Dynamics in Semiconductor Quantum Dots: Radiationless Transitions on the Nanoscale. *J. Phys. Chem. C* **2011**, *115*, 22089-22109.
- (58) Nozik, A. J. Spectroscopy and Hot Electron Relaxation Dynamics in Semiconductor Quantum Wells and Quantum Dots. *Annu. Rev. Phys. Chem.* **2001**, *52*, 193-231.
- (59) Nozik, A. J. Exciton Multiplication and Relaxation Dynamics in Quantum Dots: Applications to Ultrahigh-Efficiency Solar Photon Conversion. *Inorg. Chem.* **2005**, *44*, 6893-6899.
- (60) Chuang, C.H.; Chen, X.; Burda, C. Femtosecond Time-Resolved Hot Carrier Energy Distributions of Photoexcited Semiconductor Quantum Dots. *Ann. Phys.* **2013**, *525*, 43-48.

- (61) Gumber, S.; Eniodunmo, O.; Ivanov, S. A.; Kilina, S.; Prezhdo, O. V.; Ghosh, D.; Tretiak, S. Hot Carrier Relaxation Dynamics in Non-Stoichiometric CdSe Quantum Dots: Computational Insights. *J. Mater. Chem. A* **2023**, *11*, 8256-8264.
- (62) Schaller, R. D.; Pietryga, J. M.; Goupalov, S. V.; Petruska, M. A.; Ivanov, S. A.; Klimov, V. I. Breaking the Phonon Bottleneck in Semiconductor Nanocrystals via Multiphonon Emission Induced by Intrinsic Nonadiabatic Interactions. *Phys. Rev. Lett.* **2005**, *95*, 196401.
- (63) Urayama, J.; Norris, T. B.; Singh, J.; Bhattacharya, P. Observation of Phonon Bottleneck in Quantum Dot Electronic Relaxation. *Phys. Rev. Lett.* **2001**, *86*, 4930.
- (64) Bockelmann, U.; Bastard, G. Phonon Scattering and Energy Relaxation in Two-, One-, and Zero-Dimensional Electron Gases. *Phys. Rev. B* **1990**, *42*, 8947.
- (65) Pietryga, J. M.; Park, Y. S.; Lim, J.; Fidler, A. F.; Bae, W. K.; Brovelli, S.; Klimov, V. I. Spectroscopic and Device Aspects of Nanocrystal Quantum Dots. *Chem. Rev.* **2016**, 10513–10622.
- (66) Schaller, R. D.; Pietryga, J. M.; Goupalov, S. V.; Petruska, M. A.; Ivanov, S. A.; Klimov, V. I., Kambhampati, P. Unraveling the Structure and Dynamics of Excitons in Semiconductor Quantum Dots. *Acc. Chem. Res.* **2011**, *44*, 1–13
- (67) Breaking the Phonon Bottleneck in Semiconductor Nanocrystals via Multiphonon Emission Induced by Intrinsic Nonadiabatic Interactions. *Phys. Rev. Lett.* **2005**, *95*, 196401.
- (68) Benisty, H.; Sotomayor-Torres, C. M.; Weisbuch, C. Intrinsic Mechanism for the Poor Luminescence Properties of Quantum-Box Systems. *Phys. Rev. B.* **1991**, *44*, 10945.
- (69) Bae, W. K.; Padilha, L.A.; Park, Y. S.; McDaniel, H.; Robel, I.; Pietryga, J. M.; Klimov, V. I. Controlled Alloying of the Core–Shell Interface in CdSe/CdS Quantum Dots for Suppression of Auger Recombination. *ACS Nano* **2013**, *7*, 3411-3419.

- (70) Bae, W. K.; Park, Y. S.; Lim, J.; Lee, D.; Padilha, L. A.; McDaniel, H.; Robel, I.; Lee, C.; Pietryga, J. M.; Klimov, V. I. Controlling the Influence of Auger recombination on the Performance of Quantum-Dot Light-Emitting Diodes. *Nat. Commun.* **2013**, *4*, 2661.
- (71) Klimov, V. I.; Mikhailovsky, A. A.; McBranch, D. W.; Leatherdale, C. A.; Bawendi, M. G. Quantization of multiparticle Auger rates in Semiconductor Quantum Dots. *Science* **2000**, *287*, 1011-1013.
- (72) Zegrya, G. G.; Andreev, A. D. Mechanism of Suppression of Auger Recombination Processes in Type-II Heterostructures. *Appl. Phys. Lett.* **1995**, *67*, 2681-2683.
- (73) Smith, C.; Abram, R. A.; Burt, M. G. Auger Recombination in a Quantum Well Heterostructure. *J. Phys. C: Solid State Phys.* **1983**, *16*, 171.
- (74) Beard, M. C. Multiple Exciton Generation in Semiconductor Quantum Dots. *J. Phys. Chem. Lett.* **2011**, *2*, 1282-1288.
- (75) Goodwin, H.; Jellicoe, T. C.; Davis, N. J.; Böhm, M. L. Multiple Exciton Generation in Quantum Dot-Based Solar Cells. *Nanophotonics* **2018**, *7*, 111-126.
- (76) Rawalekar, S.; Kaniyankandy, S.; Verma, S.; Ghosh, H. N. Ultrafast Charge Carrier Relaxation and Charge Transfer Dynamics of CdTe/CdS Core–Shell Quantum Dots as Studied by Femtosecond Transient Absorption Spectroscopy. *J. Phys. Chem. C* **2010**, *114*, 1460-1466.
- (77) Sambur, J. B.; Novet, T.; Parkinson, B. A. Multiple Exciton Collection in a Sensitized Photovoltaic System. *Science* *2010*, *330*, 63-66.
- (78) Hines, D. A.; Kamat, P. V. Recent Advances in Quantum Dot Surface Chemistry. *ACS Appl. Mater. Interfaces* **2014**, *6*, 3041–3057.
- (79) Boles, M. A.; Ling, D.; Hyeon, T.; Talapin, D. V. The Surface Science of Nanocrystals. *Nat. Mater.* **2016**, *15*, 141–153.

- (80) Kilina, S.; Ivanov, S.; Tretiak, S. Effect of Surface Ligands on Optical and Electronic Spectra of Semiconductor Nanoclusters. *J. Am. Chem. Soc.* **2009**, *131*, 7717–7726.
- (81) Das, S.; Rakshit, S.; Datta, A. Interplay of Multiexciton Relaxation and Carrier Trapping in Photoluminescent CdS Quantum Dots Prepared in Aqueous Medium. *J. Phys. Chem. C* **2020**, *124*, 28313–28322.
- (82) Mondal, N.; Samanta, A. Ultrafast Charge Transfer and Trapping Dynamics in a Colloidal Mixture of Similarly Charged CdTe Quantum Dots and Silver Nanoparticles. *J. Phys. Chem. C* **2016**, *120*, 650–658.
- (83) Zhang, Z.; Hu, M.; Jia, T.; Du, J.; Chen, C.; Wang, C.; Liu, Z.; Shi, T.; Tang, J.; Leng, Y. Suppressing the Trapping Process by Interfacial Charge Extraction in Antimony Selenide Heterojunctions. *ACS Energy Lett.* **2021**, *6*, 1740–1748.
- (84) Kaur, A.; Goswami, T.; Babu, K. J.; Shukla, A.; Bhatt, H.; Ghosh, H. N. Efficient Hot Electron Transfer and Extended Separation of Charge Carriers at the 1P Hot State in Sb₂Se₃/CdSe p–n Heterojunction. *J. Phys. Chem. Lett.* **2022**, *13*, 11354–11362.
- (85) Shockley, W.; Queisser, H. J. Detailed Balance Limit of Efficiency of P-n Junction Solar Cells. *J. Appl. Phys.* **1961**, *32*, 510–519.
- (86) Ahmed, I.; Shi, L.; Pasanen, H.; Vivo, P.; Maity, P.; Hatamvand, M.; Zhan, Y. There is Plenty of Room at the Top: Generation of Hot Charge Carriers and Their Applications in Perovskite and Other Semiconductor-Based Optoelectronic Devices. *Light Sci. Appl.* **2021**, *10*, 174.
- (87) Conibeer, G. J.; König, D.; Green, M. A.; Guillemoles, J. F. Slowing of Carrier Cooling in Hot Carrier Solar Cells. *Thin solid films* **2008**, *516*, 6948–6953.
- (88) Xue, J.; Bao, J. Interfacial Charge Transfer of Heterojunction Photocatalysts: Characterization and Calculation. *Surf. Interfaces* **2021**, *25*, 101265.
- (89) Limpert, S. C.; Bremner, S. P. Hot Carrier Extraction using Energy Selective Contacts and Its Impact on the Limiting Efficiency of a Hot Carrier Solar Cell. *Appl. Phys. Lett.* **2015**, *107*, 1073902

-
- (90) Liu, C.; Lu, Y.; Shen, R.; Dai, Y.; Yu, X.; Liu, K.; Lin, S. Dynamics and Physical Process of Hot Carriers in Optoelectronic Devices. *Nano Energy* **2022**, *95*, 106977.
- (91) Kaur, A.; Goswami, T.; Rondiya, S. R.; Jadhav, Y. A.; Babu, K. J.; Shukla, A.; Yadav, D.K.; Ghosh, H. N. Enhanced Charge Carrier Separation and Improved Biexciton Yield at the p–n Junction of SnSe/CdSe Heterostructures: A Detailed Electrochemical and Ultrafast Spectroscopic Investigation. *J. Phys. Chem. Lett.* **2021**, *12*, 10958-10968.
- (92) Ghorai, N.; Sachdeva, M.; Kharbanda, N.; Ghosh, H.N. Harvesting Plasmonic Near-Infrared Photons by Hot Hole Transfer in Nonstoichiometric-Semiconductor Plasmonic Heterojunctions. *ACS Photonics* **2023**, *10*, 733-742.
- (93) Ni, X.; Li, X.; Lee, J.; Liu, S.; Avrutin, V.; Özgür, Ü.; Morkoç, H.; Matulionis, A.; Paskova, T.; Mulholland, G.; Evans, K. R. InGaN Staircase Electron Injector for Reduction of Electron Overflow in InGaN Light Emitting Diodes. *Appl. Phys. Lett.* **2010**, *97*, 031110
- (94) Wang, H.; Wang, F.; Xu, T.; Xia, H.; Xie, R.; Zhou, X.; Ge, X.; Liu, W.; Zhu, Y.; Sun, L.; Guo, J. Slowing Hot-Electron Relaxation in Mix-Phase Nanowires for Hot-Carrier Photovoltaics. *Nano Lett.* **2021**, *21*, 7761-7768.
- (95) Goswami, T.; Bhatt, H.; Yadav, D. K.; Saha, R.; Babu, K.; Ghosh, H. N. Probing Ultrafast Hot Charge Carrier Migration in MoS₂ Embedded CdS Nanorods. *J. Chem. Phys.* **2022**. 156, 034704.
- (96) DuChene, J. S.; Sweeny, B. C.; Johnston-Peck, A. C.; Su, D.; Stach, E. A.; Wei, W. D.; Prolonged Hot Electron Dynamics in Plasmonic-Metal/Semiconductor Heterostructures with Implications for Solar Photocatalysis. *Angew. Chem. Int. Ed.* **2014**, *53*, 7887-7891.
- (97) Wu, K.; Zhu, H.; Liu, Z.; Rodríguez-Córdoba, W.; Lian, T. Ultrafast Charge Separation and Long-Lived Charge Separated State in Photocatalytic CdS–Pt Nanorod Heterostructures. *J. Am. Chem. Soc.* **2012**, *134*, 10337-10340.
- (98) Kaur, A.; Goswami, T.; Babu, K. J.; Ghosh, H. N. Ultrafast Hole Migration at the p–n Heterojunction of One-Dimensional SnS Nanorods and Zero-Dimensional CdS Quantum Dots. *J. Phys. Chem. Lett.* **2023**, *14*, 7483-7489.
-

- (99) Knight, M. W.; Sobhani, H.; Nordlander, P.; Halas, N. J. Photodetection with active optical antennas. *Science* **2011**, *332*, 702-704.
- (100) König, D.; Casalenuovo, K.; Takeda, Y.; Conibeer, G.; Guillemoles, J. F.; Patterson, R.; Huang, L. M.; Green, M. A. Hot Carrier Solar Cells: Principles, Materials and Design. *Phys. E: Low-Dimens. Syst. Nanostructures*. **2010**, *42*, 2862-2866.
- (101) Mukherjee, S.; Libisch, F.; Large, N.; Neumann, O.; Brown, L.V.; Cheng, J.; Lassiter, J. B.; Carter, E.A.; Nordlander, P.; Halas, N. J. Hot Electrons Do the Impossible: Plasmon-Induced Dissociation of H₂ on Au. *Nano Lett.* **2013**, *13*, 240-247.
- (102) Zhu, Y.; Cui, L.; Natelson, D. Hot-carrier enhanced light emission: The Origin of above-Threshold Photons from Electrically Driven Plasmonic Tunnel Junctions. *J. Appl. Phys.* **2020**, *128*, 233105.
- (103) Fan, X.; Wang, B.; Heng, Q.; Chen, W.; Mao, L. Facile In-Situ Synthesis of α -NiS/CdS p-n Junction with Enhanced Photocatalytic H₂ Production Activity. *Int. J. Hydrogen Energy* **2022**, *47*, 32531–32542.

CHAPTER 2

Synthesis and Characterization Techniques

This chapter deals with the complete list of synthetic procedures and the basic details of the instrumental techniques utilized to complete my thesis work. The colloidal nanocrystals (NCs), and quantum dots (QDs) have been synthesized by hot injection method. Further, different semiconductor heterostructures have been synthesized by employing the cation exchange technique. Also, the thin film heterojunctions of the metal chalcogenides have been fabricated using various techniques including spin coating and thermal evaporation. The mechanism of these methods and the underlying principle have been thoroughly discussed in this chapter. X-ray diffraction (XRD) was employed to determine the crystal structure of the NCs and thin films. The size and morphology of the materials were determined by transmission electron microscopy (TEM). TEM is a very important tool to confirm the intimate contact between two materials in a heterostructure. X-ray photoelectron spectroscopy (XPS), discovered the composition and oxidation states of the elements in nanoparticles and heterostructure systems. Field emission scanning electron microscopy (FESEM) was used to determine the elemental distribution and their atomic percentage. Mott Schottky plots were utilized to determine the type of conductivity (p or n-type) of the material. The steady-state optical properties of the synthesized materials and their heterojunctions were explored using UV-vis absorption and photoluminescence (PL) spectroscopy. The PL lifetime in the nanosecond time scale was determined through the time-correlated single photon counting (TCSPC) technique. Finally, femtosecond ultrafast transient absorption (TA) spectroscopy has been utilized to investigate the charge transfer and relaxation processes in p-n heterostructures.

2.1. Synthesis techniques

In the present thesis, we will deal with colloidal synthesis and thin film fabrication techniques particularly hot injection and thermal evaporation for the preparation of nanomaterials as well as their corresponding heterostructures.

2.1.1. Colloidal Synthesis: Hot injection method

Colloidal nanoparticles (NPs) can be synthesized via either a top-down or bottom-up approach. The top-down approach begins with a bulk material and its size is reduced to form NCs using lithography, ion beam etching and ball milling methods, etc.¹ However, these results NCs with a high density of surface defects, so they are not as appealing. In contrast, bottom-up synthesis involves taking precursor molecules with a capping agent and forming nanocrystals with control synthesis and therefore they are more frequently used.² This method includes all the chemical synthetic routes like colloidal synthesis, chemical vapor deposition (CVD), etc. The hot injection method is considered the most effective technique for the successful synthesis of high-quality nanomaterials with uniform size distribution. The theory behind the hot injection technique is described by the La Mer model as shown in **Figure 2.1A**.^{3,4}

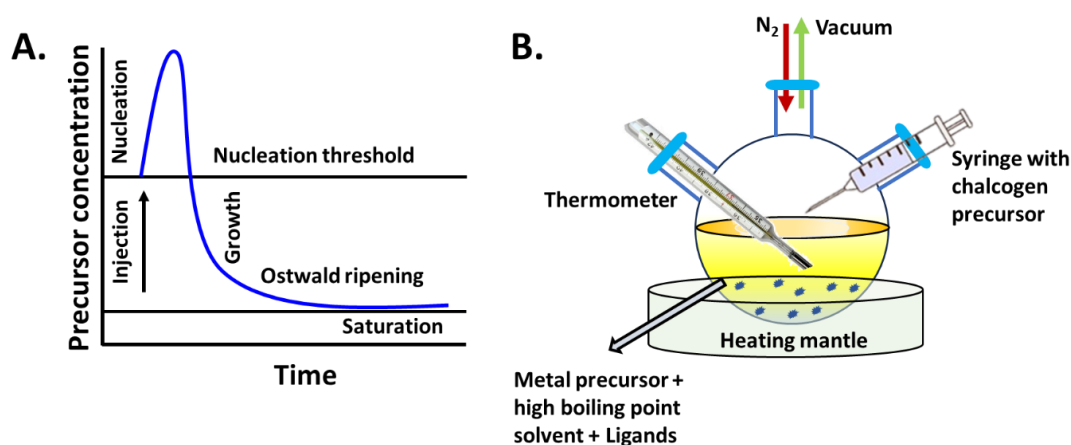


Figure 2.1. (A) Classic La Mer mechanism for nucleation and growth for synthesis of monodisperse colloidal particles. (B) Typical hot injection synthesis setup for the synthesis of metal chalcogenide nanoparticles.

According to La Mer, the process of nucleation and growth can be divided into three steps: (I) A quick increase in the concentration of free monomers in solution, (II) the monomer undergoes burst nucleation which effectively decreases the concentration of

free monomers in solution, and **(III)** when the concentration of monomer reduces below the critical level, there is almost no nucleation and growth process of nuclei proceed via Ostwald ripening.⁵ At this stage, smaller particles join to form larger particles. Separation of the nucleation from growth results in the desired narrow size distribution. In hot injection synthesis oleic acid and oleylamine are commonly used surfactants to prevent the resulting NPs from agglomeration.⁶ This method permits to control of the size and shape of the NPs.⁷ The schematic representation of the colloidal synthesis technique has been shown in **Figure 2.1 B**.

The hot injection synthesis method has received widespread attention for better shape, size, homogeneity, and composition control to obtain highly luminescent NCs and heterostructures by combining two or more materials in one structure.

2.1.2. Synthesis of colloidal p-n semiconductor heterostructures:

Cation exchange

It is desired to create semiconductor heterostructures in order to fine-tune the carrier wavefunctions of QDs and enhance their photophysical characteristics.⁸ The controlled synthesis of colloidal epitaxial hybrid nanostructures with exceptional monodispersity, uniform size, uniform shape, and high purity is made possible by the colloidal synthesis technique.^{9,10} Ion (cation/anion) exchange is indeed a fascinating method to prepare heterostructures by exchanging the ions at the interface of the heterostructure.¹¹ Semiconductor heterostructures are synthesized by a two-step synthesis. In this, nanomaterial prepared by traditional hot-injection methods can be used as anion templates for the preparation of heterostructures that would be inaccessible by direct methods. Cation exchange simply involves replacing the cations in an ionic crystal while the anionic framework remains intact. This occurs by exposing the parent ionic crystal to new cations, either in solid or solvated liquid form. The new cations enter the parent crystal as the original cations diffuse out of the crystal and into the reaction solvent. In the process of cation exchange, external cations enter the parent crystal at the same time as the original cations diffuse out of the crystal as shown in **Figure 2.2**.¹² The equivalent anion exchange has also been

reported; however, anions often have lower mobilities due to their additional valence electrons and generally bigger radius, which necessitates high reaction temperatures or prolonged reaction periods, leading to poor quality final materials.¹³

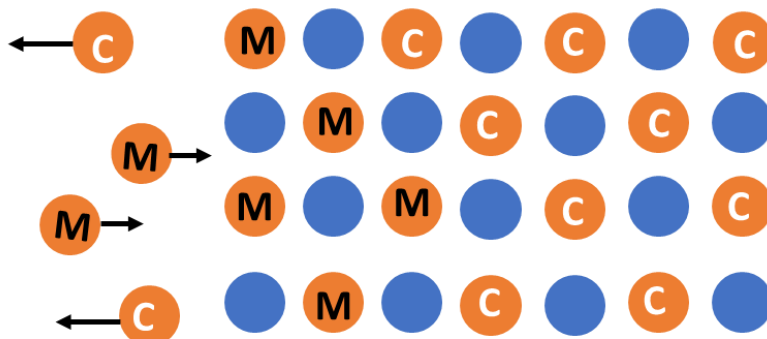
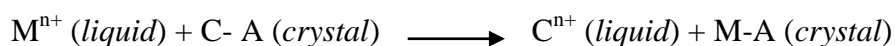


Figure 2.2. Schematic of cation exchange reaction.



By changing the experimental parameters, such as the reaction temperature, reaction time, solvent system, type and concentration of precursors, and the surfactants or ligands used, the size, shape, morphology, growth mode, and architecture of synthesized epitaxial hybrid nanostructures can be finely tuned. Through cation or anion exchange reactions, where the morphology of the nanostructures can be preserved, the compositions of synthesized epitaxial hybrid nanostructures can also be tuned post-synthesis.¹⁴ Furthermore, cation exchange is an emerging chemical method that allows low-temperature formation of colloidal NCs and heterostructures, not achievable by other methods.¹⁵

2.2. Fabrication of thin films

2.2.1. Spin Coating Method

Spin coating is a common method for depositing thin films on substrates. When a solution of a material and solvent is spun at high speeds, the centripetal force and the surface tension of the liquid together create an even covering. After any remaining solvent has evaporated, spin coating results in a thin film ranging from a few nanometres to a few microns in thickness (**Figure 2.3**). Film thickness can be easily varied by changing the spin speed, or viscosity of material.¹⁶⁻¹⁸ In my thesis, we have spin-coated CZTS, CdS as well as CZTS/CdS thin films using the spin coater (Apex Instruments).

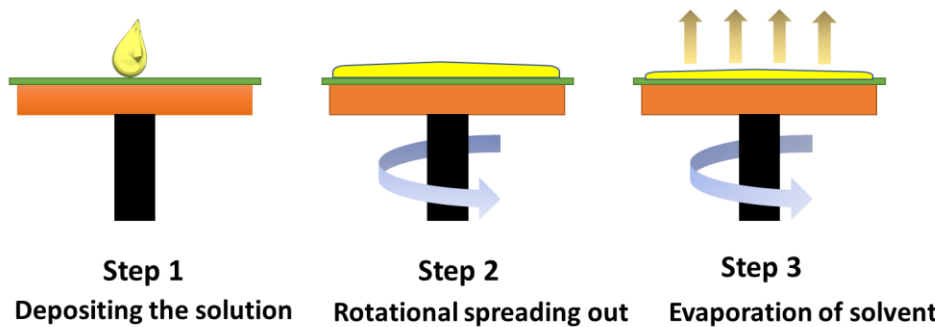


Figure 2.3. Schematic diagram for thin film deposition via spin coating technique.

2.2.2. Thermal evaporation technique

In my thesis work, we have used the thermal evaporation technique to make thin films and their heterojunctions. Thermal evaporation is a versatile high-vacuum-based coating technique that belongs to physical vapor deposition methods.^{19,20} In this, the powder source materials are evaporated at high temperatures usually in a vacuum environment, causing it to evaporate and condense onto a substrate as a thin film. The evaporation method has the advantages of easy operation, high-speed film formation, and high production efficiency. It is one of the most widely used techniques for thin film preparation.^{21,22} The picture and typical schematic diagram of the evaporation system are described in **Figure 2.4 A, B**. The material to be evaporated typically in the form of solid/powder. The powder is placed into a crucible or boat constructed of tungsten, tantalum, or molybdenum, which is built to withstand extreme temperatures as it is heated to the desired temperature using resistive heating. The thermal evaporation process is carried out in a vacuum environment to minimize contamination and ensure uniform film deposition. The different vacuum pumps are used to establish and maintain the required vacuum level inside the chamber. This ensures the removal of unwanted gases and contaminants. The chamber is evacuated to reduce gas collisions with the vapor particles. A rotary pump is used to attain the roughing vacuum of about $\sim 10^{-3}$ mbar and a turbo pump has been utilized to further achieve a high vacuum of $\sim 10^{-6}$ mbar. When the evaporation source material is heated, the thermal vibration energy of the molecules or atoms in the material exceeds the surface binding energy. The result will be a significant number of atoms evaporating or sublimating before eventually condensing to create thin films on the substrate. The substrate at which films are deposited should be placed near the crucible. Before deposition, the substrate is subsequently cleaned in an ultrasonic bath

using detergent, de-ionized (DI) water, and isopropanol. The substrate can be rotated and heated during the deposition process. The deposition chamber is pumped to a pressure of less than 5×10^{-6} Pa before evaporation. Pirani gauge was used to measure the roughing pressure in the main and load lock chamber while penning gauge was used to measure high pressure in main chamber.²³ Excess of source powder kept in a tungsten or tantalum boat which is twined with tungsten wire. The deposition rate was controlled by turning the current of the tungsten filament, and thickness was monitored by microcrystalline quartz balance. A typical evaporation system is described in **Figure 2.4B**.

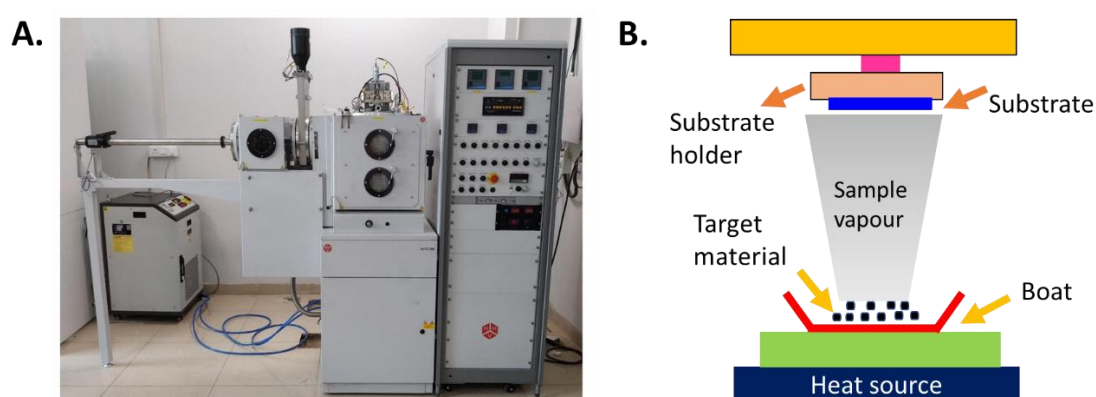


Figure 2.4. (A) Picture of the instrumental set-up for thermal and magnetron sputtering system, and (B) Basic layout of the evaporation process.

In my thesis, we have used the AUTO 500 thermal evaporation and magnetron sputtering coating system from Hind High Vacuum (HHV) Co. Ltd.

2.3. Synthesis procedures

2.3.1. Materials used

Copper (II) acetylacetonate ($\text{Cu}(\text{AcAc})_2$), Zinc acetate ($\text{Zn}(\text{OAc})_2$), Tin (II) chloride (SnCl_2), Sulphur powder (S), Cadmium oxide (CdO), Trioctylphosphine (TOP), Selenium powder (Se), Antimony chloride (Sb_2Cl_3), Hexamethyldisilazane (HMDS), Tetrabutylammonium perchlorate (TBAP), Thioacetamide (TAA), Dodecanethiol (DDT) Octadecene (ODE), 1-Oleylamine (OLM), Oleic acid (OA), Chloroform (CHCl_3), Toluene (C_7H_8), Hexane (C_6H_{14}), Bulk Sb_2Se_3 powder (99.99 % pure), CdS powder (99.99 % pure), Deionized (DI) water. All the chemicals were purchased from Sigma-Aldrich, India, and used without further purification. Ethanol and methanol

(AR grade) were used for precipitating the crude products while toluene, chloroform, and hexane were used for re-dispersing the purified samples.

2.3.2. Synthesis of CZTS NPs

We executed the synthesis of CZTS NPs following a few previously reported synthetic procedures after incorporating a few minor changes.^{24,25} First, a mixture of 4 mmol Cu(AcAc)₂, 2 mmol Zn(OAc)₂, and 2 mmol SnCl₂ was dissolved in 20 mL OLM and transferred in a 100 ml three-neck round bottom (RB) flask. This solution was stirred vigorously in the flask in the nitrogen (N₂) atmosphere and heated at 130°C for 30 min until the solution became brownish. Once it became brownish, it was injected with Sulphur solution prepared by adding 10 mmol S in 8 mL OLM and then heated up to 260°C and kept for 1 hour. It was noticed that the colour of the solution changed from dark brownish to blackish. After that, the reaction was cooled down to room temperature. The resultant solution was centrifuged at 6000 rpm for 10 minutes. The precipitate was washed with ethanol three times to remove the unreacted precursors and finally re-dispersed in toluene.

2.3.3. Synthesis of CdS QDs

We have used the hot injection method to synthesize CdS QDs.²⁶ Cadmium oleate solution was prepared by adding 4 mmol CdO, 11.6 mL ODE, and 3.4 mL of OA into the three-neck RB flask, and the solution was heated to 300°C under N₂ atmosphere. Separately, the S solution was prepared by adding 2 mmol Sulfur powder into 1.2 mL TOP and 4.5 mL ODE, which was injected into cadmium oleate solution at 300 °C under N₂ atmosphere, and the reaction was maintained at 300°C for 10 min. Finally, the solution was allowed to cool down to room temperature. The crude product was centrifuged at 7000 rpm for 5 min. The precipitate was washed with methanol and re-dispersed in chloroform.

2.3.4. Fabrication of CZTS/CdS heterojunction

CZTS and CdS solutions were deposited on a glass substrate with the help of a spin coater to engineer thin film heterojunctions. The glass substrates were properly cleaned with soap solution, de-ionized (DI) water and finally with acetone in an ultrasonic bath for 10 min each and dried. The CZTS solution was spin-coated on

glass at 1000 rpm for 40 s and dried at room temperature. To prepare the CZTS/CdS thin film heterojunction, the as-prepared CZTS thin film on glass was spin-coated with CdS solution at 800 rpm for 50 s at room temperature and dried. Under similar conditions, the CdS thin film was also prepared separately on a glass substrate for reference.

2.3.5. Synthesis of SnSe NSs

The synthesis of SnSe nanosheets (NSs) was carried out following previously reported synthetic procedures with minor modifications.^{27,28} First, to prepare 1M TOP-Se solution, 5 mmol Se powder was dissolved in 10 mL TOP. For the synthesis of SnSe NSs, 0.2 mmol of SnCl₂ and 25 mL of OLM were added into a three-neck round bottom flask. Then, TOP-Se stock solution and 1mL of HMDS were also added and stirred for 15 min. Finally, the solution was stirred vigorously in the flask in the N₂ atmosphere and heated to 240° C which resulted in the formation of SnSe NSs. The solution was kept at this temperature for 10 min and it was cooled quickly by removing the reaction flask from the heating mantle. The SnSe NSs are precipitated by adding 30 mL ethanol and then centrifuged at 9000 rpm for 10 min. The precipitate was washed with ethanol three times to remove the unreacted precursors and finally re-dispersed in toluene.

2.3.6. Synthesis of CdSe QDs

CdSe QDs are synthesized employing previously reported synthetic procedure with minor modifications.^{29,30} Briefly, cadmium oleate solution was prepared by adding 4 mmol (138 mg) CdO, 40 mL ODE, and 7 mL of OA into the three-neck RB flask and the solution was heated to 300°C under an N₂ atmosphere. Separately, the Se solution was prepared by adding 0.5 mmol (40 mg) Se powder into 5 mL ODE and 4 ml of OA, which was injected into cadmium oleate solution at 300 °C under N₂ atmosphere and the reaction temperature was maintained at 300°C for 10 min. Finally, the solution was allowed to cool down to room temperature. The crude product was centrifuged at 7000 rpm for 5 min. The precipitate was washed with methanol and re-dispersed in toluene for further characterization.

2.3.7. Synthesis of SnSe/CdSe heterostructure

SnSe/CdSe heterostructure was synthesized using CdSe QDs synthesized before as a template. Typically, in a 25 mL round-bottom flask, the metal precursor (1.5 mmol) SnCl₂, and 10 mL OLM were degassed at 100 °C for 10 min. The reaction flask was re-stored with N₂ and the reaction temperature was raised to 120 °C while stirring for one hour. 1 mL of the CdSe suspension (0.05 mmol in toluene) was added slowly into the above reaction flask and the reaction mixture was stabilized at 120 °C for 10 min. Subsequently, OA was added to the mixture when the temperature of the mixture decreased to 80 °C. After 20 min, the reaction was cooled to room temperature using cold water. The ethanol was added, then the suspension was centrifuged and the supernatant was removed. The SnSe/CdSe heterostructure was then dispersed in toluene for further characterization.

2.3.8. Synthesis of Sb₂Se₃/CdSe heterostructure

Sb₂Se₃/CdSe heterostructure was prepared by reacting Sb precursor with a solution of CdSe QDs. The pre-synthesized CdSe QDs were used as a template. In a typically, 25 mL three-neck RB flask, 20 mg Sb₂Cl₃, and 10 mL OLM were added and degassed at 110 °C for 10 min. The reaction flask was purged with N₂ and the reaction temperature was raised to 150 °C. Here, the reaction was kept for 25 min. 1 mL of the CdSe QDs solution (0.03 mmol in toluene) was added slowly into the reaction flask and the reaction mixture was maintained at 120 °C for 10 min. Afterward, the reaction was cooled down to room temperature. Excess ethanol was added, then the suspension was centrifuged and the supernatant was removed. Further, precipitate containing Sb₂Se₃/CdSe heterostructure was collected and then dispersed in toluene for further study.

2.3.9. Synthesis of Sb₂Se₃ QDs

Sb₂Se₃ QDs were synthesized via complete cation exchange of CdSe QDs with Sb³⁺ ions. In a typically, three-neck RB flask, 50 mg Sb₂Cl₃, and 10 mL OLM were degassed at 100 °C for 10 min. The reaction flask was purged with N₂ and the reaction temperature was raised to 150 °C. Here, the reaction was kept for 20 min. 1 mL of CdSe QDs (0.05 mmol in toluene) was added slowly into the above reaction

flask and the reaction mixture was stabilized at 120 °C for 10 min. Afterward, the reaction was cooled down to room temperature using cold water. Ethanol was added, then the suspension was centrifuged, and the supernatant was removed. The Sb₂Se₃ QDs were then dispersed in toluene for further characterization.

2.3.10. Synthesis of SnS NRs

The synthesis of SnS nanorods (NRs) was carried out using the hot injection method.³¹ In a typical synthesis, 1 mmol SnCl₂ was dissolved in 5 ml of OLM and ODE in a three-neck RB flask. The mixture was stirred continuously and evacuated at 120° C for 30 min. Afterward, the temperature was dropped to 80 °C. Sulphur precursor was prepared by dissolving S powder in 1 mmol TAA and 2 mL OLM and was swiftly injected into the tin precursor. After that, 1mL of DDT was added after 5 min. Then, the solution was heated to 150 °C and was maintained for 30 min and then it was cooled quickly by removing the reaction flask from the heating mantle. The SnS NRs are precipitated by ethanol and then centrifuged at 9000 rpm for 10 min. The precipitate was washed with ethanol three times to remove the unreacted precursors and finally re-dispersed in hexane.

2.3.11. Synthesis of CdS QDs stock solution

CdS QDs are synthesized employing previously reported synthetic procedures with minor modifications.³² Cadmium oleate solution was prepared by adding 4 mmol CdO, 11.6 mL 1-ODE, and 3.4 mL OA into the three-neck RB flask and the solution was heated to 260 °C under N₂ atmosphere. Separately, the S solution was prepared by adding 2 mmol S powder into 1.2 mL TOP and 4.5 mL 1-ODE, which was injected into cadmium oleate solution at 300 °C under N₂ atmosphere and the reaction was maintained at 300 °C for 10 min. Finally, the solution was allowed to cool down to room temperature. The crude product was centrifuged at 7000 rpm for 5 min. The precipitate was washed with methanol and re-dispersed in hexane.

2.3.12. Synthesis of SnS@CdS p-n heterojunction

0.5 mL of original SnS NRs were purified and re-dispersed in 5 mL of ODE, which was then loaded in a three-neck flask and degassed at 120 °C with N₂ purging for about 30 min. The temperature was raised to 180 °C for the slow injection of 2 ml CdS

stock solution. Then, the temperature was increased up to 220 °C and was maintained for 10 min. Afterward, the reaction solution was allowed to cool down to room temperature. Finally, the product was washed with ethanol and redispersed in hexane for further characterization.

2.3.13. Deposition of Sb₂Se₃ film

Sb₂Se₃ films were fabricated by thermal evaporation of 99.99% pure Sb₂Se₃ powder using thermal evaporation thin film deposition method.^{33,34} Glass was used as substrates. Before deposition, the substrate was subsequently cleaned in an ultrasonic bath using detergent, de-ionized water, and isopropanol. The deposition chamber was pumped to a pressure of less than 5×10^{-6} Pa before evaporation. Excess Sb₂Se₃ powder was kept in a tungsten or tantalum boat which was twined with tungsten wire. The deposition rate was controlled by turning the current of the tungsten filament, and thickness was monitored by microcrystalline quartz balance. The evaporation source was positioned 31.5 cm away from the sample holder. The evaporation source was preheated for 5 min before opening the shutter to deposit Sb₂Se₃ film. Deposition rate was kept at approximately 10 Å/s and lasted for 10 min. Continuous rotation of the sample holder with 3 rad/min during the deposition process facilitated the formation of homogeneous films. Afterward, the shutter was closed and the samples were cooled down to room temperature naturally.

2.3.14. Deposition of CdS film

CdS thin films were fabricated using a thermal evaporation deposition technique following a previously reported procedure with minor modifications.³⁵ High-purity CdS powder kept in a tungsten boat was evaporated inside the vacuum chamber. The deposition was carried out on a substrate maintained at room temperature.

2.3.15. Deposition of Sb₂Se₃/CdS thin film p-n heterojunction

To prepare the Sb₂Se₃/CdS thin film p-n heterojunction, CdS powder was evaporated over as-prepared Sb₂Se₃ films keeping all the experimental conditions same. The excess CdS powder to be deposited was kept in a boat and the deposition rate was controlled by turning the current of the tungsten filament.

2.4. Characterization Techniques

2.4.1. X-Ray Diffraction (XRD)

X-rays are electromagnetic radiation of wavelength $\sim 1\text{\AA}$ which is of the same order as the interplanar lattice plane of the crystal. XRD is a very important experimental technique that has been used to determine the crystal structure of solids, including lattice constants and identification of unknown materials.^{36,37}

Principle: In XRD, a collimated beam of X-rays falls on a specimen, and it diffracts from the crystalline planes of the specimen based on Bragg's law³⁸:

$$n\lambda = 2d\sin\theta$$

where n is the diffraction order, λ is the incident X-ray wavelength, d is the interplanar distance for a particular crystal plane and θ is the angle of diffraction (**Figure 2.5**). The intensity of X-rays is measured as a function of the diffraction angle (2θ) and the specimen's orientation. This diffraction pattern is used to identify the specimen's structural properties and its crystalline phases. The diffraction peak positions are accurately measured with XRD; thus, it is the best method for characterizing homogeneous and inhomogeneous strains. Homogeneous strain usually shifts the peak position of diffracted rays while inhomogeneous strains can cause a broadening of diffraction peaks that increases with $\sin\theta$. Moreover, the finite size of crystallite can also cause the peak broadening but in this case, broadening is independent of $\sin\theta$. In the absence of inhomogeneous strain, the average particle size can be calculated from the XRD peak width using Scherrer's equation,

$$x = \frac{k\lambda}{\beta\cos\theta}$$

where x is the average particle size, K is the shape factor (usually close to 1), β is the full width at half maximum (FWHM) of the peak and θ is the diffraction angle.

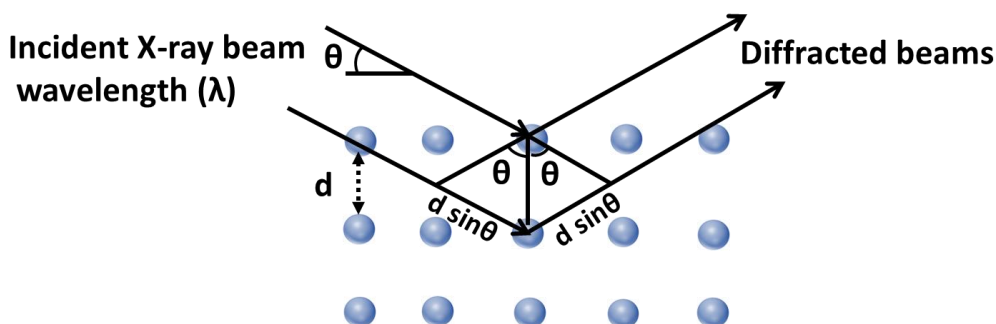


Figure 2.5. Diffraction of incident X-rays by a crystal and Bragg's law.

Instrumentation: The basic components of XRD consist of an X-ray source, sample holder, and X-ray detector as shown in **Figure 2.6**. A cathode tube within the source is heated to create electrons, which are then accelerated to strike the target material by applying enough voltage. X-rays are produced when inner shell electrons in a material are removed by electrons with sufficient energy (specific to the target material). This X-ray would have a spectrum of different wavelengths that would be specific to the target material and consist of many wavelengths. To create a monochromatic X-ray beam to strike the material, this X-ray spectrum is filtered using foils or crystal monochromators. Using precisely positioned optics and a monochromator, the reflected X-ray beams are focused on the detector. The detector gathers, processes, and sends the signal to the computer at a count rate. When the bombarding X-ray beams are following Bragg's law, constructive interference occurs and a peak is visible in the output data. The sample and the X-ray source maintain an angle of θ during the measurement, whereas the detector maintains an angle of 2θ .

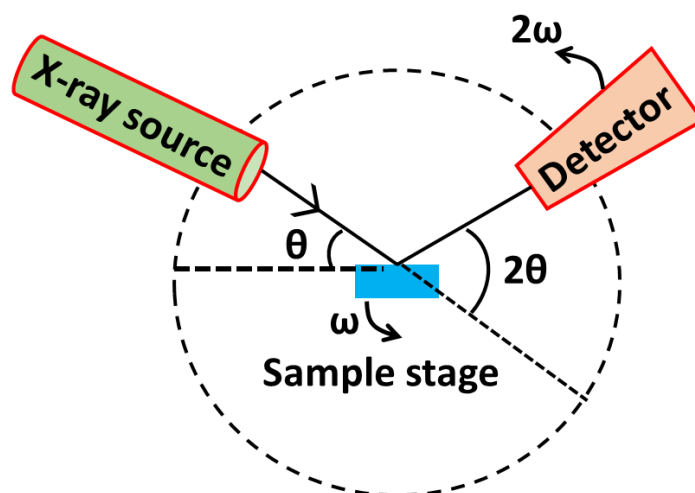


Figure 2.6. The basic layout of powder X-ray diffractometer.

For my thesis, we have utilized a Bruker D8 ADVANCE PXRD equipped with Cu K α radiation (1.5418 Å), operating at an accelerating voltage of 40 kV and a current of 25 mA. The resulting XRD patterns were compared to databases maintained by the Joint Committee on Powder Diffraction Standards (JCPDS).

2.4.2. X-ray Photoelectron Spectroscopy (XPS)

XPS was employed to examine the surface composition and oxidation states of elements present in the sample. It is a powerful surface characterizing tool where soft X-ray beams either Mg K α ($h\nu = 1253.6$ eV) or Al K α ($h\nu = 1486.6$ eV) are directed to the sample surface.³⁹⁻⁴¹

Principle: The operation of XPS is based on the principle of the photoelectric effect. Monochromatic X-ray photons that strike the sample surface cause the atoms in that material to eject electrons from their inner orbitals (**Figure 2.7**). The kinetic energy (KE) of these ejected electrons is dependent on the binding energy (BE) of the electron and the spectrometer work function (Φ) and may be determined using Einstein's equation:

$$KE = h\nu - BE - \phi$$

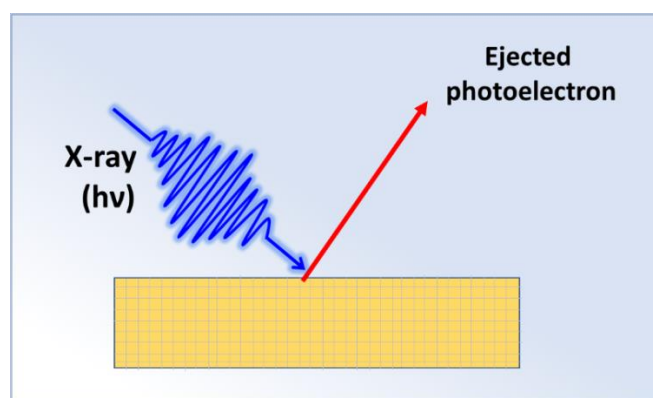


Figure 2.7. The basic principle of XPS.

where $h\nu$ is the energy of the photon, BE is the binding energy of the atomic orbital from which the electron originates, and ϕ is the spectrometer work function. XPS mainly measures the KE of the electrons since the other two parameters are constant. The binding energy of ejected electrons depends upon the nature of orbitals from where they are expelled. Due to spin-orbit coupling with intensities of 1:2, 2:3, and 3:4, respectively, the p, d, and f orbitals break into $p_{1/2}$ and $p_{3/2}$, $d_{3/2}$ and $d_{5/2}$, $f_{5/2}$ and $f_{7/2}$ levels.

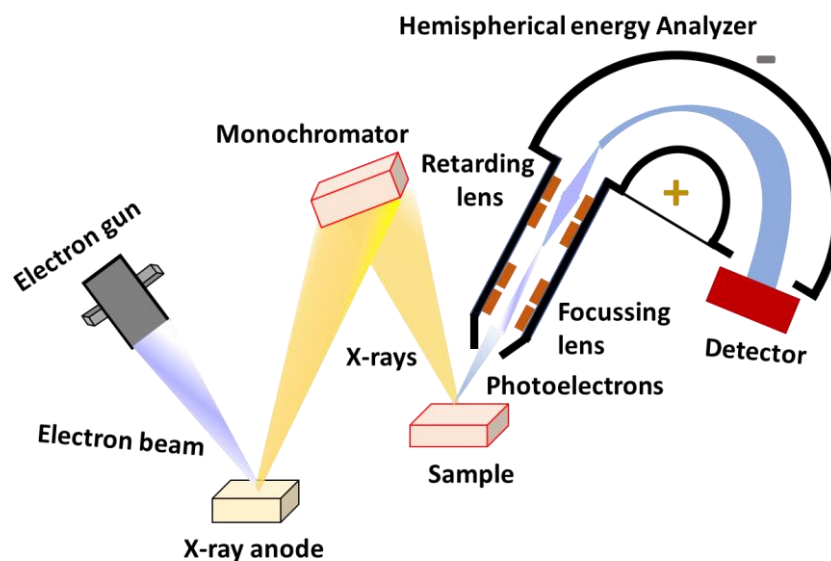


Figure 2.8. Outline of an XPS setup.

Instrumentation: XPS instruments consist of several key components (**Figure 2.8**) which are discussed below:

1. **Ultrahigh vacuum system:** XPS instruments require an ultrahigh vacuum environment with operating conditions typically below 10^{-9} Torr. This vacuum is necessary because the emitted photoelectrons have low energy and can be easily absorbed by gas molecules present in the chamber. To minimize interactions of electrons with the gas, the pressure needs to be extremely low.
2. **X-ray Source:** XPS instrument use an X-ray source to excite the sample. The most commonly used X-ray sources in XPS are Al $K\alpha$ (1486.6 eV) and Mg $K\alpha$ (1253.6 eV) X-rays. These X-rays are directed through a monochromator which permits only specific energies of X-rays to reach the sample.
3. **Monochromator:** A monochromator was used to select and filter the X-rays of a particular energy to fall on the sample. This ensures that only X-rays of the desired energy range are used for excitation and analysis.
4. **Electron energy analyzer:** An electron energy analyser, often called a concentric hemispherical analyser, is used to separate photoelectrons of various kinetic energies, after passing through a few lenses and apertures. A certain voltage is maintained between these hemispheres, with the outer sphere being more negative.

5. **Argon (Ar) ion gun:** An Ar ion gun is utilized to remove environmental contaminations from the material's surface.
6. **Detector:** Electron multipliers are used as XPS detectors. To capture the most electrons, numerous electron multipliers are frequently used. These detectors transmit the data to a computer, which creates an XPS spectrum from the electrical signal.

In my thesis, we utilized a K-alpha XPS system built by Thermo Fisher Scientific, with an Al K α X-ray source of 1486.6 eV energy. For achieving a survey spectrum and a narrow scan, the CHA pass energy was kept at 200 eV and 500 eV, respectively. To keep the ultrahigh vacuum, two turbo ion pumps and one rotary pump were employed.

2.4.3. Scanning Electron Microscopy (SEM)

SEM is a powerful technique that provides information about the surface properties, topography, crystal structure, grain boundary, and elemental composition of the materials.^{42,43}

Instrumentation: The several key components of SEM are an electron gun, lenses, backscattered electron detector (BSED), secondary electron detector (SED), and energy dispersive X-ray spectrometer (EDS). The basic outline of SEM is presented in **Figure 2.9**.

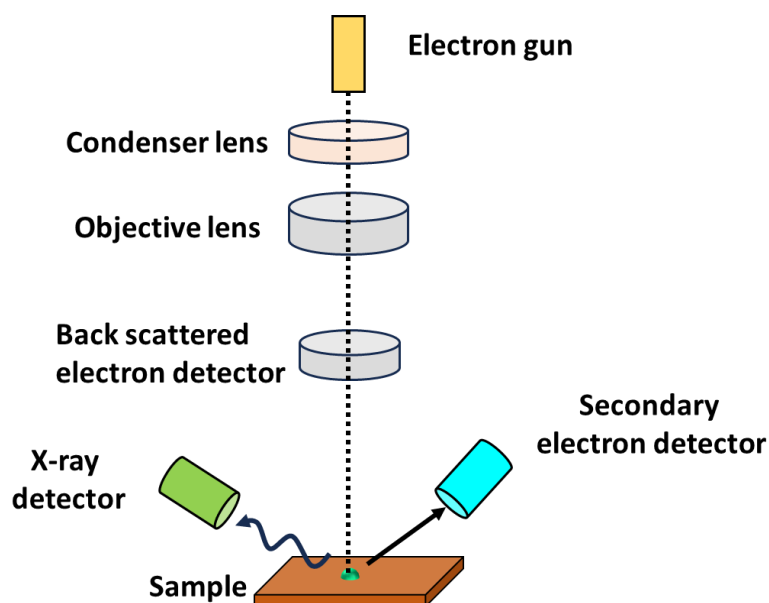


Figure 2.9. The basic layout of SEM showing the various parts of the instrument.

1. **Electron source:** The source of the electrons, the electron gun, has the ability to alter the electrons' amplitude and acceleration. Typically, numerous types of electron sources are used as electron sources. Tungsten (W) filaments, lanthanum hexaboride (LaB₆), and Schottky field emission are the most commonly utilized electron sources.
2. **Electromagnetic lens:** The electron beam generated from the electron gun is passed through electromagnetic lenses. The electromagnetic lenses could focus and de-magnify electron beams. The diameter of the electron beam after passing through the electromagnetic lens can be determined using the following equation:

$$d = \frac{1}{2B} \sqrt{\frac{2mV_0}{e}}$$

Here, d is the probe diameter in millimeters, B is the magnetic field in Tesla, e is the electron charge, m is electron mass, and V_0 is the accelerating voltage (kV) of an electron.

The sample chamber is positioned at the bottom of the electron columns and generally, it is kept under vacuum condition. Here, the vacuum is not as high as compared to the electron column, and the specimen chamber is maintained at a pressure of around 10^{-3} Pa.

3. **Detectors:** SEM incorporates several detectors to collect the signals generated by the interaction of the electron beam with the sample. The most common detectors include backscattered electron detectors, secondary electron detectors, and X-ray detectors. The main function of the detector is to receive the signal from the specimen and convert it into an electrical signal.

In my thesis work, we have utilized a JEOL scanning electron microscope (model no: JSM-7610F Plus). This instrument could acquire data at a very fast speed with high-quality images.

2.4.4. Transmission Electron Microscopy (TEM)

Introduction: TEM is a versatile technique used to investigate the structure, morphology, and properties of nano-sized materials. It has diverse applications in materials science, nanotechnology, biology, and other fields, etc. In TEM, a beam of

electrons is transmitted through a thin sample, and the resulting image is formed by detecting and interpreting the interactions of the electrons with the sample. The TEM equipment operates on the same fundamental optical principles as a light microscope but uses electrons in place of light and magnetic lenses in place of traditional glass lenses.^{44,45} Since electrons have a very short effective wavelength, TEM may be used to observe very tiny things, such molecules and nanoparticles. TEM is now the most effective method of electron microscopy, having a resolution of over 2 nm. Ernst Ruska and Max Knoll, two German physicists, created the first experimental TEM apparatus in 1931.⁴⁶ Today, TEM is widely utilized in all scientific fields to visualize the structure, morphology, flaws, and other characteristics of any material.

Principle: When an electron beam is bombarded on the specimen/sample, these high-energy incoming electrons strongly interact with the specimen atoms to produce diverse signals as illustrated in **Figure 2.10**. Some of the phenomena include X-ray emission, backscattering of electrons, inelastic and elastic scattering, secondary electron emission, etc. However, in typical TEM imaging, the only electrons that are of relevance to us are those in the forward scattered beam, which pass through the material without deviating (limited within 5° along the direct beam).

The resolution of a TEM refers to its ability to distinguish fine details and resolve closely spaced features in the sample being examined. De Broglie's equation provides the electron's wavelength as

$$\lambda = \frac{h}{p}$$

Where h is Planck's constant and p is the momentum. An electron with mass m_0 gains momentum under high voltage (E) as per the following equation

$$p = \sqrt{2Em_0}$$

Thus, λ in nm units can be represented as

$$\lambda = \frac{h}{\sqrt{2Em_0}}$$

As a high-speed electron beam is produced by an electron gun, therefore, it is crucial to consider relativistic effects. The wavelength is expressed as,

$$\lambda = \frac{h}{\sqrt{2Em_0(1+\frac{E}{2m_0c^2})}}$$

This equation demonstrates that the resolution of the TEM equipment is inversely proportional to the energy of the electron.

Thus, by using a high-energy electron beam typically 120 kV for organic samples and 200 kV for inorganic materials, atomic-level resolution can be attained using TEM.

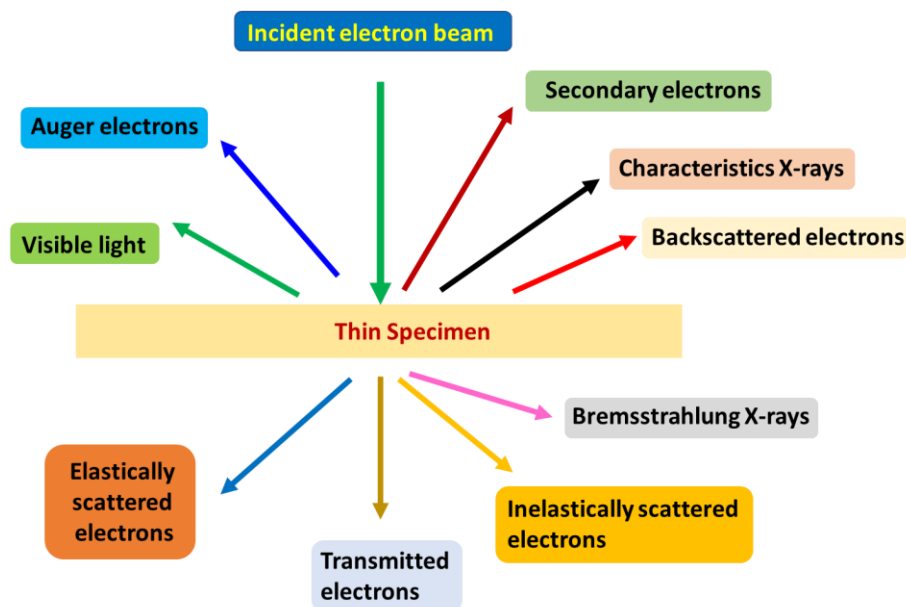


Figure 2.10. The different signals generated when a high-energy electron beam interacts with the thin specimen.

Instrumentation: The basic layout of the TEM instrument is shown in **Figure 2.11**. It is comprised of a variety of components.

1. **Electron Source:** The TEM utilizes an electron gun as its source of electrons and it is positioned at the top of the TEM column. Thermionic guns and field-emission guns (FEG) are the two different categories of electron guns. In a thermionic emission gun, the filament is placed inside the Wehnelt cylinder. Different types of filaments are available including W and single crystals of LaB₆. LaB₆ is currently the most widely used filament as it can produce a beam that is around ten times brighter than a W filament and has a significantly longer lifespan. In comparison to the W filament, the LaB₆ filament can also offer better coherency and less energy dispersion. The FEG can give around 100 times more

brightness than LaB_6 when compared to a thermionic gun, as well as a smaller beam spot size, more coherency, and less energy spread, however, a significantly higher vacuum level is needed.⁴⁸

- 2. Condenser System:** Electromagnetic lenses are utilized to focus and shape electron beams. They can either magnify or demagnify the picture. There are two condenser lenses: the first condenser lens regulates beam size and the second controls beam intensity.
- 3. Specimen:** The sample to be studied is prepared to be very thin. This thin section allows the electron beam to pass through the sample with minimal scattering and interaction, enabling high-resolution imaging. To maintain the specimen, TEM grids should be employed. On the TEM grid, diluted materials are drop-casted and dried in vacuum.
- 4. Vacuum:** A TEM system can only function in a high vacuum. In the air, electrons cannot travel much. Less scattering will occur between the electrons and the air particles in a suitable vacuum.

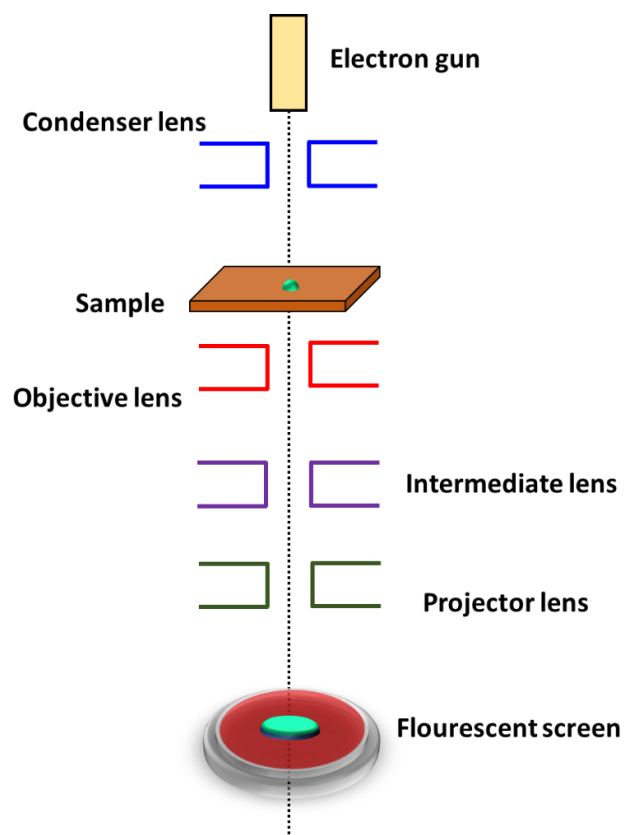


Figure 2.11. The basic layout of TEM showing the various parts of the instrument.

5. **Objective lens and aperture:** The objective lens is employed to focus and enlarge the object. It is the most significant lens because it creates the specimen's initial image and diffraction pattern. The intermediate and project lenses that follow further enlarge the image and diffraction pattern. After high magnifications, any initial picture or diffraction pattern aberrations will worsen.
6. **Projector lens:** The pictures produced by the intermediate lens are enlarged even further by the projector lens. The projector lens has a large depth of focus, which allows the final pictures to be sharp at a considerable distance along the optical axis. The final picture magnification M is expressed as,

$$M = M_{\text{Obj}} \times M_{\text{Int}} \times M_{\text{Proj}}$$

Here, the objective, intermediate, and projector lenses' relative magnifications are denoted as M_{Obj} , M_{Int} , and M_{Proj} .

7. **Imaging:** A fluorescence plate receives the transmitted electron beam projections, which create a picture of the sample region that was focused for the measurement. This plate has a CCD camera positioned beneath it, which records the pictures and sends them as micrographs to the computer. This brilliant field picture was created solely as a result of transmitted electrons. TEM is now utilized for more than just imaging samples; it may also be used for quantitative material analysis. Energy dispersive X-ray spectroscopy (EDS) may be used to get a quantitative study of the elements contained in the sample and their relative proportion. As the high-energy electron beam collides with the sample surface, core electrons from the constituent atoms are expelled. To fill the ensuing vacancies, electrons from higher energy states are released by the emission of X-rays unique to the elements found in the sample. A graph of emitted X-rays' relative intensity as a function of energy is plotted. Based on the peak intensities and a reference sample, quantitative analysis was done.

JEM-2100 Plus from JEOL with an operating voltage of 200 kV was utilized in this thesis to capture the TEM images and gather morphological data for the as-prepared NCs. It makes use of LaB₆ as the electron gun and enables the achievement of extremely high TEM resolution.

2.4.5. Mott Schottky (MS) plots

Mott Schottky (MS) plot is a characterization technique based on Mott-Schottky theory and it provide details regarding charge-carrier concentration of semiconductors and flat band potential. Moreover, MS plots also describe the type of conductivity (p or n-type) of a semiconductor through the obtained slope.^{49,50} If the slope of the MC plot is positive then the semiconductor will be n-type and if the slope is negative then the semiconductor will be p-type. We have used MS plots to determine the type of conductivity of a semiconductor.

2.5. Steady-state optical studies

2.5.1. Steady-state absorption spectroscopy (UV-Vis)

This UV-VIS spectroscopy is widely used to characterize nanomaterials, organic compounds and semiconductor QDs. It provides information regarding the electronic transitions existing within the material.

Principle: The interaction of light and matter is the basis for UV-Vis absorption spectroscopy. When light is incident on material, it may be absorbed by the molecules in it. As a result, the material undergoes an electronic transition from the ground state to the higher excited states.⁵¹⁻⁵³ In essence, an optical spectrometer provides a quantitative measure of a material's absorbance as a function of wavelength. The absorption capabilities of the materials are described by Beer-Lambert's law. Beer's law states that material absorption (A) is influenced by the concentration (c) of the material, whereas Lambert's law states that radiation absorption is influenced by the length of the absorption path (l), regardless of the intensity of the incident radiation. Now, if I_0 is the intensity of the incident radiation and I is the intensity after transmission, then the absorbance of the material can be defined as

$$A = \log \left(\frac{I_0}{I} \right) = \epsilon c l$$

Where, ϵ is the molar absorption coefficient of the material.

Instrumentation: The absorption spectrometer consists of several key components viz light source, monochromator, sample stage, and detector.⁵⁴ The basic optical setup of the steady-state absorption spectrometer is displayed in **Figure 2.12**. UV-Vis

absorption spectroscopy uses a stable and broad-spectrum light source. Single Xenon lamps may often produce radiations across the UV-Vis range. However, they are highly pricey and have stability problems. Therefore, in modern times, tungsten (W) or halogen lamps are employed for the visible region together with deuterium arc lamps as the UV light source. Next, the monochromator is placed in the path of the source light and is responsible for the separation of the different colours. It consists of prism or diffraction grating that disperses the incident light into its various wavelengths. The light from the monochromator is then split into two beams, one passing through the sample solution and the other in a reference sample. The reference sample is needed for all measurements and is simply a cuvette filled with the same solvent as the one in which the sample is dispersed. These beams hit a detector, which turns the variation in absorption caused by the sample's presence into an electrical signal and transmits it to a computer.

In this present work, we used a Shimadzu-made UV-2600 spectrometer with an operating range of 190 nm to 900 nm with two light sources of deuterium and a halogen lamp. Data collection in the NIR region was carried out by utilizing a Cary 5000 UV-VIS-NIR spectrophotometer with an operating range from 175 - 3300 nm. Pb `Smart detector has been used to detect long-wavelength absorption, making it an ideal tool for material science research.

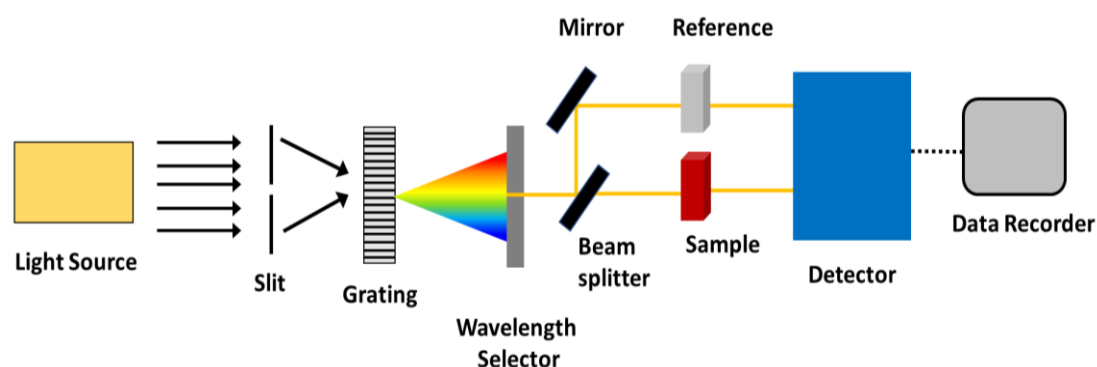


Figure 2.12. Basic optical setup of steady state absorption spectrometer, showing different parts of the instrument.

2.5.2. Photoluminescence spectroscopy

The photoluminescence spectroscopy (PL) method is utilized for examining the emission of light from materials after they have absorbed photons. After electromagnetic radiation has been absorbed, the excited charge carriers inside the

material tend to relax and return to the ground state. They then release their energy in the form of heat or light, depending on whether they take a radiative or non-radiative path. PL spectroscopy is used to analyze these radiative events. The emission usually occurs at a longer wavelength (lower energy) than the excited light. This is because charge carriers first relax down to the lowest vibrational level of the excited state before embracing radiative recombination. It is a crucial instrument for gaining a thorough understanding of the energy or charge transfer processes present in a system, sample quality and purity, the presence of defect states, particle size, band structure of the system, etc.⁵⁵ Photoluminescence is formally divided into two categories fluorescence and phosphorescence. Fluorescence occurs fast with the emission of photons. The emission rate of fluorescence is of the order of 10^9 s^{-1} while the emission rate of phosphorescence is slow (10^3 - 10^0) s^{-1} .⁵⁶ PL quantum yield (PLQY) (Φ) is a measure that is widely used to assess how successfully a material emits the absorbed photons by fluorescence or, on occasion, phosphorescence ($N_{\text{emitted}}/N_{\text{absorbed}}$). It is a relative measurement of the radiative (k_r) and non-radiative emission rate constants (k_{nr}). Mathematically, it is represented as⁵⁷:

$$\Phi = \frac{k_r}{k_r + k_{nr}}$$

PLQY of the sample can be calculated by using the following equation:

$$\Phi(\text{sample}) = \frac{A_{\text{sample}}}{A_{\text{reference}}} \times \frac{OD_{\text{reference}}}{OD_{\text{sample}}} \times \frac{\eta^2(\text{sample})}{\eta^2(\text{reference})} \times \Phi(\text{reference})$$

Where, Φ , A , and OD stand for the PLQY, area under the photoluminescence curve, and optical density of sample and reference, respectively. η represents the refractive indices of respective solvents of the sample and reference.

Instrumentation: Photoluminescence spectroscopy instrumentation typically consists of several basic key components to detect and analyze the emitted light from a sample: light source, monochromator, sample assembly, and detector. PL spectroscopy setups generally use Xenon lamp since it produces bright, intense white light with a broad wavelength range that extends from the UV domain at 230 nm to the near-infrared area of the electromagnetic spectrum. This light is first passed through an excitation monochromator to select the appropriate wavelengths for different excitations (**Figure 2.13**).

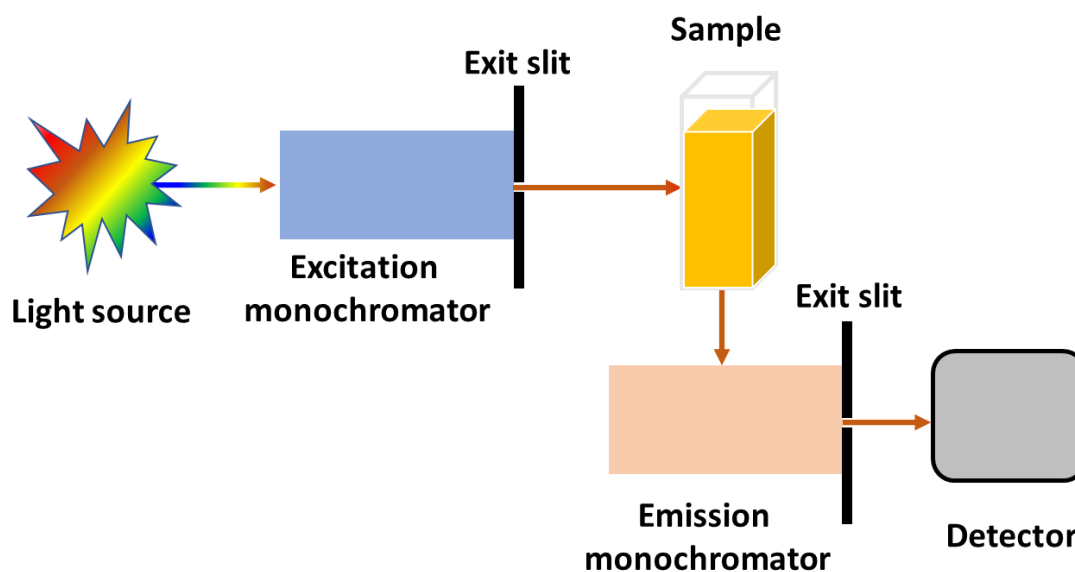


Figure 2.13. Optical layout of photoluminescence spectrofluorometer.

The monochromator uses a combination of rotating diffraction gratings to select the centre wavelength that will be transmitted further and slits to decide the bandpass of the excitation wavelengths. Afterwards, the sample is exposed to the output beam from the excitation monochromator which leads to radiative emission from the sample. The emission beam is passed to the emission monochromator which once again separates various wavelength components before being directed into the detector. A photomultiplier tube (PMT) is typically used as the detector. It translates optical changes into electrical signals, which are then sent to the computer. The sample emits radiation, and that radiation scatters in all directions. To avoid the unnecessary incidence of the high-intensity excitation wavelength on the detector, unlike the steady-state absorption apparatus, the detector in the PL spectroscopy setup is placed at a 90° angle to the incident beam. For the PL measurements used in this research, we deployed an Edinburgh FS5 spectrofluorometer. Its light source is a 150 W CW Ozone-free xenon arc lamp. This fluorometer enables stimulation of the samples at wavelengths between 230 and 1000 nm, and monitoring of the subsequent emission between 200 and 870 nm. The emission detector uses a single photon counting detection technique and is a Photomultiplier PMT-900 having a spectral range of 200 nm to 900 nm.

2.6. Techniques to Monitor Ultrafast Processes in Semiconductor NCs

2.6.1. Time-Correlated Single Photon Counting (TCSPC)

The time-dependent luminescence study presents a crucial method to determine the intensity of luminescence as a function of time after the excited state is created.^{58,59} Time-correlated single photon counting (TCSPC) is a method frequently employed to assess the time-dependent luminescence intensity and for measuring the lifetime of a fluorophore or luminous sample in its excited state. In the time resolved PL (TRPL) experiment, a high repetition rate pulsed laser source is used to excite the samples. TCSPC measures the single photon's arrival time with respect to the excitation of a reference laser pulse. The start signal is a laser reference pulse, and the stop signal is photoluminescence from the sample. The period between the start and stop signals is monitored. The time difference between start and stop is recorded as a histogram after each measurement is done. For a complete decay curve of the photoluminescence lifetime, this measurement is done numerous times. It is crucial that in TCSPC, each laser pulse excitation event only counts one photon. In histogram statistics, multiphoton events lead to inaccurate results also known as the "pulse pile-up effect".

Instrumentation: **Figure 2.14** displays the schematic for the TCSPC spectrophotometer. The setup for TCSPC generally consists of several parts that work together to produce excellent temporal resolution and photon counting capabilities. The general components used in basic TCSPC setup are an excitation source (pulsed laser diode), monochromator, photomultiplier tube (PMT), time-to-amplitude converter (TAC), constant fraction discriminator (CFD), multi-channel analyser (MCA), a computer-based program for fitting and analyzing data. The temporal delay between excitation and emission is measured using specialized electronics. The laser pulse from the excitation source is split into two parts; one portion excites the sample, while the other portion is sent to a photodiode to provide the electrical signal for CFD. CFD processes this signal and precisely calculates the pulse's moment of arrival. This signal is sent to a time-to-amplitude converter (TAC), which produces a voltage ramp, which is a rise in voltage that occurs linearly over time on the nanosecond timeframe. The sample emits photons upon photo-excitation, which are captured at right angles to

the excitation source and transmitted via a monochromator before being picked up by PMT. The signal from PMT is transmitted to CFD which delivers a signal to terminate the voltage ramp after precisely calculating the signal's arrival time. Afterward, the signal is sent to TAC which converts the signal to voltage that is proportional to the time delay (t) between the excitation and emission. A PGA (programmable gain amplifier) amplifies the voltage as needed and it is translated into numerical value by the analog to digital converter (ADC). The voltage is transformed into a digital value, which is then recorded as a single event with the given time delay. By repeatedly doing this procedure with a pulsed light source, the histogram is generated by MCA. The final result is a plot between counts vs. different delay times.

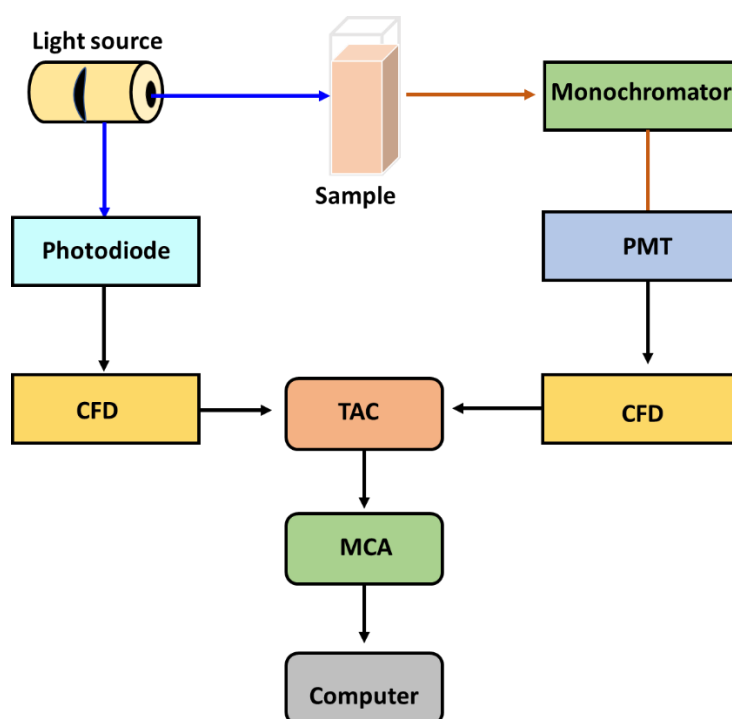


Figure 2.14. Schematic of the TCSPC spectrophotometer.

In my thesis, we have used the Deltaflex Modular Fluorescence Lifetime System (HORIBA Scientific), spectrofluorometer with a standard 90° arrangement. We have used a pulsed laser diode with a wavelength of 402 nm having IRF of 200 ps for photoexcitation.

2.6.2. Pump-Probe Transient Absorption (TA) spectroscopy

As is well known, charge transfers in semiconductor materials occur in the sub-ps time domain. To analyze the precise time scale of the related processes, TCSPC having ns time resolution is therefore insufficient.⁶⁰ Moreover, the main drawback of

TCSPC is that analysis cannot commence until photoluminescence is present in the experimental materials. Therefore, non-radiative processes such as charge carrier relaxation, intraband carrier cooling, charge recombination, and charge separation cannot be detected using time-resolved PL experiments. Ultrafast TA spectroscopy is an effective experimental technique utilized to study the dynamics of such photoinduced processes in materials which occur typically in femtoseconds (10^{-15} s) to picoseconds (10^{-12} s) range.^{61,62}

2.6.3. Principle and origin of various signals in TA data

In TA spectroscopy, the sample is excited with a pump laser, and the pump-induced variations in the absorption are monitored with a broadband probe beam, revealing important details regarding the charge carrier relaxation and recombination dynamics. The optical delay is maintained between pump and probe pulses either by increasing the optical path of the probe beam or by decreasing the path of the pump beam. Adjusting the pump-probe time delay and tracking changes in absorbance, give information about the dynamics of photophysical processes. The difference between the probe light's absorption in the presence and absence of the pump is used to examine the change in optical absorption.⁶³

$$\Delta A = A_{\text{with pump}} - A_{\text{without pump}}$$

The change in optical density can be determined by Beer Lambert's law, according to which $A = \log(I_0/I)$

Using this, we can rewrite ΔA as:

$$\begin{aligned} A &= \log \left[\frac{I_0^{probe}(\lambda)}{I^{probe}(\lambda, \Delta t)} \right]_{\text{with pump}} - \log \left[\frac{I_0^{probe}(\lambda)}{I^{probe}(\lambda, \Delta t)} \right]_{\text{without pump}} \\ &= \log \frac{[I^{probe}(\lambda)]_{\text{without pump}}}{[I^{probe}(\lambda, \Delta t)]_{\text{with pump}}} \end{aligned}$$

The value of ΔA can be both negative and positive, resulting in negative and positive signals in TAS, which are denoted as ground state bleach (*GSB*) and photoinduced absorption (*PIA*) or excited state absorption (*ESA*), respectively. When $I^{probe}(\lambda)$ (**with pump**) $>$ $I^{probe}(\lambda, \Delta t)$ (**without pump**), ΔA will be negative. This is due to the existence of ground-state bleach or stimulated emission. If there is ground state absorption, a pump pulse will raise the system to a higher energy state and reduce

probe absorption in the same transition region. This results in causing the probe to transmit an immense amount of intensity to the detector. Stimulated

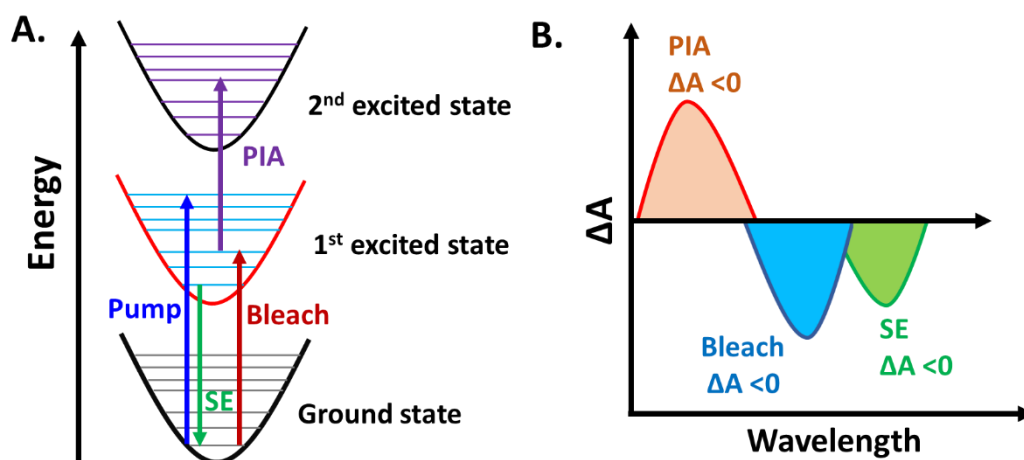


Figure 2.15. (A) Different types of TA signals; Bleach, SE, and PIA. (B) origin of signals.

Emission occurs when the probe wavelength coincides with the emission spectrum. It results in increased intensity of the probe on the detector and consequently negative ΔA (Figure 2.15 B). However, ΔA will be positive when $I^{probe}(\lambda)$ (with pump) $<$ $I^{probe}(\lambda, \Delta t)$ (without pump). The positive absorption corresponds to photoinduced absorption (PIA) depicted in Figure 2.15A.

The basic layout of a typical pump-probe setup is shown in Figure 2.16.

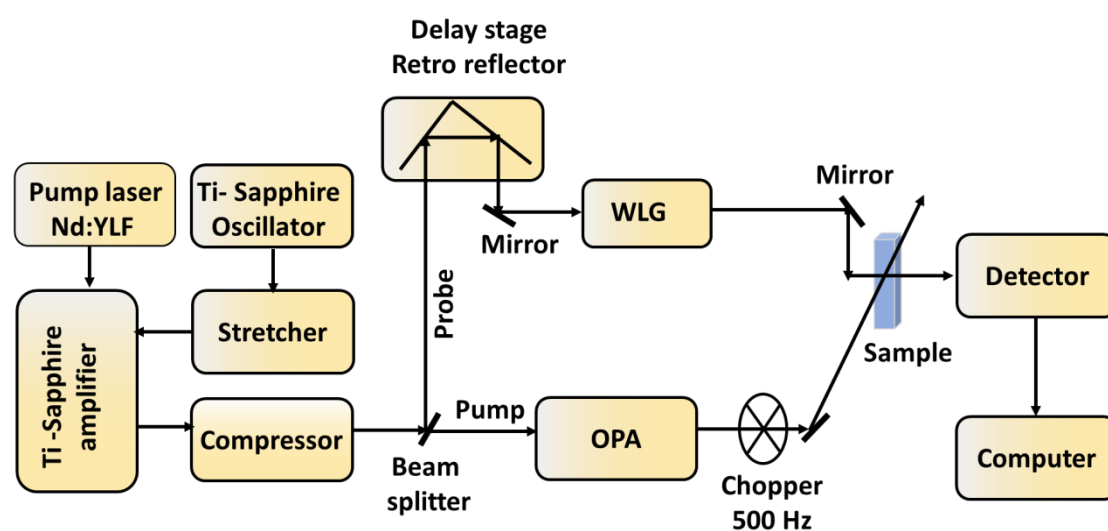


Figure 2.16. Schematic diagram of transient absorption setup.

2.6.4. Instrumentation of femtosecond transient absorption spectroscopy setup

The basic experimental setup of femtosecond TAS is comprised of several major components. such as the Astrella ultrafast amplifier laser system, an optical parametric amplifier (OPA), and a spectrometer. Each of these components will be covered in more detail in the following section.

2.6.4.1. Ti-sapphire oscillator/seed laser: ultra-short pulse generation

Ti-sapphire oscillator also known as seed laser is a tunable solid-state laser that consists of Ti^{3+} ions doped sapphire (Al_2O_3) crystals which act as gain medium. Before now, most ultrafast lasers were built using an organic dye gain medium. However, as opposed to these dye lasers Ti-sapphire laser can withstand much higher pump outputs, better thermal conductivity, broad emission spectra, and large bandwidth. Ti-doped sapphire has emerged as a versatile gain medium for producing and amplifying ultrashort pulses. The basic layout of the oscillator is displayed in **Figure 2.17**. Ti-sapphire crystal has been excited at 532 nm wavelength with continuous wave (CW) diode pumped solid state (DPSS) laser having a high power of 5W. The pump laser used to excite Ti-sapphire crystal is a Neodymium doped yttrium aluminum garnet (Nd: YAG) laser. The Ti-sapphire gain medium is positioned inside a cavity (between two or more mirrors) where the laser may be confined for an appropriate amount of time to generate ultrashort laser pulses. ‘fs’ or ‘ps’ pulses are created using the Kerr lens mode-locking approach. A highly intense laser beam changes the medium’s refractive index nonlinearly as it passes through a non-linear material (here, Ti-sapphire). The Kerr effect indicates that change in the refractive index of the medium can be expressed as,

$$n(\omega) = n_0(\omega) + n_2(\omega) I(r)$$

Here, $n_0(\omega)$ is the linear index of the medium. $n_2(\omega)$ is the non-linear refractive index which determines the extent of coupling between the electric field and the refractive index.

When a laser beam pass through the laser cavity as a Gaussian distribution, the intensity of beam can be expressed as,

$$I(r) = \exp(-gr^2)$$

Where, r is the distance from the centre of the beam, and g is the shape factor.

This suggests that the refractive index varies with laser beam intensity and is highest in the centre as opposed to the sides. This results in the self-focussing of the beam also called the Kerr effect. The higher-intensity portion of the beam is transmitted easily as compared to lower lower-intensity part. The CW mode is unstable because of this power-dependent loss. This method of creating a pulsed laser is also known as "Kerr lens mode-locking" or "Self-mode-locking" due to the medium's involvement in the focusing procedure. As the laser beam undergoes Group velocity dispersion (GVD) while passing repeatedly through the cavity, it is eliminated by putting two prisms inside the cavity.

In the present thesis, the "Astrella Ultrafast Laser system" is utilized. A Ti-sapphire oscillator (Vitara-T) is employed to generate 'fs' laser pulses. A CW DPSS laser (Verdi-G series) with an average power of 5 W is used to pump the gain medium. This green laser is produced by pumping a Nd-YAG crystal with a diode laser (808 nm). The oscillator generates laser pulses with an average power of 500 mW, 800 nm wavelength, and a repetition rate of 80 MHz every 20 fs. The multipass amplifier system will further amplify this output, also referred to as the "Seed laser."

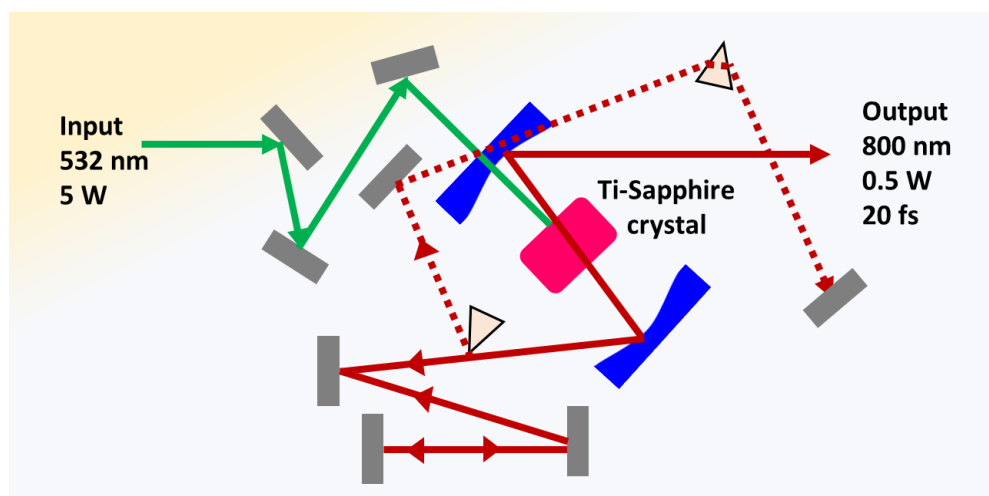


Figure 2.17. The basic layout of femtosecond Ti-sapphire oscillator for generation of ultrashort laser pulses.

2.6.4.2. Ti-Sapphire amplifier

We require strong ultrafast laser pulses for both practical applications and numerous scientific studies. The Ti: Sapphire laser's pulse is not powerful enough to excite the material for the pump-probe experiment. Regenerative amplifiers are typically used to amplify low energy output pulse from the oscillator and reduce their repetition rate from MHz to KHz. The Neodymium doped Yttrium Lithium Fluoride (Nd: YLF) diode laser, has been used to pump the regenerative amplifier. The Ti-sapphire amplifier system consists of several components including pulse stretcher, Ti sapphire amplifier, and synchronization electronics.

2.6.4.3. Pulse stretcher

A pulse stretcher is employed to temporally stretch the femtosecond pulse from seed laser to picosecond pulses, thus reducing the intensity of the pulses. It is very crucial to stretch the beam since the peak power of pulses from the seed laser are extremely high which can destroy the optics of the regenerative amplifier. The principle of the pulse stretcher is shown in **Figure 2.18**. It works on the chirped pulse amplification technique (CPA). It is comprised of plane mirrors, spherical mirrors, and diffraction grating.

When the seed pulse passes through the stretcher, the longer and shorter wavelengths of the seed pulse are sent in different directions and at varied diffraction angles by the stretcher's diffraction grating. The architecture makes it possible for shorter wavelengths to travel more distance as compared to larger ones. As a result, the longer wavelength beams exit the stretcher faster as compared to shorter ones, thereby stretching the pulse. The vertical retroreflector transmits the beam back to the stretcher four times, allowing for the spatial reconstruction of the beam.

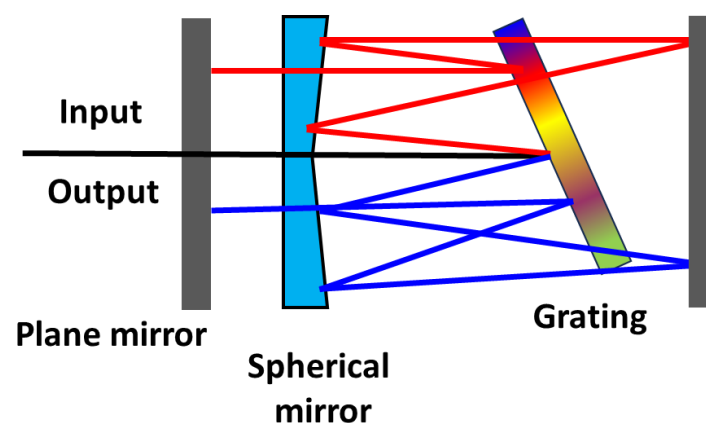


Figure 2.18. Schematic illustration of femtosecond pulse stretcher.

2.6.4.4. Pulse picker

The pulse picker receives the stretched pulses and lowers the repetition rate from 80–90 MHz to 1KHz. It picks only one pulse from a train of stretched pulses and directs it to the Ti-sapphire cavity. And blocks the other pulses to direct in the amplification system. Pulse picker utilizes the electro-optical pockel cell effect. The pulse picker is comprised of polariser and pockel cells. Horizontally stretched pulses are picked up by the pulse picker and dumped when there is no voltage provided to the pockel cell. However, when voltage is applied, the pulses' polarisation changes to vertical, allowing them to pass through the polarizer and be used for further amplification. Two pockel cells are situated in our system, acting as quarter-wave plates (causing a shift in the polarisation of $\lambda/4$) when a voltage is applied. For seed pulse trains to achieve the necessary amplification, these pockel cells serve as the entry and exit gates. To ensure that just the necessary pulses are selected from the whole pulse train and amplified further, synchronization electronics are in place to regulate the application of voltage to the pockel cells. The Synchronisation and Delay Generator (SDG) Elite unit manages these electronics. This regulates the applied voltage to maintain the right delay between the pockel cells.

2.6.4.5. Pump laser

Pump laser is used to establish the population inversion of the gain medium and this is obtained from revolution. The pump laser is diode diode-pumped Q-switched Neodymium doped Yttrium Lithium Fluoride (Nd: YLF) laser having the output of 527 nm wavelength with a repetition rate of 1kHz.

2.6.4.6. Ti-sapphire amplifier: Regenerative amplifier

The pulses chosen by the pulse picker are then injected into the Ti^{3+} : Sapphire cavity, which acts as the gain medium for the Regenerative Amplifier and amplifies the injected pulse by many orders (amplification factor $> 10^6$) by making several round trips in the laser cavity. The outline of the Ti-sapphire amplifier is described in **Figure 2.19**. The typical amplifier consists of a quarter wave plate, two pockel cells, mirrors, and a polarizer. Seed pulses reach the regenerative amplifier once the pulse has stretched from femtoseconds to picoseconds, and the Pockels cell (PC 1) then

selects the pulses. The pump laser achieves the population inversion. The seed laser and the pump laser are both focused on the same spot of the crystal. When the seed pulse passes through the gain medium (Ti: sapphire crystal), which is controlled by PC1, it is trapped inside the amplifier and amplified each time. To obtain more energy, the seed pulse passes through the gain medium between 15 and 20 times. When the energy increase over the seed pulse is 10^6 times greater, the amplified pulses are extracted from the cavity for the pump-probe femtosecond experiment (by modulating the PC2). The number of passes is dependent on the round-trip time between the mirrors (M1, M2), and maximal gain and energy are attained after a specific round-trip duration. Here, a quarter wave plate ($\lambda/4$) converts the linear polarisation to circular polarisation. At Brewster's angle, the polarizer reflects light polarisation parallel to the plane and transmits it parallel to the plane of reflection. Depending on the voltage used, the Pockels cells act as a fourth ($\lambda/4$) or half ($\lambda/2$) wave plate.

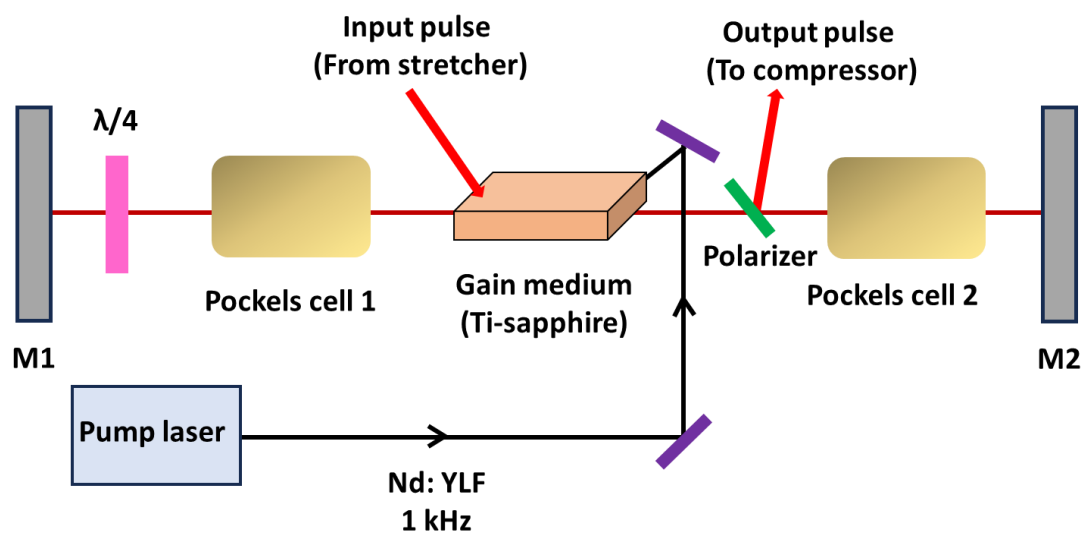


Figure 2.19. Schematic representation of Ti-sapphire amplifier.

2.6.4.7. Pulse compressor

It is used to compress the amplified stretched pulse back to the femtosecond pulse. The basic outline of the femtosecond pump compressor is shown in **Figure 2.20**. The compressor is made up of two gratings arranged so that the longer wavelength components must travel farther than the shorter wavelength components. Its working is opposite to that of a pulse stretcher. After compression, the main laser then releases

its compressed fs laser pulses, which are utilized in pump-probe spectroscopy. Our primary laser setup generates 800-nm laser pulses with a pulse width of around 50 fs, a repetition rate of about 1 kHz, and an energy of about 5 mJ per pulse.

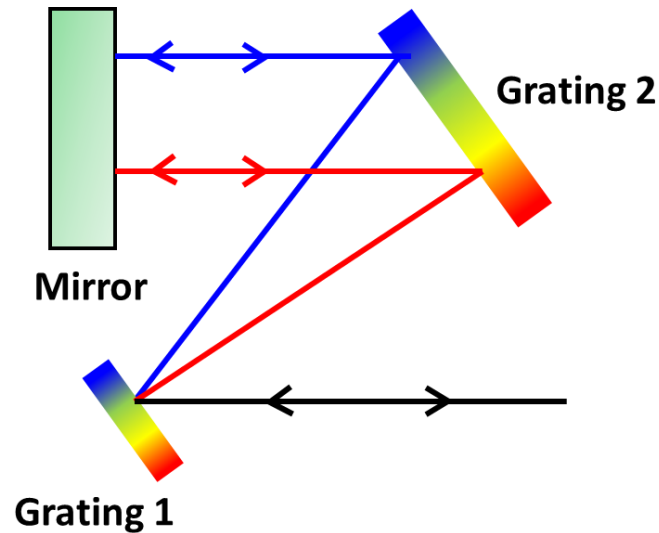


Figure 2.20. Optical layout of pulse compressor.

2.7. Optical Parametric Amplifier (OPA)

The beam splitter (65:35) divides the output pulse from the main laser into two components.

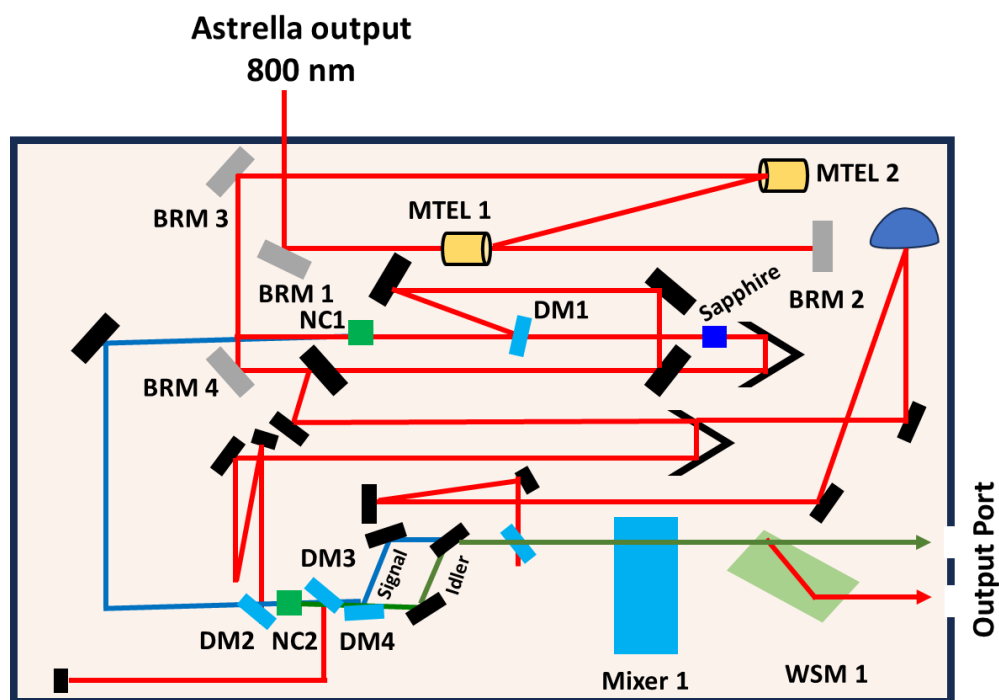


Figure 2.21. The basic outline of an OPERA-SOLO setup.

The higher and lower energy beams are referred to as pump and probe beams. The wavelength of pump beam can be tuned to the desired wavelength using an optical parametric amplifier (OPA). The overall layout of OERA-SOLO (OPA set-up) is illustrated in **Figure 2.21**. The orientation of certain optics has been controlled by rotation and translational stages which are operated using a computer. After entering OPA, the pump is incident on a beam splitter which divides it into two components having energy in the ratio 20:80. The low energy component is directed to sapphire which produces a white light continuum (WLC). This white light component along with another portion of the transmitted beam from BS1 passes through the non-linear crystal (NC1) where they overlap non-collinearly. This leads to the generation of signal and idler beams. The wavelength of the signal beam can be tuned by adjusting the delay between the WLC and pump beam as well as the angle of the non-linear crystal. According to the law of conservation of energy, the frequency of signal and idler beams can be related as:

$$\omega_p = \omega_s + \omega_i$$

The idler beam and residual pump are blocked by a beam blocker and only the signal beam is allowed to pass through. This signal beam and the remaining component of the pump beam overlap inside another non-linear crystal (NC2) which results in another signal and idler beams. These signal and idler beams are separated using dichroic mirrors which are then finally collected at the output port of OPERA-SOLO. The frequency mixture can tune the wavelength from UV to NIR range according to the requirement via second harmonics generation, sum frequency generation (SFG), and difference frequency generation (DFG). Second harmonics and SFG are produced by Type-1 phase matching non-linear Barium Borate (BBO) crystal. These mixtures are controlled by a computer. The output of the mixtures is directed to wavelength selectors (WSM) which are employed to select the desired frequency.

In my thesis, we have used "OPERA SOLO" from "Light Conversion" to create tuneable wavelengths between 280 to 2600 nm. The apparatus employs computer-based translational and rotational stages to accurately calibrate the output wavelength available at the exit end of OPERA SOLO.

2.8. Transient Absorption Spectrometer

In this dissertation, the TA spectrometer utilized is Helios Fire from Ultrafast Systems. The beam from the main laser having 800 nm wavelength has been divided into pump and probe beams with the help of a beam splitter. The block diagram of the transient absorption spectrometer is depicted in **Figure 2.22**. The Helios Fire system is made up of several crucial components, including a pump chopper, delay stage, crystals for generating white light, detector, etc. The probe beam from the main laser is fed to the spectrometer directly using an assembly of mirrors whereas the pump beam is directed to the chopper which is operated at 500 Hz to block each alternate pump pulse. The probe beam is passed through the delay stage which consists of a retroreflector and mirrors inside the spectrometer. This delayed probe pulse is directed at the proper crystals to create white light continuums with a variety of wavelengths. CaF₂ crystal is used to generate the probe light in the UV region, Sapphire is used to generate the probe light in the visible range, and Yttrium Aluminium Garnet (YAG) crystal is utilized to generate the probe light in the NIR region. The crystal stage is linked with the computer and the probing region can be selected from the software. Two detectors are housed in the setup: a complementary metal-oxide semiconductor (CMOS) sensor and an InGaAs sensor for UV/Vis and NIR detection, respectively. The range of UV, VIS, and NIR regions are 350-650 nm, 450-800 nm, and 800-1600 nm, respectively. The instrument response function (IRF) of the instrument is typically ~ 100 fs. White light goes through a filter and is focused on the sample. To achieve spatial overlap, the pump beam is focused at the same location on the sample as the probe. After passing through the sample, the pump is blocked whereas the probe is directed to the detector which is connected to a computer system. The data can be collected from Helios Fire software and analyzed using the Surface Explorer software.

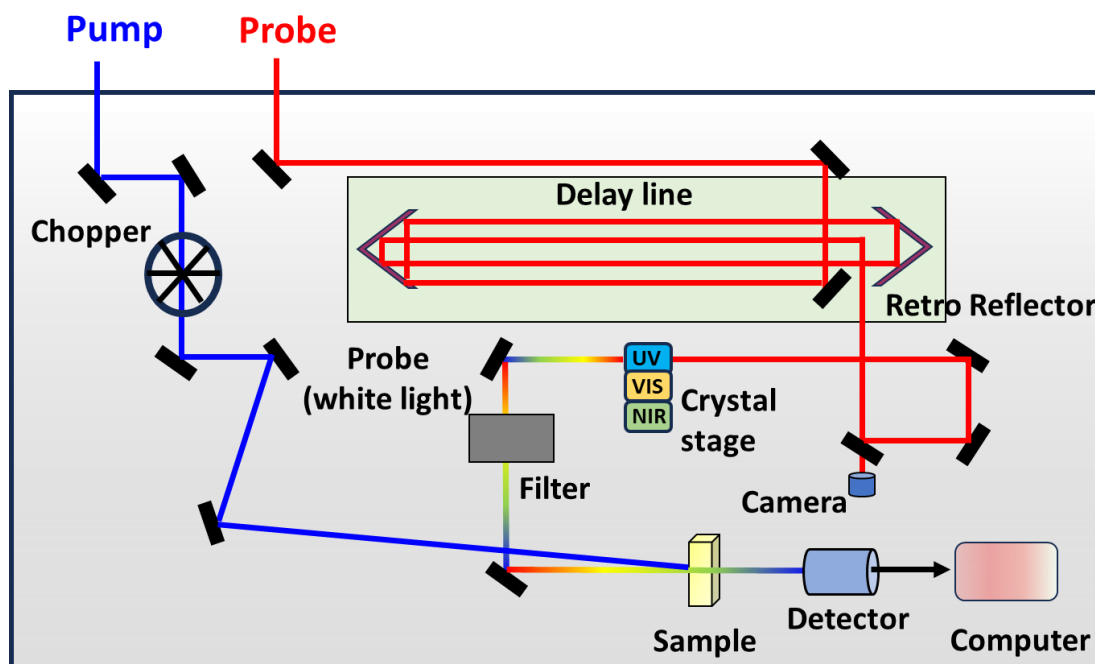


Figure 2.22. Optical layout of the Helios Fire transient absorption spectrometer.

2.9. Surface XplorerTM software

The TA fitting was conducted using the Surface Explorer software which is based on LabVIEWTM. This software provides all the fitting parameters, including both the time constants and their corresponding weights. The fitting operation uses the following function which allows us to fit a kinetic trace for the selected wavelength with a sum of convoluted exponentials:

$$S(t) = e^{-\left(\frac{t-t_p}{t_p}\right)^2} * \sum_i A_i e^{(t-t_0)/t_p}$$

$$t_p = \text{IRF} / 2. \ln 2$$

Here, IRF is the width of the instrument response function (full-width half maximum), t_0 is the time zero, A_i , and t_i are amplitudes and decay times respectively, * is the convolution function.

2.10. References

- (1) Biswas, A.; Bayer, I.S.; Biris, A.S.; Wang, T.; Dervishi, E.; Faupel, F. Advances in Top–Down and Bottom–up Surface Nanofabrication: Techniques, Applications & Future Prospects. *Adv. Colloid Interface Sci.* **2012**, *170*, 2-27.

- (2) Dabhane, H.; Ghotekar, S.; Tambade, P.; Pansambal, S.; Murthy, H. A.; Oza, R.; Medhane, V. A review on Environmentally Benevolent Synthesis of CdS Nanoparticle and Their Applications. *J. Environ. Chem. Ecotoxicol.* **2021**, *3*, 209-219.
- (3) Murray, C.; Norris, D.J.; Bawendi, M.G. Synthesis and Characterization of Nearly Monodisperse CdE (E= Sulfur, Selenium, Tellurium) Semiconductor Nanocrystallites. *J. Am. Chem. Soc.* **1993**, *115*(19), 8706-8715.
- (4) LaMer, V. K.; Dinegar, R. H. Theory, Production and Mechanism of Formation of Monodispersed Hydrosols. *J Am Chem Soc* **1950**, *72*, 4847–4854.
- (5) Thanh, N.T.; Maclean, N.; Mahiddine, S. Mechanisms of Nucleation and Growth of Nanoparticles in Solution. *Chem. Rev.* **2014**, *114*(15), 7610-7630.
- (6) De Mello Donegá, C.; Liljeroth, P.; Vanmaekelbergh, D. Physicochemical evaluation of the hot- injection method, a synthesis route for monodisperse nanocrystals. *Small* **2005**, *1*(12), 1152-1162.
- (7) Murray, C.B.; Kagan, C.R.; Bawendi, M.G. Synthesis and Characterization of Monodisperse Nanocrystals and Close-Packed Nanocrystal Assemblies. *Annu. Rev. Mater. Sci.* **2000**, *30*(1), 545-610.
- (8) Selinsky, R.S.; Ding, Q.; Faber, M.S.; Wright, J. C.; Jin, S. Quantum Dot Nanoscale Heterostructures for Solar Energy Conversion. *Chem. Soc. Rev.* **2013**, *42*(7), 2963-2985.
- (9) Rivest, J. B.; Jain, P. K. Cation Exchange on the Nanoscale: An Emerging Technique for New Material Synthesis, Device Fabrication, and Chemical Sensing. *Chem. Soc. Rev.* **2013**, *42*(1), 89-96.
- (10) Cozzoli, P. D.; Pellegrino, T.; Manna, L. Synthesis, Properties and Perspectives of Hybrid Nanocrystal Structures. *Chem. Soc. Rev.* **2006**, *35*(11), 1195-1208.

- (11) Beberwyck, B. J.; Surendranath, Y.; Alivisatos, A. P. Cation Exchange: A Versatile Tool for Nanomaterials Synthesis. *J. Phys. Chem. C* **2013**, *117*(39), 19759-19770.
- (12) Wang, Y.; Wang, Q.; Zhan, X.; Wang, F.; Safdar, M.; He, J. Visible Light Driven Type II Heterostructures and Their Enhanced Photocatalysis Properties: A Review. *Nanoscale* **2013**, *5*(18), 8326-8339.
- (13) Ling, T.; Jaroniec, M.; Qiao, S. Z. Recent Progress in Engineering the Atomic and Electronic Structure of Electrocatalysts Via Cation Exchange Reactions. *Adv. Mater.* **2020**, *32*(46), 2001866.
- (14) Tan, C.; Chen, J.; Wu, X.J.; Zhang, H. Epitaxial Growth of Hybrid Nanostructures. *Nat. Rev. Mater.* **2018**, *3*(2), 1-13.
- (15) Casavola, M.; van Huis, M.A.; Bals, S.; Lambert, K.; Hens, Z.; Vanmaekelbergh, D. Anisotropic Cation Exchange in PbSe/CdSe Core/Shell Nanocrystals of Different Geometry. *Chem. Mater* **2012**, *24*(2), 294-302.
- (16) Sahu, N.; Parija, B.; Panigrahi, S. Fundamental Understanding and Modeling of Spin Coating Process: A review. *Ind. J. Phys.* **2009**, *83*(4), 493-502.
- (17) Na, J.Y.; Kang, B.; Sin, D. H.; Cho, K.; Park, Y.D. Understanding Solidification of Polythiophene Thin Films During Spin-Coating: Effects of Spin-Coating Time and Processing Additives. *Sci. Rep.* **2015**, *5*(1), 13288.
- (18) Swami, S.K.; Kumar, A.; Dutta, V. Deposition of Kesterite $\text{Cu}_2\text{ZnSnS}_4$ (CZTS) Thin Films by Spin Coating Technique for Solar Cell Application. *Energy Procedia* **2013**, *33*, 198-202.
- (19) Yao, S.; Wang, J.; Cheng, J.; Fu, L.; Xie, F.; Zhang, Y.; Li, L. Improved performance of thermally evaporated Sb_2Se_3 thin-film solar cells via substrate-cooling-speed control and hydrogen-sulfide treatment. *ACS Appl. Mater. Interfaces* **2020**, *12*(21), 24112-24124.
- (20) Chen, C.; Li, W.; Zhou, Y.; Chen, C.; Luo, M.; Liu, X.; Zeng, K.; Yang, B.; Zhang, C.; Han, J.; Tang, J. Optical Properties of Amorphous and Polycrystalline Sb_2Se_3 Thin Films Prepared by Thermal Evaporation. *Appl. Phys. Lett.* **2015**, *107*(4), 043905

- (21) Liu, X.; Chen, C.; Wang, L.; Zhong, J.; Luo, M.; Chen, J.; Xue, D. J.; Li, D.; Zhou, Y.; Tang, J. Improving the Performance of Sb₂Se₃ Thin Film Solar Cells Over 4% by Controlled Addition of Oxygen During Film Deposition. *Prog. Photovolt.: Res. Appl.* **2015**, *23*(12), 1828-1836.
- (22) Zhang, L.; Wu, K.; Yu, J.; Yu, Y.; Wei, Y. Sb₂Se₃ Films Fabricated by Thermal Evaporation and Post Annealing. *Vacuum* **2021**, *183*, 109840.
- (23) El Radaf, I. M. Structural, Optical, Optoelectrical and Photovoltaic Properties of the Thermally Evaporated Sb₂Se₃ Thin Films. *Appl. Phys. A* **2019**, *125*, 832.
- (24) Zhou, M.; Gong, Y.; Xu, J.; Fang, G.; Xu, Q.; Dong, J. Colloidal CZTS Nanoparticles and Films: Preparation and Characterization. *J. Alloys Compd.* **2013**, *574*, 272–277.
- (25) Yang, H.; Jauregui, L. A.; Zhang, G.; Chen, Y. P.; Wu, Y. Nontoxic and Abundant Copper Zinc Tin Sulfide Nanocrystals for Potential High-Temperature Thermoelectric Energy Harvesting. *Nano Lett.* **2012**, *12*, 540–545.
- (26) Yu, W. W.; Peng, X. Formation of High-Quality CdS and Other II-VI Semiconductor Nanocrystals in Noncoordinating Solvents: Tun-able Reactivity of Monomers. *Angew. Chem., Int. Ed.* **2002**, *41*, 2368–2371.
- (27) Zhong, Y.; Zhang, L.; Sun, M.; Wang, M.; Chen, W.; Lin, S.; Xie, D.; Zhu, H. Large Scale Self-Assembly of SnSe Nanosheets Prepared by the Hot-Injection Method for Photodetector and Capacitor Applications. *Mater. Today Energy* **2019**, *12*, 418-425.
- (28) Vaughn, D.D.; In, S.I.; Schaak, R.E. A Precursor-Limited Nanoparticle Coalescence Pathway for Tuning the Thickness of Laterally-Uniform Colloidal Nanosheets: The Case of SnSe. *ACS Nano* **2011**, *5*(11), 8852-8860.
- (29) Debnath, T.; Maity, P.; Ghosh, H. N. Super Sensitization: Grand Charge (Hole/Electron) Separation in ATC Dye Sensitized CdSe, CdSe/ZnS Type-I, and CdSe/CdTe Type-II Core-Shell Quantum Dots. *Chem. Eur. J.* **2014**, *20*, 13305-13313.

- (30) Mazing, D. S.; Brovko, A.M.; Matyushkin, L.B.; Aleksandrova, O.A.; Moshnikov, V.A. Preparation of Cadmium Selenide Colloidal Quantum Dots in Non-Coordinating Solvent Octadecene. *J. Phys. Conf. Ser.* **2015**, 661, 012033.
- (31) Wu, Y.; Wei, T.; An, X.; Liu, L.-M. Colloidal Synthesis of SnS Nanocrystals with Dimension-Dependent Photoelectrochemical Properties. *New J. Chem.* **2019**, 43, 74577462.
- (32) Kaur, A.; Goswami, T.; Babu, K. J.; Ghorai, N.; Kaur, G.; Shukla, A.; Rondiya, S. R.; Ghosh, H. N. Probing Ultrafast Charge Separation in CZTS/CdS Heterojunctions through Femtosecond Transient Absorption Spectroscopy. *J. Phys. Chem. C* **2020**, 124, 1947619483.
- (33) Liu, X.; Chen, J.; Luo, M.; Leng, M.; Xia, Z.; Zhou, Y.; Qin, S.; Xue, D. J.; Lv, L.; Huang, H.; Niu, D. Thermal Evaporation and Characterization of Sb₂Se₃ Thin Film for Substrate Sb₂Se₃/CdS Solar Cells *ACS Appl. Mater. Interfaces* **2014**, 6(13), 10687-10695.
- (34) Li, Y. Z.; Li, F.; Liang, G. X.; Zheng, W. L.; Xu, Y. M.; Zheng, Z. H.; Fan, P. Sb₂Se₃ thin films fabricated by thermal evaporation deposition using the powder prepared via mechanical alloying. *Surf. Coat. Technol.* **2019**, 358, 1013-1016.
- (35) Memarian, N.; Rozati, S. M.; Concina, I.; Vomiero, A. Deposition of Nanostructured CdS Thin Films by Thermal Evaporation Method: Effect of Substrate Temperature. *Mater.* **2017**, 10(7), 773.
- (36) Harris, K.D.; Tremayne, M.; Kariuki, B.M. Contemporary Advances in the Use of Powder X- ray diffraction for Structure Determination. *Angew. Chem., Int. Ed.* **2001**, 40(9), 1626-1651.
- (37) Holder, C. F.; Schaak, R.E. Tutorial on Powder X-ray Diffraction for Characterizing Nanoscale Materials. *ACS Nano* **2019**, 13, 7359-7365.
- (38) Cullity, B. D. *Elements of X-ray Diffraction*. Addison-Wesley Publishing, 1956.

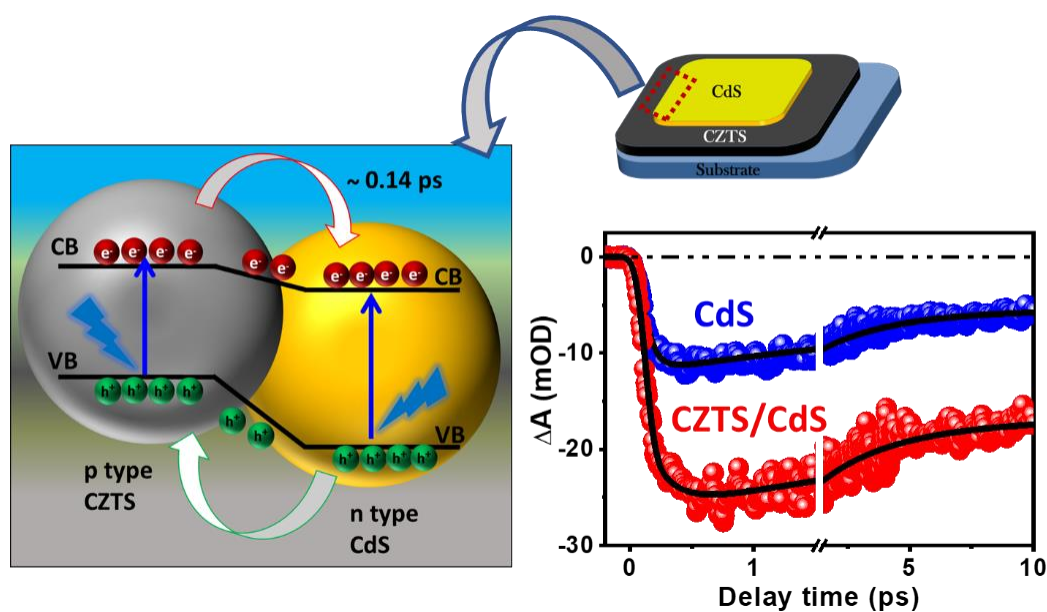
- (39) Chastain J.; King Jr, R. C. *Handbook of X-ray Photoelectron Spectroscopy*. Perkin-Elmer Corporation. 1992, 40, 221.
- (40) Fadley CS. X-ray photoelectron spectroscopy: Progress and perspectives. *J. Electron Spectrosc. Relat. Phenom.* **2010**, 178, 2-32.
- (41) Seah, M. P. The Quantitative Analysis of Surfaces by XPS: A Review. *Surf Interface Anal.* **1980**, 2(6), 222-239.
- (42) Vernon-Parry, K. D. *Scanning Electron Microscopy: An Introduction*. *III-Vs Review* 2000, 13(4),40-44.
- (43) Inkson, B. J. *Scanning Electron Microscopy (SEM) and Transmission Electron Microscopy (TEM) for Materials Characterization*. In *Materials characterization using nondestructive evaluation (NDE) methods* 2016, 17-43 Woodhead publishing.
- (44) Kaech, A. *An Introduction to Electron Microscopy Instrumentation. Imaging and Preparation*. Zurich: Center for Microscopy and Image Analysis, University of Zurich, 2013.
- (45) Sierra, C.F.E. Fundamentals of Transmission Electron Microscopy, The Technique with the Best Resolution in The World. *Screen* **2019**, 9, 10.
- (46) Freundlich, M.M., Origin of the Electron Microscope: The History of a Great Invention, and of a Misconception Concerning the Inventors, is Reviewed. *Science.* **1963**, 142, 185-188.
- (47) Stroud, R. M.; Long, J. W.; Pietron, J. J.; Rolison, D. R., A Practical Guide to Transmission Electron Microscopy of Aerogels. *J. Non-Cryst. Solids* **2004**, 350, 277-284.
- (48) Dhere, R. G.; Al-Jassim, M. M.; Yan, Y.; Jones, K. M.; Moutinho, H. R.; Gessert, T.A.; Sheldon, P.; Kazmerski, L. L. CdS/CdTe Interface Analysis by Transmission Electron Microscopy. *J. Vac. Sci. Technol. A: Vac. Surf. Films* **2000**, 18,1604-1608.
- (49) Fan, X.; Wang, B.; Heng, Q.; Chen, W.; Mao, L. Facile In-Situ Synthesis of α -NiS/CdS pn Junction with Enhanced Photocatalytic H₂ Production Activity. *Int. J. Hydrog. Energy.* **2022**, 47, 32531-32542.

- (50) Zubair, M.; Svenum, I. H.; Rønning, M.; Yang, J. Core-Shell Nanostructures of Graphene-Wrapped CdS Nanoparticles and TiO₂ (CdS@G@ TiO₂): The Role of Graphene in Enhanced Photocatalytic H₂ generation. *Catalysts* **2020**, *10*, 358.
- (51) Tony, O. *Fundamentals of Modern UV-Visible Spectroscopy*, 2000.
- (52) Owen, T. *Fundamentals of UV-visible Spectroscopy*, Hewlett-Packard Company, 1996.
- (53) Patterson, J. D.; Bailey, B. C. *Solid-State Physics: Introduction to The Theory*. Springer Science & Business Media, 2007.
- (54) Tissue, B. M. *Ultraviolet and Visible Absorption Spectroscopy*. Characterization of Materials 2002.
- (55) Bhunia, S. K.; Saha, A.; Maity, A. R.; Ray, S. C.; Jana, N. R. Carbon nanoparticle-based fluorescent bioimaging probes. *Sci. Rep.* **2013**, *3*, 1473.
- (56) Lakowicz J. R. *Principles of Fluorescence Spectroscopy*. Boston, MA: springer US, 2006, 1-50
- (57) Riehle, F.S.; Yu, K. Role of `Alcohol in the Synthesis of CdS Quantum Dots. *Chem. Mater.* **2020**, *32*, 1430-1438.
- (58) Wahl, M.; Rahn, H. J.; Gregor, I.; Erdmann, R.; Enderlein, J. Dead-Time Optimized Time-Correlated Photon Counting Instrument with Synchronized, Independent Timing Channels. *Rev. Sci. Instrum.* **2007**, *78*, 033106.
- (59) Jobin, H.; Ibh, Y. *A Practical Guide to Time-Resolved Luminescence Lifetime Determination Using Dedicated Time-Correlated Single-Photon Counting Systems*, 2009.
- (60) Zhang, J.; Zhu, B.; Zhang, L.; Yu, J. Femtosecond Transient Absorption Spectroscopy Investigation into the Electron Transfer Mechanism in Photocatalysis. *Chem. Comm.* **2023**, *59*, 688-699.
- (61) Rullière, C. *Femtosecond Laser Pulses*. Ed., Springer 2005.

- (62) Maiuri, M.; Garavelli, M.; Cerullo, G. Ultrafast Spectroscopy: State of The Art and Open Challenges. *J. Am. Chem. Soc.* **2019**, *142*, 3-15.
- (63) Berera, R.; van Grondelle, R.; Kennis, J. T. Ultrafast Transient Absorption Spectroscopy: Principles and Application to Photosynthetic Systems. *Photosynth. Res.* **2009**, *101*, 105-118.

CHAPTER 3

Probing Ultrafast Charge Separation in CZTS/CdS Heterojunctions through Femtosecond Transient Absorption Spectroscopy



J. Phys. Chem. C 2020, 124, 36, 19476–1948

Abstract

Chalcogenide-based type II heterojunctions are considered to be a promising candidate for optoelectronic device fabrication such as in solar cells, photodetectors, and light-emitting diodes. Type-II heterosystems effectively help in the delocalization of charge carriers owing to facile band arrangements, preventing the recombination of photogenerated carriers resulting in improved photovoltaic efficiency. Herein, we report the synthesis of CZTS nanoparticles and CdS quantum dots using a facile and low-cost hot-injection method followed by fabrication of CZTS, CdS, and CZTS/CdS heterojunction thin films with the help of a spin-coating technique at room temperature. We demonstrated through a combination of steady-state photoluminescence and femtosecond pump–probe spectroscopy experiments that a type-II, staggered band alignment of a CZTS/CdS junction is encouraging for charge carrier transport. We monitored the ultrafast charge carrier dynamics in the junction and confirmed the efficient separation of photoexcited charge carriers in the CZTS/CdS heterojunction. In the CZTS/CdS heterojunction, the photoexcited electrons are transferred from CZTS to CdS, which resulted in a drastic increment of the bleach signal intensity compared to that of bare CdS. Similarly, the photoexcited holes are transferred from CdS to CZTS, monitored by steady-state and time-resolved spectroscopy. A slower bleach recovery confirms the spatial charge separation at the interface of the CZTS/CdS heterojunction, placing electrons and holes at CdS and CZTS, respectively. The controlled introduction of charge carriers and charge separation dynamics in the heterointerface reported here provides a promising approach toward designing CZTS-based solar cells and will open up new avenues for developing more efficient Cu chalcogenide-based photovoltaic and photocatalytic devices.

3.1. Introduction

Development of more and more renewable energy sources could be the possible way for the upcoming energy crisis on the world's doorstep, in order to counter the scarcity of regular non-renewable (fossil fuel) energy sources in the near future.¹ Amongst those, solar energy-based optical devices could be the most intriguing option where the sun's energy is directly converted into electricity as well as catalyzing crucial chemical reactions.^{2,3} Photovoltaics and photo-catalysis based on heterojunctions have enjoyed overwhelming attention in recent years, where the charge carriers at the hetero-interface play a crucial role.⁴⁻⁶ The fate of the photo-excited charge carriers dictates the performances of the devices, which need to be extracted before they recombine in order to get better device efficiency. Various techniques have been adopted to efficiently separate the photogenerated electron-hole pairs in semiconductor materials through doping with metal or making heterojunctions. Amongst different other materials Cu-based chalcogenide systems have been a standout as potential photocathode due to their outstanding photovoltaic performances, preferable band positions, and cost effectivity.⁷⁻⁹ Also, having ~30% theoretical upper limit for the solar energy conversion efficiency (Shockley-Queisser efficiency) in a p-n junction makes these materials exquisite for solar cell applications.¹⁰ Currently copper Indium Gallium Selenide (CIGS) is dominating the thin-film solar cell market, although its prospect is limited by a low abundance of indium in the earth's crust. In this scenario, copper zinc tin sulfide (CZTS) is emerging as a potential photovoltaic material¹¹ riding on its excellent earth abundance,³ non-toxicity, direct bandgap (1.5 eV),¹² high absorption coefficient (10^4 cm^{-1}),^{13,14} and high carrier mobility. Among different heterostructures, CZTS and cadmium sulfide (CdS) is the most studied heterojunction where narrow bandgap CZTS forms a staggered type II band alignment with wide bandgap CdS.¹⁵ Plenty of articles are being reported worldwide regarding CZTS thin-film solar cell using CdS buffer layer for extracting electrons.¹⁶ Mitzi et al. reported the maximum conversion efficiency of 12.6% for CZTSSe thin-film-based solar cells in 2013.¹⁷ Several recent pieces of literature are available on CZTS/CdS heterojunction based photocatalysts,¹⁸ and solar cells.^{14,19} The performance of any optoelectronic device largely depends on the behaviour of its photo-excited charge carriers. For the betterment of the efficiency of the heterojunction-based optoelectronic devices, a clear understanding of photo-physics involved at the interface is foremost important and needs to be explored in

detail before the fabrication of the device. In order to attain the theoretical Shockley-Queisser limit, the excessive energy carried by the hot carriers upon photo-excitation above-band-gap needs to be harvested, and in this way, the energy losses can be minimized.^{20,21} An efficient way of eliminating energy losses is the extraction of the carriers while they are still hot before they dissipate their energy through various processes. Transient absorption spectroscopy is a unique technique for studying optically excited materials (be it a pristine system or a heterojunction) monitoring non-radiative relaxation processes of the hot carriers occurring in an ultrafast time scale, which are crucial in determining their optoelectronic behaviours. According to the study by Courel et al.,²² the CdS/CZTS interface recombination is introduced as the most important loss mechanism and it is measurably responsible for carrier trapping. Although CZTS is the most-studied material in the quaternary chalcogenides system, there is still a lack of detailed knowledge about charge carrier dynamics in CZTS/CdS heterojunction, which is critical for further progress in device fabrication. This collected evidence motivates us to investigate ultrafast charge carrier dynamics of CZTS/CdS heterojunction for photovoltaic devices and photocatalytic applications.

In this chapter, we present a detailed study of charge carrier dynamics at the interface of CZTS/CdS heterojunction with the help of femtosecond transient absorption spectroscopy. High-quality CZTS NPs and CdS QDs were prepared by the facile and low-cost hot injection method. The CZTS, CdS, and CZTS/CdS heterojunction thin films were fabricated by spin coating technique on glass at room temperature. We observed efficient electron transfer from photo-excited CZTS to CdS region and hole transfer from CdS to CZTS in the heterojunction after optical light irradiation. This understanding of photo-excited behaviours of hot carriers at an interface would help in improving device performance in CZTS-based heterojunctions.

3.2. Results and Discussion

3.2.1. Structural characterization

This work primarily aims to explore the native transient behavior of photoexcited charge carriers in a heterojunction, consisting of p-type Cu chalcogenides quaternary CZTS, and n-type binary CdS-based materials. The CZTS NPs and CdS QDs were synthesized by hot injection method and were characterized by powder X-ray diffraction (XRD), high-resolution transmission electron microscopy (HR-TEM), and

UV–VIS–NIR absorption spectroscopy. XRD patterns of synthesized CZTS NPs and CdS QDs are shown in **Figures 3.1(A) and 3.1(B)**, respectively. CZTS diffraction peaks at $2\theta \sim 28.5^\circ, 33^\circ, 39.6^\circ, 47.5^\circ, 56.2^\circ, 69.1^\circ$ and 76.3° corresponds to (112), (200), (220), (312), (008) and (332) diffraction planes assigned to tetragonal structure of kesterite phase of CZTS which exactly matched with the database in the standard JCPDS data file (JCPDS # 26-0575).²⁶ The featured intense peaks indicate good crystallinity and the results are in agreement with earlier reports.²⁷ **Figure 3.1(B)** represents diffraction patterns of CdS with standard JCPDS lines indicated below in the figure. The XRD peaks of CdS QDs at $2\theta \sim 26.1^\circ, 43.8^\circ, 51.4^\circ, 70.7^\circ$ corresponds to (111), (220), (311) and (331) diffraction planes, which confirm the formation of zinc blend structure of CdS (JCPDS # 00-001-0647).²⁸ From Scherrer's equation, the particle sizes of CZTS and CdS NCs were found to be about 11 nm and 4 nm, respectively, which were further confirmed by high-resolution transmission electron microscopy (HR-TEM) measurements. TEM and HR-TEM images of CZTS and CdS are displayed in **Figures 3.1(C) and 3.1(D)**. TEM images of CZTS NPs exhibit spherical morphology with an average size of ~ 11 nm.

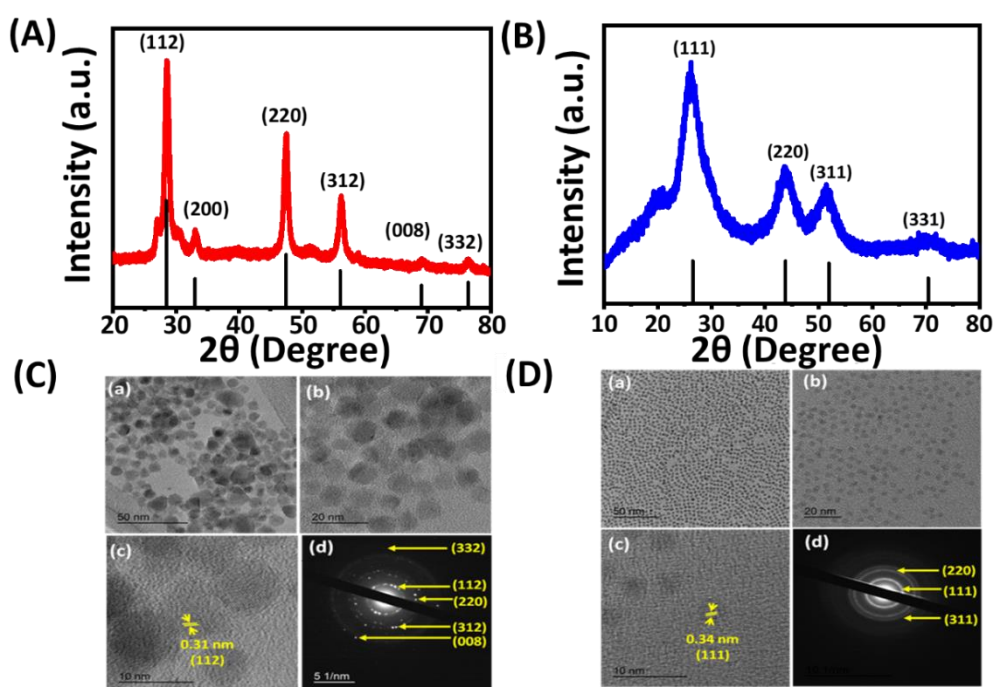


Figure 3.1. XRD patterns of (A) CZTS NPs, JCPDS lines show tetragonal structure of kesterite CZTS; (B) CdS QDs, JCPDS lines show zinc blend structure of CdS; (C) HR-TEM images of (a-c) CZTS NPs and (d) SAED pattern of corresponding CZTS NPs and (D) HRTEM images (a-c) of CdS QDs and (d) SAED pattern of corresponding CdS QDs.

HRTEM image clearly indicates that the nanoparticles are single-crystalline and the lattice fringe of 0.31 nm matches well with the (112) plane of CZTS. Further, the TEM image of CdS exhibits uniform spherical morphology with an average diameter of ~ 4 nm. HRTEM image indicates the d spacing of 0.34 nm corresponds to the (111) plane of CdS. **Figure 3.1Cd** and **Figure 3.1Dd** represent the SAED patterns of CZTS NPs and CdS QDs respectively. The presence of concentric rings as shown in the figures stands out for the high crystallinity of the material systems.

3.2.2. Optical studies

The optical properties of CZTS NPs and CdS QDs have been monitored by using UV-VIS absorption spectroscopy and are shown in **Figure 3.2**. CZTS NCs exhibit a broad absorption band in the UV-Vis region ranging from 300 to 800 nm. The optical bandgap of CZTS is calculated to be 1.7eV by extrapolating $(\alpha hv)^2$ versus hv plot (**Inset: Figure 3.2A**). The obtained band gap is larger than the reported bulk bandgap of 1.5 eV in the literature due to the decrease in the size of the CZTS particles.²⁹ **Figure 3.2Bb** shows the steady state optical absorption spectrum of CdS QDs representing two distinct absorption bands peaking at 433 and 409 nm, which can be attributed to $1S_{3/2}$ (h)- $1S(e)$ [1S] and $1S_{1/2}$ (h)- $1S(e)$ [2S] transitions³⁰ respectively. The CdS NCs exhibit discrete transitions arising due to a strong quantum confinement effect because of their smaller particle size (~ 4 nm) compared to the corresponding exciton Bohr diameter of about 5 nm.³¹ **Figure 3.2Bc** shows the photoluminescence spectra of CdS QD solution in chloroform.

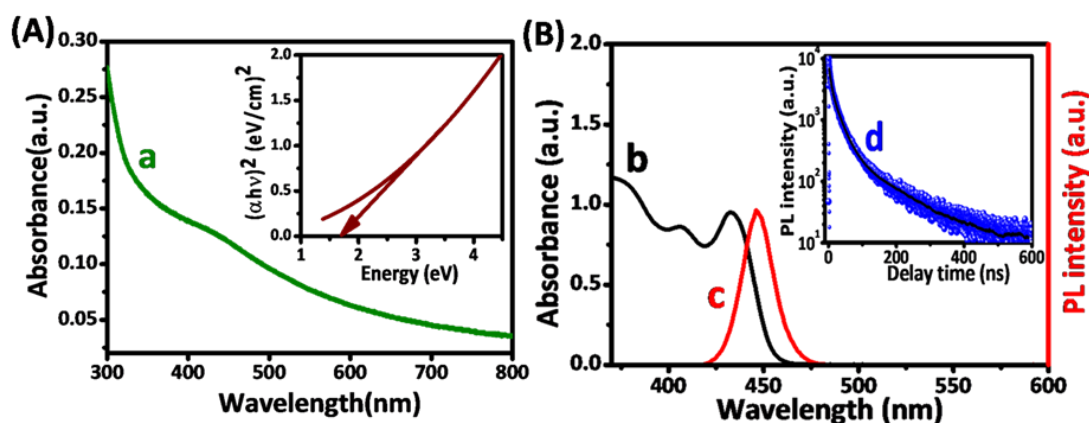


Figure 3.2. (A) Steady-state optical absorption spectra of (a) CZTS NPs and tauc plot (inset), (B) Steady-state (b) optical absorption, and (c) corresponding photoluminescence (PL) spectra of CdS QD, (d) Time-resolved PL decay trace of CdS QD after exciting sample at 402 nm and monitoring at 445 nm (inset).

The PL spectrum of CdS QDs shows a sharp emission peak at 445 nm which can be attributed to recombination due to photo-excited band-edge electrons and holes. Time-resolved luminescence studies have been carried out for CdS QDs and are shown in **Figure 3.2B inset**. The decay is monitored at 445 nm after exciting the sample at a 402 nm laser pulse. The average photoluminescence lifetime of CdS QDs was determined to be 18 ns. Now to investigate interfacial charge carrier dynamics between CZTS NPs and CdS QDs, CZTS, CdS, and CZTS/CdS heterojunction thin films were fabricated on top of glass substrate employing spin coating method and then optical studies were carried out in order to characterize these. The absorption spectra of CZTS, CdS, and CZTS/CdS thin film samples are shown in **Figure 3.3A**. The absorption spectrum of CZTS film shows broad absorption spectra in the entire visible region. In the case of CdS, the first absorption peak at 433 nm can be attributed to 1S excitonic peak and the second absorption peak at 405 nm can be attributed to 2S excitonic peak as discussed for solution case. We have also carried out photoluminescence studies of the thin film samples, particularly in CdS and CZTS/CdS thin films as shown in **Figure 3.3B**.

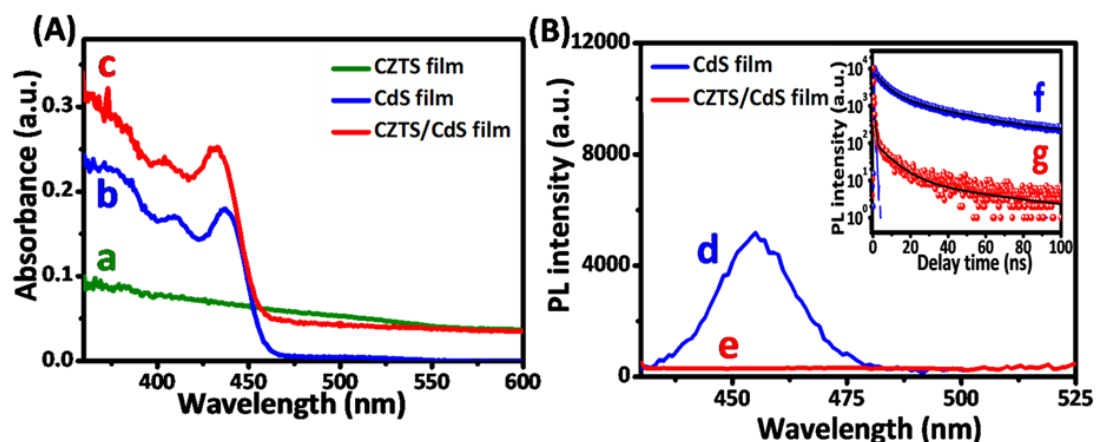


Figure 3.3. (A) Steady-state optical absorption spectra of (a) CZTS film (b) CdS film (c) CZTS/CdS film, (B) Photoluminescence (PL) spectra of (d) CdS film (e) CZTS/CdS film; **Inset:** Time-resolved PL decay trace of (f) CdS film and (g) CZTS/CdS film after monitoring at 455 nm and exciting at 402 nm.

CdS thin film exhibits a luminescence band in the range of 420-480 nm peaking around 455 nm, whereas, this luminescence band is completely quenched in CZTS/CdS heterojunction thin film. From the staggered type II band alignment of CZTS and CdS³² it can be considered that the PL signal is vanishing due to the migration of holes from valence band CdS to CZTS valence band as shown in

Scheme 3.1. To elucidate the hole transfer process, we have carried out time-resolved emission studies of CdS and CZTS/CdS thin films on monitoring photoluminescence decay trace at 455 nm after exciting at 402 nm laser light and displayed in **Figure 3.3B inset**. The average PL lifetime of CdS thin film in the absence and in the presence of CZTS was found to be 14.6 ns and 2.3 ns. This decrement of luminescence lifetime can be attributed to the hole transfer process in CZTS/CdS heterojunction. The hole transfer (HT) rate constant can be calculated by employing the following expression,

$$k_{HT} = 1/\tau_{CZTS/CdS} - 1/\tau_{CdS} \quad (1)$$

where $\tau_{CZTS/CdS}$ and τ_{CdS} denotes the luminescence lifetime of a particular system. Using the average lifetime values of 14.6 ns (CdS) and 2.3 ns (CZTS/CdS) the hole transfer rate constant can be determined to be $0.366 \times 10^9 \text{ sec}^{-1}$.

3.2.3. Ultrafast transient absorption studies

In this work, ultrafast dynamics of photoexcited charge carrier at the interface of CZTS/CdS heterojunction were monitored after comparing the ultrafast charge carrier dynamics of pristine CZTS and CdS thin films by femtosecond transient absorption spectroscopy. The samples were excited with a 350 nm pump pulse with $200 \mu\text{J}/\text{cm}^2$ laser fluence and the photo-induced changes were probed in the UV-vis region. Experimental conditions were kept the same throughout the analysis.

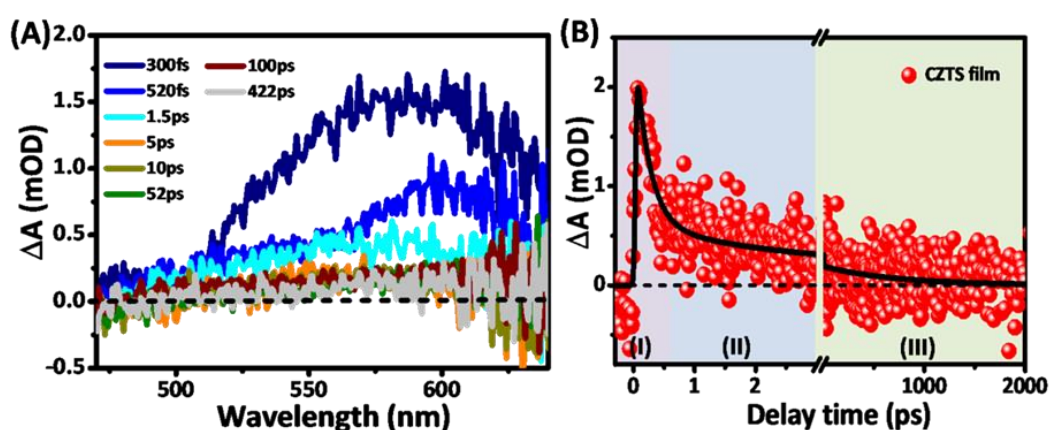


Figure 3.4. (A) Transient absorption spectra of CZTS thin film at different probe delays following photo-excitation of 350 nm laser pulse with $200 \mu\text{J}/\text{cm}^2$ laser fluence; and (B) Transient decay kinetics of photo-induced absorption signal, monitored at 580nm (I: Ultrafast trapping of photo-excited carriers, II and III: Trap mediated slow recombination).

In **Figure 3.4A**, we presented the transient absorption (TA) spectra of CZTS thin film in the region (440 – 680 nm) as a function of different probe delay, exhibiting a broad positive absorption band in the entire spectral region with a peak around 580 nm. Interestingly, we did not observe any photoinduced bleach signal in any of the probing regions of our transient spectra. We suspect poor quantum confinement (NC size: 11nm, Bohr radius of CZTS: 2.5-3.3 nm)²⁶ and large density of trap states in CZTS favors photoinduced absorption over ground state bleach in the system. Although Pundsack et al. reported that CZTS NCs produce positive signals even in a strongly confined atmosphere³³. Also in our recent study on CZTS nanocrystals, we observed a similar positive absorption band in the transient absorption spectrum after exciting the samples at 420 nm.³⁴ One may assume from these results that, the intrinsic high density of states in CZTS energy bands would solely be responsible for the observed photoinduced absorption signal in transient experiments, screening the ground state bleach feature. The temporal evolution of this transient absorption signal is monitored at 580 nm and represented in **Figure 3.4B**. The growth of the signal is very fast (< 100 fs) so we failed to extract precise growth time components, owing to our experimental limitations. However, the transient decay kinetics can be fitted with three exponential fitting parameters, with time constants being $\tau_1=0.23$ ps (76.4%), $\tau_2=2.3$ ps (14.5%), $\tau_3=>1$ ns (9.1%) (also listed in **Table 3.1**). It is observed that the majority of the photo-induced absorption signal depletes at a very fast rate. We ascribe the fast time constant τ_1 to the fast-trapping process of the conduction band electrons, due to its negligible dependence on excitonic pump fluence (**Figure 3.5**), which rules out the possibility of auger type recombination process. We observed that with increasing laser fluence, transient signal intensity increases, but the time components remain almost unchanged throughout the fluence range as represented in **Table 3.2**. This abrupt trap-mediated decay of transient signal indicates the presence of localized deep trap states in the band gap region of the system. Hereafter, the sluggish recombination of trapped carriers would be responsible for the slower decay dynamics of the transient signal.

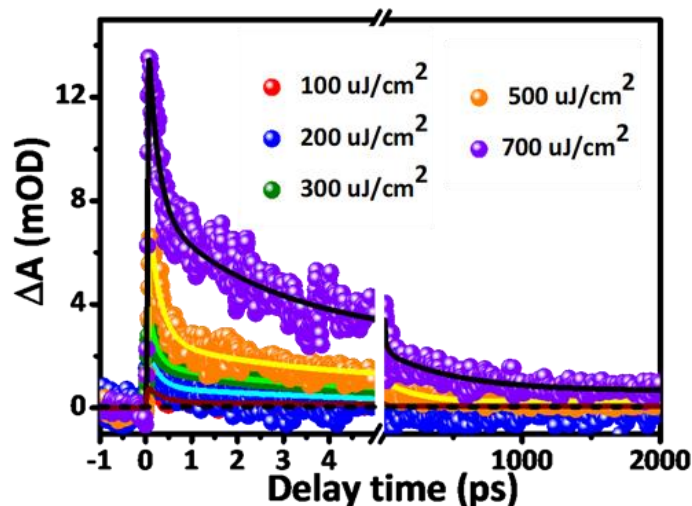


Figure 3.5. Fluence-dependent transient absorption kinetics of CZTS thin film on glass substrate after probing at wavelength 580 nm and exciting at 350 nm laser light. Laser power varied from 100 $\mu\text{J}/\text{cm}^2$ – 700 $\mu\text{J}/\text{cm}^2$.

As shown in **Figure 3.6 (A)**, we have discussed the TA spectra of pristine CdS film at different time delays after exciting the sample at 350 nm. The CdS transient spectra consist of bleach at 432 nm along with a 412 nm hump, which was attributed to the formation of band edge exciton $\{1S, 1S_{3/2}(h)-1S(e)\}$ and hot exciton $\{2S, 1S_{1/2}(h)-1S(e)\}$ in the CdS system, as discussed in the steady state absorption spectra (**Figure 3.3Ab**) earlier. Also, we observed a weak photo-induced absorption signal in the blue region of the spectra and a sharp bi-excitonic peak³⁵ at the red side of band-edge bleach. The TA spectra at an early time scale ($\Delta\tau \sim 120$ fs) match with the second-order derivative of steady-state optical absorption spectra as presented in **Figure 3.7**. This clearly indicates that the derivative-like feature at longer wavelength of band edge bleach in the TA spectra can be attributed to a biexciton induced stark effect. The bi-exciton signal detected here is probe-induced induced, emerges due to the Coulombic interaction between the hot exciton generated by the pump pulse and the band edge exciton generated by the probe pulse as reported in the literature.^{30,36} In our earlier investigations we have detected similar bi-excitonic features for CuIS_2 and AgIS_2 NCs³⁷⁻³⁹ on the red side of the bleach maxima. **Figure 3.6B** represents the dynamic profiles of the band edge exciton and the biexciton feature is monitored at 432 nm and 457 nm respectively, and is fitted multi-exponentially.

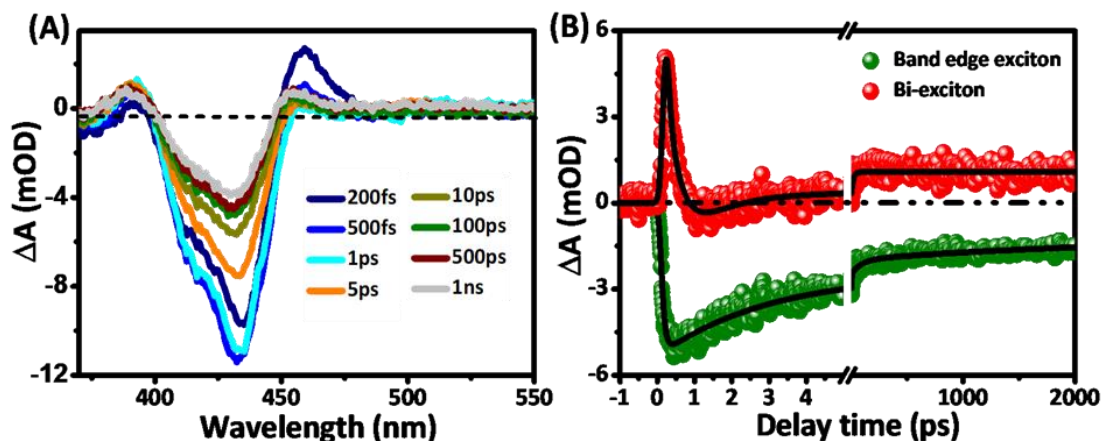


Figure 3.6. (A) Transient absorption spectra of CdS thin film at different probe delays, following photo-excitation of 350 nm laser pulse with $200 \mu\text{J}/\text{cm}^2$ laser fluence, and (B) Transient decay kinetics at (a) 432 nm (Band edge exciton) and (b) 457 nm (Bi-exciton).

The excitonic bleach signal rise with single exponential pulse-width (<100 fs) limited growth time scale and decay with time components of $\tau_1 = 3$ ps (46.6%), $\tau_2 = 130$ ps (14.6%), and $\tau_3 = 1$ ns (38.8%) as shown in **Table 3.1**. This ultrafast growth at the excitonic bleach position indicates fast cooling of electrons from higher excitonic states to the band-edge position within the conduction band of CdS QDs. The bleach recovery time comprises all the processes through which the system returns to its original ground state. The faster recovery time constant is due to the trapping processes of photo-excited charge carriers while the slower time components correspond to the long-lived states which may be due to radiative charge recombination or relaxation through a series of non-radiative channels.⁴⁰ The 457 nm signal represents a characteristic dynamic profile of a bi-exciton, undergoes fast auger decay to produce its excitonic form followed by an excitonic decay process. The excitonic signal is very poor and gets trapped easily in the thin film.

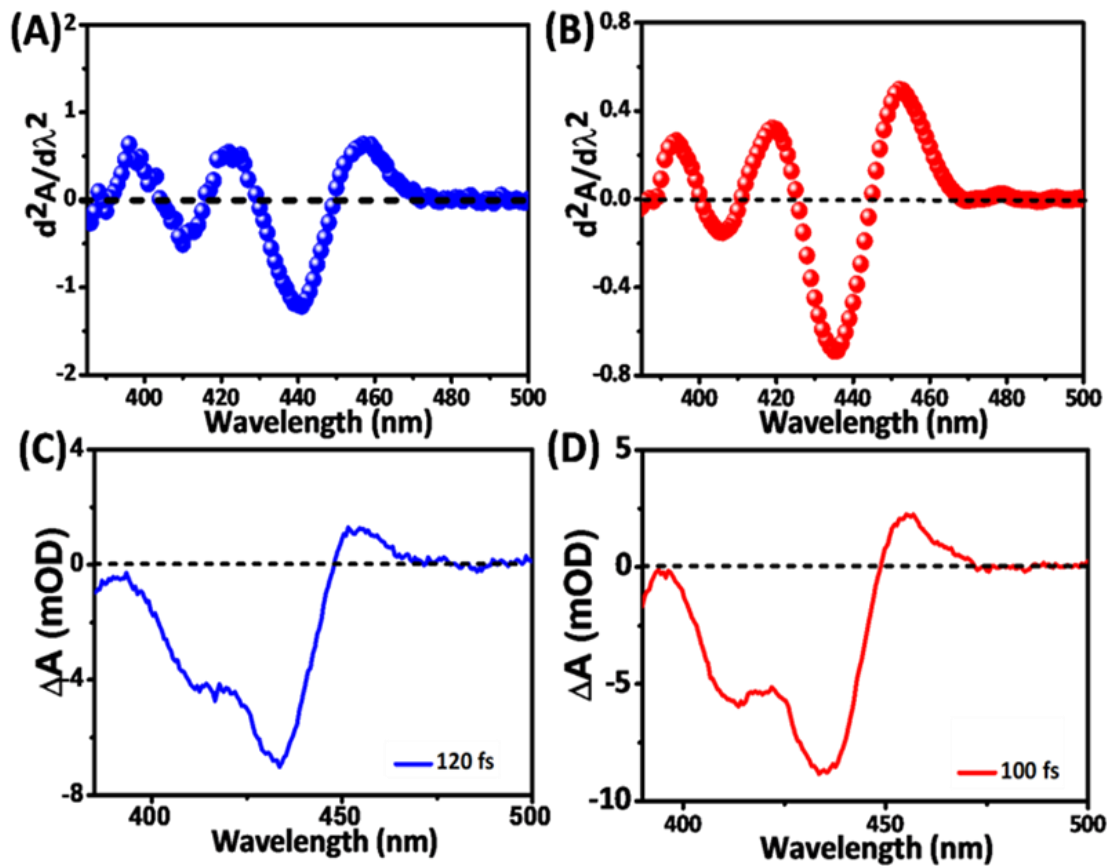


Figure 3.7. Second order derivative of steady-state absorption of (A) CdS thin film (B) CZTS/CdS hetero-junction film. Early time TA spectra of (C) CdS (120 fs) thin film and of (D) CZTS-CdS hetero-junction (100 fs), which match well with the second order derivative of steady state optical absorption spectra (A and B) respectively. This observation clearly indicates the presence of a biexciton-induced stark effect in the TA spectra.

Our main aim of the present investigation is to study photo-excited charge carrier dynamics in the CZTS/CdS interface following photo-excitation using a femtosecond laser pulse. **Figure 3.8A** represents the transient absorption spectra at different time delays in CZTS/CdS heterojunction film keeping similar experimental conditions as that of CZTS film (**Figure 3.4A**) and CdS film (**Figure 3.6A**).

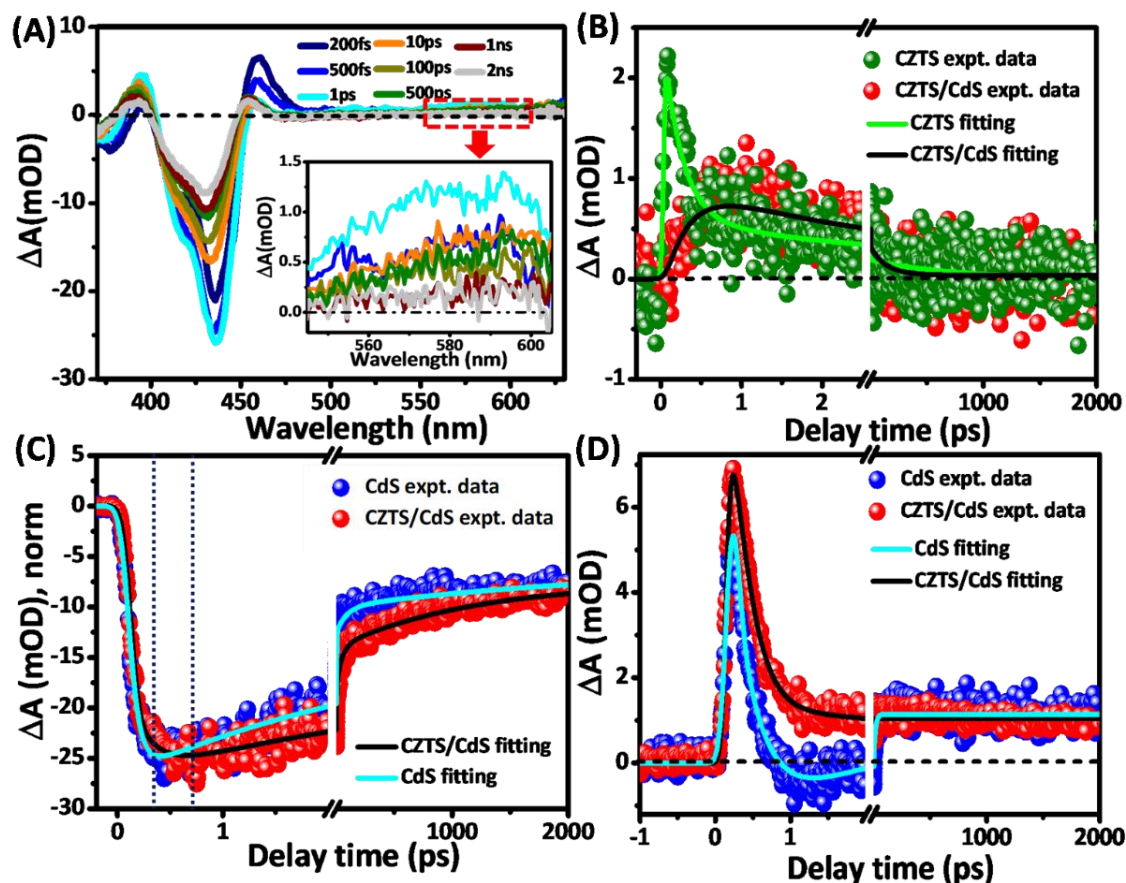
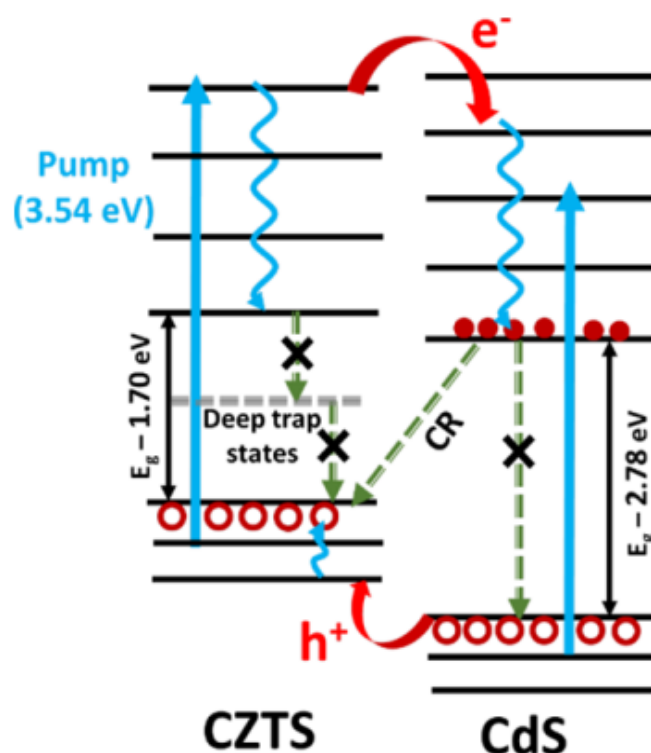


Figure 3.8. (A) Transient absorption spectra of CZTS/CdS heterojunction film, following 350 nm photo-excitation, with $200 \mu\text{J}/\text{cm}^2$ laser fluence; (inset: Enlarged photoinduced absorption signature of CZTS in the red region of the spectra in heterojunction film); (B) Transient decay profiles of CZTS photoinduced absorption signal in absence and presence of CdS; (C) Formation and recovery dynamics of band edge bleach signal for CdS thin film and CZTS/CdS thin film probing at 432 and 434 nm respectively; Dotted lines represent enhancement of CdS exciton growth time in presence of CZTS in the hetero-junction film; and (D) Bi-exciton dynamics in pure CdS and CZTS/CdS, normalizing with respect to their excitonic bleach intensity.

The transient spectra of the hetero-junction film comprise of both CdS and CZTS signatures as observed in their respective pristine cases. However, interestingly the intensity of both the bleach signal and bi-exciton signal for CdS film considerably increases. On the contrary the depletion of CZTS photoinduced absorption was observed in the hetero-junction film as compared to that of pristine CZTS film. As all the experimental conditions are kept similar, one may interpret that enhancement of the CdS signal in hetero-junction film is due to the influence of photoexcited CZTS. We have already discussed photo-excited hole transfer from CdS to CZTS

corroborating the quenching of steady-state photoluminescence of CdS in the presence of CZTS. Although possessing a much lower effective mass of electrons⁴¹ and superior degeneracy of hole states⁴² in CdS NCs allow these negative charge carriers to be the dominant character for the transient bleach signal. So, the transient signals are mostly affected by the separation of photo-excited electrons in the system. Type II band alignment of CZTS and CdS proposes electron transfer from CZTS to CdS and justifies the increase in signal intensity of both transient bleach and bi-exciton in the hetero-junction film as shown in **Figure 3.8A** and **Scheme 3.1**. The photoinduced absorption of CZTS is decreased almost two times in the heterojunction, as presented in **Figure 3.8B**. In fact, the fast-trapping process of CZTS is almost absent in the presence of CdS (**Figure 3.8B**).

Scheme 3.1. Simplified schematic illustrations of the relaxation pathway of photo-excited charge carriers in CZTS/CdS heterojunction after 350 nm pump irradiation. The energy diagrams are loosely adapted from previously reported literature.^{33,34} Here, the crossed processes represent the minimal probability of that particular relaxation pathway in the case of heterojunction, compared to their pristine cases. CR represents charge recombination.



This observation also confirms the migration of photoinduced hot electrons from CZTS to CdS in the hetero-junction. Now photo-induced bleach signal in the CdS domain in the heterojunction film directly correlates with the modified electron population in the conduction band edge of CdS. The comparative bleach kinetic profiles of CdS and CZTS/CdS are displayed in **Figure 3.8C**, where the growth time of bleach (140 fs) is found to be slower in the presence of CZTS as compared to bare CdS, which is pulse width limited. This observation clearly suggests that the electron cooling is slower in the case of the CZTS/CdS system and indicates enhanced electron population in the conduction band edge, validating our earlier electron transfer assumption

Table 3.1. Kinetics fitting parameters at different key wavelengths for CZTS, CdS thin films, and CZTS/CdS heterojunction after exciting the samples at 350 nm.

System	Probe wavelength (nm)	τ_{growth}	τ_1	τ_2	τ_3	τ_4
CZTS	574	< 0.1 ps (+ 100 %)	0.23 ps (- 76.4%)	2.3 ps (- 14.5%)	>1 ns (- 9.1 %)	-
CdS	432	< 0.1 ps (+ 100%)	3ps (-46.6%)	130 ps (-14.6%)	>1 ns (-38.8%)	-
	457	< 0.1 ps (+ 100%)	0.16 ps (-100 %)	0.62 ps (+ 31.2%)	7.1 ps (+ 68.8%)	>1 ns (-100%)
CZTS/ CdS	434	0.14 ps (+ 100%)	3.7 ps (- 33.2%)	269 ps (- 28.4%)	>1 ns (- 38.4%)	-
	461	< 0.1 ps (+94 %)	0.2 ps (-82.9%)	1.8 ps (-7.2%)	7.4 ps (+ 6 %)	>1 ns (-9.9%)
	574	0.16 ps (+ 100%)	1.8 ps (-60.3%)	158 ps (- 35.6%)	>1 ns (- 4.1%)	-

We have also observed charge separation induced slower bleach recovery (charge recombination) in heterojunction. In addition to the transient bleach kinetics of CZTS/CdS, we have also monitored bi-exciton kinetics at 461 nm and compared with pristine CdS, shown in **Figure 3.8D**. It demonstrates the fate of CdS bi-excitonic feature, both formation and decay in presence of CZTS. The transient kinetics were fitted multi-exponentially and the time constants are shown in **Table 3.1**. The formation of bi-excitonic feature is not much influenced by the CZTS contact and

subsequent charge separations. In fact, its decay is quite sluggish and slowly dissociates to form excitons. We assume this behaviour arises from greater defect concentration in the hetero-interface. Also, hole transfer did not necessarily have much effect over bi-exciton formation in the heterojunction. This might be due to slower hole transfer in the junction owing to large effective mass of holes⁴³ in CdS, that photoexcited holes are being cooled to the valance band edge to form biexcitons before being migrated to the CZTS domain. In **Scheme 3.1**, we proposed a simplified schematic band alignment of CZTS and CdS, portraying inner photophysical processes after 350 nm pump excitation. This experimental investigation will help in designing better heterojunctions which would have immense applications in the development of highly efficient thin film solar cells or other optoelectronic devices.

Table 3.2. Kinetics fitting parameters at different key wavelengths for CZTS, CdS thin films, and CZTS/CdS p-n heterojunction at 350 nm photo-excitation with different laser intensity. Laser Intensity was kept at 100 $\mu\text{J}/\text{cm}^2$, 200 $\mu\text{J}/\text{cm}^2$, 300 $\mu\text{J}/\text{cm}^2$, 500 $\mu\text{J}/\text{cm}^2$ and 700 $\mu\text{J}/\text{cm}^2$.

Pump fluence ($\mu\text{J}/\text{cm}^2$)	Growth	Decay		
	τ_1	τ_2	τ_3	τ_4
100	<100fs (-100%)	0.24ps (73.3%)	2.7ps (14%)	>1ns (12.7%)
200	<100fs (-100%)	0.23ps (70.4%)	2.3ps (22.1%)	>1ns (7.5%)
300	<100fs (-100%)	0.25ps (63.6%)	1.9ps (22%)	>1ns (14.4%)
500	<100fs (-100%)	0.28ps (68%)	2ps (19.4%)	>1ns (12.6%)
700	<100fs (-100%)	0.20ps (52.2%)	2.1ps (34.2%)	>1ns (13.6%)

3.3. Conclusion

In this chapter, we have attempted to understand ultrafast charge carrier dynamics of CZTS/CdS heterojunction with type-II staggered band alignment under the influence of an internal electric field with the help of femtosecond transient pump-probe spectroscopy. CZTS NPs and CdS QDs were prepared by hot injection method,

followed by fabrication of CZTS, CdS, and CZTS/CdS heterojunction thin films with the help of spin coating technique. Steady-state and time-resolved photoluminescence studies confirm hole transfer from photoexcited CdS to CZTS in the heterojunction film due to its thermodynamical viability. In transient studies, we observed trap-mediated photoinduced absorption dominates over band edge bleach in CZTS thin film. Ultrafast transient absorption and time-resolved luminescence studies demonstrate fast charge separation where photo-excited electrons transferred from photo-excited CZTS to CdS and photo-excited hole transferred from photo-excited CdS to CZTS in the heterojunction film. The drastic increase in bleach intensity and enhanced electron population in the conduction band edge in CdS in the heterojunction film clearly suggests electron transfer from the CZTS domain to the CdS domain establishing the charge transfer efficiency in the heterointerface. We have also observed that the hole transfer process in the interface necessarily occurs from the CdS valance band edge, unlike electronic migration. This kind of improved charge separation and slow recombination of charge carriers in the heterojunction would have a great impact on the device's performance. Our results help to explain the robust separation of photoexcited charge carriers between the CZTS/CdS heterojunction and highlight a route to improved solar cells. These results will help to model carrier transport mechanisms across similar heterojunctions and we hope that the present study will attract further investigations to address electron-hole separation issues in photovoltaic and photo-catalytic devices.

3.4. References

- (1) Pal, K.; Singh, P.; Bhaduri, A.; Thapa, K. B. Current Challenges and Future Prospects for a Highly efficient (>20 %) Kesterite CZTS Solar Cell: A Review. *Sol. Energy Mater. Sol. Cells* **2019**, *196*, 138–156.
- (2) Bagher, A. M.; Vahid, M. M. A.; Mohsen, M. Types of Solar Cells and Application. *Am. J. Opt. Photonics* **2015**, *3*, 94-113.
- (3) Lee, T. D.; Ebong, A. U. A Review of Thin Film Solar Cell Technologies and Challenges. *Renew. Sustain. Energy Rev.* **2017**, *70*, 1286–1297.

-
- (4) Sun, L.; Zhao, Z.; Li, S.; Su, Y.; Huang, L.; Shao, N.; Liu, F.; Bu, Y.; Zhang, H.; Zhang, Z. Role of SnS₂ in 2D-2D SnS₂/TiO₂ Nanosheet Heterojunctions for Photocatalytic Hydrogen Evolution. *ACS Appl. Nano Mater.* **2019**, *2*, 2144–2151.
 - (5) Nozik, A. J.; Beard, M. C.; Luther, J. M.; Law, M.; Ellingson, R. J.; Johnson, J. C. Semiconductor Quantum Dots and Quantum Dot Arrays and Applications of Multiple Exciton Generation to Third Generation Photovoltaic Solar Cells. *Chem. Rev.* **2010**, *110*, 6873–6890.
 - (6) Wang, H.; Zhang, L.; Chen, Z.; Hu, J.; Li, S.; Wang, Z.; Liu, J.; Wang, X. Semiconductor Heterojunction Photocatalysts: Design, Construction, and Photocatalytic Performances. *Chem. Soc. Rev.* **2014**, *43*, 5234–5244.
 - (7) Yu, X.; Shavel, A.; An, X.; Luo, Z.; Ibanez, M.; Cabot, A. Cu₂ZnSnS₄-Pt and Cu₂ZnSnS₄-Au Heterostructured Nanoparticles for Photocatalytic Water Splitting and Pollutant Degradation. *J. Am. Chem. Soc.* **2014**, *136*, 9236–9239.
 - (8) Katagiri, H.; Jimbo, K.; Maw, W. S.; Oishi, K.; Yamazaki, M.; Araki, H.; Takeuchi, A. Development of CZTS-Based Thin Film Solar Cells. *Thin Solid Films* **2009**, *517*, 2455–2460.
 - (9) Yang, W.; Oh, Y.; Kim, J.; Jeong, M. J.; Park, J. H.; Moon, J. Molecular Chemistry-Controlled Hybrid Ink-Derived Efficient Cu₂ZnSnS₄ Photocathodes for Photoelectrochemical Water Splitting. *ACS Energy Lett.* **2016**, *1*, 1127–1136.
 - (10) Shockley, W.; Queisser, H. J. Detailed Balance Limit of Efficiency of P-n Junction Solar Cells. *J. Appl. Phys.* **1961**, *32*, 510–519.
 - (11) Yan, C.; Huang, J.; Sun, K.; Johnston, S.; Zhang, Y.; Sun, H.; Pu, A.; He, M.; Liu, F.; Eder, K.; et al. Cu₂ZnSnS₄ Solar Cells with over 10% Power Conversion Efficiency Enabled by Heterojunction Heat Treatment. *Nat. Energy* **2018**, *3*, 764–772.
 - (12) Ye, K.; Siah, S. C.; Erslev, P. T.; Akey, A.; Settens, C.; Hoque, S. B.; Hopkins, P.; Teeter, G.; Buonassisi, T.; Jaramillo, R. Tuning Electrical, Optical, and Thermal Properties through Cation Disorder in Cu₂ZnSnS₄. *Chem. Mater.* **2019**, *31*, 8402–8412.
-

- (13) Cho, J. W.; Ismail, A.; Park, S. J.; Kim, W.; Yoon, S.; Min, B. K. Synthesis of $\text{Cu}_2\text{ZnSnS}_4$ Thin Films by a Precursor Solution Paste for Thin Film Solar Cell Applications. *ACS Appl. Mater. Interfaces* **2013**, *5*, 4162–4165.
- (14) Walsh, A.; Chen, S.; Wei, S. H.; Gong, X. G. Kesterite Thin-Film Solar Cells : Advances in Materials Modelling of $\text{Cu}_2\text{ZnSnS}_4$. *Adv. Energy Mater.* **2012**, *2*, 400–409.
- (15) Yan, C.; Liu, F.; Song, N.; Ng, B. K.; Stride, J. A.; Tadich, A.; Hao, X. Band Alignments of Different Buffer Layers (CdS, Zn(O, S), and In_2S_3) on $\text{Cu}_2\text{ZnSnS}_4$. *Appl. Phys. Lett.* **2014**, *104*, 173901-173904.
- (16) Kaur, K.; Kumar, N.; Kumar, M. Strategic Review of Interface Carrier Recombination in Earth Abundant Cu–Zn–Sn–S–Se Solar Cells : Current Challenges and Future Prospects. *J. Mater. Chem. A* **2017**, *5*, 3069–3090.
- (17) Wang, W.; Winkler, M. T.; Gunawan, O.; Gokmen, T.; Todorov, T. K.; Zhu, Y.; Mitzi, D. B. Device Characteristics of CZTSSe Thin-Film Solar Cells With 12.6% Efficiency. *Adv. Energy Mater.* **2013**, *4*, 1–5.
- (18) Yuan, M.; Wang, J. L.; Zhou, W. H.; Chang, Z. X.; Kou, D. X.; Zhou, Z. J.; Tian, Q. W.; Meng, Y. N.; Zhou, Y. M.; Wu, S. X. $\text{Cu}_2\text{ZnSnS}_4$ -CdS Heterostructured Nanocrystals for Enhanced Photocatalytic Hydrogen Production. *Catal. Sci. Technol.* **2017**, *7*, 3980–3984.
- (19) Ferhati, H.; Djeflal, F. Graded Band-Gap Engineering for Increased Efficiency in CZTS Solar Cells. *Opt. Mater.* **2018**, *76*, 393–399.
- (20) Kahmann, S.; Loi, M. A. Hot Carrier Solar Cells and the Potential of Perovskites for Breaking the Shockley-Queisser Limit. *J. Mater. Chem. C* **2019**, *7*, 2471–2486.
- (21) Mondal, S.; Aepuru, R.; Dana, J.; Ghorai, N.; Ghosh, H. N. Biexciton Dissociation Dynamics in Nanohybrid Au-CuInS₂ Nanocrystals. *J. Phys. Chem. C* **2018**, *122*, 28497–28505.
- (22) Courel, M.; Andrade-Arvizu, J. A.; Vigil-Galán, O. Towards a CdS/ $\text{Cu}_2\text{ZnSnS}_4$ Solar Cell Efficiency Improvement: A Theoretical Approach. *Appl. Phys. Lett.* **2014**, *105*, 233501.

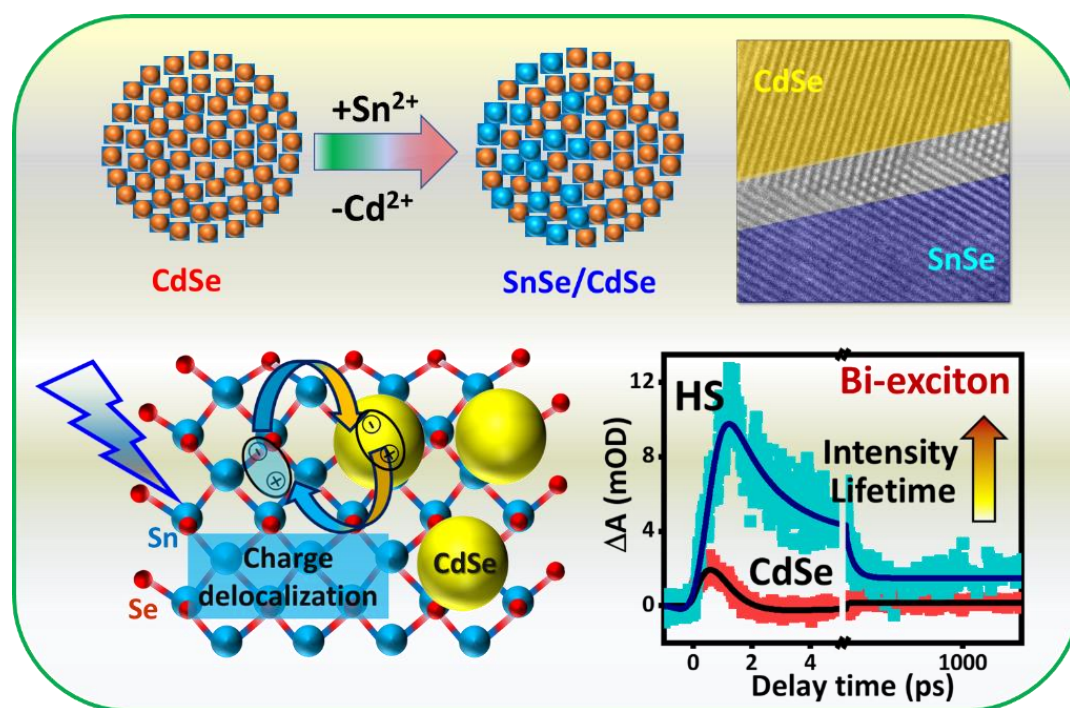
-
- (23) Zhou, M.; Gong, Y.; Xu, J.; Fang, G.; Xu, Q.; Dong, J. Colloidal CZTS Nanoparticles and Films: Preparation and Characterization. *J. Alloys Compd.* **2013**, *574*, 272–277.
- (24) Yang, H.; Jauregui, L. A.; Zhang, G.; Chen, Y. P.; Wu, Y. Nontoxic and Abundant Copper Zinc Tin Sulfide Nanocrystals for Potential High-Temperature Thermoelectric Energy Harvesting. *Nano Lett.* **2012**, *12*, 540–545.
- (25) Yu, W. W.; Peng, X. Formation of High-Quality CdS and Other II-VI Semiconductor Nanocrystals in Noncoordinating Solvents: Tunable Reactivity of Monomers. *Angew. Chem. Int. Ed.* **2002**, *41*, 2368–2371.
- (26) Khare, A.; Wills, A. W.; Ammerman, L. M.; Norris, D. J.; Aydil, E. S. Size Control and Quantum Confinement in $\text{Cu}_2\text{ZnSnS}_4$ Nanocrystals. *Chem. Commun.* **2011**, *47*, 11721–11723.
- (27) Su, Z.; Tan, J. M. R.; Li, X.; Zeng, X.; Batabyal, S. K.; Wong, L. H. Cation Substitution of Solution-Processed $\text{Cu}_2\text{ZnSnS}_4$ Thin Film Solar Cell with over 9% Efficiency. *Adv. Energy Mater.* **2015**, *5*, 2–8.
- (28) Soltani, N.; Gharibshahi, E.; Saion, E. Band Gap of Cubic and Hexagonal CdS Quantum Dots-Experimental and Theoretical Studies. *Chalcogenide Lett.* **2012**, *9*, 321–328.
- (29) Guo, Q.; Hillhouse, H. W.; Agrawal, R. Synthesis of $\text{Cu}_2\text{ZnSnS}_4$ Nanocrystal Ink and Its Use for Solar Cells. *J. Am. Chem. Soc.* **2009**, *131*, 11672–11673.
- (30) Kobayashi, Y.; Nishimura, T.; Yamaguchi, H.; Tamai, N. Effect of Surface Defects on Auger Recombination in Colloidal CdS Quantum Dots. *J. Phys. Chem. Lett.* **2011**, *2*, 1051–1055.
- (31) Zeiri, L.; Patla, I.; Acharya, S.; Golan, Y.; Efrima, S. Raman Spectroscopy of Ultranarrow CdS Nanostructures. *J. Phys. Chem. C* **2007**, *111*, 11843–11848.
- (32) Rondiya, S. R.; Rokade, A.; Sharma, P.; Chaudhary, M.; Funde, A.; Jadhav, Y.; Haram, S.; Pathan, H.; Jadkar, S. CZTS/CdS: Interface Properties and Band Alignment Study towards Photovoltaic Applications. *J. Mater. Sci. Mater. Electron.* **2018**, *29*, 4201–4210.
-

- (33) Pundsack, T. J.; Chernomordik, B. D.; Aydil, E. S.; Blank, D. A. Excited-State Dynamics in CZTS Nanocrystals. *J. Phys. Chem. Lett.* **2013**, *4*, 2711–2714.
- (34) Rondiya, S. R.; Jadhav, Y.; Dzade, N. Y.; Ahammed, R.; Goswami, T.; De Sarkar, A.; Jadkar, S.; Haram, S.; Ghosh, H. N. Experimental and Theoretical Study into Interface Structure and Band Alignment of the $\text{Cu}_2\text{Zn}_{1-x}\text{Cd}_x\text{SnS}_4$ Heterointerface for Photovoltaic Applications. *ACS Appl. Energy Mater.* **2020**, *3*, 5153–5162.
- (35) Wu, K.; Cordoba, W. E.; Yang, Y.; Lian, T. Plasmon-Induced Hot Electron Transfer from the Au Tip to CdS Rod in CdS-Au Nanoheterostructures. *Nano Lett.* **2013**, *13*, 5255–5263.
- (36) Sewall, S. L.; Cooney, R. R.; Anderson, K. E. H.; Dias, E. A.; Sagar, D. M.; Kambhampati, P. State-Resolved Studies of Biexcitons and Surface Trapping Dynamics in Semiconductor Quantum Dots. *J. Chem. Phys.* **2008**, *129*, 084701-084708.
- (37) Debnath, T.; Maiti, S.; Maity, P.; Ghosh, H. N. Subpicosecond Exciton Dynamics and Biexcitonic Feature in Colloidal CuInS_2 Nanocrystals: Role of In-Cu Antisite Defects. *J. Phys. Chem. Lett.* **2015**, *6*, 3458–3465.
- (38) Dana, J.; Debnath, T.; Ghosh, H. N. Involvement of Sub-Bandgap States in Subpicosecond Exciton and Biexciton Dynamics of Ternary AgInS_2 Nanocrystals. *J. Phys. Chem. Lett.* **2016**, *7*, 3206–3214.
- (39) Debnath, T.; Ghosh, H. N. Ternary Metal Chalcogenides: Into the Exciton and Biexciton Dynamics. *J. Phys. Chem. Lett.* **2019**, *10*, 6227–6238.
- (40) Liu, Z.; Ji, G.; Guan, D.; Wang, B.; Wu, X. J. Enhanced Charge-Carrier Transfer by CdS and Ag_2S Quantum Dots Co-Sensitization for TiO_2 Nanotube Arrays. *J. Colloid Interface Sci.* **2015**, *457*, 1–8.
- (41) Dalven, R. Calculation of Effective Masses in Cubic CdS and CdSe. *Phys. Status Solidi B* **1971**, *48*, K23-K26.

- (42) Lambright, S.; Butaeva, E.; Razgoniaeva, N.; Hopkins, T.; Smith, B.; Perera, Dimuthu.; Corbin, Jonathan.; Khon, E.; Thomas, R.; Moroz, P.; et al. Enhanced Lifetime of Excitons in Non-Epitaxial Au/CdS Core/Shell Nanocrystals. *ACS Nano* **2013**, *8*, 1–4.
- (43) Klimov, V. I.; Mcbranch, D. W. Auger-Process-Induced Charge Separation in Semiconductor Nanocrystals. *Phys. Rev. B* **1997**, *55*, 173–179.

CHAPTER 4

Enhanced Charge Carrier Separation and Improved Bi-exciton Yield at the p-n Junction of SnSe/CdSe Heterostructures



J. Phys. Chem. Lett. 2021, 12, 45, 10958–10968

Abstract

Tin chalcogenides (SnX, X=S, Se) based heterostructure (HS) are promising materials for the construction of low-cost optoelectronic devices. Here, we have reported the synthesis of SnSe/CdSe HS using the controlled cation exchange reaction. The (400) plane of SnSe and (111) plane of CdSe, confirm the formation of an interface between SnSe and CdSe. The Type- I band alignment is estimated for SnSe/CdSe HS with a small conduction band offset (CBO) of 0.72 eV through cyclic voltammetry measurement. Transient absorption (TA) studies demonstrate drastic enhancement of CdSe biexciton signal, pointing toward the hot carrier transfer from SnSe to CdSe in a short time scale. The fast growth and recovery of CdSe bleach in the presence of SnSe indicates charge transfer back to SnSe. The observed delocalization of carriers in these two systems is crucial for an optoelectronic device. Our findings will provide new insights for the fabrication of cost-effective photovoltaic devices based on SnSe-based heterostructures.

4.1. Introduction

The generation of renewable energy is crucial in order to meet the world's current energy demands. The development of novel materials becomes a key feature for the evolution of technology and to fulfill the world's rising energy requirement.¹ Over the past few years, improved solar cell efficiency has been reported with copper indium gallium selenide (CIGS) and cadmium telluride (CdTe) absorber materials, however, scarcity and toxicity of the constitute elements hamper further development.² The quaternary $\text{Cu}_2\text{ZnSn}(\text{S}/\text{Se})_4$ (CZTSSe) systems have also captured much attention in the field of photovoltaics due to their direct band gap ($E_g = 1.1\text{eV}$)³, high absorption coefficient (10^4 cm^{-1})⁴ and stability². The highest power conversion efficiency (PCE) of 12.6% has been achieved by Se-rich CZTSSe thin film solar cells with a $\text{S}/(\text{S} + \text{Se})$ compositional ratio of 0.24.⁵ The major obstacles in achieving high performance of CZTSSe-based photovoltaic and photocatalytic devices are controlling the formation of secondary phases, inherent Cu-Zn antisite defects, and poor band alignment.⁴ Hence, alternative materials that contain lead-free earth-abundant, as well as non-toxic elements, need to be explored for solar cell applications. Nowadays, two-dimensional (2D) metal chalcogenides and their heterostructures have gained incredible interest owing to their diverse range of properties that enable applications in photocatalysis, optoelectronics, and energy conversion and storage.⁶ As compared to their bulk counterparts, 2D materials possess quantum confinement which gives rise to innovative electronic and optical properties like strong coulombic interactions, strong spin-orbit coupling, efficient light-matter interactions, higher carrier mobility, and an increase in the electronic band gap, etc. Moreover, these materials are abundant, and mechanically strong, rendering them well suitable for future-generation photovoltaic cells.^{7,8} 2D materials can also improve the photocatalytic performance by maximizing the specific surface area which creates additional active sites, which is a crucial factor for improved catalytic processes.⁸ Recently, tin selenide (SnSe) nanosheets (NSs) have shown excellent properties for photovoltaic applications and could be the future energy source due to its earth abundance, non-toxicity, bandgap tunability up to near-infrared (NIR) region,⁹ high absorption coefficient (10^5 cm^{-1})¹⁰, a p-type semiconductor with a high concentration of carriers (10^{15} , 10^{18} cm^{-3}).¹¹ Moreover, it shows high stability of formation due to its binary nature which overcomes the problems associated with structural, stoichiometry, and secondary

phase formation commonly occurring in quaternary CIGS and CZTS(Se) materials.^{12,13} Further, designing heterostructures based on 2D materials provides tuning of band alignment, new capability for controlling the charge carrier relaxation trails, and wave function engineering via tuning of band offsets and overlap of the electron-hole wavefunction.^{14,15} Moreover, these heterostructures harvest a wider range of solar spectrum and offer slower recombination and fast extraction of charge carriers, which are crucial factors for the construction of highly efficient photovoltaic and photocatalytic devices.

The transfer of hot charge carriers generated in one semiconductor to another semiconductor in heterostructures improves the photoconversion process of the photovoltaic cell via utilizing excess energy which otherwise is wasted as heat, which in turn increases the overall PCE. Various methods have been reported for large-scale production of nanocrystals and nano-heterostructures including chemical vapor deposition (CVD), hydrothermal or solvothermal, and electrochemical methods for epitaxial growth of heterostructures.¹⁶ The aforementioned methods exhibit certain shortcomings including time-consuming, tedious, harsh environment conditions, high temperature, and difficulty controlling the formation of nano-heterostructures.¹⁷ Whereas, the ion (cation/anion) exchange method is a versatile chemical method for the synthesis of heterostructures with high-quality interfaces at low temperatures, tunable shape, size, and band alignment by changing the composition and experimental conditions.¹⁶ This method provides close proximity between the two materials as the crystallographic facets growth of the second phase could be easily achieved, thereby enhancing the probability of the formation of proper heterojunction between the two materials.¹⁸ Moreover, the formation of heterostructures can be achieved in a highly controlled manner which cannot be attained by other methods. Hee et al. reported the conversion of CdSe, CdS, and CdTe nanocrystals (NCs) to corresponding Ag-chalcogenides by a complete replacement reaction of the Cd²⁺ by Ag⁺ through the cation exchange method.^{19,20} Casavola et al. developed PbSe/CdSe core-shell NCs of different geometry using the cation exchange method.²¹ Similarly, SnTe/CdTe and CdTe/SnTe Core/Shell NCs were prepared by Jang et al. using cation exchange combined with the Kirkendall effect.²² Cation exchange is a promising method for the formation of colloidal nanocrystal and nano-heterostructures at low temperatures. The heterostructures offer better extraction of charge carriers, minimum

energy losses, high degree of surface passivation and collectively enhance the device performance as compared to that of pristine nanostructures. Recently, solar cells with SnS and SnSe as absorber materials have been widely reported.^{23,24} The wide bandgap, n-type Cd-chalcogenides have been widely used as a buffer layer in SnSe/SnS-based absorber layer solar cells. However, the maximum experimentally reported efficiency for SnS and SnSe-based absorber materials was 4.36 % and 6.44 %, ^{25,26} respectively, which is far less than the theoretical value of 30 %, therefore, improved efficiency can be expected for SnX, X=S, Se based solar cells.^{27, 28} The performance of any optoelectronic device chiefly depends on the behavior of its photoexcited charge carriers. A clear understanding of the photophysics involved at the interface is of foremost importance and needs to be explored in detail before the fabrication of any device for the improvement of efficiency based on heterojunction-based materials.

In this chapter, we have successfully synthesized high-quality SnSe/CdSe HS by a low-cost, robust, and user-friendly hot injection method to elucidate the charge carrier dynamics at the interface of SnSe and CdSe. SnSe/CdSe HS has been synthesized using the cation exchange method. The incorporation of Sn in the CdSe QDs host has been confirmed by powder X-ray diffraction (XRD), energy dispersive X-ray spectroscopy (EDX), and cyclic voltammetry (CV) studies. High-resolution transmission electron microscopy (HRTEM) confirms the formation of an interface between cubic CdSe/orthorhombic SnSe in the SnSe/CdSe HS system. The SnSe/CdSe HS is found to have a low conduction band offset of 0.72 eV, which is important for efficient device performance.²⁹ We have demonstrated the charge carrier dynamics of photogenerated electrons and holes in detail using ultrafast transient absorption (TA) spectroscopy. It is observed that the formation of SnSe/CdSe HS completely altered the exciton and biexciton dynamics as interpreted from ultrafast TA studies. We observed efficient hot carrier transfer from photoexcited SnSe to the CdSe region and then back transfer of charge carriers to SnSe according to the band alignment. The detailed understanding of photoexcited hot carriers at an interface may provide utmost aid to gain an understanding of different photophysical processes like carrier cooling, transfer, and recombination processes occurring in the SnSe/CdSe heterostructure system which in turn helps in designing more efficient SnSe-based heterojunction devices.

4.2. Results and discussion

4.2.1. Synthesis and structural characterization of materials

The chief aspect of this work is to synthesize and explore the detailed photophysics of photoexcited charge carriers at the p-n junction of the newly synthesized SnSe/CdSe heterostructure. The SnSe nanosheets (NSs), and CdSe quantum dots (QDs) were synthesized using the hot-injection method, and a two-step synthesis procedure was utilized to prepare SnSe/CdSe HS. The pre-synthesized CdSe QDs were used as a template and then SnSe/CdSe HS system was synthesized via cation exchange with Sn^{2+} ions at a moderate temperature of 120° C. Schematic illustration of the synthesis process of SnSe/CdSe HS via partial cation exchange has been demonstrated in **Figure 4.1(A)**. The cationic radii of Sn^{2+} and Cd^{2+} are comparable (118 and 97 pm)¹⁵ and thus help to accelerate the following cation exchange reaction.



The as-prepared SnSe NSs, CdSe QDs, and SnSe/CdSe HS samples were characterized by XRD, HRTEM, optical absorption, and CV studies. Powder XRD patterns were used to examine the structural properties of these systems. **Figure 4.1 (B, a)** shows the XRD patterns of the SnSe NSs with diffraction peaks at $2\theta \sim 26.5^\circ$, 30.6° , 31.2° , 37.9° , 43.5° , 47.2° , 49.7° , 54.5° , 64.9° , which are indexed to (210), (111), (400), (311), (020), (302), (511), (420), and (800) diffraction planes of the orthorhombic crystal structure of SnSe, respectively (JCPDS: 00-48-1224).³⁰ From the XRD of SnSe NSs, it can be seen that the (400) plane appears as the strongest orientation in the case of SnSe NSs.³¹ **Figure 4.1C** shows the atomic force microscopy (AFM) image of SnSe NSs, and the thickness was calculated to be in the range of 25-30 nm as shown in the inset. The reported thickness of the monolayer of SnSe is ~1 nm, which indicates that synthesized SnSe NSs are multilayers.³² The XRD pattern of pure CdSe QDs was collected following drop-casting over a glass substrate and is shown in **Figure 4.1(B, b)**. The peaks obtained at 25.1° , 42.4° , 49.2° , and 67.1° correspond to the reflection from (111), (220), (311), and (331) diffraction planes of zinc blend structure of CdSe (JCPDS:00-019-0191).³³

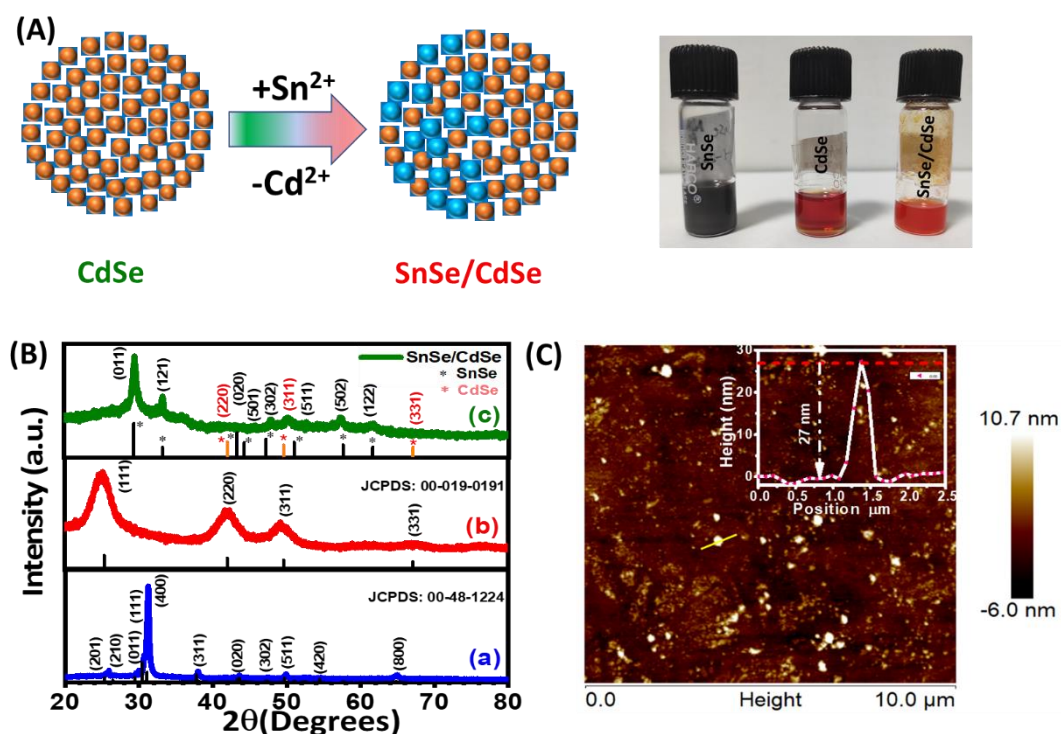


Figure 4.1. (A) *Left Panel:* Schematic illustration for the synthesis of SnSe/CdSe HS. *Right panel:* photographic image of prepared materials (B) Powder X-ray diffraction pattern of (a) SnSe NSs (b) CdSe QDs (c) SnSe/CdSe HS; JCPDS lines are also indicated (C) AFM image of SnSe NSs on the silicon substrate (inset: corresponding height profile).

The XRD patterns of SnSe/CdSe HS shown in **Figure 4.1 (B, c)** indicate the presence of both the cubic phase of CdSe and the orthorhombic phase of SnSe which are further confirmed via HRTEM images. The various key structural parameters such as lattice parameters, interplanar spacing d_{hkl} (nm), strain (ϵ), and dislocation density (ρ_d) calculated from XRD analysis for SnSe NSs, CdSe QDs, and SnSe/CdSe HS system are indicated in **Table 4.1**. **Figure 4.2 (a-c)** shows the transmission electron microscopic images of as-synthesized SnSe NSs, which possess typical sheet-like morphology. The size distribution histogram (**Figure 4.3 A**) demonstrates that the average long-edge length is ~ 700 nm and the average short-edge length is ~ 400 nm. The HRTEM image of SnSe NSs (**Figure 4.2d**) indicates the d -spacing of 0.29 nm which corresponds to the (400) diffraction plane of SnSe NSs and perfectly correlates with the XRD analysis. The obtained d spacing is well matched with earlier reports.³⁴ The transmission electron microscopy (TEM) and HRTEM images of CdSe QDs shown in **Figure 4.2 (e-h)**, reveal the spherical morphology of CdSe QDs, and the average size is found to be ~ 4 nm (**Figure 4.3B**).

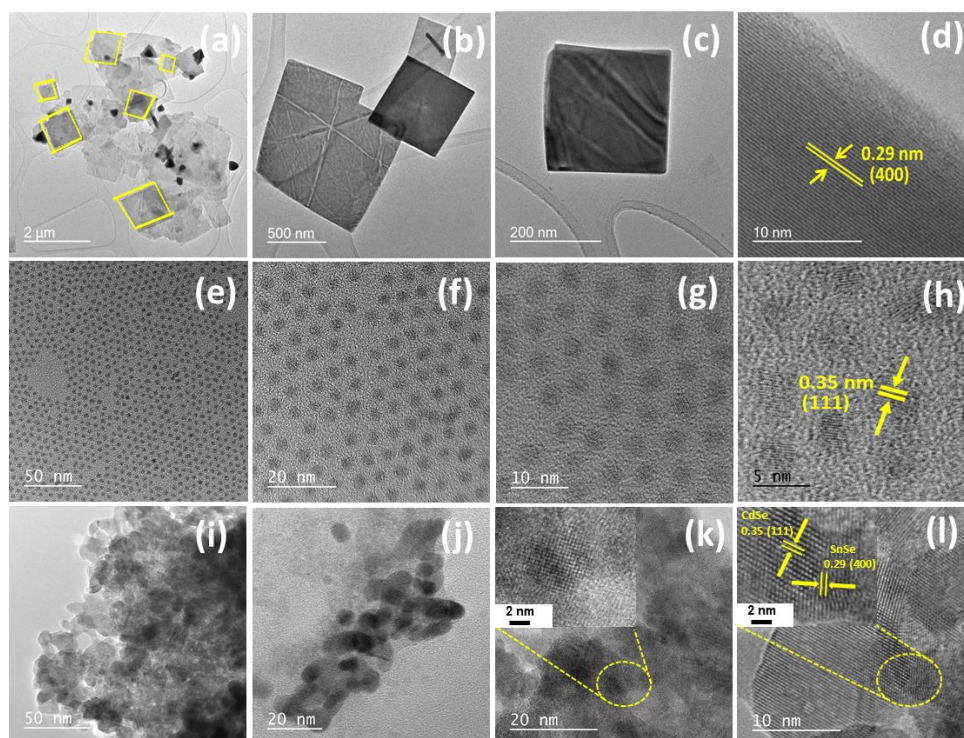


Figure 4.2. TEM and HRTEM images of (a-d) SnSe NSs, (e-h) CdSe QDs, and (i-l) SnSe/CdSe HS. Inset of (k) and (l) shows HRTEM images indicating the retained morphology of particles after cation exchange and the interface between the (111) plane of cubic CdSe and (400) plane of orthorhombic SnSe, respectively.

The d-spacing of 0.35 nm observed in the HRTEM image (**Figure 4.2h**) is consistent with the (111) lattice plane of cubic CdSe QDs. The observed d spacing is matched with previously reported literature.³⁵ Moreover, the obtained selected area electron diffraction (SAED) patterns of SnSe NSs and CdSe QDs are shown in **Figure 4.3 (C, D)**, which indicates the high crystallinity of the prepared materials. The TEM images of SnSe/CdSe HS formed via cation exchange are shown in **Figure 4.2 (i-l)** confirming the formation of two distinct phases. The morphology of particles is still spherical as that of CdSe QDs (used as a template) after cation exchange which indicates that the shape and morphology of CdSe particles in the SnSe/CdSe HS system are retained as shown in **Figure 4.2(k) inset**. The clear grain boundary is observed as shown in the HRTEM image (**Figure 4.2l, inset**) with the lattice spacing of 0.35 nm and 0.29 nm, which are assigned to the (111) plane of cubic CdSe QDs and (400) plane of the orthorhombic phase of SnSe NSs, respectively. HRTEM images of SnSe/CdSe HS (**Figure 4.2k, l**) indicate the formation of a proper interface between SnSe and CdSe in SnSe/CdSe HS with fewer interfacial defects. The presence and

uniform atomic distribution of the prepared samples has been confirmed through EDX.

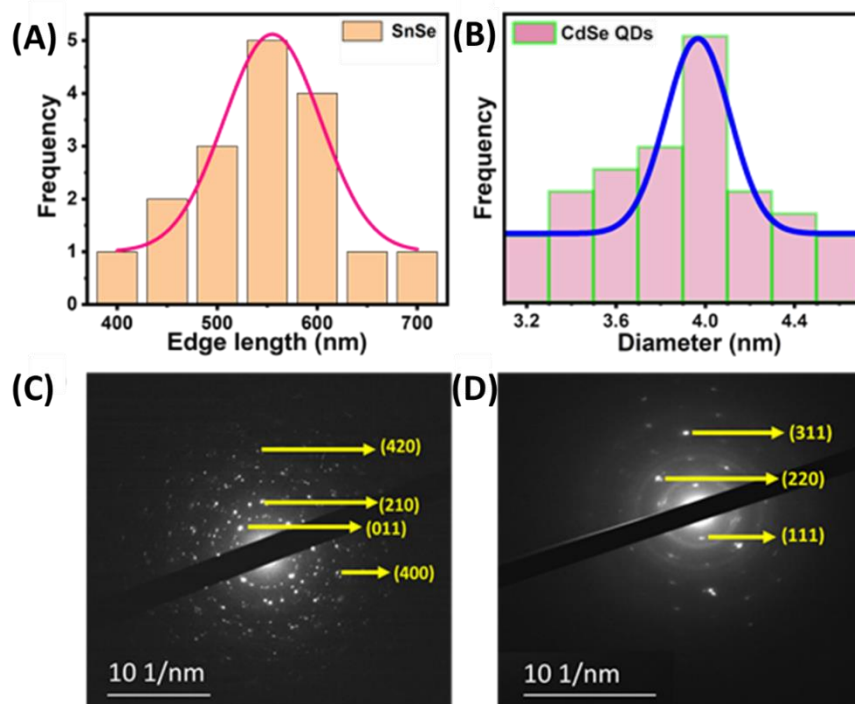


Figure 4.3. Particle size distribution and SAED pattern of (A, C) SnSe NSs, and (B, D) CdSe QDs.

Figure 4.4 shows the peaks corresponding to all Sn, Se, and Cd elements which clearly confirms the incorporation of Sn in CdSe resulting in the formation of SnSe/CdSe HS after the cation exchange reaction.

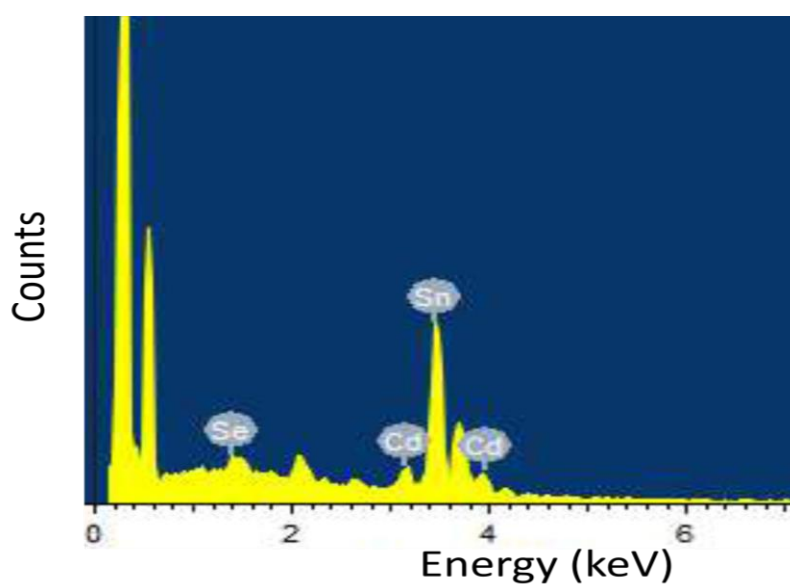


Figure 4.4. EDX spectrum of SnSe/CdSe HS.

4.2.2. Optical studies

Understanding the carrier cooling and transfer dynamics across the junction of SnSe/CdSe HS plays a pivotal role in improving the performance of devices such as solar cells, photodetectors, etc.^{36,37} The optical absorption spectrum of SnSe NSs presented in **Figure 4.5A(a)**, shows a broad absorption band in the region from 400 to 1600 nm peaking around 700 nm. The bandgap of SnSe was calculated using a tauc plot which is shown in **Figure 4.5A inset**. The bandgap energy of SnSe NSs was estimated by extrapolating the linear part of $(\alpha hv)^2$ versus hv curve to $(\alpha hv)^2 = 0$. The estimated bandgap energy of SnSe NSs was found to be 1.0 eV, which is in good agreement with the values reported in earlier literature.³⁸ The photoluminescence (PL) spectrum of SnSe NSs exhibits a strong peak centred at 1124 nm (**Figure 4.5C, inset**), which matches well with the earlier report.³⁹ In the absorption spectrum of CdSe QDs (**Figure 4.5B (b)**), two peaks appeared at ~558 nm, and 455 nm corresponds to $(1S(e)-1S_{3/2}(h), 1S)$ and $(1P(e)-1P_{3/2}(h), 1P)$ electronic transitions, respectively.⁴⁰ The band edge excitonic peak corresponds to the bandgap of ~2.22 eV which is considerably higher than the bulk bandgap of ~1.9 eV,⁴¹ indicates quantum confinement of the newly synthesized CdSe QDs. The size of particles is confirmed from the sizing curve reported by Peng et al. and is determined to be ~ 4 nm, which is in good agreement with HRTEM images (**Figure 4.2f**).⁴² The photoluminescence spectra (PL) of CdSe QDs in toluene shown in **Figure 4.5C**, exhibit a narrow PL band with the maximum emission peak at 569 nm. PL quantum yield (PLQY) of CdSe QDs is determined to be ~ 26 % (**Table 4.2**). The optical spectra of SnSe/CdSe HS comprise the signature of both pristine CdSe QDs and SnSe NSs. The absorption peaks of CdSe QDs slightly shifted to the shorter wavelength along with a broad absorption of SnSe NSs in the VIS-NIR region.

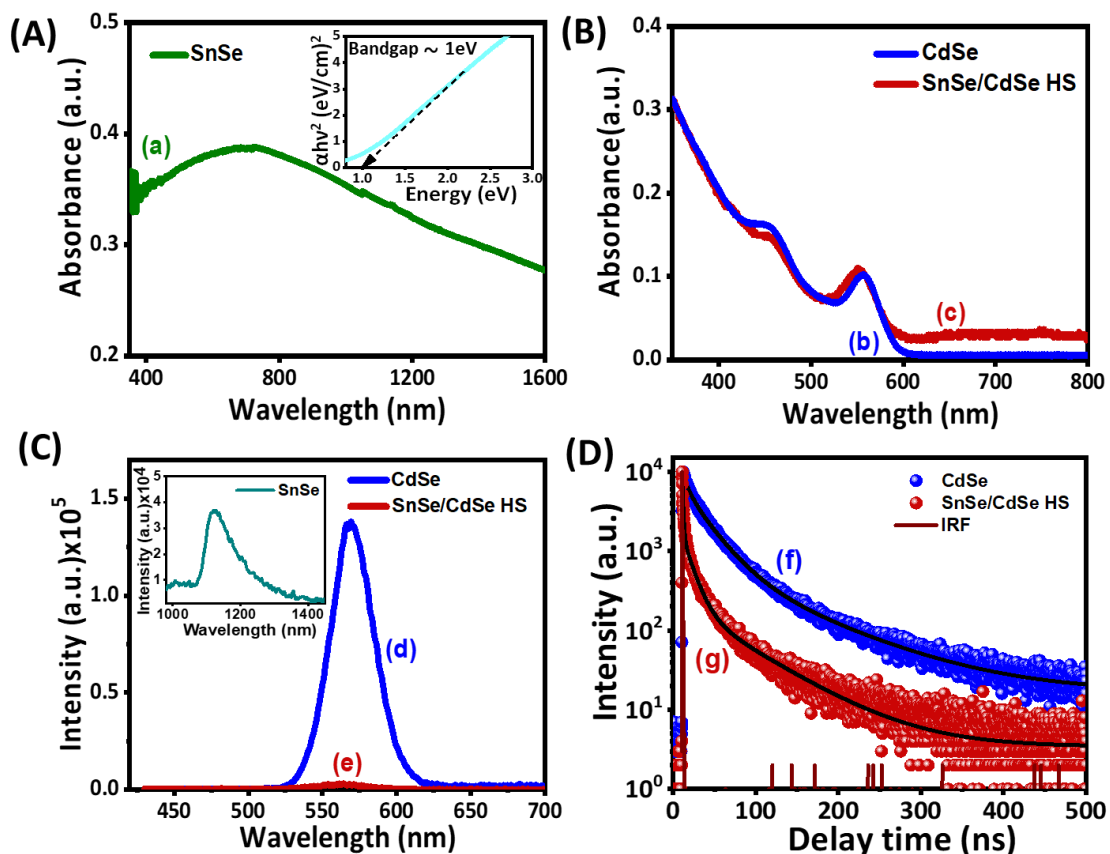


Figure 4.5. Steady-state optical absorption spectrum of (A) (a) SnSe NSs, and tauc plot (inset); (B) Steady-state optical absorption of (b) CdSe QDs and (c) SnSe/CdSe HS; (C) Steady-state PL spectra of (d) CdSe QDs and (e) SnSe/CdSe HS; (inset: PL of SnSe NSs) dispersed in toluene and (D) Time-resolved PL decay trace of (f) CdSe QDs and (g) SnSe/CdSe HS after exciting the sample at 402 nm and monitoring at 569 nm.

Table 4.1. The various key structural parameters such as lattice parameters (hkl), interplanar spacing d_{hkl} (nm), strain (ϵ), and dislocation density (ρ_d) for SnSe NSs, CdSe QDs and SnSe/CdSe HS system.

Samples	Planes (hkl)	d_{hkl} (nm)	Lattice Parameter			Dislocation Density (ρ_d) $\times 10^{16} \text{ m}^{-2}$	Strain (ϵ) $\times 10^{-3}$	Unit Cell Volume (\AA^3)
			a (\AA°)	b (\AA°)	c (\AA°)			
SnSe	400	0.2863	11.8	4.14	4.27	0.18	1.47	208.59
CdSe	111	0.3546	6.14	6.14	6.14	15.55	13.66	231.47
SnSe/CdSe HS	-	0.3027	-	-	-	1.09	3.62	-

Table 4.2. Quantum yield calculation.

Sample	Area of sample	Area of reference (Rhodamine B)	OD sample (420 nm)	OD reference (420 nm)	PLQY (%)
CdSe	3.15×10^7	3.53×10^7	0.08	0.06	26%
SnSe/CdSe HS	10234	3.53×10^7	0.024	0.06	<1%

This blue shift in the excitonic peaks can be due to the shrinkage of CdSe on the formation of HS with SnSe. Interestingly, it is observed from the PL spectra that the band edge emission of the CdSe quantum dot is greatly quenched in the presence of SnSe in SnSe/CdSe HS upon 420 nm excitation. This indicates the transfer of charge carriers from CdSe QDs to SnSe NS in the HS system, which is the thermodynamically viable process according to band alignment of synthesized SnSe/CdSe heterostructure. Now to elucidate the carrier transfer phenomena, time-resolved PL studies of CdSe and SnSe/CdSe HS were carried out monitoring at 569 nm. Time-resolved PL studies of pure CdSe QDs and SnSe/CdSe HS are shown in **Figure 4.5(D)**. The average lifetime of SnSe/CdSe HS is found to be 3.8 ns, which is almost 7 times lower than that of pure CdSe QDs (26 ns). This decrement in average lifetime suggests the transfer of charge carriers from CdSe to SnSe in the SnSe/CdSe HS system. Also, the PLQY of SnSe/CdSe HS is reduced to <1 % (From 26% of pure CdSe, **Table 4.2**). The decreased PLQY can be ascribed to the decrement of radiative recombination of charge carriers in the case of SnSe/CdSe HS.

4.2.3. Cyclic voltammetric and band edge measurements

The detailed fundamental understanding of many processes viz. charge transfer kinetics, dynamics at the semiconductor (donor)/ semiconductor (acceptor) interface (absorber/buffer), semiconductor/electrolyte interfaces, band edge (valance and conduction band) positions, trap states as well as midgap states play a very crucial role in the final performance of an optoelectronic device. Prior knowledge of these critical parameters i.e. electronic band structure is of utmost importance for fabricating high throughput optoelectronic devices. In the last two decades, CV

techniques have proved themselves as superpotential and simple methods to estimate these critical parameters, over traditional methods like ultraviolet photoelectron spectroscopy (UPS) and scanning tunneling spectroscopy (STS) with high reproducibility and accuracy.^{43,44}

In the present CV investigation, the colloidal dispersions (1mg/mL) of each sample (SnSe, CdSe, and SnSe/CdSe HS) have been drop cast (100 μ L) on the glassy carbon (GC) electrode surface followed by vacuum drying and used as the working electrode. The controlled CV measurements (without NCs sample) have been performed on bare GC electrodes in the presence of tetrabutylammonium perchlorate (TBAP) supporting electrolyte in dried dichloromethane (DCM) solvent. The controlled CVs for all the samples are shown in **Figure 4.6(A, Aa, B)**, with dotted lines. None of the blank CV does show any redox reaction at the GC working electrode, suggesting a clean surface of GC. However, in the same TBAP supporting electrolyte solution GC electrodes loaded with the NCs samples were introduced, followed by CV measurement and shown in solid red lines in **Figure 4.6 (A, Aa, B)**. **Figure 4.6A and 4.6A(a)** depicts the CV recorded on the SnSe and CdSe nanoparticles loaded on the GC electrode separately. The CVs recorded for SnSe and CdSe show two prominent reduction and oxidation (redox) peaks. Based on the direction and nature of the current-potential sign anodic and cathodic peaks were labeled as A_1 and C_1 .

This redox peak suggests that these samples are very electroactive and support redox reactions. From **Figure 4.6 (A)** for SnSe CV, the oxidation (anodic A_1) and reduction (cathodic C_1) peaks were observed at 0.66V and -0.53V vs. normal hydrogen electrode (NHE), respectively. These A_1 and C_1 peaks that appeared in CV are nothing but the SnSe NSs sample oxidize and reduce at specific potential attributed to the charge transfer mediated through band edges (valence band (VB) and conduction band (CB)). The absence of complementary peaks after the A_1 and C_1 peaks suggests the single electron transfer followed by chemical reaction and low stability in charged conditions.

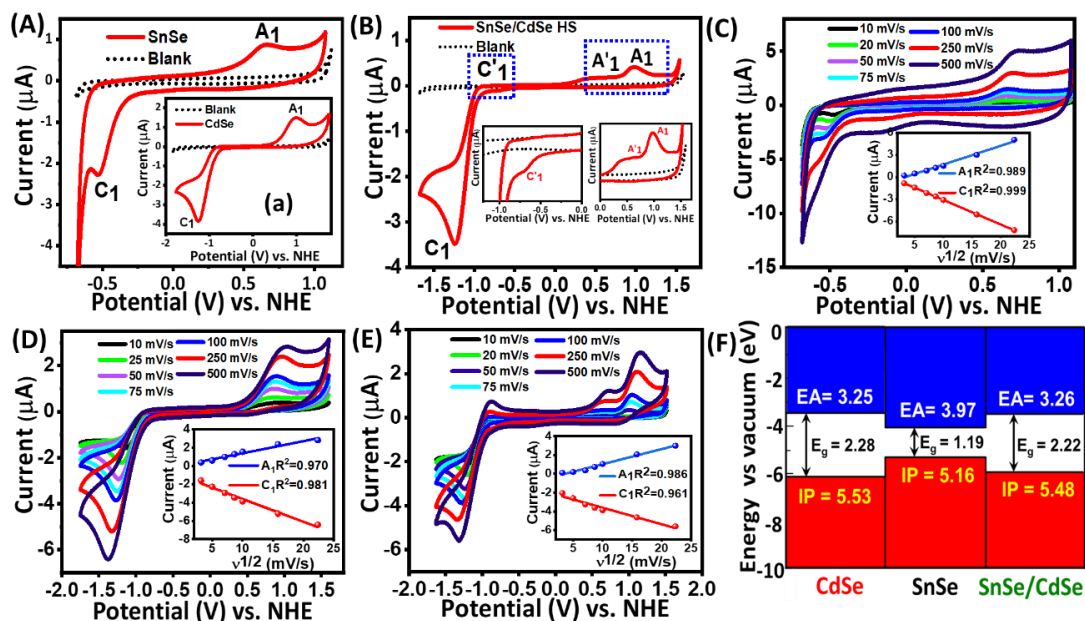


Figure 4.6. Cyclic Voltammogram recorded for the SnSe NSs, CdSe QDs, and SnSe/CdSe HS. The dotted line in Figure (A, A(a), B) represents the controlled CV in TBAP-DCM without the NCs sample and red solid lines for (A) SnSe, (A, a) CdSe and (B) SnSe/CdSe HS. The inset of Figure 4B shows the enlarged view of the anodic and cathodic peaks. Figure 4 (C, D, E) scan rate dependant current response for the CVs recorded for (C) SnSe, (D) CdSe, and (E) SnSe/CdSe HS. The inset of Figure 4(C, D, E) shows the linear regression fitting for current values as a function of under square root of the scan rate. (F) Schematic energy band diagram of SnSe/CdSe HS, with small band offset (0.72 eV) at the interface.

The oxidation and reduction peaks noticed in the CV are due to the donation and acceptance of electrons from and to the respective band edges, and the peak potential difference (A_1 and C_1) is considered to be the quasiparticle gap (electrochemical bandgap). Similarly, **Figure 4.6 (A, a)** depicts the CV recorded on CdSe NCs, where distinct A_1 and C_1 peaks are noted at 1.03 V and -1.25 V vs. NHE, respectively. **Figure 4.6B** shows the SnSe/CdSe HS, CV with similar distinct A_1 and C_1 redox peaks at 0.98 V and -1.24 V vs. NHE, respectively. Interestingly, when we performed the CV measurements for the SnSe/CdSe HS sample, we noticed two additional peaks apart from the regular A_1 at 0.98 V and C_1 at -1.24 V, which are marked as A'_1 at 0.55 V and C'_1 at -0.70 V, respectively. While after careful observation it is found that the A'_1 and C'_1 peak difference is 1.25 V, which is in close agreement with the peak difference of SnSe of 1.19 V. In addition to this, the peak positions (A_1 and C_1) of CdSe and SnSe/CdSe HS are also very close, furthermore, there is a potential

shifting of A'_1 and C'_1 from A_1 and C_1 of SnSe NSs by 110 mV and 170 mV, these observations are attributed to the formation of HS between CdSe and SnSe and strong interaction between this HS.⁴⁵ The obtained values of band edges (VB and CB) are converted with respect to vs. vacuum and summarized in **Table 4.3**. The quasiparticle gap is measured for the SnSe NSs, CdSe QDs, and SnSe/CdSe HS, the estimated values are 1.19 eV, 2.28 eV, and 2.22 eV, respectively. These electrochemical values of the bandgap are in very close agreement with the optical bandgap values obtained from absorbance spectra.

Table 4.3. Summarized data for the electrochemical measurements (CV), the band structure parameters (VB vs. NHE, CB vs. NHE, VB vs. Vacuum (Vac), CB vs. Vac and Electrochemical (Eg) band gap).

Sample	VB vs. NHE (V)	CB vs. NHE (V)	VB vs. Vac (eV)	CB vs. Vac (eV)	Eg (eV)
SnSe	0.66	-0.53	-5.16	-3.97	1.19
CdSe	1.03	-1.25	-5.53	-3.25	2.28
CdSe/SnSe HS	0.55/0.98	-0.70/-1.24	-5.48	-3.26	1.25/2.22

The decrease in bandgap and shift in the valence band of SnSe/CdSe HS is observed as compared to pure CdSe QDs. **Figure 4.6 (C, D, E)** depicts the scan rate-dependent CVs for the SnSe, CdSe, and SnSe/CdSe HS in the range of 10 mVs^{-1} to 500 mVs^{-1} . From **Figure 4.6 (C, D, E)** it is seen that anodic and cathodic peak currents (I_{pa} and I_{pc}) increase linearly as a function of the square root of scan rate ($v^{1/2}$) for SnSe NSs, CdSe QDs, and SnSe/CdSe HS. The inset of **Figure 4.6 (C, D, E)** represents peak current vs. $v^{1/2}$ attributed to the diffusion-controlled process. Furthermore, to understand the charge transfer kinetics and dynamics, these band edge positions are estimated through CV used to construct the band diagram and converted to a local vacuum. The energy level of valence and conduction band edges of the SnSe, CdSe, and SnSe/CdSe HS were determined by CV measurement. These CV measurements allow the detailed investigation of band alignment with the help of electrochemical bandgap, ionization potential (IP), and electron affinity (EA). We have used IP and EA values to construct the band alignment of SnSe/CdSe HS which is shown in **Figure 4.6F**. The conduction band offset (CBO) at the SnSe/CdSe HS

interface is estimated at 0.72 eV, which is an encouraging factor for solar devices. The small CBO in SnSe/CdSe HS indicates that free electrons generated after excitation will diffuse much faster and can be collected before their recombination with free holes in the valence band. Thus, highlights a route to improve device performances and fabrication of efficient solar cells.^{46,47}

4.2.4. Transient absorption studies

The excited state photophysics of the charge carriers plays a vital role in identifying the intrinsic characteristics of the material, which is fundamental information for proceeding toward any potential application.^{48,49} In this work, we studied the photoexcited charge transfer and recombination dynamics at the interface of SnSe/CdSe HS and compared it with pristine CdSe QDs and SnSe NSs system with the aid of femtosecond TA spectroscopy. The samples were excited with 350 nm pump pulses using a fluence of 200 $\mu\text{J}/\text{cm}^2$ and the change in absorption was recorded in the visible region. **Figures 4.7A, and B** present TA spectra of pristine SnSe NSs at the early and longer delay time, respectively. The spectra primarily show a broad positive signal in the entire region with two distinct absorption bands (peaking at 460 and 590 nm). Positive TA signal implies that probe-mediated photoinduced absorption of excited-state charge carriers toward higher energy levels dominates over any state-filling effect in the SnSe NSs system. In addition to that, a photoinduced bleach signal appears at the 500-650 nm region of the spectra at an early longer time scale (<1 ps and > 500 ps). This indicates that state filling-induced bleach signal is also present in the system. But it is masked in the presence of a strong photoinduced absorption signal in the time scale of > 1ps to < 500 ps. Here, the negative signal peaks around 550 nm. Hence, the state that corresponds to this bleach signal must be a higher energy conduction band, not a conduction band edge, as the bandgap of SnSe is very low (1.19 eV, 1042 nm). Earlier Qiu et al. reported a positive signal for SnSe NSs on exciting the sample with 800 nm laser pulses.⁵⁰ The decay kinetics of these two positive signals were monitored at 460 and 590 nm and presented in **Figures 4.7C and 4.7D**.

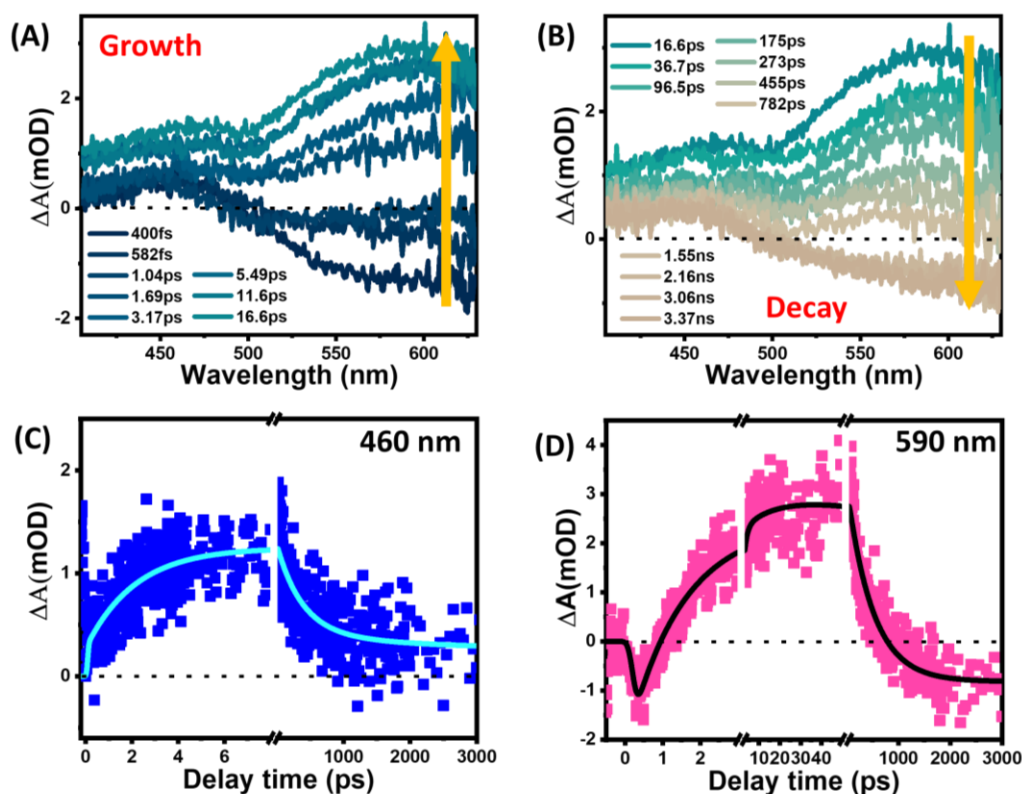


Figure 4.7. TA spectra of the SnSe NSs at (A) early time scale and (B) longer time scale following photoexcitation of a 350 nm laser pulse with $200 \mu\text{J}/\text{cm}^2$ laser fluence. Corresponding kinetic profiles monitoring at (C) 460 nm and (D) 590 nm.

The kinetics were fitted multi-exponentially and the fitting components are listed in **Table 4.4**. The 590 nm kinetics comprises a negative signature of the bleach signal both in the early and longer time scales. The rise and decay of the early negative signal are very fast and found to be IRF limited (< 100 fs) in our instrument. Whereas the positive signal takes a longer time to grow and can be fitted with two growth time scales (1.1 ps and 7.8 ps). The 460 nm positive feature possesses only a positive signature throughout the measurement time (> 3 ns). In fact, the growth and decay dynamics are also different as compared to that of the 590 nm signal. This indicates that these two transient features are independent in nature and correspond to separate optical transitions in the SnSe NSs system. **Figure 4.8A** represents the TA spectra of the pristine CdSe QDs at different time delays after exciting the sample at 350 nm laser pulse with a fluence of $200 \mu\text{J}/\text{cm}^2$. The spectra consist of a band edge bleach peak at 560 nm along with a broad hump at 525 nm and a high energy bleach at 474 nm, which can be ascribed to $\{1S, 1S(e)- 1S_{3/2}(h)\}$, $\{2S, 1S(e)- 2S_{3/2}(h)\}$ and $\{1P, 1P(e)- 1P_{3/2}(h)\}$ electronic transitions, respectively, in the CdSe QDs system, as discussed in the steady-state absorption spectra (**Figure 4.5Bb**) earlier.

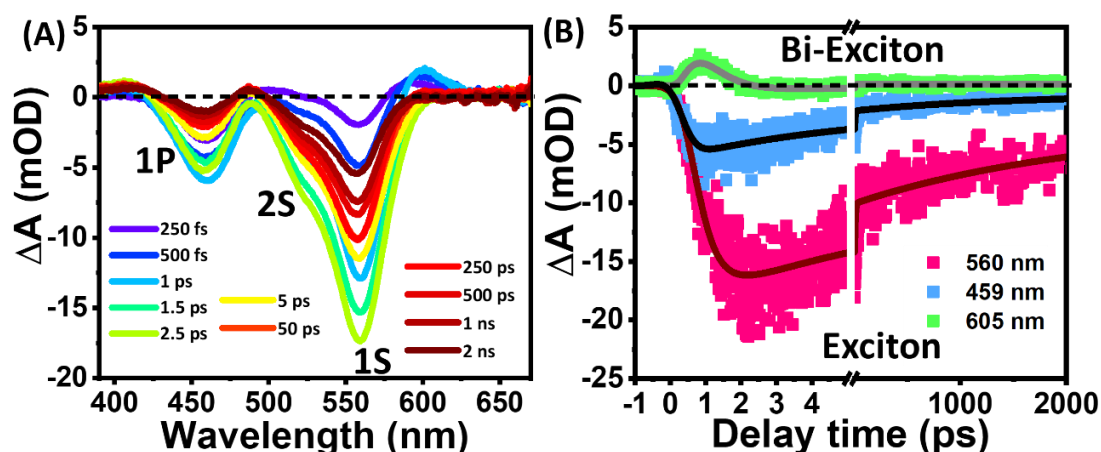


Figure 4.8. (A) Transient absorption spectra of CdSe QDs following photoexcitation of 350 nm laser pulse with $200 \mu\text{J}/\text{cm}^2$ laser fluence. (B) Transient dynamic profiles of 1S, 1P exciton, and band edge bi-exciton signals monitoring at 560, 459, and 605 nm.

Along with these bleach signals, we observed a weak photoinduced absorption signal in the blue region and a sharp bi-excitonic signal in the red region of transient spectra.^{51,52} **Figure 4.8B** shows the kinetics of both the excitons and bi-excitonic features in CdSe system monitoring at a probe wavelength of 560 nm, 459 nm, and 605 nm, respectively. The bleach kinetics has been fitted multi-exponentially with time components displayed in **Table 4.5**. The ultrafast growth with a time component of 0.46 ps for the band-edge excitonic bleach position indicates the intraband cooling of hot charge carriers from the higher excitonic states to the band-edge position of CdSe QDs. The fast and intermediate components in the decay of bleach are attributed to the nonradiative trapping of charge carriers whereas the longer component arises due to radiative and non-radiative recombination of electrons and holes.⁵³ The probe-induced biexciton signal at 605 nm described in **Figure 4.8B** is fitted multi-exponentially and fitted components are shown in **Table 4.5**. The biexciton dissociates into its exciton via auger decay which further undergoes the recombination process.

Now, to probe the carrier dynamics in the p-n junction comprised with the hetero-interface of SnSe NSs and CdSe QDs, we excited the SnSe/CdSe HS with 350 nm laser pulses (**Scheme 4.1A**). The other experimental conditions were kept the same as that of pristine ones. **Figure 4.9A** presents TA spectra of SnSe/CdSe HS for 350 nm pump excitation and $200 \mu\text{J}/\text{cm}^2$ laser fluence, in a wide range of pump-probe

delay times. These TA spectra primarily constitute 1S and 1P excitonic bleach signals of the CdSe QDs entity. However, the positions of these bleach features are slightly blue-shifted as compared to the pristine CdSe QDs system. This could be the indication of the lower size distribution of CdSe QDs in the presence of SnSe NSs. To establish the individual effect of CdSe and SnSe in the HS, we have plotted the TA spectrum of each CdSe QDs, SnSe NSs, and the HS at 1 ps pump-probe delay time (**Figure 4.9B**). At an early time scale, the TA spectra are dominated by CdSe. However, the effect of SnSe is clearly visible in the SnSe/CdSe heterostructure. However, the CdSe QDs characteristics are substantially modified in the presence of SnSe. The 2S excitonic hump is missing in the HS spectrum. Also, the photoinduced absorption signals, as well as the bi-excitonic signal, are enhanced in the HS. In fact, the overall intensity of the signal is enhanced in the HS, as compared to pristine CdSe QDs. This indicates toward improved charge carrier population in the CdSe moiety in the presence of SnSe NSs at an early time scale. Interestingly, this enhancement is only prominent for ground state features (1S exciton and bi-exciton), which indicates the involvement of electron transfer to the lower excitonic state (1S) of CdSe from photoexcited SnSe.

Table 4.4. Kinetic fitting parameters for SnSe NSs solution under 350 nm pump excitation with $200\mu\text{J}/\text{cm}^2$ laser fluence.

System	Probe $\lambda(\text{nm})$	τ_{g1}	τ_{g2}	τ_1	τ_2
SnSe	460 nm	2.04 ps (100%)	-	120 ps (-62%)	>1ns (38%)
	590 nm	1.5 ps (88.8%)	7.8 ps (11.2%)	160 ps (-80%)	>1 ns (-20%)

To further investigate these observations, the transient dynamics are monitored at different probe wavelengths. In **Figure 4.9C**, the kinetic profiles of CdSe 1S excitons are compared in the absence and presence of SnSe. The rise and decay of this signal are much faster than that of pristine CdSe, despite the high intensity of the HS signal. One can elucidate from this the observation that, the greater charge carrier population in the CdSe region in a shorter time scale eventually gets depleted in the presence of SnSe in the HS (which is actually very much thermodynamically viable).

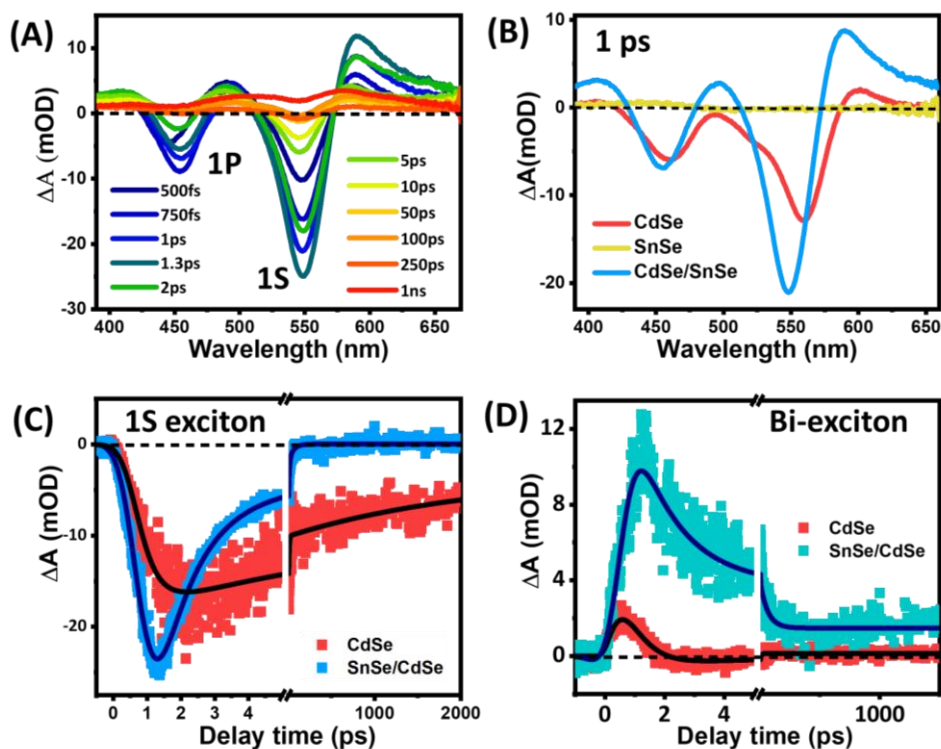


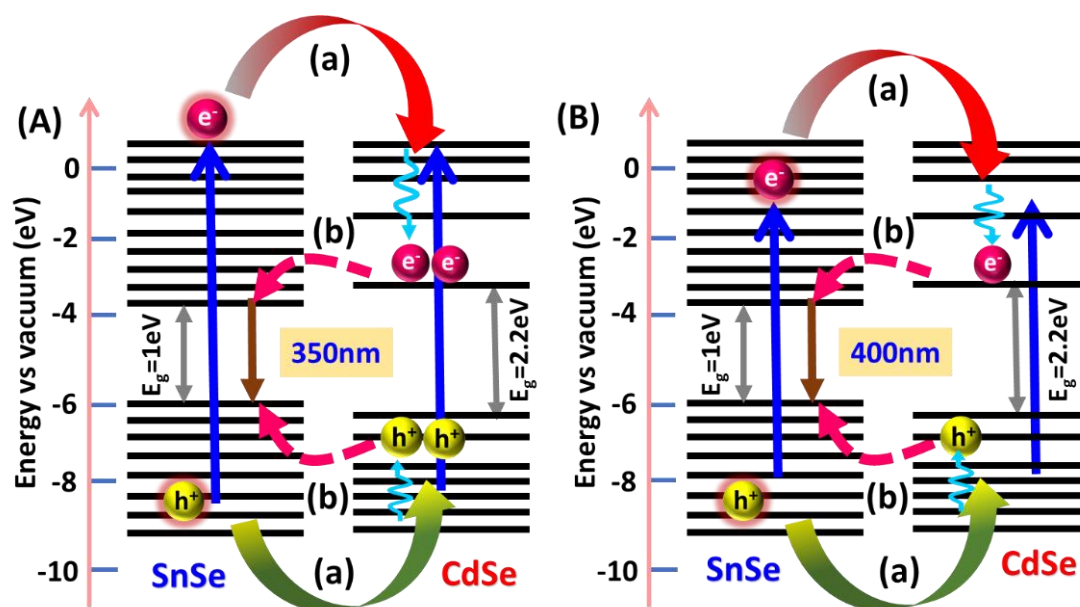
Figure 4.9. Transient absorption spectra of the (A) SnSe/CdSe HS at different probe delays. (B) Comparative transient spectra of CdSe, SnSe, and the HS at 1 ps probe delay time. Comparative dynamic profiles of CdSe and SnSe/CdSe HS for (C) 1S exciton and (D) band edge bi-exciton. The experiments were carried out after exciting at 350 nm.

Table 4.5. Kinetic fitting parameters at excitonic bleach and biexciton position for CdSe QDs and SnSe/CdSe HS system under 350 nm pump excitation with $200\mu\text{J}/\text{cm}^2$ laser fluence.

System	Probe λ (nm)	τ_g	τ_1	τ_2	τ_3	τ_4
CdSe	560	0.46ps	12ps	145ps	>1ns	
	1S bleach	(100%)	(-39.1%)	(-14.1%)	(-46.8%)	
SnSe/ CdSe HS	604	0.16ps	0.47ps	1.3ps	8.6ps	>1ns
	Biexciton	(100%)	(-100%)	(17.2%)	(82.2%)	(-100%)
SnSe/ CdSe HS	549nm	0.26ps	1.99ps	22ps		
	1S bleach	(100%)	(-85.5%)	(-14.5%)		
SnSe/ CdSe HS	590nm	0.24	4.35 ps	160 ps	>1ns	
	Biexciton	(100%)	(-65.9%)	(-18.0%)	(-16.1%)	

These charge carriers present in CdSe during a shorter time scale can be extracted for photovoltaic device applications. Now the question is why the charge carrier population gets enhanced in the first place. To find out that, we excited the samples with lower pump energy (400 nm) and compared all the dynamical features with 350 nm pump excitation data (**Figure 4.10**). In 400 nm excitation, the dynamics of 1S exciton is quite faster than that of pristine CdSe, but the signal intensity was found to be lower (**Figure 4.10 B, C**).

Scheme 4.1 Schematic Illustration of the different processes taking place in SnSe/CdSe heterostructure system upon (A) 350 nm and (B) 400 nm pump excitation. Here (a) corresponds to the transfer of hot carriers (both electrons and holes) from SnSe to the CdSe system and (b) implies the back transfer of band edge electrons and holes from CdSe to SnSe which is a thermodynamically viable process.



This means for 350 nm excitation SnSe charge carriers are excited to higher energy states and get delocalized into the CdSe levels. This charge transfer results in higher signal intensity of CdSe excitonic bleach in the HS. For 400 nm excitation, this probability of hot carrier transfer is lower and that is why we end up with lower intensity bleach signals in HS as compared to that of 350 nm excitation (**Scheme 4.1B**). Similarly, for the bi-excitonic feature, the signal intensity is much higher (almost four times) in the case of HS as compared to that of pristine CdSe (**Figure 4.9D**).

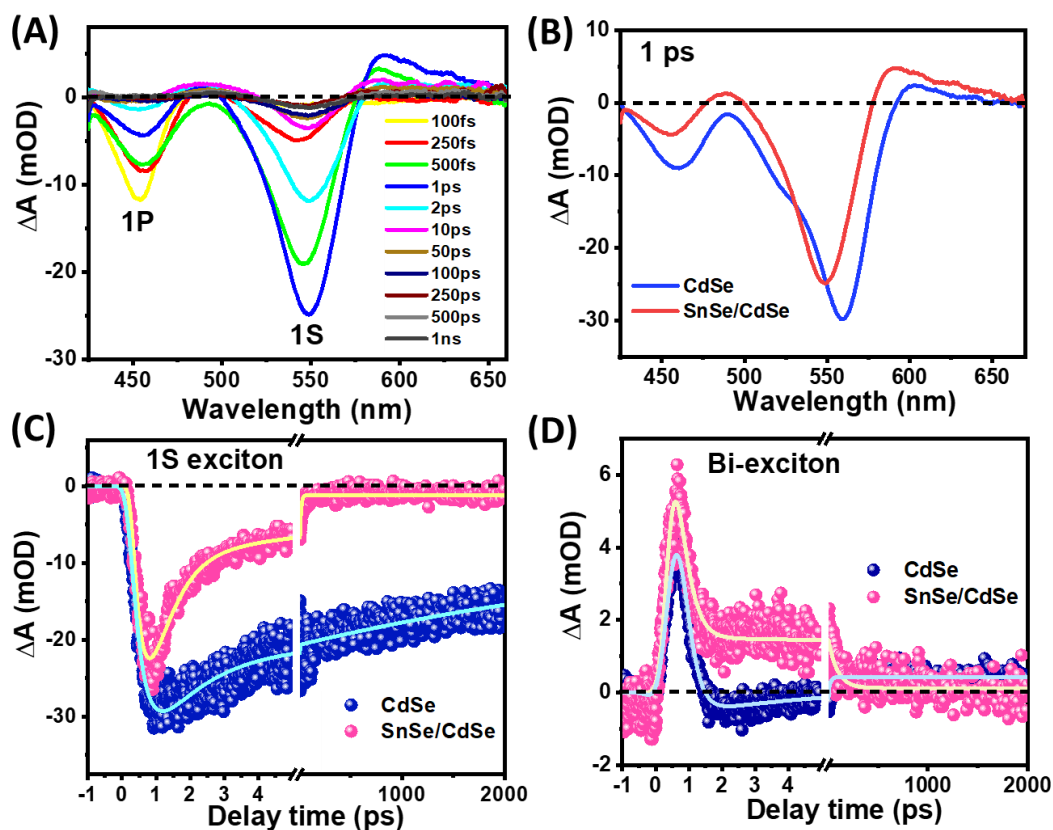


Figure 4.10. Transient absorption spectra of the (A) SnSe/CdSe HS at different probe delays. (B) Comparative transient spectra of CdSe, and SnSe/CdSe HS at 1 ps probe delay time. Comparative dynamic profiles of CdSe and SnSe/CdSe HS for (C) 1S exciton and (D) band edge bi-exciton. The experiments were carried out after exciting at 400 nm laser pulse.

Table 4.6. Kinetic fitting parameters at excitonic bleach and biexciton position for CdSe QDs and SnSe/CdSe HS system under 400 nm pump excitation with $200\mu\text{J}/\text{cm}^2$ laser fluence.

System	Probe λ (nm)	τ_g	τ_1	τ_2	τ_3	τ_4
CdSe	558	0.25	8ps	120ps	>1ns	
	1S bleach	(100%)	(-32.4%)	(-14.9%)	(-52.7%)	
SnSe/ CdSe HS	604	0.12ps	0.39ps	1.25	7ps	>1ns
	Biexciton	(100%)	(-100%)	(25%)	(75%)	(-100%)
SnSe/ CdSe HS	549	0.16	1.8ps	11.4ps	>1ns	
	1S bleach	(100%)	(-77.1%)	(-17.7%)	(-52%)	
SnSe/ CdSe HS	590	0.12ps	0.38ps	23.2ps	>1ns	
	Biexciton	(100)	(-68.8%)	(-21.9%)	(-9.3%)	

On the other hand, the increment of the bi-excitonic signal is only 2 times higher in HS as compared to CdSe after 400 nm excitation (**Figure 4.10D**). Interestingly, the dynamics of the bi-exciton signal are very different from the pristine one for 400 nm excitation **Table 4.6**. The decay of this signal is very slow and never gets decayed into excitonic forms like typical bi-excitonic signatures. It is true for both 350 and 400 nm photo-excitations. We assume that, immediately after the formation of the bi-excitonic features, the corresponding charge carriers get trapped in the SnSe/CdSe interfacial defect states and decay slowly. This slow decay time of bi-exciton/trapped carriers could be crucial for photonic devices as the charge carriers can now be easily extracted in that long period and would improve the device's performance.

4.3. Conclusion

In summary, we have successfully synthesized SnSe/CdSe HS by hot injection followed by the cation exchange method for the first time. The structural, morphological, optical, and CV studies reveal the formation of heterostructure with type I band alignment. The epitaxial growth of the (400) plane of SnSe along the (111) plane of CdSe has been confirmed through HRTEM analysis. CV measurements elucidated distinct cathodic and anodic peaks and estimated electrochemical band bandgap. We have studied band alignment and band offset for a clear understanding of the concurrent carrier transport mechanism at and across the SnSe/CdSe HS. The charge carrier dynamics of photoexcited bare SnSe and CdSe systems as well as in SnSe/CdSe HS system were explored using femtosecond TA spectroscopy. The bi-exciton signal was found to be significantly enhanced in the HS as compared to pristine CdSe QDs owing to the rapid transfer (delocalization) of hot carriers from SnSe to CdSe. Moreover, this biexciton signal does not get dissociated into excitons following its regular decay manner. Rather these biexcitons get trapped in the interfacial trap states and decay at a very slow rate. This enhances the charge carrier extraction probability and would be of immense help for the device applications. Subsequent fast recovery of band edge bleach in SnSe/CdSe HS confirms the efficient charge separation process that occurred from CdSe to SnSe owing to the thermodynamic viability of type 1 arrangement. The successful synthesis of a SnSe-based heterostructure system using a facile and economical cation exchange method will have immense potential for low-cost next-generation Sn-based high-efficiency solar cells, photoelectrochemical cells, and photodetector devices.

4.4. References

- (1) Diner, F. The Analysis on Photovoltaic Electricity Generation Status, Potential and Policies of the Leading Countries in Solar Energy. *Renew. Sustain. Energy Rev.* **2011**, *15*, 713-720.
- (2) Cho, J. W.; Ismail, A.; Park, S. J.; Kim, W.; Yoon, S.; Min, B. K. Synthesis of $\text{Cu}_2\text{ZnSnS}_4$ Thin Films by a Precursor Solution Paste for Thin Film Solar Cell Applications. *ACS Appl. Mater. Interfaces* **2013**, *5*, 4162-4165.
- (3) Sun, K.; Yan, C.; Liu, F.; Huang, J.; Zhou, F.; Stride, J. A.; Green, M.; Hao, X. Over 9% Efficient Kesterite $\text{Cu}_2\text{ZnSnS}_4$ Solar Cell Fabricated by Using $\text{Zn}_{1-x}\text{Cd}_x\text{S}$ Buffer Layer. *Adv. Energy Mater.* **2016**, *6*, 1600046.
- (4) Siebentritt, S.; Schorr, S. Kesterites-a Challenging Materials for Solar Cell. *Prog. Photovolt.: Res. Appl.* **2012**, *20*, 512-519.
- (5) Wang, W.; Winkler, M. T.; Gunawan, O.; Gokmen, T.; Todorov, T. K.; Zhu, Y.; Mitzi, D. B. Device Characteristics of CZTSSe Thin-Film Solar Cells With 12.6% Efficiency. *Adv. Energy Mater.* **2013**, *4*, 1-5.
- (6) Li, Y.; Gao, C.; Long, R.; Xiong, Y. Photocatalyst Design Based on Two-Dimensional Materials. *Mater. Today Chem.* **2019**, *11*, 197-216.
- (7) Bhimanapati, G. R.; Lin, Z.; Meunier, V.; Jung, Y.; Cha, J.; Das, S.; Xiao, D.; Son, Y.; Strano, M. S.; Cooper, V. R.; et al. Recent Advances in Two-Dimensional Materials Beyond Graphene. *ACS Nano* **2015**, *9*, 11509-11539.
- (8) Chauhan, P.; Patel, A. B.; Solanki, G. K.; Machhi, H. K.; Sumesh, C. K.; Soni, S. S.; Patel, V.; Pathak, V. M. Ultrasonically Exfoliated Nanocrystal-Based Z-Scheme $\text{SnSe}_2/\text{WSe}_2$ Heterojunction for a Superior Electrochemical Photoresponse. *J. Phys. Chem. C* **2021**, *125*, 14729-14740.
- (9) Shi, W.; Gao, M.; Wei, J.; Gao, J.; Fan, C.; Ashalley, E.; Li, H.; Wang, Z. Tin Selenide (SnSe): Growth, Properties, and Applications. *Adv. Sci.* **2018**, *5*, 1700602.
- (10) Zheng, D.; Fang, H.; Long, M.; Wu, F.; Wang, P.; Gong, F.; Wu, X.; Ho, J. C.; Liao, L.; Hu, W. High-Performance Near-Infrared Photodetectors Based on p-Type SnX ($X = \text{S}, \text{Se}$) Nanowires Grown via Chemical Vapor Deposition. *ACS Nano* **2018**, *12*, 7239-7245.

- (11) Patel, K.; Solanki, G.; Patel, K.; Pathak, V.; Chauhan, P. Investigation of Optical, Electrical and Optoelectronic Properties of SnSe Crystals. *Eur. Phys. J. B* **2019**, *92*, 1-11.
- (12) Shinde, D. V.; Min, S. K.; Sung, M. M.; Shrestha, N. K.; Mane, R. S.; Han, S. H. Photovoltaic Properties of Nanocrystalline SnSe-CdS. *Mater. Lett.* **2014**, *115*, 244-247.
- (13) Walsh, A.; Chen, S.; Wei, S. H.; Gong, X. G. Kesterite Thin Film Solar Cells: Advances in Materials Modelling of $\text{Cu}_2\text{ZnSnS}_4$. *Adv. Energy Mater.* **2012**, *2*, 400-409.
- (14) Bose, R.; Manna, G.; Jana, S.; Pradhan, N. $\text{Ag}_2\text{S-AgInS}_2$: p-n Junction Heteronanostructures with Quasi Type-II Band Alignment. *Chem. Commun.* **2014**, *50*, 3074-3077.
- (15) Todescato, F.; Minotto, A.; Signorini, R.; Jasieniak, J. J.; Bozio, R. Investigation into the Heterostructure Interface of CdSe Based Core-Shell Quantum Dots Using Surface Enhanced Raman Spectroscopy. *ACS Nano* **2013**, *7*, 6649-6657.
- (16) Tan, C.; Chen, J.; Wu, X. J.; Zhang, H. Epitaxial Growth of Hybrid Nanostructures. *Nat. Rev. Mater.* **2018**, *3*, 1-13.
- (17) Dong, H. S.; Hughes, S. M.; Yin, Y.; Alivisatos, A. P. Cation Exchange Reactions in Ionic Nanocrystals. *Science* **2004**, *306*, 1009-1012.
- (18) Jain, P. K.; Amirav, L.; Aloni, S.; Alivisatos, A. P. Nanoheterostructure Cation Exchange: Anionic Framework Conservation. *J. Am. Chem. Soc.* **2010**, *132*, 9997-9999.
- (19) Robinson, R. D.; Sadtler, B.; Demchenko, D. O.; Erdonmez, C. K.; Wang, L. W.; Alivisatos, A. P. Spontaneous Superlattice Formation in Nanorods through Partial Cation Exchange. *Science* **2007**, *317*, 355-358.
- (20) Dong, H. S.; Hughes, S. M.; Yin, Y.; Alivisatos, A. P. Cation Exchange Reactions in Ionic Nanocrystals. *Science* **2004**, *306*, 1009-1012.
- (21) Casavola, M.; Van Huis, M. A.; Bals, S.; Lambert, K.; Hens, Z. Vanmaekelbergh, D. Anisotropic Cation Exchange in PbSe/CdSe Core/Shell Nanocrystals of Different Geometry. *Chem. Mater.* **2012**, *24*, 294-302.

- (22) Jang, Y.; Yanover, D.; Čapek, R. K.; Shapiro, A.; Grumbach, N.; Kauffmann, Y.; Sashchiuk, A.; Lifshitz, E. Cation Exchange Combined with Kirkendall Effect in the Preparation of SnTe/CdTe and CdTe/SnTe Core/Shell Nanocrystals. *J. Phys. Chem. Lett.* **2016**, *7*, 2602-2609.
- (23) Drozd, V. E.; Nikiforova, I. O.; Bogevolnov, V. B.; Yafyasov, A. M.; Filatova, E. O.; Papazoglou, D. ALD Synthesis of SnSe Layers and Nanostructures. *J. Phys. D. Appl. Phys.* **2009**, *42*, 125306.
- (24) Chauhan, P.; Patel, A. B.; Narayan, S.; Prasad, J.; Sumesh, C. K.; Solanki, G. K.; Patel, K. D.; Soni, S. S.; Jha, P. K.; Pathak, V. M.; Patel, V. Superior Electrochemical Activity of CdSe Thin Film by Chromium Substitutional Doping. *J. Alloys Compd.* **2021**, *862*, 158016.
- (25) Barrios-Salgado, E.; Nair, M. T. S.; Nair, P. K. Chemically Deposited SnSe Thin Films: Thermal Stability and Solar Cell Application. *ECS J. Solid State Sci. Technol.* **2014**, *3*, Q169-Q175.
- (26) Teghil, R.; Santagata, A.; Marotta, V.; Orlando, S.; Pizzelle, G.; Giardini-Guidoni, A. Characterization of the Plasma Plume and of Thin Film Epitaxially Produced during Laser Ablation of SnSe. *Appl. Surf. Sci.* **1995**, *90*, 505-514.
- (27) Xu, H.; Hao, L.; Liu, H.; Dong, S.; Wu, Y.; Liu, Y.; Cao.; Wang.; Ling.; Li.; Xu, Z.; Xue.; Yan, K. Flexible SnSe Photodetectors with Ultrabroad Spectral Response up to 10.6 μm Enabled by Photobolometric Effect. *ACS Appl. Mater. Interfaces* **2020**, *12*, 35250-35258.
- (28) Minnam Reddy, V. R.; Lindwall, G.; Pejjai, B.; Gedi, S.; Kotte, T. R. R.; Sugiyama, M.; Liu, Z. K.; Park, C. α -SnSe Thin Film Solar Cells Produced by Selenization of Magnetron Sputtered Tin Precursors. *Sol. Energy Mater. Sol. Cells* **2018**, *176*, 251-258.
- (29) Wadhav, S.; Jadhav, Y.; Thakur, P. Synthesis of Metal-Free Phosphorus Doped Graphitic Carbon Nitride-P25 (TiO_2) Composite: Characterization, Cyclic Voltammetry and Photocatalytic Hydrogen Evolution. *Sol. Energy Mater. Sol. Cells* **2021**, *223*, 110958.

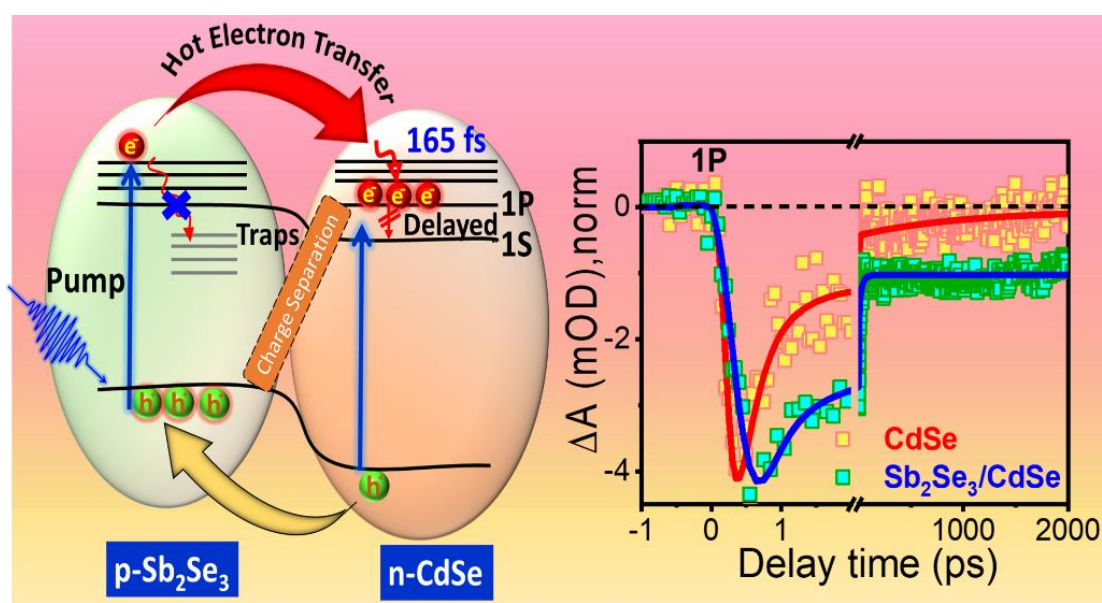
-
- (30) Vaughn, D. D.; In, S. II; Schaak, R. E. A Precursor-Limited Nanoparticle Coalescence Pathway for Tuning the Thickness of Laterally-Uniform Colloidal Nanosheets: The Case of SnSe. *ACS Nano* **2011**, *5*, 8852-8860.
- (31) Indirajith, R.; Rajalakshmi, M.; Gopalakrishnan, R.; Ramamurthi, K. Effects of Annealing on Thermally Evaporated SnSe Thin Films. *Ferroelectrics* **2011**, *413*, 108-114.
- (32) Li, X.; Song, Z.; Zhao, H.; Zhang, W.; Sun, Z.; Liang, H.; Zhu, H.; Pei, J.; Li, L.; Ruan, S. SnSe Nanosheets: From Facile Synthesis to Applications in Broadband Photodetections. *Nanomaterials* **2021**, *11*, 1-13.
- (33) Polovitsyn, A.; Dang, Z.; Movilla, J. L.; Martín-García, B. Mart, B.; Khan, A. H.; Bertrand, G. H. V.; Brescia, R.; Moreels, I. Synthesis of Air-Stable CdSe/ZnS Core – Shell Nanoplatelets with Tunable Emission Wavelength. *Chem. Mater.* 2017, *29*, 5671-5680.
- (34) Li, L.; Chen, Z.; Hu, Y.; Wang, X.; Zhang, T.; Chen, W.; Wang, Q. Single-Layer Single-Crystalline SnSe Nanosheets. *J. Am. Chem. Soc.* **2013**, *135*, 1213-1216.
- (35) Yang, L.; McCue, C.; Zhang, Q.; Uchaker, E.; Mai, Y.; Cao, G. Highly Efficient Quantum Dot-Sensitized TiO₂ Solar Cells Based on Multilayered Semiconductors (ZnSe/CdS/CdSe). *Nanoscale* **2015**, *7*, 3173-3180.
- (36) Kaur, A.; Goswami, T.; Babu, K. J.; Ghorai, N.; Kaur, G.; Shukla, A.; Rondiya, S. R.; Ghosh, H. N. Probing Ultrafast Charge Separation in CZTS/CdS Heterojunctions through Femtosecond Transient Absorption Spectroscopy. *J. Phys. Chem. C* **2020**, *124*, 19476-19483.
- (37) Eid, J.; Usman, A.; Gereige, I.; Van Duren, J.; Lyssenko, V.; Leo, K.; Mohammed, O. F. Ultrafast Pump-Probe Reflectance Spectroscopy: Why Sodium Makes Cu(In,Ga)Se₂ Solar Cells Better. *Sol. Energy Mater. Sol. Cells* **2015**, *140*, 33-37.
- (38) Pejjai, B.; Minnam Reddy, V. R.; Seku, K.; Pallavolu, M. R.; Park, C. Eco-Friendly Synthesis of SnSe Nanoparticles: Effect of Reducing Agents on the Reactivity of a Se-Precursor and Phase Formation of SnSe NPs. *New J. Chem.* **2018**, *42*, 4843-4853.
-

- (39) Patel, K.; Chauhan, P.; Patel, A.B.; Solanki, G.K.; Patel, K.D; Pathak, V.M. Orthorhombic SnSe Nanocrystals for Visible-Light Photodetectors. *ACS Appl. Nano Mater.* **2020**, *3*, 11143-11151.
- (40) Klimov, V. I. Spectral and Dynamical Properties of Multiexcitons in Semiconductor Nanocrystals. *Annu. Rev. Phys. Chem.* **2007**, *58*, 635-673.
- (41) Soloviev, V. N.; Eichhöfer, A.; Fenske, D.; Banin, U. Molecular Limit of a Bulk Semiconductor: Size Dependence of the “Band Gap” in CdSe Cluster Molecules. *J. Am. Chem. Soc.* **2000**, *122*, 2673-2674.
- (42) Okuhata, T.; Katayama, T.; Tamai, N. Ultrafast and Hot Electron Transfer in CdSe QD-Au Hybrid Nanostructures. *J. Phys. Chem. C* **2020**, *124*, 1099-1107.
- (43) Jasieniak, J.; Califano, M.; Watkins, S. E. Size-Dependent Valence and Conduction Band-Edge Energies of Semiconductor Nanocrystals. *ACS Nano* **2011**, *5*, 5888-5902.
- (44) Inamdar, S. N.; Ingole, P. P.; Haram, S. K. Determination of Band Structure Parameters and the Quasi-Particle Gap of CdSe Quantum Dots by Cyclic Voltammetry. *ChemPhysChem* **2008**, *9*, 2574-2579.
- (45) Markad, G. B.; Battu, S.; Kapoor, S.; Haram, S. K. Interaction between Quantum Dots of CdTe and Reduced Graphene Oxide: Investigation through Cyclic Voltammetry and Spectroscopy. *J. Phys. Chem. C* **2013**, *117*, 20944-20950.
- (46) Rondiya, S. R.; Jadhav, Y.; Dzade, N. Y.; Ahammed, R.; Goswami, T.; De Sarkar, A.; Jadkar, S.; Haram, S.; Ghosh, H. N. Experimental and Theoretical Study into Interface Structure and Band Alignment of the $\text{Cu}_2\text{Zn}_{1-x}\text{Cd}_x\text{SnS}_4$ Heterointerface for Photovoltaic Applications. *ACS Appl. Energy Mater.* **2020**, *3*, 5153-5162.
- (47) Rondiya, S.; Jadhav, Y.; Nasane, M.; Jadkar, S.; Dzade, N. Y. Interface Structure and Band Alignment of CZTS/CdS Heterojunction: An Experimental and First-Principles DFT Investigation. *Materials* **2019**, *12*, 4040.

- (48) Goswami, T.; Rani, R.; Hazra, K. S.; Ghosh, H. N. Ultrafast Carrier Dynamics of the Exciton and Trion in MoS₂ Monolayers Followed by Dissociation Dynamics in Au@MoS₂ 2D Heterointerfaces. *J. Phys. Chem. Lett.* **2019**, *10*, 3057-3063.
- (49) Kaur, G.; Justice Babu, K.; Ghorai, N.; Goswami, T.; Maiti, S.; Ghosh, H. N. Polaron-Mediated Slow Carrier Cooling in a Type-1 3D/0D CsPbBr₃@Cs₄PbBr₆ Core-Shell Perovskite System. *J. Phys. Chem. Lett.* **2019**, *10*, 5302-5311.
- (50) Ye, Y.; Xian, Y.; Cai, J.; Lu, K.; Liu, Z.; Shi, T.; Du, J.; Leng, Y.; Wei, R.; Wang, W.; Liu, X.; Bi, G.; Qiu, J. Linear and Nonlinear Optical Properties of Few-Layer Exfoliated SnSe Nanosheets. *Adv. Opt. Mater.* **2019**, *7*, 2-9.
- (51) Maiti, S.; Dana, J.; Jadhav, Y.; Debnath, T.; Haram, S. K.; Ghosh, H. N. Electrochemical Evaluation of Dopant Energetics and the Modulation of Ultrafast Carrier Dynamics in Cu-Doped CdSe Nanocrystals. *J. Phys. Chem. C* **2017**, *121*, 27233-27240.
- (52) Shukla, A.; Kaur, G.; Babu, K. J.; Ghorai, N.; Goswami, T.; Kaur, A.; Ghosh, H. N. Effect of Confinement on the Exciton and Biexciton Dynamics in Perovskite 2D Nanosheets and 3D-Nanocrystals *J. Phys. Chem. Lett.* **2020**, *11*, 6344-6352.
- (53) Debnath, T.; Maiti, S.; Maity, P.; Ghosh, H. N. Subpicosecond Exciton Dynamics and Biexcitonic Feature in Colloidal CuInS₂ Nanocrystals: Role of In-Cu Antisite Defects. *J. Phys. Chem. Lett.* **2015**, *6*, 3458-3465.

CHAPTER 5

Efficient Hot Electron Transfer and Extended Separation of Charge Carriers at the 1P Hot State in $Sb_2Se_3/CdSe$ p-n Heterojunction



J. Phys. Chem. Lett. 2022, 13, 48, 11354–11362

Abstract

Utilization of hot carriers is crucial in improving the efficiency of solar energy devices. In this work, we have fabricated $\text{Sb}_2\text{Se}_3/\text{CdSe}$ p-n heterojunction via the cation exchange method and investigated the possibility of hot electron transfer and relaxation pathways through ultrafast spectroscopy. The enhanced intensity of CdSe hot excitonic (1P) bleach in a heterostructure system confirmed the hot electron transfer from Sb_2Se_3 to CdSe. Both the 1S and 1P signals are dynamically very slow in the hetero-system, validating this charge migration phenomenon. Interestingly, the recovery of the 1P signal is much slower than that of 1S. This is very unusual as 1S is the lowest energy state. This observation indicates the strength of hot electron transfer in this unique heterojunction, which helps in increasing the carrier lifetime in the hot state. Extended separation of charge carriers and enhanced hot carrier lifetime would be extremely helpful in extracting carriers and boosting the performance of optoelectronic devices.

5.1. Introduction

To address the issue of rising global energy demands, the utilization of renewable and clean solar energy is highly required.¹ Recently, quantum dots (QDs) heterostructure have emerged as promising candidates for next-generation solar cells as they exhibit unique properties such as broad absorption coefficient, tunable bandgap, and multiple exciton generation with single photon absorption.^{2,3} In addition, quantum dot solar cells (QDSCs) present a theoretically predicted power conversion efficiency (PCE) of 45% in a single-junction QDSC and up to 66% in a multiple-junction QDSC as a result of efficient multiple-exciton generation and hot-electron extraction, with the potential to exceed the Shockley- Queisser limit.⁴⁻⁶ Recently, antimony chalcogenides (Sb_2X_3 , X=S, Se) QD-based heterostructures have attracted overwhelming attention as light harvesters in the field of photovoltaic and photocatalytic applications.^{7,8} Sb_2Se_3 is a p-type semiconductor having fascinating properties such as low toxicity⁹ and cost¹⁰, high abundance, high chemical stability¹¹, high absorption coefficient (10^5 cm^{-1})¹², narrow band gap (1.1-1.3 eV), and considerable carrier mobility ($\sim 10 \text{ cm}^2\text{V}^{-1}\text{s}^{-1}$).¹³ Until now, the highest PCE of Sb_2X_3 , (X=S, Se) solar cells has been reported to be 7.5% and 9.2% respectively^{14,15}, which is far below the theoretically predicted efficiency of 32% for Sb_2X_3 , (X=S, Se) based solar cells. This is due to the presence of a high concentration of interfacial defect states, which results in fast trapping and recombination of the charge carriers in the Sb_2X_3 materials.¹⁶ Also, the excessive energy of carriers greater than the bandgap of the semiconductor is lost to heat due to the rapid cooling of hot carriers through the emission of phonons. Extraction of these hot carriers is considered to be a promising way to overcome this loss. To resolve all these issues, the fabrication of heterojunction with type II band alignment of semiconductors has been considered to be a convincing method as it offers broad wavelength tunability, better separation and extraction of charge carriers and their longer lifetime, thus suppressing the deleterious recombination rate of the photogenerated electron and hole.¹⁷ With this approach, charge carriers can be spatially separated in the heterojunction as a result of decreases in coulombic interaction between electrons and holes. It facilitates the transport of the charge carriers that can be efficiently extracted and utilized which is essential for the betterment of device performance.¹⁸ The heterojunction of Sb_2Se_3 with CdSe has attained enormous attention which we have synthesized via low-cost cation exchange

method. Cation exchange is an effective technique to synthesize heterostructures as it provides proper band alignment, adjustable shape, and size by changing the constituents and experimental conditions.¹⁹⁻²¹ CdSe is a wide bandgap n-type semiconductor which is widely used for optoelectronic applications. However, owing to the fast recombination of charge carriers and toxicity of CdSe,²²⁻²³ it is important to make its heterostructure with less toxic and p-type Sb₂Se₃ semiconductor to improve the charge separation and reduce the toxicity. It forms a type II band structure with p-type Sb₂Se₃ resulting in the formation of a p-n junction which is helpful for efficient spatial separation of photoinduced electron-hole pairs due to in-built electric fields that are favourable for the improved performance of QDs-based photovoltaic devices. Earlier Wang et al. reported the synthesis of ZnSe/Sb₂Se₃ hollow microspheres coated by nitrogen-doped carbon with enhanced sodium ion storage capability using the cation exchange method.²⁴ There are few reports available on Sb₂Se₃/CdSe-based solar cells but the efficiency is far less than the theoretically predicted limit.² Guo et al., reported the improved efficiency of 4.5% for Sb₂Se₃/CdSe solar cells.²⁵ To further improve the performance of the device, it is of utmost importance to understand the fundamental properties of the photogenerated electron and hole pairs at the interface like interfacial charge transfer, carrier trapping, relaxation, and recombination process. However, to the best of our knowledge, these studies have not been explored in detail for Sb₂Se₃/CdSe p-n heterojunction.

In this chapter, we have successfully synthesized Sb₂Se₃/CdSe p-n heterojunction and investigated the charge transfer and relaxation mechanism through femtosecond transient absorption (TA) spectroscopy. TA studies reveal the transfer of hot electrons from Sb₂Se₃ to CdSe, resulting in extensive charge separation at the hot CdSe states. Our study confirmed the efficient spatial separation of the electrons and holes at the interface of Sb₂Se₃ and CdSe which is highly desired for the efficient performance of any photovoltaic and photocatalytic device.

5.2. Results and discussion

5.2.1. Synthesis and characterizations

The synthesis of Sb₂Se₃/CdSe heterostructure was carried out via partial cation exchange of pre-synthesized CdSe QDs with Sb³⁺ cations. In the presence of excess Sb³⁺ ions, the CdSe quantum dots are completely converted into Sb₂Se₃. The overall

method to fabricate $\text{Sb}_2\text{Se}_3/\text{CdSe}$ heterostructure and pure Sb_2Se_3 QDs from CdSe QDs is illustrated in **Figure 5.1**. Briefly, CdSe QDs are prepared via the facile hot injection method as reported in our previous work. Next, $\text{Sb}_2\text{Se}_3/\text{CdSe}$ heterostructure is synthesized via a partial cation exchange reaction during which the Sb^{3+} cations substitute for Cd^{2+} . Initially, the Cd^{2+} ion is exchanged with the Sb^{3+} ion, which results in the charge imbalance in the CdSe QDs. To balance the charge on the QD surface, more Cd^{2+} ions diffused out from the QD surface to balance the overall charge of CdSe, which leads to the formation of more Cd^{2+} vacancies in the CdSe QDs.

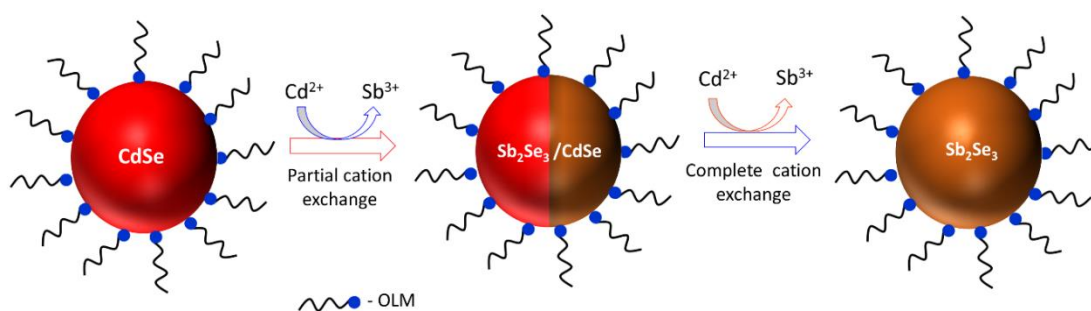


Figure 5.1. Schematic diagram illustrating the synthetic process of $\text{Sb}_2\text{Se}_3/\text{CdSe}$ heterostructure and Sb_2Se_3 from CdSe QDs.

Simultaneously, Sb^{3+} ions entering the CdSe host lattice react with the neighbouring Se^{2-} ions to form Sb_2Se_3 . The sufficient concentration of Sb^{3+} ion leads to the insertion of more Sb^{3+} ions which will force more Cd^{2+} ions to detach out of CdSe QDs surface. So, a cascade of reactions is started at one side of the CdSe QD surface, resulting in the formation of the $\text{Sb}_2\text{Se}_3/\text{CdSe}$ heterostructure.²⁶ Furthermore, an excess amount of Sb^{3+} cations results in the complete conversion of CdSe QDs resulting in the formation of Sb_2Se_3 QDs as shown in **Figure 5.1**. The cationic radii of Sb^{3+} and Cd^{2+} are similar and therefore helpful to accelerate the cation exchange reaction. Transmission electron microscopy (TEM) and high-resolution transmission electron microscopy (HRTEM) analysis were carried to find out the morphology and size of pure CdSe, pure Sb_2Se_3 , and $\text{Sb}_2\text{Se}_3/\text{CdSe}$ heterostructure. The representative TEM images of the prepared samples are displayed in **Figure 5.2**. TEM images of CdSe and Sb_2Se_3 QDs (**Figure 5.2 A, B**) reveal the uniform size of particles with an average diameter of ~ 3.8 nm as calculated from the size distribution histogram (**Figure 5.3**) which is consistent with the earlier reports.²⁷ As shown in **Figure 5.2C**, $\text{Sb}_2\text{Se}_3/\text{CdSe}$ hetero-structure exhibits spherical morphology as that of CdSe

indicating that the structure and size are well retained during the cation exchange process. The TEM image displays an average diameter of ~ 4 nm for $\text{Sb}_2\text{Se}_3/\text{CdSe}$ QDs. The slight increase in size of CdSe is due to the formation of hetero-structure with Sb_2Se_3 . Further, HRTEM images of the heterojunction clearly indicate that the Sb_2Se_3 and CdSe phases having clear interface as indicated in **Figure 5.2F**.

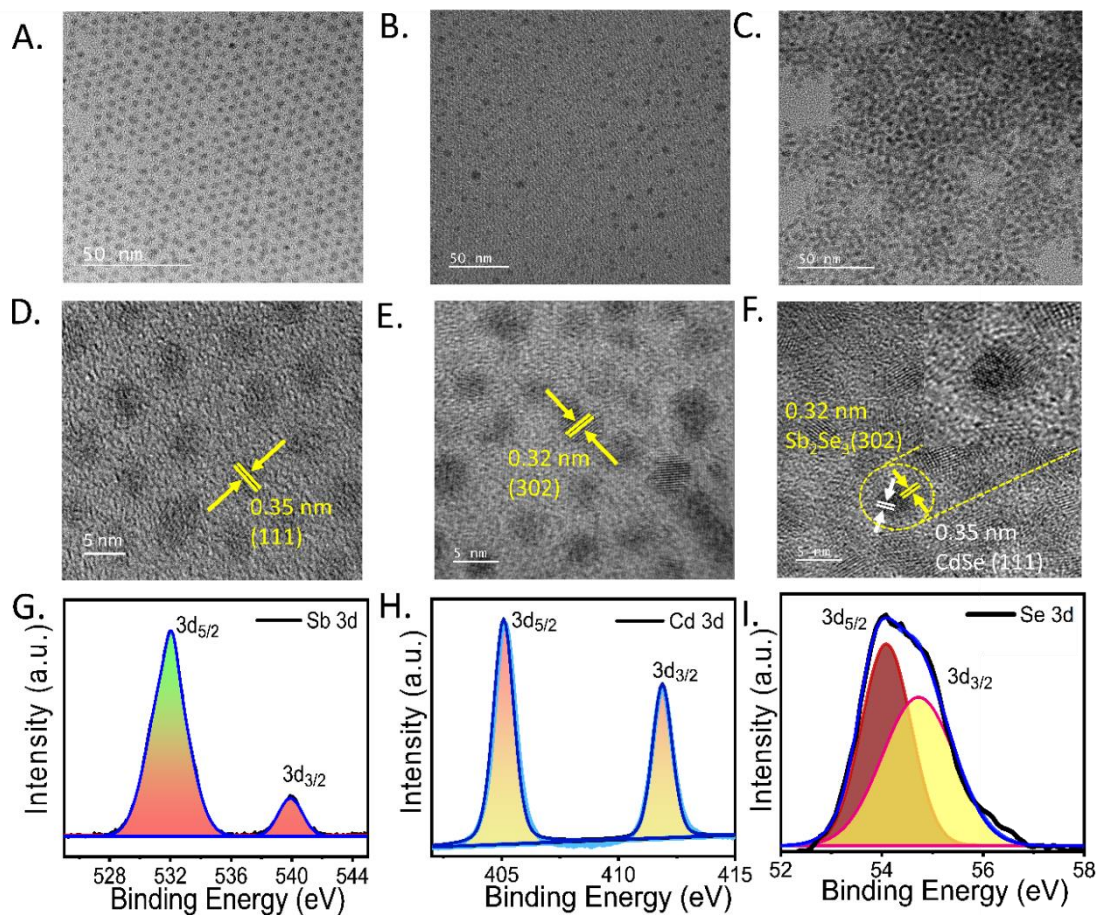


Figure 5.2. TEM and HRTEM images of bare CdSe QDs (**A, D**); Sb_2Se_3 QDs (**B, E**); $\text{Sb}_2\text{Se}_3/\text{CdSe}$ heterostructure (**C, F**); inset of Figure 5.2F: enlarged view of $\text{Sb}_2\text{Se}_3/\text{CdSe}$ heterostructure. XPS analysis of $\text{Sb}_2\text{Se}_3/\text{CdSe}$ heterostructure: high-resolution scan of (**G**) Sb 3d_{5/2}, 3d_{3/2} (**H**) Cd 3d_{5/2}, 3d_{3/2}, (**I**) Se 3d_{5/2}, Se 3d_{3/2} signals.

The lattice fringes with an interplanar spacing of 0.32 nm and 0.35 nm, are assigned to (302) crystal plane of orthorhombic Sb_2Se_3 and (111) plane of cubic CdSe QDs, respectively. This type of intimate interfacial contact is helpful for the charge transfer at the interface between Sb_2Se_3 and CdSe QDs. Because of the small lattice mismatch between the two crystal lattice planes of Sb_2Se_3 and CdSe QDs, there is a high possibility of epitaxial growth of Sb_2Se_3 over CdSe QDs resulting in the formation of $\text{Sb}_2\text{Se}_3/\text{CdSe}$ hetero-structure as revealed by HRTEM images. Moreover,

the presence of Sb_2Se_3 in the $\text{Sb}_2\text{Se}_3/\text{CdSe}$ heterostructures has been established through X-ray photoelectron spectroscopy (XPS), and the elemental chemical states and binding energies of the elements were probed.

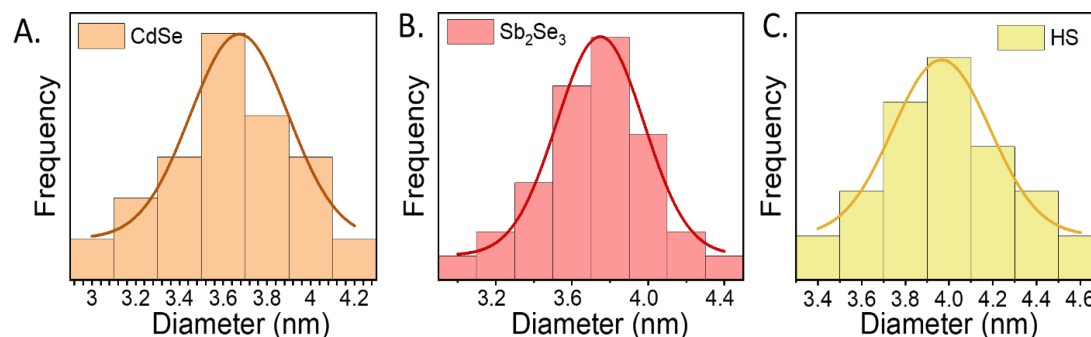


Figure 5.3. Particle size distribution of (A) CdSe QDs, (B) Sb_2Se_3 QDs, and (C) $\text{Sb}_2\text{Se}_3/\text{CdSe}$ heterostructure.

A high-resolution XPS study clearly confirms all Sb, Cd, and Se elements in the heterostructure. The high-resolution scan of Cd 3d is shown in **Figure 5.2H**. The binding energies of Cd 3d in heterojunction measured at ~ 405.1 and 411.9 eV, attributed to Cd $3d_{5/2}$ and Cd $3d_{3/2}$ respectively. **Figure 5.2G** exhibited two significant peaks at 532 and 540 eV, which can be assigned to $3d_{3/2}$ and $3d_{5/2}$ orbitals of Sb, respectively. The core level Se $3d_{5/2}$ and Se $3d_{3/2}$ peaks are located at 53.8 and 54.7 eV (**Figure 5.2I**) indicating the presence of Se in the 2- oxidation state. All the detected binding energy values are well-matched with the previous reports.²⁸⁻³⁰ The detailed XPS measurements of pristine CdSe and Sb_2Se_3 QDs have been provided in **Figure 5.4** and **Figure 5.5**, respectively.

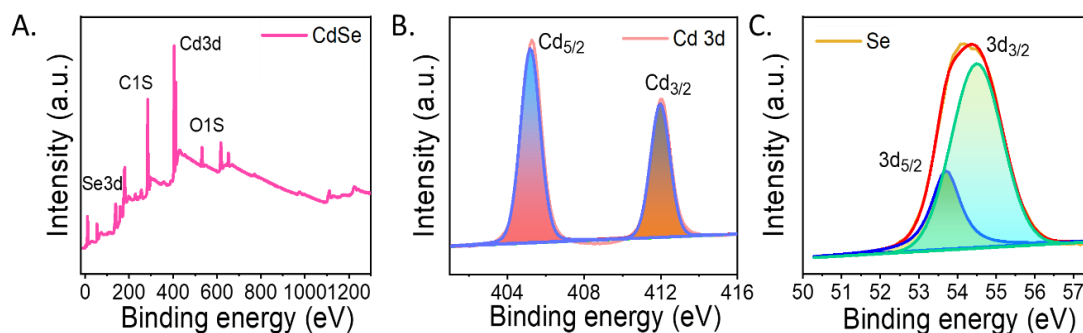


Figure 5.4. (A) XPS survey spectra and high resolution XPS spectra of (B) Cd $3d_{5/2}$, $3d_{3/2}$ (C) Se 3p signals for CdSe sample.

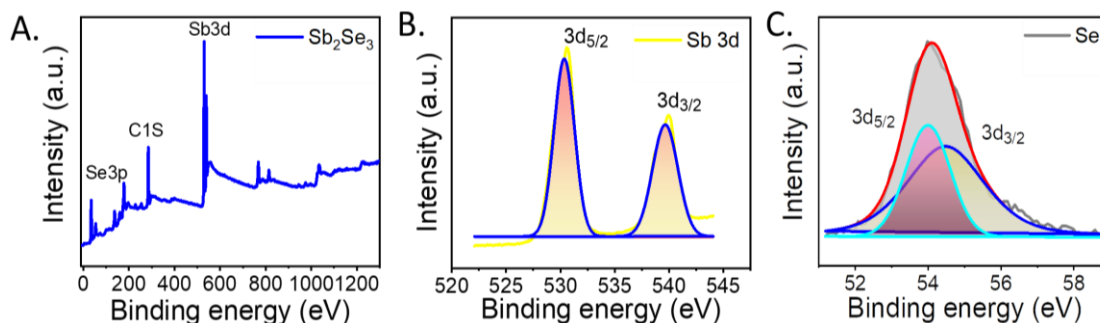


Figure 5.5. XPS survey spectra of (A) Sb_2Se_3 QDs, high-resolution XPS scan of (B) Sb 3d, and (C) Se 3d, signals for Sb_2Se_3 QDs.

The composition of the heterostructure was verified by energy dispersive X-ray spectroscopy (EDX) attached to TEM. The EDX spectroscopic images of $\text{Sb}_2\text{Se}_3/\text{CdSe}$ hetero-structure show incorporation of Sb as shown in **Figure 5.6**. The crystal structure of the as-prepared Sb_2Se_3 , CdSe QDs, and $\text{Sb}_2\text{Se}_3/\text{CdSe}$ heterostructure system are determined using the powder X-ray powder diffraction (XRD). The XRD pattern of bare CdSe QDs, Sb_2Se_3 QDs, and $\text{Sb}_2\text{Se}_3/\text{CdSe}$ heterostructure are shown in **Figure 5.7**. The CdSe QDs show diffraction peaks at 25.1° , 45.2° , 53.6° , and 65.9° , which are well consistent with the (111), (220), (311), and (331) crystal planes of zinc blende phase of CdSe (JCPDS No: 00-019-0191) as indicated in **Figure 5.7Aa**.³¹ The XRD pattern of Sb_2Se_3 QDs (**Figure 5.7Ab**) demonstrate its orthorhombic crystal structure³² (JCPDS No. 15-0861) with lattice constants $a=11.79$, $b=3.985$, $c=11.64$. The diffraction peaks at $2\theta \sim 23.7^\circ$, 27.4° , 31.7° , 34.12° , 38.5° , 41.2° , 45.19° , 54.79° , 56.8° , 58.9° , 63.8° , 67.09° , 68.6° , 73.7° , 76.3° have been indexed to the (011), (302), (104), (204), (304), (502), (115), (322), (406), (422), (704), (620), (714), (517), and (814) diffraction planes of Sb_2Se_3 QDs. The XRD peaks of $\text{Sb}_2\text{Se}_3/\text{CdSe}$ heterojunction shown in **Figure 5.7Ac** comprises planes of both orthorhombic Sb_2Se_3 as well as cubic CdSe, which clearly confirms the formation of heterostructure between Sb_2Se_3 and CdSe QDs. No impurity peaks related to Cd, Se, and Sb were found in the heterostructure, which indicates the formation of high purity $\text{Sb}_2\text{Se}_3/\text{CdSe}$ heterostructure.

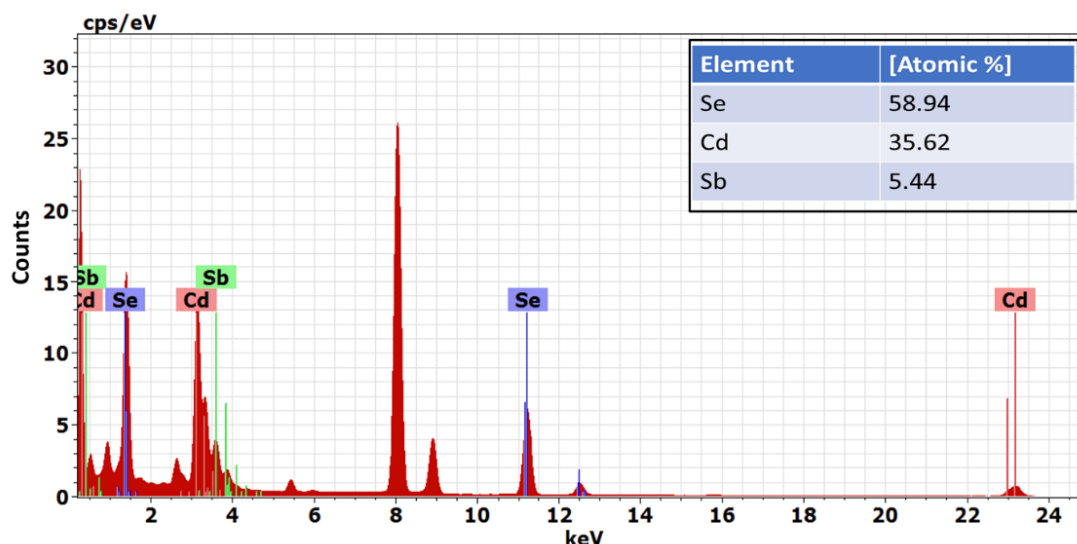


Figure 5.6. Energy dispersive X-ray spectrum of $\text{Sb}_2\text{Se}_3/\text{CdSe}$ heterostructure. Inset: Observed atomic percentage of Sb, Cd, and Se.

5.2.2. Optical studies

The optical properties of the as-prepared materials have been explored by UV-VIS absorption spectroscopy. **Figure 5.7B** illustrates the absorption spectra of Sb_2Se_3 QDs, CdSe QDs, and $\text{Sb}_2\text{Se}_3/\text{CdSe}$ heterojunction in toluene. The CdSe QDs exhibit discrete excitonic peaks at 563 nm and 454 nm, attributed to $1\text{S}_{3/2}(\text{h})-1\text{S}(\text{e})$, 1S and $1\text{P}_{1/2}(\text{h})-1\text{P}(\text{e})$, 1P electronic transitions.³³ The steady-state optical absorption spectrum of Sb_2Se_3 displays a broad absorption in the range of 300-800 nm.³⁴ We did not observe any distinguishable peak for Sb_2Se_3 due to the absence of quantum confinement as a result of a small Bohr exciton radius.³⁵ To find the bandgap of Sb_2Se_3 , a tauc plot was performed, and the band gap was determined to be 1.5 eV as shown in **Figure 5.7B inset**. Bandgap values were determined by extrapolating the linear region of the higher photon energy to the x-axis ($\alpha = 0$). The calculated bandgap is found to be more than the reported bulk bandgap of 1.1-1.2 eV, this might be due to a decrease in the size of the particles. In the presence of Sb_2Se_3 , it is observed that the lowest exciton band of CdSe QDs is red-shifted from 563 nm to 587 nm and its photoluminescence (PL) band shifts from 587 nm to 601 nm in the heterostructure.^{36, 37} The redshift is attributed to decrease in confinement and additional strain due to the growth of Sb_2Se_3 on the seed CdSe.

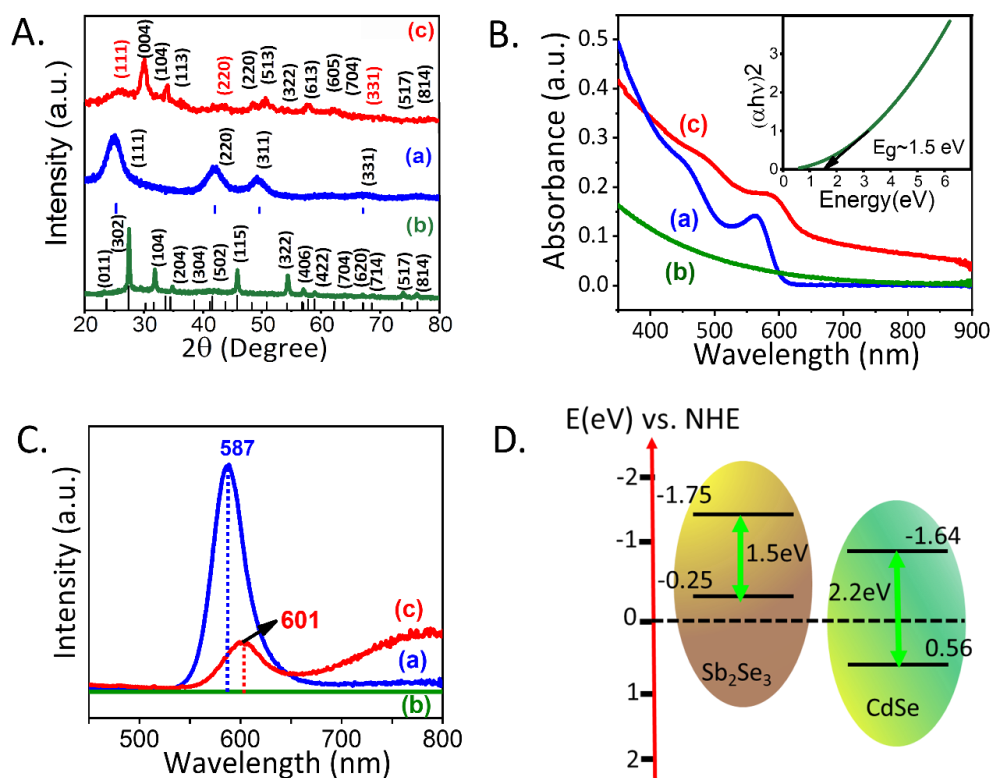


Figure 5.7. (A) Powder X-ray diffraction pattern of (a) CdSe QDs, (b) Sb_2Se_3 QDs, and (c) $\text{Sb}_2\text{Se}_3/\text{CdSe}$ heterostructure; JCPDS lines are also specified; (B) Steady-state optical absorption spectrum of (a) CdSe QDs, (b) Sb_2Se_3 QDs, and (c) $\text{Sb}_2\text{Se}_3/\text{CdSe}$ heterostructure; **Inset:** tauc plot of Sb_2Se_3 ; (C) Steady-state PL spectra of (a) CdSe QDs, (b) Sb_2Se_3 QDs, and (c) $\text{Sb}_2\text{Se}_3/\text{CdSe}$ heterostructure, upon 400 nm photoexcitation; (D) Energy level positions of Sb_2Se_3 QDs and CdSe QDs as calculated from both the XPS spectra and the Tauc plot.

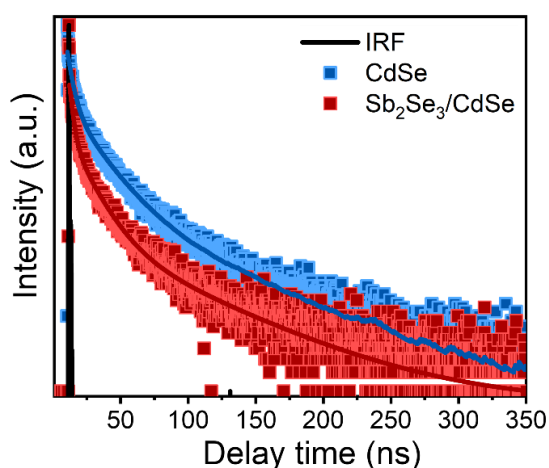


Figure 5.8. Time-resolved photoluminescence (PL) measurements for CdSe and $\text{Sb}_2\text{Se}_3/\text{CdSe}$ heterostructure after exciting the samples at 402 nm and lifetime is monitored at 587 nm and 601 nm for CdSe QDs and $\text{Sb}_2\text{Se}_3/\text{CdSe}$ heterostructure, respectively.

Table 5.1: Fitting components of time-resolved luminescence for CdSe QDs and Sb₂Se₃/CdSe heterostructure monitored at 587 nm and 601 nm, respectively upon 402 nm excitation.

System	τ_1 (ns)	A ₁ (%)	τ_2 (ns)	A ₂ (%)	τ_3 (ns)	A ₃ (%)	τ_{avg} (ns)	χ^2
CdSe QDs (587 nm)	10	19.85	32	65.34	142	14.8	22	1.18
Sb₂Se₃/CdSe Heterostructure (601 nm)	1.25	21.69	9.67	39.72	55.8	38.59	5	1.15

Table 5.2. Summarized Data for XPS valence band spectra and the Band Structure Parameters (VB vs NHE, CB vs NHE, VB vs Vacuum (Vac), CB vs Vac, and (E_g) Bandgap).

Sample	VB vs NHE	CB vs NHE	VB vs Vac	CB vs Vac	E _g (eV)
Sb₂Se₃	-0.25	-1.75	-4.25	-3.75	1.5
CdSe	0.56	-1.64	-5.06	-2.86	2.2

Moreover, the presence of Sb₂Se₃ results in an increased absorption of CdSe in Sb₂Se₃/CdSe in the near-infrared (NIR) region, suggesting strong interaction between Sb₂Se₃ and CdSe in the heterojunction. The corresponding steady-state PL emission spectra of bare Sb₂Se₃ and CdSe quantum dots as well as Sb₂Se₃/CdSe heterostructure are shown in **Figure 5.7C**. CdSe QDs exhibit a PL peak at 587 nm, which corresponds to the bandedge or excitonic emission having a small full width at half maximum of 18 nm, indicating the formation of monodisperse QDs. The sharp PL in CdSe QDs is due to the radiative recombination of photogenerated bandedge electron and hole pairs. The PL intensity of CdSe QDs is greatly quenched in the presence of Sb₂Se₃, attributed to the transfer of holes from the valence band (VB) of CdSe to

VB of Sb₂Se₃ which is a thermodynamically feasible process according to the type II band alignment of Sb₂Se₃/CdSe heterostructure as shown in **Figure 5.7D**. We did not find any PL emission peak from bare Sb₂Se₃ QDs in the given spectral region. The absence of excitonic emission in Sb₂Se₃ is due to the presence of anionic surface which acts as a trap for the charge carriers.³² Apart from CdSe excitonic PL, the spectra of heterostructure show an additional broad peak in the range 680-800 nm, which can be attributed to defect-induced PL.³⁸

To monitor the hole transfer process, the lifetime is monitored at PL maxima for both pure CdSe and $\text{Sb}_2\text{Se}_3/\text{CdSe}$ heterostructure systems using a time-correlated single photon counting (TCSPC) system as shown in **Figure 5.8**. The average lifetime of CdSe QDs gets reduced from 22 ns to 5 ns in the presence of Sb_2Se_3 in $\text{Sb}_2\text{Se}_3/\text{CdSe}$ heterostructure (Fitting components in **Table 5.1**), ascribed to the transfer of photo-excited holes from CdSe to Sb_2Se_3 which is a thermodynamically favourable process. The PL quantum yield (PLQY) of CdSe and $\text{Sb}_2\text{Se}_3/\text{CdSe}$ QDs is calculated to be 25% and <1%, respectively. In **Figure 5.7D**, we presented the relative band structure positions of Sb_2Se_3 and CdSe QD systems with the help of UV-VIS absorption and XPS spectra. The valence band maximum (VBM) positions of the Sb_2Se_3 and CdSe QDs are found to be -0.25 and 0.56 eV, respectively, as determined from extrapolation of the onset in the XPS valence band spectra (**Figure 5.9**). The conduction band minima (CBM) of the Sb_2Se_3 and CdSe QDs were calculated to be -1.65, and -1.64 eV, respectively, combining the optical band gap and the VBM position (**Table 5.2**). Based on the above investigation, the possible energy band structure between Sb_2Se_3 and CdSe forms the type II band alignment as shown in **Figure 5.7D**.

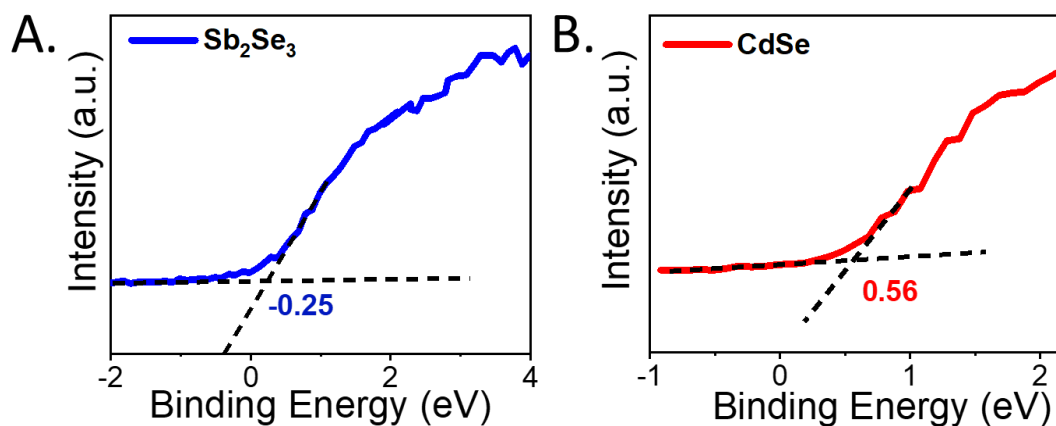


Figure 5.9. Determination of valence band positions of (A) Sb_2Se_3 QDs and (B) CdSe QDs from the XPS valence band spectra.

5.2.3. Transient absorption studies

To elucidate the photophysics of excited charge carriers such as cooling, charge trapping and transfer as well as charge recombination pathways involved at the junction between Sb_2Se_3 and CdSe QDs on an ultrafast time scale, the femtosecond transient absorption spectroscopy has been employed.³⁹ The transient absorption

technique is a powerful tool to monitor the excited state dynamics of single QDs as well as heterostructure systems.⁴⁰⁻⁴³ Such a detailed analysis can assist in achieving an understanding of the different photophysical processes involved and possible transfer mechanisms, namely, the charge-transfer route at the interface that also governs their future applications. The TA spectra of Sb_2Se_3 , CdSe QDs, as well as $\text{Sb}_2\text{Se}_3/\text{CdSe}$ heterostructure, have been recorded in the visible region. All the experimental conditions were kept the same throughout the experiments. **Figure 5.10(A)** shows the differential absorption spectra of the Sb_2Se_3 QDs after photo-excitation with 410 nm laser pulse as a function of different pump-probe delay times. The transient spectra show a positive absorption band in the 500-675 nm region with a peak around 605 nm. The positive signal that appears in the transient absorption spectra of the Sb_2Se_3 QDs can be attributed to the trapped charge carriers (both electrons and holes).⁴⁴

It is found that no transient bleach is observed in pure Sb_2Se_3 , due to the high density of trap states in the Sb_2Se_3 QDs. In our earlier investigations, we detected similar kinds of photo-induced absorption (PIA) for Sb_2Se_3 film resulting from the presence of different kinds of traps in the system.⁴⁵ The kinetic data can be fitted multi-exponentially as shown in **Figure 5.10D**, and the fitting parameters are given in the supporting information (**Table 5.3**). The growth kinetics for Sb_2Se_3 QDs at 605 nm is fitted with a single exponential component which is instrument response function (IRF) limited and decay kinetics is fitted multi-exponentially with time components of 4 ps, 22 ps, and >1ns. The decay dynamics of the transient absorption signal can be attributed to the trapping and recombination dynamics of the photo-generated charge carriers. The TA spectra of the photoexcited pristine CdSe QDs and $\text{Sb}_2\text{Se}_3/\text{CdSe}$ heterostructure at different time delays are shown in **Figure 5.10 (B, C)**. On comparing the TA spectrum of $\text{Sb}_2\text{Se}_3/\text{CdSe}$ with that of CdSe, we observed some interesting spectral differences.

The TA spectra of CdSe show three distinct features, two photobleaching signals with maxima at 563 nm and 470 nm, attributed to bandedge (1S) and hot state (1P) excitonic bleaches as discussed in the steady state absorption spectra, and a positive absorption signal in the red region after 563 nm bleach ascribed to stark induced biexciton effect.⁴⁶⁻⁴⁸

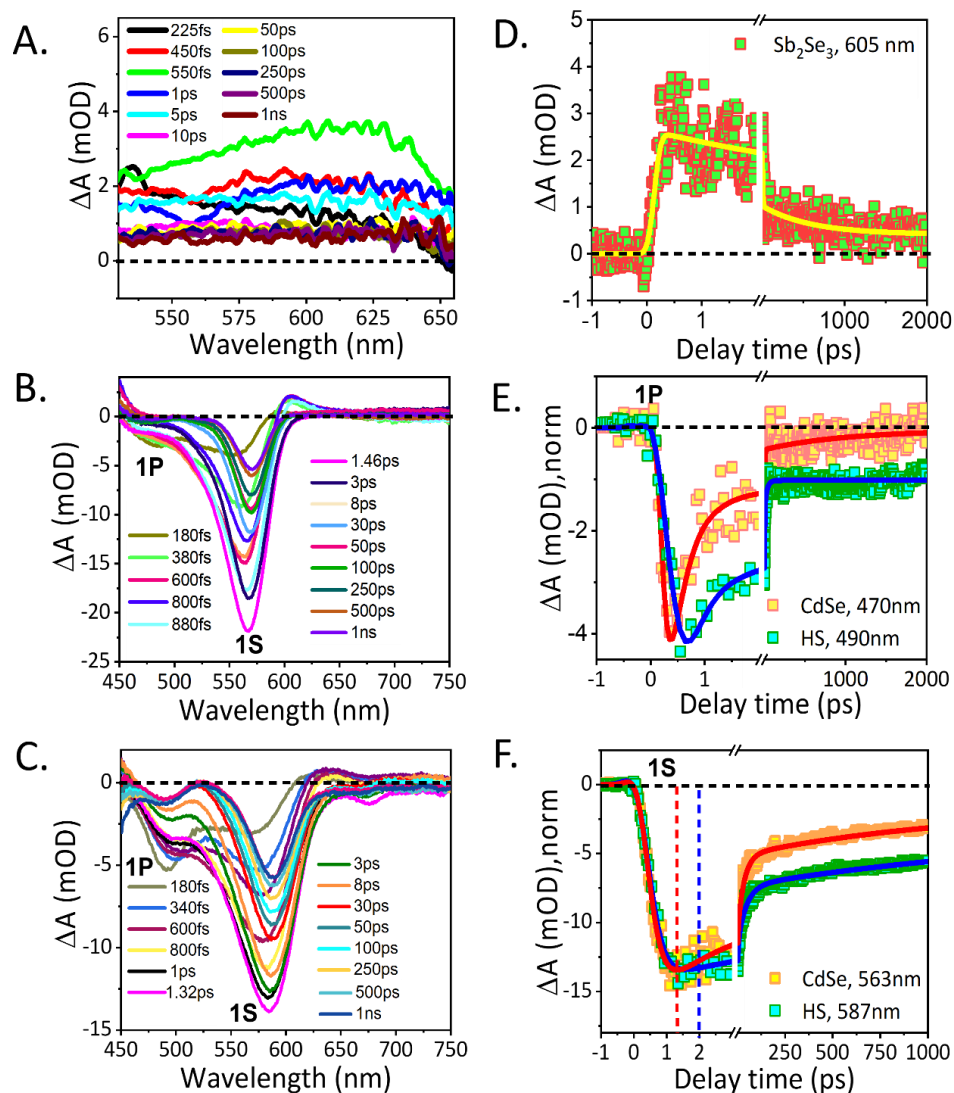


Figure 5.10. Transient absorption spectra of (A) Sb₂Se₃ QDs, (B) CdSe QDs, and (C) Sb₂Se₃/CdSe hetero-structure at different probe delay following photoexcitation of a 410 nm. laser pulse with $200 \mu\text{J}/\text{cm}^2$ laser fluence; (D) Transient decay kinetics of photo-induced absorption signal of Sb₂Se₃ QDs monitored at 605 nm; (E) Bleach recovery kinetics of 1P excitonic bleach at 470 and 490 nm for CdSe QDs and Sb₂Se₃/CdSe heterostructure respectively; and (F) Bleach recovery kinetics of 1S excitonic bleach at 563 and 587 nm for CdSe QDs and Sb₂Se₃/CdSe heterostructure respectively.

To follow the charge carrier dynamics, carrier cooling, charge transfer, and recombination dynamics, we have carried out the temporal analysis of pure CdSe QDs, Sb₂Se₃ QDs as well as Sb₂Se₃/CdSe heterostructure systems at different wavelengths. We have monitored the transient decay kinetics at both bandedge (1S) and hot exciton (1P) bleach for bare CdSe and Sb₂Se₃/CdSe heterostructure upon

photoexcitation with 410 nm pump pulse and are shown in **Figure 5.10 (E) and (F)**, respectively.

Table 5.3. Kinetic fitting parameters of PIA signal of Sb_2Se_3 QDs, excitonic bleach, and bi-excitonic position for CdSe QDs and $\text{Sb}_2\text{Se}_3/\text{CdSe}$ heterostructure system upon 410 nm pump excitation with $200\mu\text{J}/\text{cm}^2$ laser fluence.

System	τ_g	τ_1	τ_2	τ_3
Sb_2Se_3 (612nm)	<100fs (100%)	4ps (62.7%)	22ps (17.3%)	>1ns (20%)
CdSe (1S)	0.34ps (-100%)	8ps (48.5%)	123ps (23.5%)	>1ns (28%)
$\text{Sb}_2\text{Se}_3/\text{CdSe}$ Heterostructure (1S)	0.5 ps (-100%)	10ps (50%)	150ps (13.5%)	>1ns (36.5%)
CdSe (1P)	<100fs (-100%)	3ps (86%)	60ps (8%)	>1ns (6%)
$\text{Sb}_2\text{Se}_3/\text{CdSe}$ Heterostructure (1P)	165fs (-100%)	5ps (70%)	100ps (5.8%)	>1ns (24.2%)

The transient kinetics at 1S bleach of CdSe is fitted with single exponential growth with a time constant of 0.34 ps and multi-exponential decay listed in **Table 5.3**. The 1P bleach of CdSe is fitted with a fast growth time which is IRF limited.

Now to understand the carrier dynamics of the photo-excited carriers involved across the p-n junction of $\text{Sb}_2\text{Se}_3/\text{CdSe}$ heterostructure at an ultrafast time scale, we have monitored the kinetics of the bleaches at 587 nm (1S), 490 nm (1P) in heterostructure system and compared with that of bare CdSe QDs. The decay kinetics of CdSe in heterostructure is significantly affected in the presence of Sb_2Se_3 . **Figure 5.10 (E)** shows the kinetics of hot exciton (1P) bleach of CdSe QDs in the presence and absence of Sb_2Se_3 . It is interesting to observe that the intensity of 1P bleach of CdSe increased almost two times in the presence of Sb_2Se_3 , moreover, it becomes broad as compared to 1P bleach of CdSe QDs (**Figure 5.10B and 5.10C**). This can be attributed to the delocalization/transfer of photogenerated hot electrons from the upper excitonic states of Sb_2Se_3 to the 1P hot state of CdSe. There is a competition between the hot electron transfer and the trapping process in the $\text{Sb}_2\text{Se}_3/\text{CdSe}$ heterostructure. It is found that the growth of 1P bleach of $\text{Sb}_2\text{Se}_3/\text{CdSe}$ heterostructure is 165 fs

which is found to be slower as compared to the growth of pure CdSe QD (<100 fs). As the growth is assigned to charge carrier cooling from upper excitonic states to the conduction band edge, so here, the observed slower growth and increase in intensity of 1P bleach in the $Sb_2Se_3/CdSe$ heterostructure system clearly suggests that instead of trapping in the defect states present in Sb_2Se_3 QDs, the hot electrons get transferred from photo-excited states of Sb_2Se_3 to hot state of CdSe as the relative population of carriers in hot state of CdSe is much higher in heterojunction as compared to bare CdSe. Thus, the hot electron transfer at the $Sb_2Se_3/CdSe$ interface is more dominant than the trapping process. The decay of transient bleach has been fitted multi-exponentially with time constants provided in the supporting information (**Table 5.3**). We have observed slow recovery of 1P and 1S bleach of CdSe in the presence of Sb_2Se_3 as compared to that of pure CdSe QDs as shown in **Figure 5.10E**. Recovery of 1S and 1P bleach portrays the depopulation of bandedge and excited state electrons. The signal intensity of 1P bleach does not decay even after 2 ns. The slow recovery of 1P bleach is attributed to the spatial separation of photogenerated charge carriers as a result of the decoupling of electrons and holes in the heterojunction, the electron being in CdSe and the hole in Sb_2Se_3 . Since, coulombic interaction between electrons and holes decreases and they recombine slowly, as a result, the hot carriers in the 1P state of CdSe have a longer lifetime in the presence of Sb_2Se_3 , thus these hot carriers can be extracted and are crucial for the improvement of efficiency of any device as shown in **Scheme 5.1**. Similarly, we have observed the slower growth of 1S bleach in $Sb_2Se_3/CdSe$ heterostructure with a growth time constant of 500 fs and 340 fs in the presence and absence of Sb_2Se_3 , respectively. Besides this, slow decay of 1S bleach was observed in the heterostructure system as shown in **Figure 5.10F**. This slow decay time of hot carriers could be crucial for any photonic devices as now the charge carriers can be easily extracted and would improve the performance of the devices.

Near band edge excitation: We have further excited the samples on the lower-energy side (pump wavelength ~750 nm, energy ~1.65eV), keeping the density of injected carriers the same as that of 410 nm pump excitation. At this pump wavelength, CdSe does not get excited (the band gap of CdSe QDs ~2.2 eV), however electrons and holes are generated in the Sb_2Se_3 domain as the energy of the pump is higher as compared to the bandgap of Sb_2Se_3 ($E_g = 1.5$ eV). **Figure 5.11A, B** shows the TA spectra of $Sb_2Se_3/CdSe$ heterostructure upon 750 nm pump excitation and transient

kinetic trace monitored at 587 nm probe wavelength. The appearance of instantaneous broad bleach (530-640 nm) clearly confirms the transfer of electrons from the Sb_2Se_3 to the CdSe domain in the heterostructure which is a thermodynamically feasible process according to the band alignment (**Figure 5.7D**) and fitting components for bleach are given in **Table 5.4**. The bleach in the region between 530-640 nm appears possible only when the electrons are present at bandedge states of CdSe. The recovery of heterostructure bleach is faster for 750 nm photoexcitation as compared to when excited with 410 nm pump excitation. This observation can be attributed to the fact that two channels are available for electrons. The electrons can migrate from Sb_2Se_3 to CdSe band edge states but also there is a possibility of their trapping in defect states present in Sb_2Se_3 as well as at the interface. The positive signal with a peak at 486 nm is attributed to the trapped carriers. As the electrons upon 750 nm, photoexcitation has lower energy and are excited to near bandedge, lying close to the trap states, so the possibility of trapping of electrons is higher upon 750 nm photoexcitation as compared to when excited with 410 nm pump pulse. Here, we did not get excited state bleach (1P) of CdSe, as the energy of the 750 nm pump is not enough to generate excessive hot carriers which otherwise is possible for 410 nm pump excitation. This observation clearly indicates the transfer of electrons from Sb_2Se_3 to CdSe QDs in the $\text{Sb}_2\text{Se}_3/\text{CdSe}$ heterostructure system (**Scheme 5.2**). Extraction of hot carriers are significant for hot carrier solar cells and other optoelectronic devices, which can extend PCE beyond the Shockley-Queisser limit of $\sim 30\%$ and 60% for single and multi-junction solar cells, respectively.

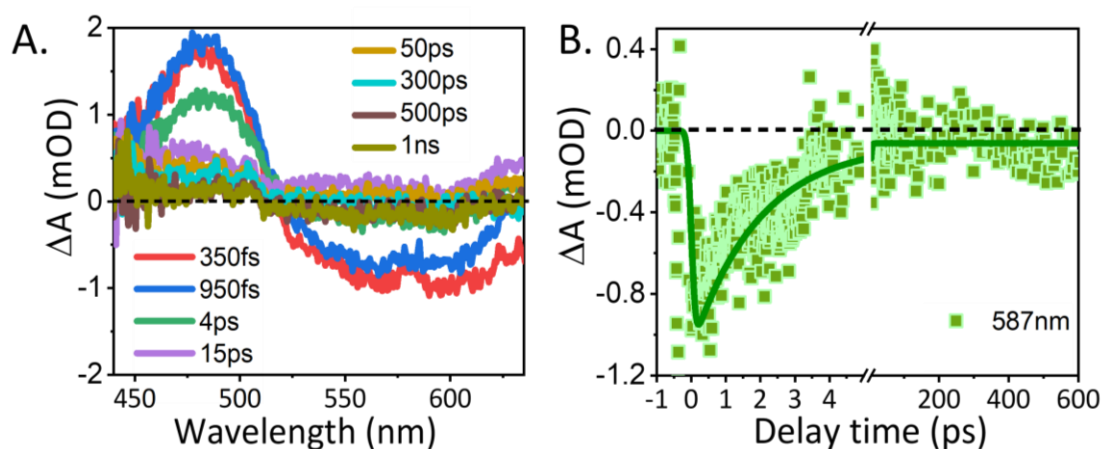


Figure 5.11. (A) Transient absorption spectra of the $\text{Sb}_2\text{Se}_3/\text{CdSe}$ heterostructure at different probe delays following photoexcitation with 750 nm laser pulse; and (B) Transient decay kinetics of negative bleach signal probed at 587 nm.

Scheme 5.1. Simple Schematic representing the electron and hole transfer at the interface of $\text{Sb}_2\text{Se}_3/\text{CdSe}$ heterostructure, for high energy (3.0 eV) pump excitation.

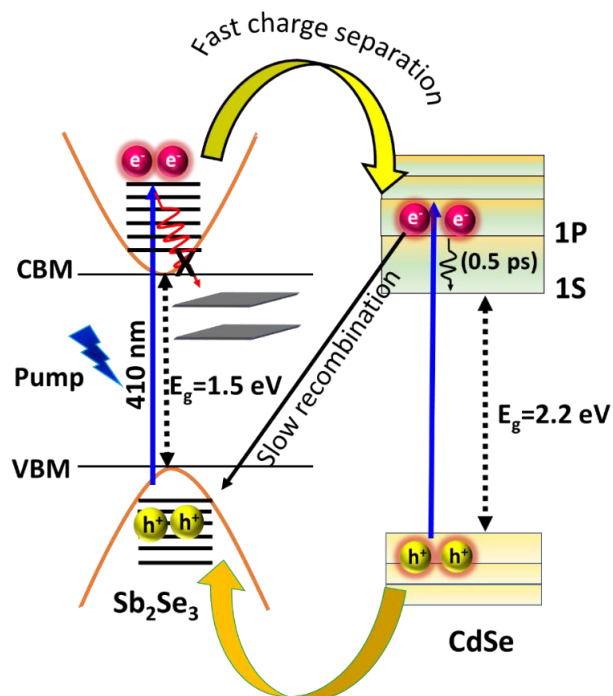
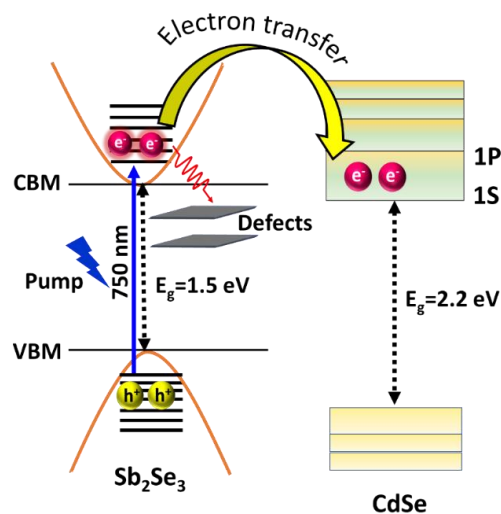


Table 5.4. Kinetic fitting parameters at excitonic bleach position in $\text{Sb}_2\text{Se}_3/\text{CdSe}$ heterostructure system under 750 nm pump excitation.

System	τ_g	τ_1	τ_2
$\text{Sb}_2\text{Se}_3/\text{CdSe}$	<100fs	1.8ps	>1ns
Heterostructure (587 nm)	(100%)	(94.2%)	(6.2%)

Scheme 5.2. Schematic Illustration of the different processes taking place in $\text{Sb}_2\text{Se}_3/\text{CdSe}$ heterostructure system upon 750 nm pump excitation.



5.3. Conclusion

In summary, we have fabricated $\text{Sb}_2\text{Se}_3/\text{CdSe}$ p-n heterojunction through the cation exchange process for the very first time and explored their interfacial photophysical processes with the help of ultrafast transient absorption spectroscopy. HRTEM images clearly suggest an intimate contact between Sb_2Se_3 and CdSe in the hetero-system, substantiating the formation of the p-n heterojunction. The PL measurements indicated the hole transfer from CdSe to Sb_2Se_3 , which was thermodynamically viable considering their respective band positions. In the transient study, the heterosystem consisted of both the signature of Sb_2Se_3 and CdSe. Though the visible range transient spectra were primarily dominated by the CdSe bleach signals covering most of the region, with a small positive hump of Sb_2Se_3 at the red wing of the spectra. Interestingly, the 1P excitonic bleach was found to be more prominent in the heterosystem. This is itself a testimony to hot electron migration from Sb_2Se_3 to CdSe. From the comparative dynamic profiles, we found that both the 1P and 1S bleach signals are slower in the heterosystem, which again substantiates the electron migration phenomena. In fact, the hetero-system slowed down the 1P signal more efficiently than that of the 1S one. This is an incredible observation, as hot electron migration influenced the separation of charge carriers in a hot excitonic state (1P), not in the usual lowest excitonic state (1S). Enhanced charge carrier lifetime of the hot state would be helpful in the extraction of those charge carriers in a device setup. We further confirmed the electron transfer process between Sb_2Se_3 and CdSe employing a lower energy (lower than the CdSe band gap) pump. The excitation of the hetero-system with a 750 nm pump also yielded a CdSe bleach signal, even though it was not excited. Our detailed spectroscopic investigation in this p-n heterojunction would help in the fabrication of many new heterojunctions and uplift the field of condensed matter-based optoelectronic devices.

5.4. References

- (1) Li, S.; Xu, W.; Meng, L.; Tian, W.; Li, L. Recent Progress on Semiconductor Heterojunction-Based Photoanodes for Photoelectrochemical Water Splitting. *Small Sci.* **2022**, 2100112.
- (2) Choi, M. J.; Kim, Y.; Lim, H.; Alarousu, E.; Adhikari, A.; Shaheen, B. S.; Kim, Y. H.; Mohammed, O. F.; Sargent, E. H.; Kim, J. Y.; Jung, Y. S. Tuning Solute-Redistribution Dynamics for Scalable Fabrication of Colloidal Quantum-Dot Optoelectronics. *Adv. Mater.* **2019**, *31*, 1805886.
- (3) Raffaele, R. P.; Castro, S. L.; Hepp, A. F.; Bailey, S. G. Quantum Dot Solar Cells. *Prog. Photovoltaics Res. Appl.* **2002**, *10*, 433-439.
- (4) Kamat, P. V. Quantum Dot Solar Cells. Semiconductor Nanocrystals as Light Harvesters. *J. Phys. Chem. B*, **2008**, *113*, 18737-18753.
- (5) Kramer, I. J.; Sargent, E. H. The Architecture of Colloidal Quantum Dot Solar Cells: Materials to Devices. *Chem. Rev.* **2014**, *114*, 863-882.
- (6) Nozik, A.J.; Beard, M.C.; Luther, J.M.; Law, M.; Ellingson, R. J.; Johnson, J. C. Semiconductor Quantum Dots and Quantum Dot Arrays and Applications of Multiple Exciton Generation to Third-Generation Photovoltaic Solar Cells. *Chem. Rev.* **2010**, *110*, 6873-6890.
- (7) Zhou, Y.; Li, Y.; Luo, J.; Li, D.; Liu, X.; Chen, C.; Song, H.; Ma, J.; Xue, D. J.; Yang, B.; Tang, J. Buried Homojunction in CdS/Sb₂Se₃ Thin Film Photovoltaics Generated by Interfacial Diffusion. *Appl. Phys. Lett.* **2017**, *111*, 013901.
- (8) Li, Z.; Liang, X.; Li, G.; Liu, H.; Zhang, H.; Guo, J.; Chen, J.; Shen, K.; San, X.; Yu, W.; Schropp, R. E. I.; Mai, Y. 9.2%-Efficient Core-Shell Structured Antimony Selenide Nanorod Array Solar Cells. *Nat. Commun.* **2019**, *10*, 1-9.
- (9) Wang, W.; Strössner, F.; Zimmermann, E.; Schmidt-Mende, L. Hybrid Solar Cells from Sb₂S₃ Nanoparticle Ink. *Sol. Energy Mater. Sol. Cells* **2017**, *172*, 335-340.

-
- (10) Mavlonov, A.; Razykov, T.; Raziq, F.; Gan, J.; Chantana, J.; Kawano, Y.; Nishimura, T.; Wei, H.; Zakutayev, A.; Minemoto, T.; Zu, X.; Li, S.; Qiao, L. A Review of Sb_2Se_3 Photovoltaic Absorber Materials and Thin-Film Solar Cells. *Sol. Energy* **2020**, *201*, 227-246.
- (11) Yang, Z.; Wang, X.; Chen, Y.; Zheng, Z.; Chen, Z.; Xu, W.; Liu, W.; Yang, Y., Michael; Zhao, J.; Chen, T.; Zhu, H. Ultrafast Self-Trapping of Photoexcited Carriers Sets the Upper Limit on Antimony Trisulfide Photovoltaic Devices. *Nat. Commun.* **2019**, *10*, 1-8.
- (12) Shen, K.; Zhang, Y.; Wang, X.; Ou, C.; Guo, F.; Zhu, H.; Liu, C.; Gao, Y.; Schropp, R. E. I.; Li, Z.; Liu, X.; Mai, Y. Efficient and Stable Planar n-i-p Sb_2Se_3 Solar Cells Enabled by Oriented 1D Trigonal Selenium Structures. *Adv. Sci.* **2020**, *7*, 1-10.
- (13) Wang, X.; Tang, R.; Yin, Y.; Ju, H.; Li, S.; Zhu, C.; Chen, T. Interfacial Engineering for High Efficiency Solution Processed Sb_2Se_3 Solar Cells. *Sol. Energy Mater. Sol. Cells* **2019**, *189*, 5-10.
- (14) Luo, M.; Leng, M.; Liu, X.; Chen, J.; Chen, C.; Qin, S.; Tang, J. Thermal evaporation and characterization of superstrate $\text{CdS}/\text{Sb}_2\text{Se}_3$ solar cells. *Appl. Phys. Lett.* **2014**, *104*, 173904.
- (15) Wen, X.; Chen, C.; Lu, S.; Li, K.; Kondrotas, R.; Zhao, Y.; Chen, W.; Gao, L.; Wang, C.; Zhang, J.; et al. Vapor transport deposition of antimony selenide thin film solar cells with 7.6% efficiency. *Nat. Commun.* **2018**, *9*, 1-10.
- (16) Kuposov, A. Y. Antimony Selenide Nanostructures: Morphology Control through Modulation of Ligand Chemistry and Variation of the Precursor Ratio. *CrystEngComm* **2017**, *19* (23), 3098-3102.
- (17) Bose, R.; Manna, G.; Jana, S.; Pradhan, N. $\text{Ag}_2\text{S}-\text{AgInS}_2$: p-n Junction Heteronanostructures with Quasi Type-II Band Alignment. *Chem. Commun.* **2014**, *50*, 3074-3077.
- (18) Liu, C.; Liu, T.; Li, Y.; Zhao, Z.; Zhou, D.; Li, W.; Zhao, Y.; Yang, H.; Sun, L.; Li, F.; Li, Z. A Dendritic $\text{Sb}_2\text{Se}_3/\text{In}_2\text{S}_3$ heterojunction Nanorod Array Photocathode Decorated with a MoS_x catalyst for Efficient Solar Hydrogen Evolution. *J. Mater. Chem. A* **2020**, *8*, 23385-23394.
-

- (19) Robinson, R. D.; Sadtler, B.; Demchenko, D. O.; Erdonmez, C. K.; Wang, L. W.; Alivisatos, A. P. Spontaneous Superlattice Formation in Nanorods through Partial Cation Exchange. *Science* **2007**, *317*, 355-358.
- (20) Kriegel, I.; Wisnet, A.; Kandada, A.R.S.; Scotognella, F.; Tassone, F.; Scheu, C.; Zhang, H.; Govorov, A.O.; Rodriguez-Fernandez, J.; Feldmann, J. Cation exchange synthesis and optoelectronic properties of type II CdTe-Cu_{2-x}Te nano heterostructures. *J. Mater. Chem. C* **2014**, *2*, 3189-3198.
- (21) Jang, Y.; Yanover, D.; Capek, R. K.; Shapiro, A.; Grumbach, N.; Kauffmann, Y.; Sashchiuk, A.; Lifshitz, E. Cation Exchange Combined with Kirkendall Effect in the Preparation of SnTe/CdTe and CdTe/SnTe Core/Shell Nanocrystals. *J. Phys. Chem. Lett.* **2016**, *7*, 2602-2609.
- (22) Kauffer, F. A.; Merlin, C.; Balan, L.; Schneider, R. Incidence of the Core Composition on the Stability, the ROS Production and the Toxicity of CdSe Quantum Dots. *J. Hazard. Mater.* **2014**, *268*, 246-255.
- (23) Priester, J. H.; Stoimenov, P. K.; Mielke, R. E.; Webb, S. M.; Ehrhardt, C.; Zhang, J. P.; Stucky, G. D.; Holden, P. A. Effects of Soluble Cadmium Salts Versus CdSe Quantum Dots on the Growth of Planktonic *Pseudomonas aeruginosa*. *Environ. Sci. Technol.* **2009**, *43*, 2589-2594.
- (24) Wang, Y., Cao, D.; Zhang, K.; Kang, W.; Wang, X.; Ma, P.; Wan, Y.; Cao, D.; Sun, D. Cation-exchange Construction of ZnSe/Sb₂Se₃ Hollow Microspheres Coated by nitrogen-doped carbon with enhanced sodium ion storage capability. *Nanoscale* **2020**, *12*, 17915-17924.
- (25) Guo, L.; Grice, C.; Zhang, B.; Xing, S.; Li, L.; Qian, X.; Yan, F. Improved stability and efficiency of CdSe/Sb₂Se₃ thin-film solar cells. *Solar energy* **2019**, *188*, 586-592.
- (26) De Trizio, L.; Manna, L. Forging Colloidal Nanostructures Via Cation Exchange Reactions. *Chem. Rev.* **2016**, *116*, 10852-10887.
- (27) Wang, Y.; Wang, H.; Li, Z.; Zhao, J.; Wang, L.; Chen, Q.; Wang, W.; Sun, H. Electron Extraction Dynamics in CdSe and CdSe/CdS/ZnS Quantum Dots Adsorbed with Methyl Viologen. *J. Phys. Chem. C* **2014**, *118*, 17240-17246.

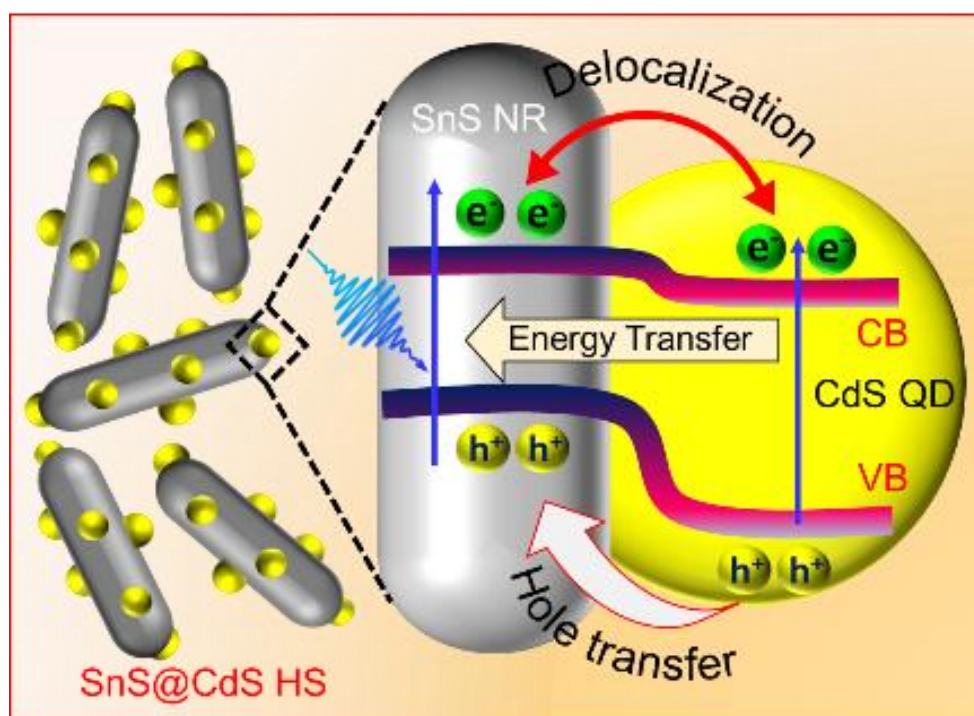
-
- (28) Meladom, S. K.; Arackal, S.; Sreedharan, A.; Sagar, S.; Das, B. C. Microwave Assisted Robust Aqueous Synthesis of Mn^{2+} -Doped CdSe QDs with Enhanced Electronic Properties. *RSC Adv.* **2018**, *8*, 26771-26781.
- (29) Temperature on the Properties of Sb_2Se_3 Thin Films and Solar Cells by Two-Step Method. *J. Mater. Sci. Mater. Electron.* **2019**, *30*, 19871-19879.
- (30) Kim, J. W.; Shim, H. S.; Ko, S.; Jeong, U.; Lee, C. L.; Kim, W. B. Thorny CdSe Nanotubes via an Aqueous Anion Exchange Reaction Process and Their Photoelectrochemical Applications. *J. Mater. Chem.* **2012**, *22*, 20889-20895.
- (31) Hao, J.; Liu, H.; Miao, J.; Lu, R.; Zhou, Z.; Zhao, B.; Xie, B.; Cheng, J.; Wang, K.; Delville, M. H. A Facile Route to Synthesize CdSe/ZnS Thick-Shell Quantum Dots with Precisely Controlled Green Emission Properties: Towards QDs Based LED Applications. *Sci. Rep.* **2019**, *9*, 1-8.
- (32) Chen, C.; Yang, Y.; Bobela, D. C.; Lu, S.; Zeng, K.; Yang, B.; Gao, L.; Beard, M. C.; Tang, J. Characterization of Basic Physical Properties of Sb_2Se_3 . *Front. Optoelectron.* **2017**, *10*, 18-30.
- (33) Wang, L.; Chen, Z.; Liang, G.; Li, Y.; Lai, R.; Ding, T.; Wu, K. Observation of a phonon bottleneck in copper-doped colloidal quantum dots. *Nat. Commun.* **2019**, *10*, 1-8.
- (34) Xia, L.; Yang, Z.; Tang, B.; Li, F.; Wei, J.; Zhou, Z. Carbon Nanofibers with Embedded Sb_2Se_3 Nanoparticles as Highly Reversible Anodes for Na-Ion Batteries. *Small* **2021**, *17*, 1-8.
- (35) Kovosov, A.Y. Antimony selenide nanostructures: morphology control through modulation of ligand chemistry and variation of the precursor ratio. *CrystEngComm* **2017**, *19*, 3098-3102.
- (36) Kipkorir, A.; Dubose, J.; Cho, J.; Kamat, P. V. CsPbBr₃-CdS Heterostructure: Stabilizing Perovskite Nanocrystals for Photocatalysis. *Chem. Sci.* **2021**, *12*, 14815-14825.
- (37) Eshet, H.; Rabani, E. The Electronic Structure of CdSe/CdS Core/Shell Seeded Nanorods: Type-I or Quasi-Type-II? *Nano Lett.* **2013**, *13*, 5880-5885.
-

-
- (38) Nandi, P.; Das, D. ZnO/CdS/CuS Heterostructure: A Suitable Candidate for Applications in Visible-Light Photocatalysis. *J. Phys. Chem. Solids* **2022**, *160*, 110344.
- (39) Kaur, A.; Goswami, T.; Babu, K. J.; Ghorai, N.; Kaur, G.; Shukla, A.; Rondiya, S. R.; Ghosh, H. N. Probing Ultrafast Charge Separation in CZTS/CdS Heterojunctions through Femtosecond Transient Absorption Spectroscopy. *J. Phys. Chem. C* **2020**, *124*, 19476-19483.
- (40) Goswami, T.; Rani, R.; Hazra, K. S.; Ghosh, H. N. Ultrafast Carrier Dynamics of the Exciton and Trion in MoS₂ Monolayers Followed by Dissociation Dynamics in Au@MoS₂ 2D Heterointerfaces. *J. Phys. Chem. Lett.* **2019**, *10*, 3057-3063.
- (41) Tisdale, W. A.; Williams, K. J.; Timp, B. A.; Norris, D. J.; Aydil, E. S.; Zhu, X. Y. Hot-Electron Transfer from Semiconductor Nanocrystals. *Science* **2010**, *328*, 1543-1547.
- (42) Justice Babu, K.; Kaur, G.; Shukla, A.; Saha, R.; Kaur, A.; Sachdeva, M.; Yadav, D.K. and Ghosh, H.N. Fast Polaron Formation and Low Carrier Mobility in Defect-Free Polyhedral CsPbBr₃ Perovskite Nanocrystals. *ACS Photonics* **2022**, *9*, 969-978.
- (43) Utterback, J. K.; Ruzicka, J. L.; Keller, H.R.; Pellows, L.M.; Dukovic, G. Electron transfer from semiconductor nanocrystals to redox enzymes. *Annu. Rev. Phys. Chem.* **2020**, *71*, 335-359.
- (44) Christians, J. A.; Leighton, D. T.; Kamat, P. V. Rate Limiting Interfacial Hole Transfer in Sb₂S₃ Solid-State Solar Cells. *Energy Environ. Sci.* **2014**, *7*, 1148-1158.
- (45) Singh, P.; Ghorai, N.; Thakur, A.; Ghosh, H. N. Temperature-Dependent Ultrafast Charge Carrier Dynamics in Amorphous and Crystalline Sb₂Se₃ Thin Films. *J. Phys. Chem. C* **2021**, *125*, 5197-5206.
- (46) Kaur, A.; Goswami, T.; Rondiya, S. R.; Jadhav, Y. A.; Babu, K. J.; Shukla, A.; Yadav, D. K.; Ghosh, H. N. Enhanced Charge Carrier Separation and Improved Biexciton Yield at the p-n Junction of SnSe/CdSe Heterostructures: A Detailed Electrochemical and Ultrafast Spectroscopic Investigation. *J. Phys. Chem. Lett.* **2021**, *12* (45), 10958-10968.
-

- (47) Kambhampati, P. Unraveling the structure and dynamics of excitons in semiconductor quantum dots. *Acc. Chem. Res.* **2011**, *44*, 1-13.
- (48) Liu, M.; Verma, S. D.; Zhang, Z.; Sung, J.; Rao, A. Nonequilibrium Carrier Transport in Quantum Dot Heterostructures. *Nano Lett.* **2021**, *21*, 8945-8951.

CHAPTER 6

Ultrafast Hole Migration at the p-n Heterojunction of One Dimensional SnS Nanorods and Zero Dimensional CdS Quantum Dots



J. Phys. Chem. Lett. 2023, 14, 33, 7483–7489

Abstract

P-n heterojunctions fabricated from one-dimensional (1D) p-type tin sulfide nanorods (SnS NRs) decorated with n-type zero-dimensional (0D) cadmium sulfide quantum dots (CdS QDs) have gained significant research attention in energy storage devices. Herein, we have successfully synthesized 1D/0D SnS@CdS heterostructure (HS) using the hot injection method. Structural and morphological studies clearly suggest that CdS QDs are uniformly anchored on the surface of SnS NRs resulting in an intimate contact between two components. The photoluminescence (PL) study revealed the transfer of photoexcited holes from CdS QDs to SnS NRs which was further confirmed by transient absorption (TA) studies. TA measurements demonstrate the hole transfer from the valence band of CdS QDs to SnS NRs and the delocalization of electrons between the conduction band of SnS NRs and CdS QDs in SnS@CdS HS, resulting in efficient charge separation across the p-n heterojunction. These findings will open up a new paradigm for improving the efficiency of optoelectronic devices.

6.1. Introduction

Semiconductor p-n heterojunctions are the basic building blocks for any optoelectronic and technological applications.¹⁻³ It improves the charge separation as well as the carrier transport, and hence increases the lifetime of carriers by preventing excitonic recombination, which is highly desirable for device applications. Among them, 1D (IV-VI) p-type tin sulfide (SnS) has emerged to be one of the promising candidates for its numerous applications including photovoltaics⁴, photocatalysis⁵, and next-generation energy storage devices^{6,7} owing to its unique properties such as high stability and tunable bandgap⁴, higher optical absorption coefficient ($>10^4 \text{ cm}^{-1}$)⁸, non-toxic and earth-abundant elements.^{9,10} Moreover, 1-D semiconductor heterostructures demonstrate the large surface-to-volume ratio, which provides a large number of active sites that result in outstanding photocatalytic, optoelectronic, and gas sensing properties.¹¹⁻¹⁴ Recently, SnS is widely used as an active absorber material in solar cell devices.¹⁵ However, the pristine SnS frequently suffer from the low charge separation efficiency and trapping of charge carriers, which seriously affects the practical application of photocatalysis. Many efforts have been made to avoid these issues by combining SnS with other nanomaterials to form a heterostructure.¹⁶⁻¹⁹ Hence, to achieve the efficient performance of devices, the coupling of p-type 1D SnS NRs with n-type 0D CdS QDs has evolved much interest in the field of photovoltaics as the depletion layer at the p-n interfacial region induces an electric field which results in improved separation ability and transport of charge carriers. CdS is a wide bandgap semiconductor with high electronic mobility, excellent thermal stability, exhibits sharp excitonic peaks and photoluminescence (PL).²⁰⁻²² SnS NRs in heterojunction with CdS QDs can achieve excellent device performance. Earlier Wang et al. reported that $\text{Sn}_{0.38}\text{S}$ -CdS superlattice nanowires display efficient gas sensing behaviour.¹⁴ Cho et al. have measured the efficiency of 4.22% for SnS@CdS thin film solar cell by improving the interface quality of the heterojunction which is still far below than the theoretical Shockley-Queisser limit.²³ In order to improvise the fabrication of the junction and enhance the device performance, it is paramount important to study the photo physics of generated charge carriers involved at the interface of this SnS NR and CdS QD heterostructure.²⁴⁻²⁶

However, to the best of our knowledge, the charge transfer dynamics in 1D/0D SnS@CdS HS has never been investigated earlier. Femtosecond (fs) transient absorption spectroscopy (TAS) is known to be a powerful technique to monitor the dynamics of photoexcited charge carriers in individual materials as well as heterosystems in the fs to nanoseconds (ns) time window. The understanding of cooling, transfer, trapping and recombination pathways of photogenerated charge carrier play a crucial role in fabricating high performance optoelectronic devices.

In this chapter, high-quality SnS@CdS p-n heterojunction, where SnS nanorods are decorated with CdS QDs have been successfully synthesized via facile and low-cost hot injection method for the very first time. X-ray diffraction (XRD), high-resolution transmission electron microscopy (HR-TEM) images, energy dispersive X-ray spectroscopy (EDX) as well as optical studies clearly depict the formation of a strong interface between p-type SnS NRs and n-type CdS QDs. Steady-state and time-resolved PL studies indicate the migration of holes from CdS QDs to SnS NRs. Further, transient absorption studies also revealed the hole transfer from the valence band of CdS QDs to SnS NRs and the delocalization of electrons between the conduction band of SnS NRs and CdS QDs which is a thermodynamically feasible process according to their band alignment. In addition, we found that charge separation in SnS NRs at a longer time scale in the presence of CdS QDs. To the best of our knowledge, to date, no report is available where the heterostructure of CdS QDs with SnS NRs is synthesized and charge carrier dynamics at their p-n junction studied. We believe that our studies are applicable to other nano-heterostructures, providing direction for a rational design of nanorod morphology for their multiple applications.

6.2. Results and discussion

6.2.1. Structural and morphological characterizations

SnS@CdS p-n heterojunction was prepared by two two-step facile and inexpensive hot injection method as demonstrated in the schematic representation shown in **Figure 6.1**. In the first step, SnS NRs and CdS QDs are synthesized by hot injection method, respectively following previous literature with minor modifications.^{27,28} In

the following step, CdS quantum dots are decorated uniformly on the surface of as-prepared SnS NRs by injecting the CdS QDs into SnS NRs at high temperature, which results in the formation of high-quality 1D/0D SnS@CdS p-n heterojunction. It is observed that as compared to bare SnS NRs, many small CdS nanoparticles were uniformly anchored on the surface of SnS NRs.

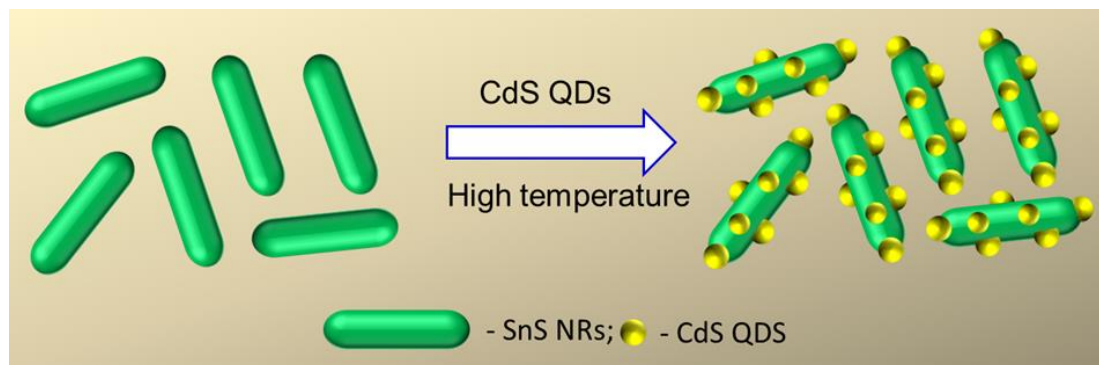


Figure 6.1. Schematic illustration for the preparation of 1D/0D SnS@CdS p-n heterojunction.

The crystal phase and morphology of as-synthesized pristine SnS NRs, CdS QDs, and SnS@CdS HS were characterized by employing XRD and transmission electron microscopy (TEM), respectively. The TEM images and XRD of bare SnS NRs and CdS QDs have been provided in **Figure 6.2**. From the TEM images, it is found that SnS possess typical rod-like morphology with an average length and width of 30 and 10 nm, respectively (**Figure 6.2A**). HR-TEM image of SnS NRs shown in **Figure 6.2B** shows the distinct lattice fringe spacing of 0.29 nm, corresponding to (111) lattice plane of orthorhombic SnS NRs.²⁹ To further examine crystal structure and phase impurity, the XRD technique was used. The observed diffraction peaks in the XRD pattern of SnS NRs in **Figure 6.2C** are assigned to (011), (021), (111), (040), (131), (141), (211), (151) (122) and (042) crystal planes elucidating the formation of an orthorhombic phase of SnS (JCPDS No. 39-0354).³⁰ These sharp and prominent peaks suggest the material has excellent crystallinity. Furthermore, no obvious peaks of elemental Sn, SnO₂, and SnS₂ could be found in the XRD spectrum. The HR-TEM images of CdS QDs indicate the spherical morphology with an average size of around 4 nm (**Figure 6.2D**). As shown in HR-TEM images (**Figure 6.2E**), the interplanar spacing between two consecutive lattice planes is observed around 0.33 nm, which is

consistent with the (111) plane of CdS QDs.³¹ The XRD patterns of pristine CdS QDs exhibit diffraction peaks corresponding to (111), (220), (311), and (331) crystal planes as displayed in **Figure 6.2F**. The observed peaks matched well with the cubic crystal structure of CdS (JCPDS No. 65-2887).³² Further, HR-TEM measurements of SnS@CdS HS were carried out to determine the morphology and interfaces of both SnS and CdS components in the heterostructure. **Figure 6.3A** shows the HR-TEM images of SnS@CdS HS, which clearly indicate that the CdS QDs are evenly decorated on the surface of SnS NRs. Moreover, the size of CdS QDs was found to be 4 nm which is identical to that of pristine CdS QDs (**Figure 6.2D**). The HR-TEM images of SnS@CdS p-n heterojunction shown in **Figure 6.3B** depict two different lattice planes separated by a sharp interface with lattice spacing 0.29 nm and 0.33 nm, corresponding to the (111) plane of SnS NRs and (111) plane of CdS QDs, respectively.

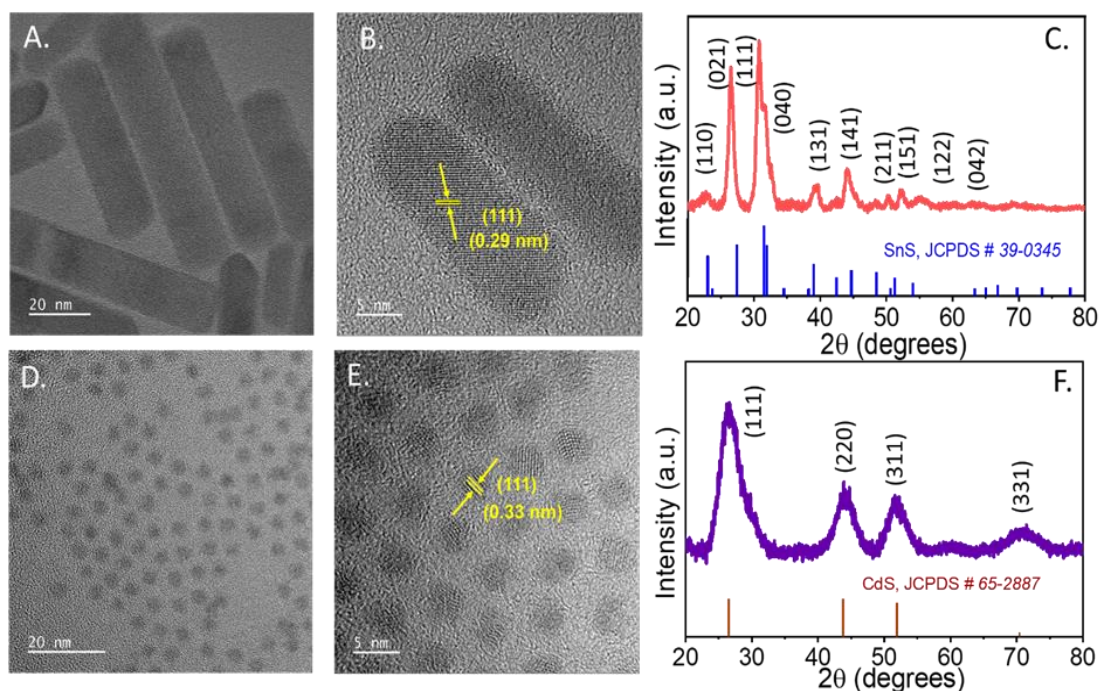


Figure 6.2. (A, D) TEM, (B, E) HR-TEM images and (C, F) XRD pattern of SnS NRs and CdS QDs, respectively (JCPDS data of (C) orthorhombic phase of SnS and (F) zinc-blende phase of CdS marked under the bottom).

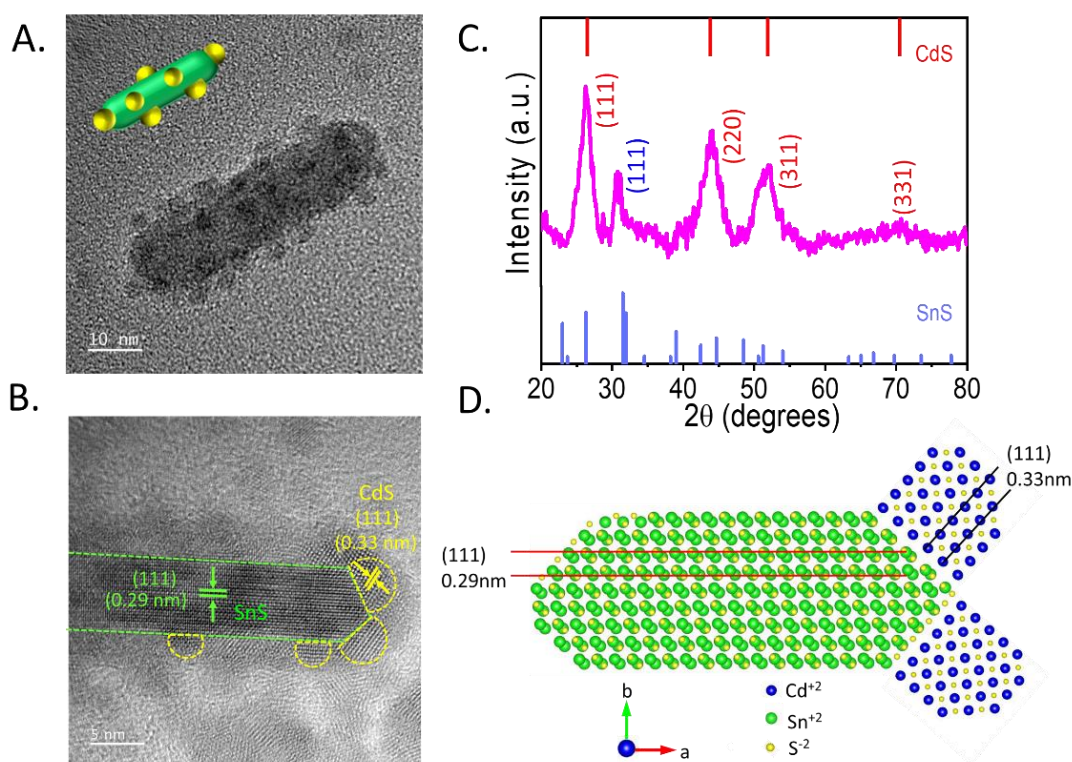


Figure 6.3. (A, B) HR-TEM images of SnS@CdS HS, dotted green and yellow lines indicated SnS NRs and CdS QDs, respectively. and (C) XRD pattern of newly synthesized SnS@CdS HS (JCPDS values also marked under the bottom for the orthorhombic phase of SnS and top for the zinc-blende phase of CdS) and (D) Atomic model showing the interface between SnS NRs and CdS QDs viewed along the c direction (we have omitted some of the CdS QDs attached to SnS NRs for clarity).

HR-TEM images clearly confirm that the (111) plane of CdS forms a strong interface and close contact with the (111) plane of SnS NRs. The XRD pattern of SnS@CdS HS exhibits peaks of both SnS NR and CdS QD components as depicted in **Figure 6.3C**. Along with the (111), (220), (311), and (331) diffraction planes of cubic CdS, we have observed an extra plane at $2\theta \sim 32^\circ$ which corresponds to the (111) plane of orthorhombic SnS. The XRD analysis clearly depicts the formation of SnS@CdS HS which was confirmed by HR-TEM analysis as discussed before. To explain the interface of HS, an atomic model has been designed and is presented in **Figure 6.3D**. The atomic model of SnS NR and CdS QD heterojunction is viewed from the c direction. It shows the interface between the (111) plane of SnS NRs and CdS QDs with d spacing of 0.29 nm and 0.33 nm, respectively.

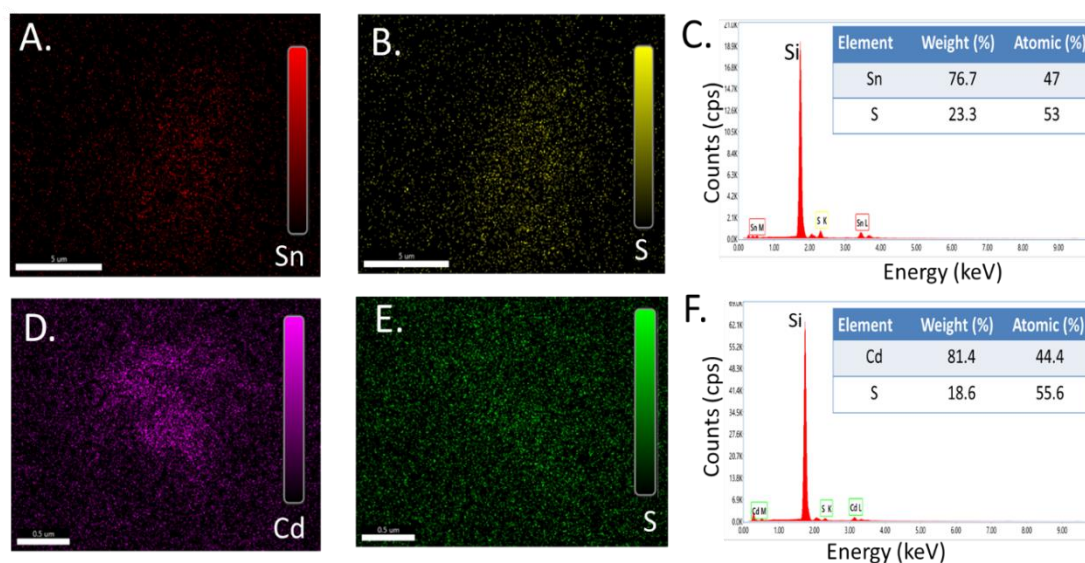


Figure 6.4. (A, B) Mapping and (C) EDX spectrum of SnS NRs indicating the homogenous distribution of Sn and S elements. (Inset: Observed atomic percentage of Sn and S). (D, E) Mapping and (F) EDX spectrum indicating the homogenous distribution of Cd and S elements in the CdS QD. (Inset: atomic percentage of Cd and S).

The strong interface between SnS NRs and CdS QDs is due to the high reaction temperatures that are beneficial for the strong heterojunction formation. Furthermore, the existence and uniform distribution of the Sn, Cd, and S, elements can be clearly detected from the EDX mapping results. The EDX mapping of bare SnS NRs, CdS QDs, and SnS@CdS HS are shown in **Figures 6.4 and 6.5** respectively. Moreover, EDX with field emission scanning electron microscope (FESEM) was used to measure the elemental distribution and the presence of elements in composition which show the presence of Sn, Cd, and S elements in SnS@CdS HS (**Figure 6.5, inset**). To investigate the chemical composition and oxidation states of various elements of the samples, X-ray photoelectron spectroscopy (XPS) analysis was carried out. XPS survey spectrum of SnS@CdS HS shown in **Figure 6.6A** indicates the presence of peaks due to Cd, Sn, and S elements. The incorporation of the Cd ion into lattice sites of SnS without altering its chemical structure is investigated by finding the oxidation states of Sn, Cd, and S obtained from XPS analysis.

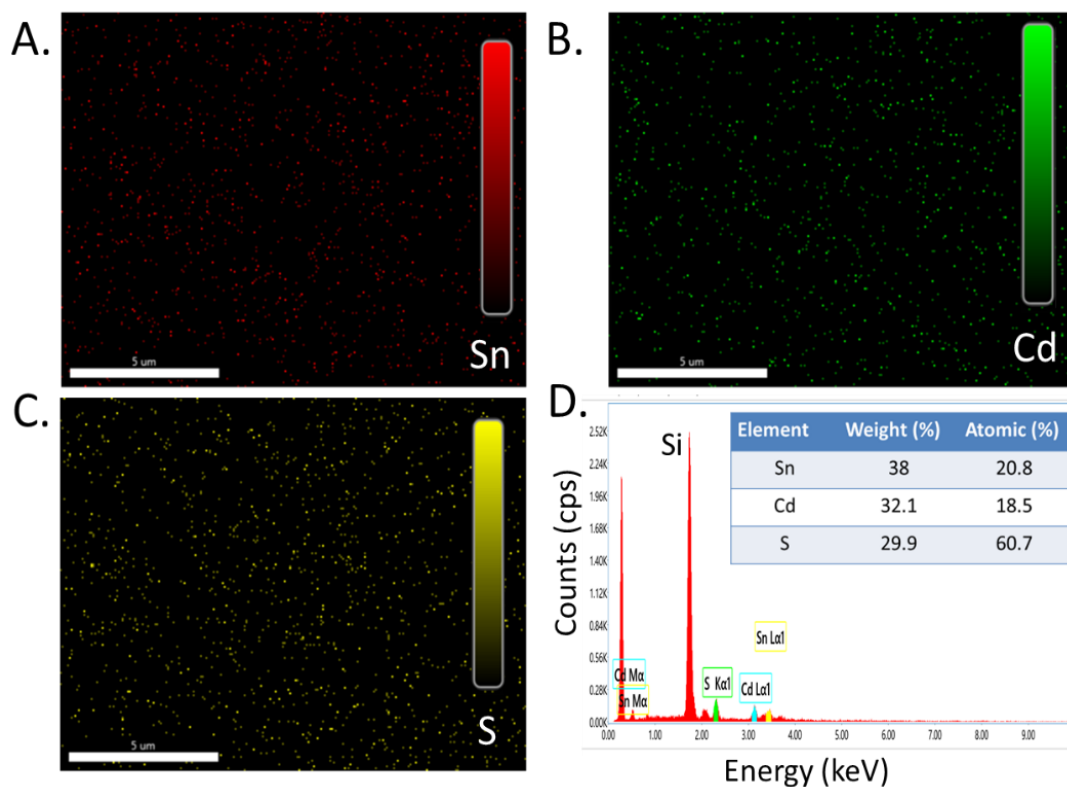


Figure 6.5. EDX Mapping images of 1D/0D SnS@CdS HS, indicating the coexistence and homogenous distribution of (A) Sn, (B) Cd, and (C) S elements in the SnS@CdS HS, (D) EDX spectrum of SnS@CdS HS. Inset: Observed atomic percentage of Sn, Cd, and S.

XPS scans of the SnS@CdS p-n heterojunction sample are shown in **Figure 6.6A**, which confirmed the presence of Sn and S along with the Cd peak. The high-resolution XPS spectra of the Cd 3d state exhibit peaks at 405 and 412 eV corresponding to Cd 3d_{5/2} and Cd 3d_{3/2} states, respectively (**Figure 6.6B**), which confirmed the presence of the Cd²⁺ oxidation state.^{33, 34} The high-resolution XPS spectra of Sn 3d state demonstrated in **Figure 6.6C** indicates doublet at 486 and 494.5 eV attributed to Sn 3d_{5/2} and Sn 3d_{3/2}, respectively and for S 2p state displays doublet at 160.9 and 161.9 eV correspond to S 2p_{3/2} and S 2p_{1/2} respectively, which prove the Sn⁺² and S⁻² oxidation states in the heterojunction (**Figure 6.6D**).³⁵

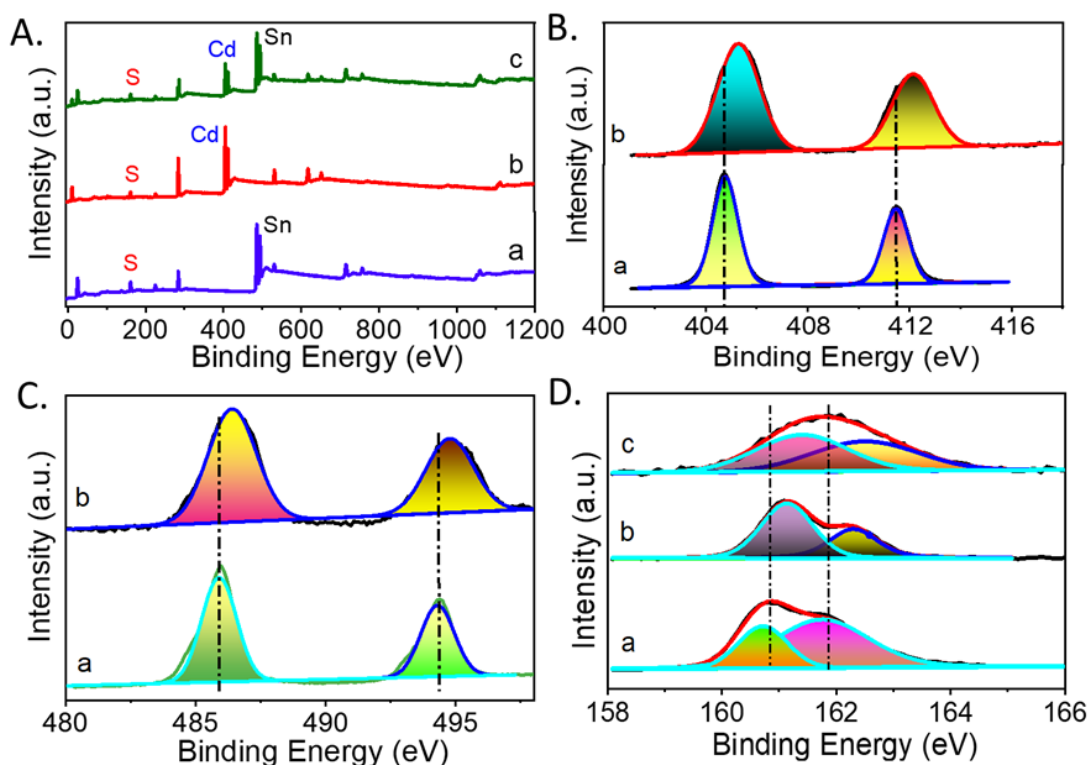


Figure 6.6. XPS analysis of SnS NRs, CdS QDs, and SnS@CdS p-n heterojunction: (A) survey scan of (a) SnS NRs.; (b) CdS QDs, (c) SnS@CdS p-n heterojunction. High-resolution XPS spectra of (B) Cd 3d in (a) pristine CdS QDs and (b) SnS@CdS HS; (C) Sn 3d in bare (a) SnS and (b) SnS@CdS; and (D) S 2p in (a) pristine SnS NRs and (b) CdS QDs as well as in (c) SnS@CdS HS.

Compared with the binding energies of pristine SnS NRs and CdS QDs, ca. 0.6 eV shift toward higher binding energy for the Sn 3d and Cd 3d is observed in SnS@CdS p-n heterojunction. Earlier Zhang et al. also reported the Cd 3d XPS spectrum shift for the CdS/WS₂ nanocomposite³⁶. The slight shift in XPS elemental analysis further proves the intimate interface and strong interaction between SnS NRs and CdS QDs in the SnS@CdS HS system. The XPS investigation further confirms the formation of a well-defined heterostructure. The interaction between SnS NRs and CdS QDs not only promotes the charge transfer and separation on the interface but also contributes to the good quality SnS@CdS p-n heterojunction construction. Further, to verify the p-type and n-type nature of the as-prepared SnS NRs and CdS QDs, we have utilized mott Schottky technique. The Mott Schottky plots of SnS NRs and CdS QDs have been shown in **Figure 6.7**. The negative and positive slopes of the tangent of mott Schottky curves confirm the p-type and n-type semiconductor nature of SnS NRs and CdS QDs, respectively.^{37,38}

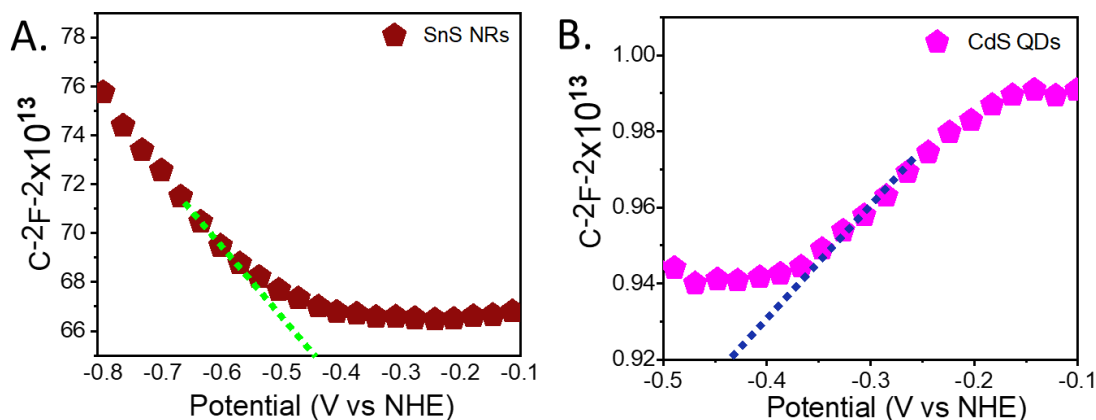


Figure 6.7. Mott Schottky plots of (A) SnS NRs and (B) CdS QDs measured at the frequency of 1kHz.

6.2.2. Optical Studies

The optical characteristics of materials play a significant role in optoelectronic device development. The steady-state optical absorption properties of SnS NRs, CdS QDs, and SnS@CdS HS are shown in **Figure 6.8A**. The synthesized SnS NRs exhibit strong and broader absorption over a wide region from 300-800 nm. Its band gap is calculated from the tauc plot. The relation between absorption coefficient and photon energy has been provided as follows (equation 1)³⁹

$$\alpha h\nu = \beta(h\nu - E_g)^{1/2} \quad (1)$$

where $h\nu$ is photon energy, β is constant relative to the material and α is the optical absorption coefficient. The bandgap of SnS NRs is calculated to be 1.3 eV as shown in **Figure 6.8B**.⁴⁰ Due to its narrow bandgap, a large part of the solar spectrum from ultraviolet (UV) to near-infrared (NIR) wavelength regions can be utilized. We did not observe any clear excitonic peak in the optical absorption spectra of SnS NRs due to the presence of a high density of defect states. Also, the size of nanorods is large as compared to the exciton Bohr radius of 7.24 nm, therefore the SnS NRs exhibit weaker confinement.⁴¹ The absorption spectrum of CdS QDs is shown in **Figure 6.8A**. The steady-state optical absorption studies clearly show band edge absorption peak for CdS QDs at 450 nm, which corresponds to the bandgap of 2.75 eV. The peaks at 450 and 390 nm are assigned to band edge $[1S_{3/2}-1S(e), 1S]$ and excited state $[1P_{3/2}-1P(e), 1P]$ electronic transitions, respectively. The CdS QDs exhibit discrete transitions arising due to a strong quantum confinement effect because of their smaller

particle size (~ 4 nm) compared to the corresponding exciton Bohr diameter of about 5 nm.⁵ The SnS@CdS HS absorption displays the signature of both CdS QD and SnS NR components. Furthermore, the absorption spectrum shows small dampening in the 1S and 1P excitonic peaks of CdS QDs and, also exhibits tail absorption in the visible region conforming to the strong electronic coupling between SnS NRs and CdS QDs.⁴²⁻⁴⁴ Moreover, after the formation of the heterostructure, no prominent shift in the peak position was found, which indicates that the size of CdS QDs is preserved.

Now to investigate the interfacial charge transfer mechanism between SnS NRs and CdS QDs in SnS@CdS heterojunction, PL spectroscopy was employed. **Figure 6.8C** shows the PL spectra of SnS, CdS, and SnS@CdS HS samples upon 400 nm photoexcitation in hexane. PL of CdS QDs exhibit a sharp peak at 462 nm, which was attributed to the radiative recombination between electrons and holes.

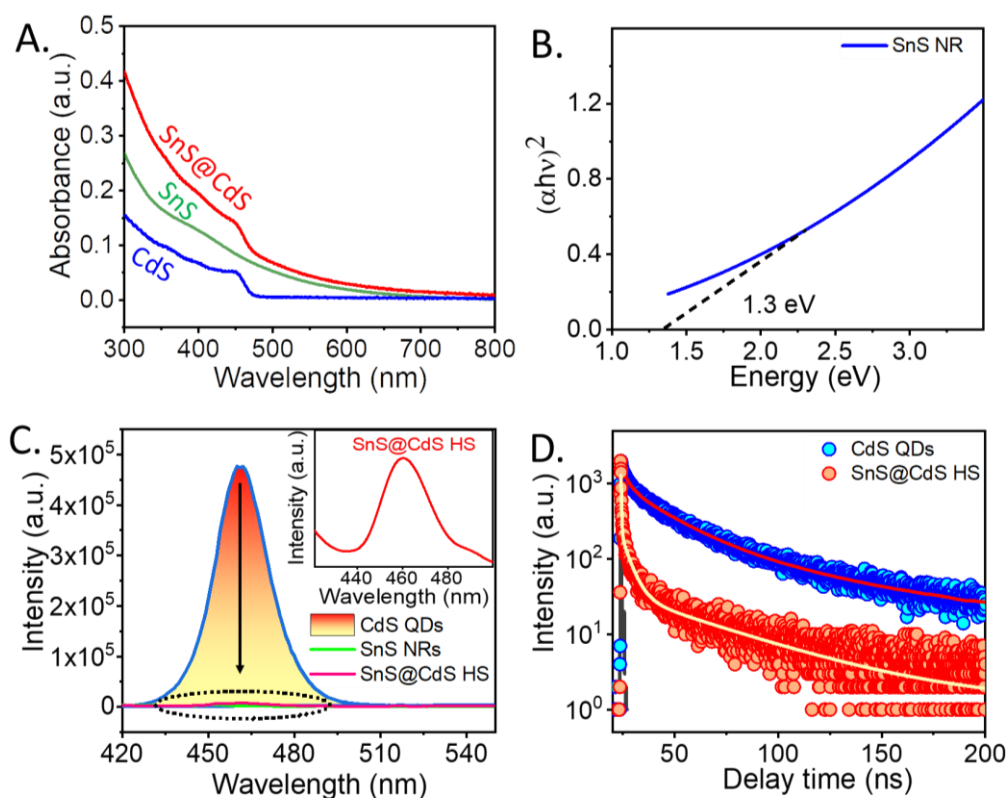


Figure 6.8. (A) Steady-state optical absorption spectra of CdS QDs, SnS NRs, and SnS@CdS HS (B) Tauc plot of SnS NRs (C) PL spectra for pristine CdS QDs, pristine SnS NRs and SnS@CdS HS in hexane upon 400 nm photoexcitation. (Inset: enlarged PL spectrum SnS@CdS HS) and (D) Time-resolved PL studies of bare CdS QDs and SnS@CdS HS after exciting the samples at 402 nm and the decay trace monitored at 462 nm.

Table 6.1. Quantum yield calculation

Sample	OD of the sample at 400 nm	OD of reference at 400 nm	Area of sample	Area of reference	PLQY
CdS QDs	0.09	0.07	7.8×10^5	1.8×10^6	22%
SnS@CdS HS	0.12	0.07	4.2×10^4	1.8×10^6	<1%

The photoluminescence quantum yield (PLQY) of CdS QDs was calculated to be 22 % (**Table 6.1**). We did not find any PL emission peak for bare SnS NRs in visible (420-550 nm) owing to the presence of defect states which act as traps, that lead to the non-radiative decay of the charge carriers. However, when the CdS QDs were decorated on the surface of SnS NRs, it is clearly seen that CdS emission is quenched drastically and PLQY becomes <1% (**Table 6.1**).⁴⁵ Furthermore, it is observed that the position of the emission peak of CdS does not change in SnS@CdS HS.

To determine the answer, it is important to find the band alignment between SnS NRs and CdS QDs. The band alignment is one of the most important aspects that affect the transportation of photogenerated carriers through the interfaces, carrier recombination, and overall performance of the solar cells or any optoelectronic devices. We have determined the band alignment at the interface of SnS NRs and CdS QDs. The valence band positions of SnS NRs and CdS QDs have been determined using XPS valence band spectra as demonstrated in **Figure 6.9**. Schematic diagrams of the band alignment at the heterointerface between the p-SnS NRs and n-CdS QDs are illustrated in **Figure 6.10**. The valence band positions of SnS and CdS samples are measured to be -0.33 eV and 1.12 eV, respectively which are consistent with the previous reports. The bandgap of SnS NRs and CdS QDs are determined to be 1.3 eV and 2.75 eV respectively. Based on the equations $E_{CB} = E_{VB} + E_g$, the conduction band positions for SnS NRs and CdS QDs were calculated to be -1.63 eV and -1.62 eV, respectively. The conduction band offset (CBO) and valence band offset (VBO) of 0.01 eV and 1.45 eV were determined for SnS@CdS, respectively, and are comparable with previous reports.³² Thus, according to valence and conduction band positions of SnS NR and CdS QDs, the decrease in CdS PL intensity in the presence of SnS was attributed to the injection of photoexcited holes from CdS QDs to SnS NRs as we already mentioned that the valence band (VB) of CdS lies below the VB of

SnS. However, we cannot rule out the possibility of energy transfer between SnS NRs and CdS QDs in SnS@CdS HS as the PL band of CdS QDs overlaps with the absorption of SnS NRs. Further, to monitor the hole injection dynamics in SnS@CdS p-n heterojunction, we have carried out a time-resolved photoluminescence study using time-correlated single photon counting (TCSPC). The emission lifetime of prepared samples has been calculated using TCSPC. We have calculated the lifetime of CdS QDs and SnS@CdS HS by fitting the lifetime data multi-exponentially, with time constants $\tau_1=3.3$ ns (52 %), $\tau_2=21$ ns (40 %), and $\tau_3=81$ ns (8 %) with $\tau_{avg}=18$ ns for CdS QDs and $\tau_1=0.25$ ns (88%), $\tau_2=4.25$ ns (10%), and $\tau_3=45.7$ ns (2 %) with $\tau_{avg}=1.5$ ns for SnS@CdS HS system. It is observed that the average lifetime of CdS QDs (λ_{em} - 462 nm) has decreased drastically from 18 ns to 1.5 ns (almost 12 times) in the presence of SnS NRs in

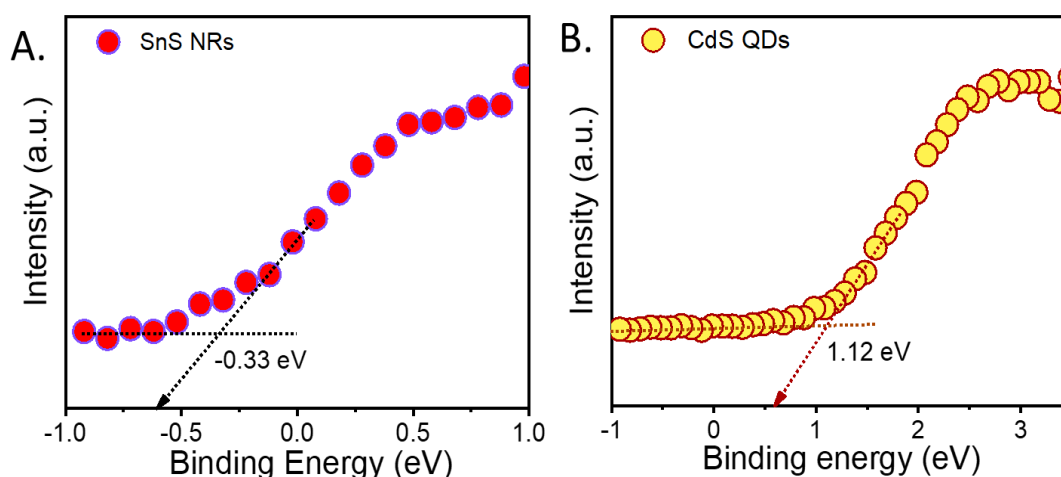


Figure 6.9. XPS valence band spectra of (A) SnS NRs and (B) CdS QDs.

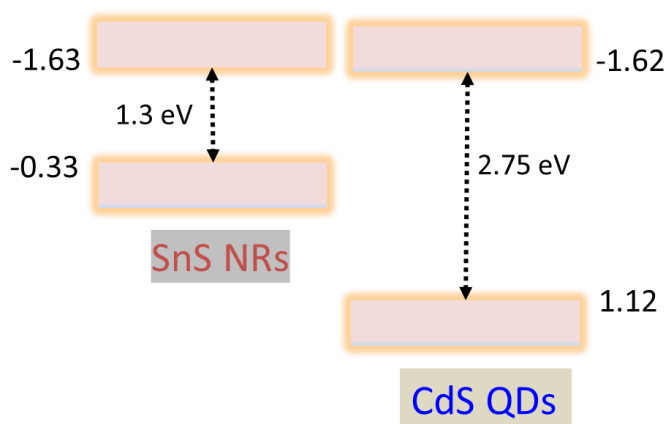


Figure 6.10. Band alignment of SnS@CdS p-n heterojunction calculated from XPS analysis.

Table 6.2. Fitting components of time resolved photoluminescence for CdS QDs and SnS@CdS HS monitored at 462 nm upon 402 nm excitation.

System	τ_1 (ns)	A_1 (%)	τ_2 (ns)	A_2 (%)	τ_3 (ns)	A_3 (%)	τ_{avg} (ns)	χ^2
CdS QDs (462 nm)	3.3	52%	21	40%	81	8%	18	1.14
SnS@CdS HS (462 nm)	0.25	88%	4.25	10%	45.7	2%	1.5	1.12

SnS@CdS HS (**Figure 6.7D**) and the fitting components are provided in **Table 6.2**. From the above results, it is indicated that photogenerated holes are migrating from the valence band of CdS QDs to the valence band of SnS NRs. Similarly, the hole transfer process is also depicted by fluorescence up-conversion studies (**Figure 6.11**). The decay kinetics of CdS become significantly faster in SnS@CdS HS. The fitting components are provided in (**Table 6.3**) Since TCSPC studies are not enough to get a clear picture of the hole transfer process in SnS@CdS HS owing to its limited time resolution. Therefore, we have utilized the transient absorption spectroscopy technique to investigate in depth charge migration phenomenon in the heterosystem and quantitatively monitor the hole transfer process.

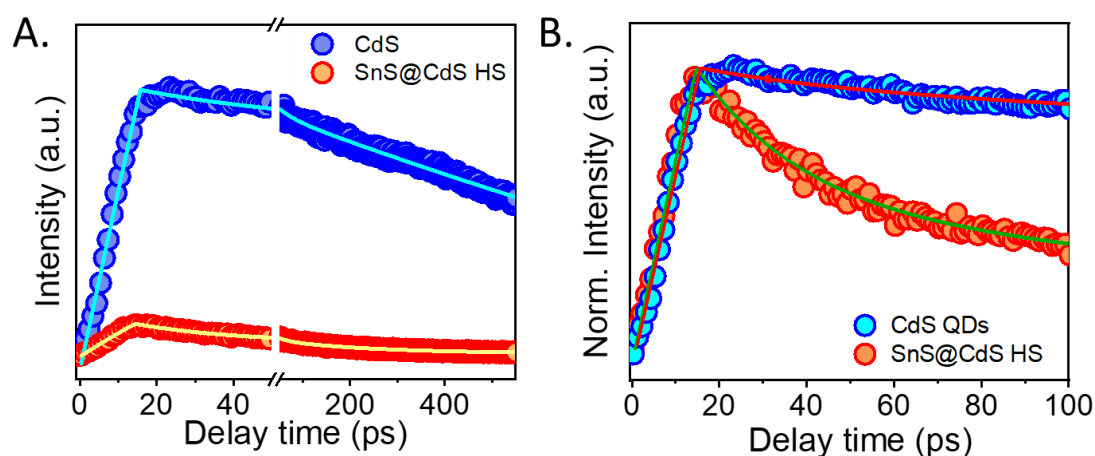


Figure 6.11. (A) Photoluminescence up-conversion trace of CdS QDs and SnS@CdS HS; (B) Normalized photoluminescence up-conversion decay of CdS QDs and SnS@CdS HS dispersed in hexane monitored at 462 nm (bandedge emission) after exciting samples at 400 nm.

Table 6.3. Fluorescence up-conversion time constants of CdS QDs and SnS@CdS HS at 462 nm wavelength after exciting the samples at 400 nm (λ_{ex}). Parentheses indicate the weight percentage of the respective components.

System	τ_1 (ps)	τ_2 (ps)	τ_3 (ps)
CdS QDs (462 nm)	3.91 (8 %)	41.7 (44 %)	277.03 (48 %)
SnS@CdS HS (462 nm)	1.6 (60 %)	10.08 (30 %)	45.7 (10 %)

6.2.3. Femtosecond transient absorption spectroscopy

To further explore the charge transfer dynamics in an early time scale with more accuracy, TA spectroscopy has been employed as it has the ability to unveil the foundation of such charge-transfer pathway by examining the difference in carrier dynamics for both pure SnS NRs and CdS QDs as well as in SnS@CdS p-n heterojunction.⁴⁶ Revealing the carrier cooling dynamics, carrier diffusion, and carrier recombination processes is extremely important to understand the working mechanism and design of highly efficient optoelectronic devices.⁴⁷⁻⁵⁰ With a strong emphasis on comprehending the charge transfer process at the p-n junction of SnS and CdS, the present investigations are mostly focused on exploring charge transfer and relaxation processes in bare SnS NRs and CdS QDs as well as their heterostructure. We have excited the samples at a 350 nm pump to explore the decay pathways of photoexcited charge carriers at the interface of SnS@CdS HS.

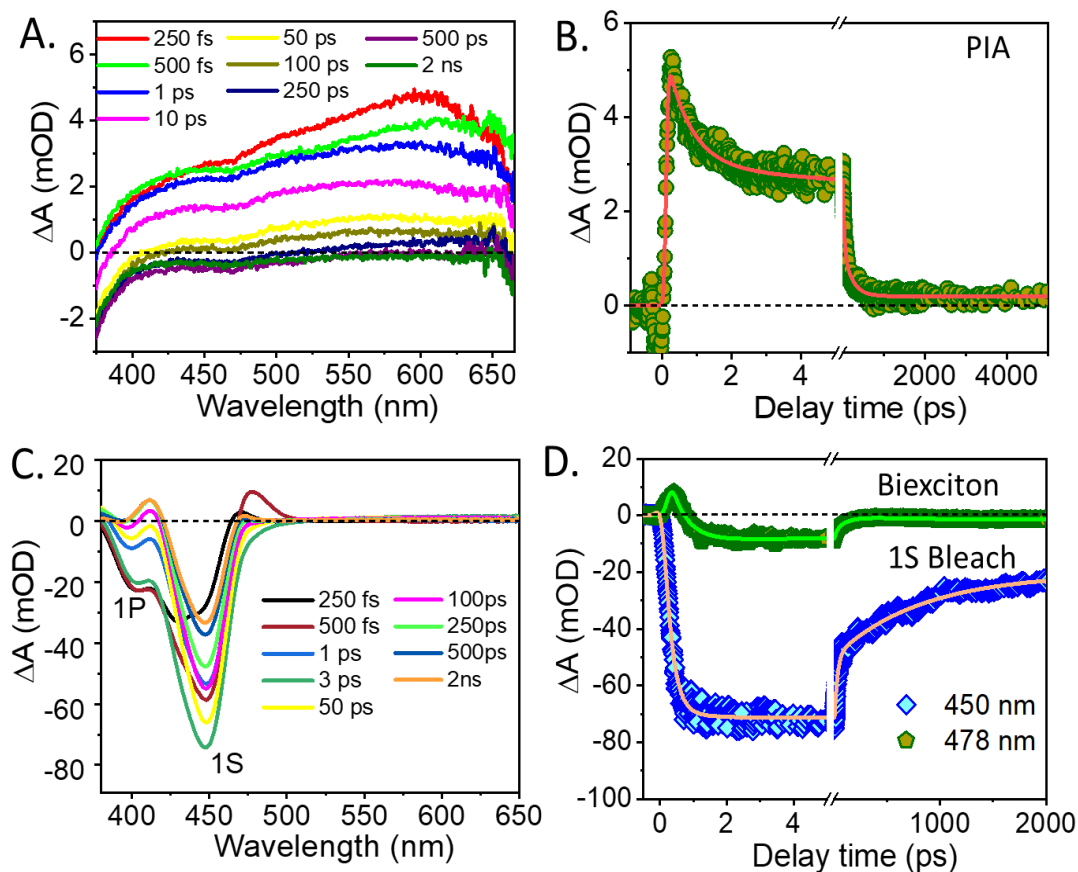


Figure 6.12. Transient absorption spectra of the (A) SnS NRs; (C) CdS QDs; (B) Transient PIA kinetics of SnS NRs probed at 607 nm. (D) Transient decay profiles of CdS QDs at 1S exciton and bandedge biexciton positions. The experiments were carried out after photo-excitation with a 350 nm laser pulse with $200 \mu\text{J}/\text{cm}^2$ laser fluence.

Figure 6.12A shows transient absorption spectra of SnS NRs upon photoexcitation with 350 nm pump. The TA spectra is recorded for different pump-probe delay. The spectrum is dominated by broad positive absorption band in the UV-VIS region with maxima at 607 nm along with a hump in the region 410-460 nm centred at 440 nm. The positive signal can be attributed to the excited state absorption of the photo-excited charge carriers. The broad photo induced absorption (PIA) or excited state absorption is consistent with the earlier reports and is a characteristic signature for carrier trapping as observed in other semiconductors.⁵¹ A similar type of PIA signal has been observed earlier in TA spectra for SnS NSs by Zhang et al. upon photoexcitation with a 1200 nm pump beam.¹⁰ The PIA recovery kinetics process of pristine SnS NRs has been evaluated by plotting the linear dependence of ΔA^{-2} versus delay time. Such temporal dependencies give a clear idea of the various active

recombination processes. **Figure 6.13**, depicts the linear dependence of ΔA^{-2} versus delay time which clearly suggests that highly efficient Auger recombination (exciton-exciton annihilation) dominates at high fluence in SnS.^{50,52} Next, we have monitored the transient kinetics at maximum signal intensity ($\lambda_{\text{probe}} = 607 \text{ nm}$) and the fitting parameters have been provided in the supporting information (**Table 6.4**). The signal grows up to 0.2 ps and afterwards, it decays multi-exponentially as shown in **Figure 6.12B**. Herein, no photoinduced bleach signal was observed due to the existence of a large density of trap states in SnS NRs which favors the PIA signal over the ground state bleach. The transient absorption spectra of bare CdS QDs at different pump-probe delay is shown in **Figure 6.12C**. TA spectra showed a bleach due to 1S excitonic ($1S_{3/2}(\text{h})-1S(\text{e})$) transition i.e., B_1 at 450 nm, and a higher energy excitonic band due to ($1P_{3/2}(\text{h})-1P(\text{e})$) transition i.e., B_2 at 400 nm arising from state filling effect of band edge and high energy exciton.^{53,54} The aforementioned observations are matched with the steady-state absorption spectrum. The derivative-like feature from 470 to 500 nm is due to stark-induced biexciton.^{55,56} The biexciton is formed due to coulombic interactions between pump-generated hot exciton and bandedge exciton generated by the probe beam. The growth of CdS QDs bleach can be fitted with a single exponential time component of 0.42 ps and decay can be fitted with multi-exponential time components (**Table 6.4**). The growth indicates the time taken by the carriers to cool down from higher excited states to the band edge state. The transient kinetics of both band edge exciton and biexciton are shown in **Figure 6.12D**.

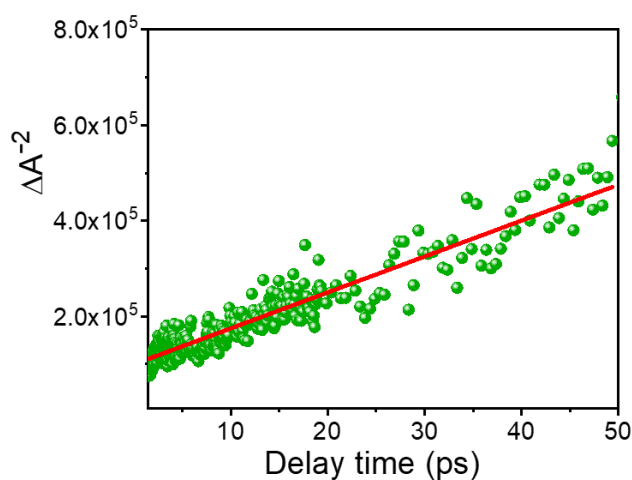


Figure 6.13. Linear dependence of ΔA^{-2} vs. early probe delay time for SnS NRs at 350 nm pump excitation.

Now in order to examine the charge relaxation and transfer dynamics at the interface of SnS NRs and CdS QDs, we have performed ultrafast transient absorption studies of SnS@CdS p-n heterojunction, keeping all the experimental conditions like that of pristine SnS NRs and CdS QDs systems. TA spectra of SnS@CdS HS upon 350 nm photoexcitation is shown in **Figure 6.14A**. The energy corresponds to 350 nm pump excitation and is capable of photoexciting both the SnS and CdS constituents of the heterostructure system across the band gap. The TA spectra exhibit bleach features of CdS QDs at 450 nm and 400 nm, respectively. Moreover, there is an additional broad PIA feature to the red side of bleach in the region 500-650 nm. Besides, it has been observed that there is a huge decrement in the bleach and biexciton intensity in the heterojunction system as compared to its bare counterpart (**Figure 6.14B, C**). The intensity of the bleach has often been related to the number density of photo-generated charge carriers. Such a significant decrease in bleach intensity is attributed to the transfer of photoexcited holes from the valence band of CdS QDs to SnS NRs which is a thermodynamically favourable phenomenon.

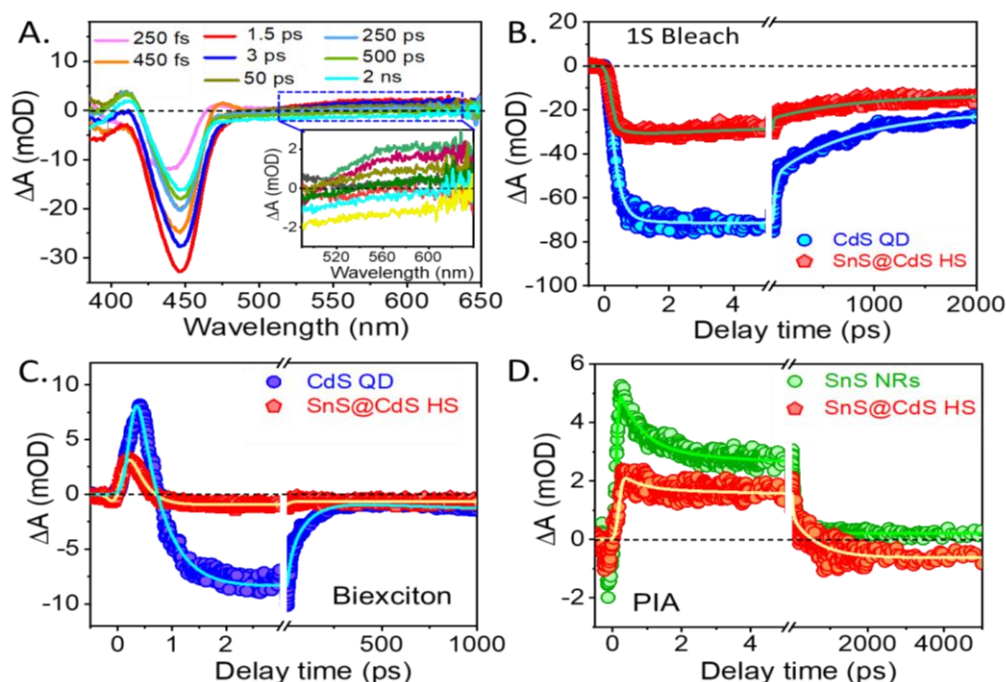


Figure 6.14. Transient absorption spectra of the (A) SnS@CdS HS at different probe delay. Inset: enlarged PIA signature in the red region of the spectra in the heterostructure system. Transient kinetics of CdS QDs and the SnS@CdS HS for the (B) 1S bleach and (C) band edge biexciton signal. (D) PIA signal of SnS NRs and SnS@CdS HS at 607 nm probe wavelength, all the experiments were carried out following 350 nm laser pulse with a $200 \mu\text{J}/\text{cm}^2$ laser fluence.

Again, the drastic decrease in bi-exciton intensity can be attributed to the delocalization/transfer of photo-excited electrons from CdS to SnS which is also a thermodynamically viable process (**Figure 6.14C**). The growth component of the band edge bleach of CdS QDs decreases from 0.42 ps to 0.15 ps in the presence of SnS NRs (**Table 6.4**). Comparing the bleach intensity of 1S exciton for pristine CdS QDs and SnS@CdS heterojunction system, it is found that the growth and recovery of bleach is faster in heterostructure as shown in **Figure 6.15A**, indicating the transfer of holes from CdS QDs to SnS NRs which is a physically feasible process according to their band alignment. Moreover, in the presence of CdS, both the growth and decay of the PIA signal of SnS NRs get relatively slower and interestingly, it eventually inverts into a long-lived broader negative or bleach signal at probe time > 520 ps as shown in **Figure 6.14D**. The slower growth of the PIA signal of SnS NRs in SnS@CdS HS is due to the migration of holes from CdS QDs to SnS NRs as discussed earlier (**Table 6.4**). The slow recovery of SnS NRs positive signal in the presence of CdS QDs (**Figure 6.15B**) demonstrates slow recombination of photoinduced charge carriers i.e., higher charge separation in SnS@CdS p-n heterojunction as holes being in the valence band of SnS NRs and electrons are delocalized in the conduction band of both SnS NRs and CdS QDs owing to their small band offset (**Scheme 6.1**).

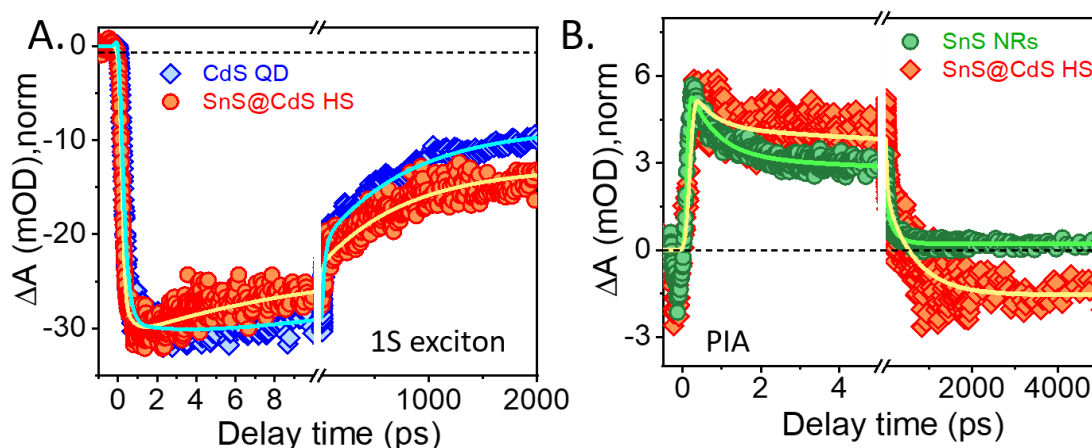
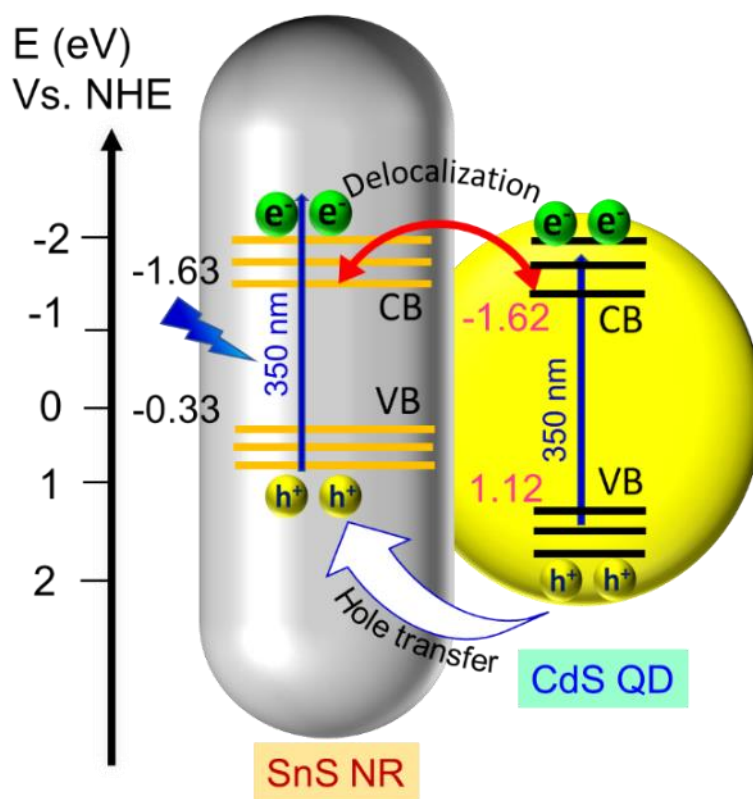


Figure 6.15. Normalized kinetics of (A) bandedge bleach of CdS QDs and SnS@CdS HS, and (B) PIA of SnS NRs and SnS@CdS HS monitored at 607 nm probe wavelength, after photo excitation with 350 nm laser pulse.

Scheme 6.1. Schematic illustration of different photophysical processes occurring at the interface of SnS@CdS p-n heterojunction.



Also, the PIA signal of SnS NRs converts into negative at a longer probe delay time. This broad bleach signal is long-lived depicting the slow recombination between SnS NRs and CdS QDs. As a result, efficient charge separation has been observed in the SnS NR system in the presence of CdS QDs. Further, in order to provide a more convincing picture of the system, we have carried out pump fluence-dependent transient absorption studies of SnS@CdS HS upon 350 nm pump excitation, keeping the pump fluence at $100 \mu\text{J}/\text{cm}^2$, $200 \mu\text{J}/\text{cm}^2$, and $500 \mu\text{J}/\text{cm}^2$ as shown in **Figure 6.16**. The time components for bleach and biexciton remain almost unchanged throughout the fluence range which rule out Auger recombination in SnS@CdS HS. From the fluence studies, we have confirmed that hole migration is efficiently taking place rather than auger recombination in SnS@CdS HS. In applications involving photovoltaic and photocatalytic devices, the spatially separated and long-lived photogenerated charge carriers are greatly required as it has been observed in SnS@CdS p-n heterojunction in the present studies.

Table 6.4. Kinetic fitting parameters at excitonic bleach, biexciton position, and PIA signal for bare CdS QDs, SnS NRs and SnS@CdS HS system upon 350 nm pump excitation with $200\mu\text{J}/\text{cm}^2$ laser fluence.

System	τ_g (ps)	τ_1 (ps)	τ_2 (ps)	τ_3 (ps, ns)	τ_4 (ns)
CdS QDs (445 nm) (1S Exciton)	0.42 (100 %)	47 (35.8 %)	285 (18.3 %)	>1 ns (45.9 %)	
SnS@CdS HS (445 nm) (1S Exciton)	0.15 (100 %)	8.7 (22.4 %)	300 (26.4 %)	>1 ns (51.2 %)	
CdS QDs (478nm) (Biexciton)	< 0.1 (100 %)	0.13 (-100 %)	0.7 (-100%)	60 ps (75 %)	>1 (25 %)
SnS@CdS HS (480 nm) (Biexciton)	< 0.1 (100 %)	0.15 (-100 %)	0.34 (100 %)	4 ps (-25.4 %)	>1 (-74.6%)
SnS NRs (607 nm) (PIA)	< 0.1 (-100 %)	1 (43.5 %)	70 (46.4 %)	> 3 ns (10.1 %)	
SnS@CdS HS (607 nm) (PIA)	0.101 (-100 %)	5 (46.4 %)	125 (53.6 %)	400 ps (-100 %)	>3 (100 %)

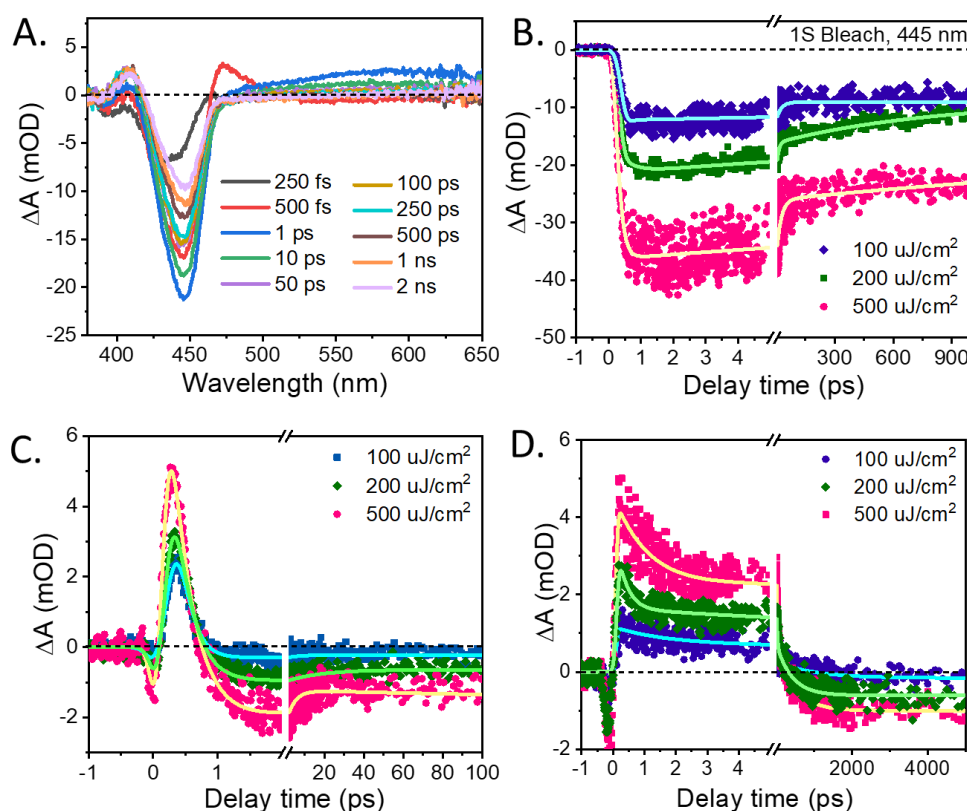


Figure 6.16. (A) TA spectra of SnS@CdS HS at pump fluence of $200\mu\text{J}/\text{cm}^2$. Transient kinetics of (B) 1S bleach, (C) biexciton, and (D) PIA signal in SnS@CdS HS system upon 350 nm pump excitation at different pump fluences ($100\mu\text{J}/\text{cm}^2$, $200\mu\text{J}/\text{cm}^2$ and $500\mu\text{J}/\text{cm}^2$).

6.3. Conclusion

In summary, we have successfully synthesized (1-D) SnS@(0-D) CdS p-n heterojunction for the very first time. The HR-TEM studies clearly confirm the formation of high-quality SnS@CdS p-n heterojunction between (111) lattice plane of SnS NRs and (111) plane of CdS QDs. The steady-state and time-resolved PL studies specify the migration of holes from CdS QDs to SnS NRs. Further, the photo-physics of hole transfer processes involved at the p-n junction of SnS@CdS HS at the femtosecond time region have been investigated using transient absorption spectroscopic techniques. The steady-state and time-resolved PL studies specify the migration of holes from CdS QDs to SnS NRs. The thorough comprehension of charge migration and recombination processes in 1D/0D SnS@CdS p-n heterojunction systems open up new opportunities to further qualify research on boosting the efficiency of solar cells as well as optoelectronic devices.

6.4. References

- (1) Lin, Y.; Guo, X.; Hu, M.; Liu, B.; Dong, Y.; Wang, X.; Li, N.; Wang, H. E. A MoS₂@SnS Heterostructure for Sodium-Ion Storage with Enhanced Kinetics. *Nanoscale* **2020**, *12*, 14689–14698.
- (2) Fan, X.; Wang, B.; Heng, Q.; Chen, W.; Mao, L. Facile In-Situ Synthesis of α -NiS/CdS p-n Junction with Enhanced Photocatalytic H₂ Production Activity. *Int. J. Hydrogen Energy* **2022**, *47*, 32531–32542.
- (3) Bose, R.; Manna, G.; Jana, S.; Pradhan, N. Ag₂S-AgInS₂: P-n Junction Heteronanostructures with Quasi Type-II Band Alignment. *Chem. Commun.* **2014**, *50*, 3074–3077.
- (4) Chao, J.; Xie, Z.; Duan, X.; Dong, Y.; Wang, Z.; Xu, J.; Liang, B.; Shan, B.; Ye, J.; Chen, D.; Shen, G. Visible-Light-Driven Photocatalytic and Photoelectrochemical Properties of Porous SnS_x (x = 1, 2) Architectures. *CrystEngComm* **2012**, *14*, 3163–3168.
- (5) Tripathi, A. M.; Mitra, S. Tin Sulfide (SnS) Nanorods: Structural, Optical and Lithium Storage Property Study. *RSC Adv.* **2014**, *4*, 10358–10366.

-
- (6) Chauhan, H.; Singh, M. K.; Hashmi, S. A.; Deka, S. Synthesis of Surfactant-Free SnS Nanorods by a Solvothermal Route with Better Electrochemical Properties towards Supercapacitor Applications. *RSC Adv.* **2015**, *5*, 17228–17235.
 - (7) Cho, J. Y.; Shin, K.; Lee, H. S.; Neerugatti, K. E.; Heo, J. Influence of Sodium Diffusion from Substrates on Performance of SnS/CdS Thin-Film Solar Cells. *J. Mater. Chem. A* **2019**, *7*, 24186–24190.
 - (8) Wang, L.; Zhai, H.; Jin, G.; Li, X.; Dong, C.; Zhang, H.; Yang, B.; Xie, H.; Sun, H. 3D Porous ZnO-SnS p-n Heterojunction for Visible Light Driven Photocatalysis. *Phys. Chem. Chem. Phys.* **2017**, *19*, 16576–16585.
 - (9) Zi, Y.; Zhu, J.; Hu, L.; Wang, M.; Huang, W. Nanoengineering of Tin Monosulfide (SnS)- Based Structures for Emerging Applications. *Small Sci.* **2022**, *2*, 2100098.
 - (10) Sarkar, A. S.; Mushtaq, A.; Kushavah, D.; Pal, S. K. Liquid Exfoliation of Electronic Grade Ultrathin Tin(II) Sulfide (SnS) with Intriguing Optical Response. *npj 2D Mater. Appl.* **2020**, *4*, 1.
 - (11) Choi, J.; Kim, N. R.; Lim, K.; Ku, K.; Yoon, H. J.; Kang, J. G.; Kang, K.; Braun, P. V.; Jin, H. J.; Yun, Y. S. Tin Sulfide-Based Nanohybrid for High-Performance Anode of Sodium-Ion Batteries. *Small* **2017**, *13*, 1–8.
 - (12) Mieszawska, A. J.; Jalilian, R.; Sumanasekera, G. U.; Zamborini, F. P. The Synthesis and Fabrication of One-Dimensional Nanoscale Heterojunctions. *Small* **2007**, *3*, 722–756.
 - (13) Choi, S. H.; Kang, Y. C. Synthesis for Yolk-Shell-Structured Metal Sulfide Powders with Excellent Electrochemical Performances for Lithium-Ion Batteries. *Small* **2014**, *10*, 474–478.
 - (14) Wang, X.; Zeng, Z.; Fan, Y.; Wang, X.; Wang, S.; Xu, J. Controllable Synthesis and Crystal Facet, Composition and Temperature Dependent Gas Sensing Properties of Sn_{1-x}S-CdS Superlattice Nanowires with Ultrafast Response. *Sens. Actuators B Chem.* **2023**, *377*, 132762.
-

- (15) Ramya, K.; Ramakrishna Reddy, K. T. Investigations on the Parameters Limiting the Performance of CdS/SnS Solar Cell. *Int. J. Energy Res.* **2018**, *42*, 1914–1920.
- (16) Feng, J.; Li, X.; Zhu, G.; Wang, Q. J. Emerging High-Performance SnS/CdS Nanoflower Heterojunction for Ultrafast Photonics. *ACS Appl. Mater. Interfaces* **2020**, *12*, 43098–43105.
- (17) Chang, Y.; Wang, J.; Wu, F.; Tian, W.; Zhai, W. Structural Design and Pyroelectric Property of SnS/CdS Heterojunctions Contrived for Low-Temperature Visible Photodetectors. *Adv. Funct. Mater.* **2020**, *30*, 2001450.
- (18) Ghosh, B.; Das, M.; Banerjee, P.; Das, S.; Fabrication of vacuum-evaporated SnS/CdS Heterojunction for PV Applications. *Sol. Energy Mater Sol. Cells* **2008**, *92*, 1099-1104.
- (19) Alikarami, S.; Soltanizade, A.; and Rashchi, F.; Synthesis of CdS–SnS Photocatalyst by Chemical Co-Precipitation for Photocatalytic Degradation of Methylene Blue and Rhodamine B under Irradiation by Visible Light. *J. Phys. Chem. Solids* **2022**, *171*, 110993.
- (20) Utterback, J. K.; Ruzicka, J. L.; Keller, H. R.; Pellows, L. M.; Dukovic, G. Electron Transfer from Semiconductor Nanocrystals to Redox Enzymes. *Annu. Rev. Phys. Chem.* **2020**, *71*, 335–359.
- (21) Choi, M.-J.; Kim, Y.; Lim, H.; Alarousu, E.; Adhikari, A.; Shaheen, B. S.; Kim, Y. H.; Mohammed, O. F.; Sargent, E. H.; Kim, J. Y.; Jung, Y. S. Tuning Solute-Redistribution Dynamics for Scalable Fabrication of Colloidal Quantum-Dot Optoelectronics. *Adv. Mater.* **2019**, *31*, 1805886.
- (22) Tezcan, F.; Ahmad, A.; Yerlikaya, G.; Zia-ur-Rehman; Paksoy, H.; Kardaş, G. The Investigation of CdS-Quantum-Dot-Sensitized Ag-Deposited TiO₂ NRAs in Photoelectrochemical Hydrogen Production. *New J. Chem.* **2022**, *46*, 9290–9297.

-
- (23) Cho, J. Y.; Kim, S. Y.; Nandi, R.; Jang, J.; Yun, H. S.; Enkhbayar, E.; Kim, J. H.; Lee, D. K.; Chung, C. H.; Kim, J. H.; Heo, J. Achieving over 4% Efficiency for SnS/CdS Thin-Film Solar Cells by Improving the Heterojunction Interface Quality. *J. Mater. Chem. A* **2020**, *8*, 20658–20665.
- (24) Kaur, A.; Goswami, T.; Babu, K. J.; Ghorai, N.; Kaur, G.; Shukla, A.; Rondiya, S. R.; Ghosh, H. N. Probing Ultrafast Charge Separation in CZTS/CdS Heterojunctions through Femtosecond Transient Absorption Spectroscopy. *J. Phys. Chem. C* **2020**, *124*, 19476–19483.
- (25) Kaur, A.; Goswami, T.; Rondiya, S. R.; Jadhav, Y. A.; Babu, K. J.; Shukla, A.; Yadav, D. K.; Ghosh, H. N. Enhanced Charge Carrier Separation and Improved Biexciton Yield at the P-n Junction of SnSe/CdSe Heterostructures: A Detailed Electrochemical and Ultrafast Spectroscopic Investigation. *J. Phys. Chem. Lett.* **2021**, *12*, 10958–10968.
- (26) Xue, J.; Bao, J. Interfacial Charge Transfer of Heterojunction Photocatalysts: Characterization and Calculation. *Surf. Interfaces* **2021**, *25*, 101265.
- (27) Wu, Y.; Wei, T.; An, X.; Liu, L. M. Colloidal Synthesis of SnS Nanocrystals with Dimension-Dependent Photoelectrochemical Properties. *New J. Chem.* **2019**, *43*, 7457–7462.
- (28) Tian, H.; Fan, C.; Liu, G.; Yuan, S.; Zhang, Y.; Wang, M.; Li, E. Ultrafast Broadband Photodetector Based on SnS Synthesized by Hydrothermal Method. *Appl. Surf. Sci.* **2019**, *487*, 1043–1048.
- (29) Bhorde, A.; Pawbake, A.; Sharma, P.; Nair, S.; Funde, A.; Bankar, P.; More, M.; Jadkar, S. Solvothermal Synthesis of Tin Sulfide (SnS) Nanorods and Investigation of Its Field Emission Properties. *Appl. Phys. A* **2018**, *124*, 133.
- (30) Xie, Q.; Zhou, H.; Lv, Z.; Liu, H.; Guo, H. Sn⁴⁺ Self-Doped Hollow Cubic SnS as an Efficient Visible-Light Photocatalyst for Cr(VI) Reduction and Detoxification of Cyanide. *J. Mater. Chem. A* **2017**, *5*, 6299–6309.
- (31) Yang, L.; McCue, C.; Zhang, Q.; Uchaker, E.; Mai, Y.; Cao, G. Highly Efficient Quantum Dot-Sensitized TiO₂ Solar Cells Based on Multilayered Semiconductors (ZnSe/CdS/CdSe). *Nanoscale* **2015**, *7*, 3173–3180.
-

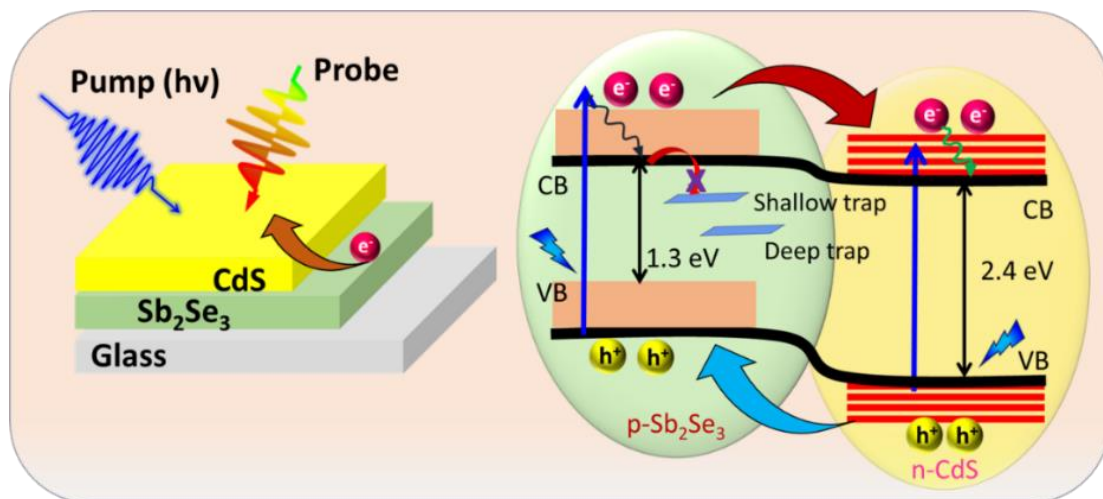
-
- (32) Soltani, N.; Gharibshahi, E.; Saion, E. Band Gap of Cubic and Hexagonal CdS Quantum Dots-Experimental and Theoretical Studies. *Chalcogenide Lett.* **2012**, *9*, 321-328.
- (33) Hao, X.; Hu, Z.; Xiang, D.; Jin, Z. Construction of CdS@Cu_{2-x}S Core-shell p-n Heterojunction with Enhanced Charge Separation for Wide Spectrum Photocatalytic H₂ Evolution. *Mol. Catal.* **2022**, *528*, 112417.
- (34) Li, W.; Ruan, X.; Lian, S.; Xie, C.; Cui, X.; Wang, J. Efficient Charge Carrier Transfer Route Induced by Z-Scheme CdS/BiOBr Heterostructure for Enhanced Photocatalytic Performance. *Mater. Lett.* **2022**, *311*, 131558.
- (35) Gedi, S.; Minnam Reddy, V. R.; Alhammadi, S.; Park, H.; Jang, C.; Park, C.; Kim, W. K. Synthesis and Characterization of π -SnS Nanoparticles and Corresponding Thin Films. *Nanomater.* **2021**, *11*, 767.
- (36) Zhang, K.; Fujitsuka, M.; Du, Y.; Majima, T. 2D/2D Heterostructured CdS/WS₂ with Efficient Charge Separation Improving H₂ Evolution under Visible Light Irradiation *ACS Appl. Mater. Interfaces* **2018**, *10*, 20458–20466.
- (37) Zhang, Y.; Jin, Z.; Yuan, H.; Wang, G.; Ma, B. Well-Regulated Nickel Nanoparticles Functional Modified ZIF-67 (Co) Derived Co₃O₄/CdS p-n Heterojunction for Efficient Photocatalytic Hydrogen Evolution. *Appl. Surf. Sci.* **2018**, *462*, 213–225.
- (38) Kaowphong, S.; Choklap, W.; Chachvalvutikul, A.; Chandet, N. A Novel CuInS₂/m-BiVO₄ p-n Heterojunction Photocatalyst with Enhanced Visible-Light Photocatalytic Activity. *Colloids Surf. A Physicochem. Eng. Asp.* **2019**, *579*, 123639.
- (39) John, S.; Geetha, V.; Francis, M. Effect of PH on the Optical and Structural Properties of SnS Prepared by Chemical Bath Deposition Method. *IOP Conf. Ser. Mater. Sci. Eng.* **2020**, *872*, 12139.
- (40) Kutwade, V. V.; Gattu, K. P.; Sonawane, M. E.; Tonpe, D. A.; Mishra, M. K.; Sharma, R. Contribution in PCE Enhancement: Numerical Designing and Optimization of SnS Thin Film Solar Cell. *J. Nanopart. Res.* **2021**, *23*, 1-9.
-

-
- (41) Hu, X.; Song, G.; Li, W.; Peng, Y.; Jiang, L.; Xue, Y.; Liu, Q.; Chen, Z.; Hu, J. Phase-Controlled Synthesis and Photocatalytic Properties of SnS, SnS₂ and SnS/SnS₂ Heterostructure Nanocrystals. *Mater. Res. Bull.* **2013**, *48*, 2325–2332.
- (42) Balakrishnan, S. K.; Kamat, P.V.; Au–CsPbBr₃ hybrid architecture: anchoring gold nanoparticles on cubic perovskite nanocrystals. *ACS Energy Lett.* **2017**, *2*, 88-93.
- (43) Wu, K.; Chen, J.; McBride, J. R.; Lian, T. Efficient hot-electron transfer by a plasmon-induced interfacial charge-transfer transition. *Science* **2015**, *349*, 632-635.
- (44) Mokari, T.; Rothenberg, E.; Popov, I.; Costi, R.; Banin, U. Selective growth of metal tips onto semiconductor quantum rods and tetrapods. *Science* **2004**, *304*, 1787-1790.
- (45) Thambidurai, M.; Muthukumarasamy, N.; Agilan, S.; Murugan, N.; Vasantha, S.; Balasundaraprabhu, R.; Senthil, T. S. Strong Quantum Confinement Effect in Nanocrystalline CdS. *J. Mater. Sci.* **2010**, *45*, 3254–3258.
- (46) Kambhampati, P. Unraveling the Structure and Dynamics of Excitons in Semiconductor Quantum Dots. *Acc. Chem. Res.* **2011**, *44*, 1–13.
- (47) Goswami, T.; Rani, R.; Hazra, K. S.; Ghosh, H. N. Ultrafast Carrier Dynamics of the Exciton and Trion in MoS₂ Monolayers Followed by Dissociation Dynamics in Au@MoS₂ 2D Heterointerfaces. *J. Phys. Chem. Lett.* **2019**, *10*, 3057–3063.
- (48) Liu, M.; Verma, S. D.; Zhang, Z.; Sung, J.; Rao, A. Nonequilibrium Carrier Transport in Quantum Dot Heterostructures. *Nano Lett.* **2021**, *21*, 8945–8951.
- (49) Kaur, A.; Goswami, T.; Babu, K. J.; Shukla, A.; Bhatt, H.; Ghosh, H. N. Efficient Hot Electron Transfer and Extended Separation of Charge Carriers at the 1P Hot State in Sb₂Se₃/CdSe p–n Heterojunction. *J. Phys. Chem. Lett.* **2022**, *13*, 11354–11362.
-

- (50) Justice Babu, K.; Kaur, G.; Shukla, A.; Saha, R.; Kaur, A.; Sachdeva, M.; Yadav, D.K. and Ghosh, H.N. Fast Polaron Formation and Low Carrier Mobility in Defect-Free Polyhedral CsPbBr₃ Perovskite Nanocrystals. *ACS Photonics* **2022**, *9*, 969-978.
- (51) Ludwig, J.; An, L.; Pattengale, B.; Kong, Q.; Zhang, X.; Xi, P.; Huang, J. Ultrafast Hole Trapping and Relaxation Dynamics in P-Type CuS Nanodisks. *J. Phys. Chem. Lett.* **2015**, *6*, 2671–2675.
- (52) Sun, D.; Rao, Y.; Reider, G. A.; Chen, G.; You, Y.; Brézin, L.; Harutyunyan, A. R.; Heinz, T. F. Observation of Rapid Exciton–Exciton Annihilation in Monolayer Molybdenum Disulfide. *Nano Lett.* **2014**, *14*, 5625-5629.
- (53) Maity, P.; Debnath, T.; Ghosh, H. N. Ultrafast Charge Carrier Delocalization in CdSe/CdS Quasi-Type II and CdS/CdSe Inverted Type I Core–Shell: A Structural Analysis through Carrier-Quenching Study. *J. Phys. Chem. C* **2015**, *119*, 26202–26211.
- (54) Zhang, F.; Xu, N.; Zhao, J.; Wang, Y.; Jiang, X.; Zhang, Y.; Huang, W.; Hu, L.; Tang, Y.; Xu, S. Quantum Confinement-Induced Enhanced Nonlinearity and Carrier Lifetime Modulation in Two-Dimensional Tin Sulfide. *Nanophotonics* **2020**, *9*, 1963-1972.
- (55) Banerjee, S.; Gupta, A.; Srivastava, R.; Datta, A. Temperature Dependent Excited State Dynamics in Dual Emissive CdSe Nano-Tetrapods. *Phys. Chem. Chem. Phys.* **2018**, *20*, 4200–4207.
- (56) Rawalekar, S.; Kaniyankandy, S.; Verma, S.; Ghosh, H. N. Ultrafast Charge Carrier Relaxation and Charge Transfer Dynamics of CdTe/CdS Core–Shell Quantum Dots as Studied by Femtosecond Transient Absorption Spectroscopy. *J. Phys. Chem. C* **2010**, *114*, 1460–1466.

CHAPTER 7

Ultrafast Electron Transfer and Efficient Charge Separation in Sb_2Se_3/CdS Thin Film p-n Heterojunction



Abstract

Harvesting solar energy for different applications requires the development of new semiconducting materials that can absorb a maximum part of the solar spectrum. Antimony selenide (Sb_2Se_3) has attracted tremendous attention over the last few years as a light-harvesting material for photovoltaic device applications owing to its phase stability, high absorption coefficient, earth abundance, and low toxicity. Here, we utilized a thermal evaporation method for depositing high-quality p- Sb_2Se_3 film and making their heterojunction with n-type CdS film. To investigate the charge transfer pathways in the heterojunction system, we then performed the transient absorption (TA) spectroscopy studies. The TA analysis reveals the electron transfer from Sb_2Se_3 to CdS thin film and spatial charge separation at the $\text{Sb}_2\text{Se}_3/\text{CdS}$ p-n heterojunction interface which are further supported by photocurrent measurements. These studies are immensely useful for the fabrication of highly efficient photovoltaic devices.

7.1. Introduction

Antimony selenide (Sb_2Se_3) is an outstanding potential material for solar cells.¹ It has captured the curiosity of researchers all around the world due to its unique and superior properties like high absorption coefficient ($>10^5 \text{ cm}^{-1}$), tunable bandgap (1.1–1.3 eV), good carrier mobility ($100 \text{ cm}^2\text{V}^{-1}\text{s}^{-1}$), and relatively earth-abundant constituents.²⁻⁴ Sb_2Se_3 demonstrates an extensive application prospect in photovoltaic, photodetector, and photocatalysis.^{3,5,6} Mai et al. reported a power conversion efficiency (PCE) of 9.2 % for Sb_2Se_3 solar cells. Till now, this is the highest PCE for Sb_2Se_3 heterojunction solar cells.⁷ Fortunately, several techniques may already be employed to create the Sb_2Se_3 absorber layer, including confined-space sublimation (CSS)⁸ vapor transport deposition (VTD)⁹⁻¹¹, sputtering¹², and chemical bath deposition^{13,14}. Among them, thermal evaporation is a frequently utilized vacuum coating process for the industrial production of large-scale light-emitting displays and other thin-film photoelectric devices.¹⁵ The thermal evaporation deposition technique offers the benefits of straightforward operation, control over deposition rate, reduced impurity integration, extremely low probability of oxide formation as a result of high vacuum, excellent film quality and a simple growth mechanism.¹⁶ This technique has been widely used for the fabrication of Sb_2Se_3 films. Sb_2Se_3 has a high saturation vapor pressure (about 1200 Pa at 550 °C) and a low melting point (around 600 °C).¹⁷ These two properties allow for the simple and high-throughput preparation of high-quality Sb_2Se_3 polycrystalline thin films using a thermal evaporation technique at a relatively low temperature. Sb_2Se_3 is an intrinsically p-type semiconductor.¹⁸ The systematic exploration of a low-bandgap Sb_2Se_3 polycrystalline thin film is encouraged by all these immensely appealing benefits. However, the performance of Sb_2Se_3 solar cells is limited due to the presence of a large density of defect states which cause the trapping of photogenerated electron-hole pairs. Thus, the electron transport layer is required which has an important impact on the efficiency of solar cells. The n-type cadmium sulfide (CdS) is frequently employed as an electron transport layer in Sb_2Se_3 devices to build $\text{Sb}_2\text{Se}_3/\text{CdS}$ p-n heterojunction. CdS film has direct band gap, low resistivity, high transmittance, and comparatively simple film development.¹⁹ We employed a thermal evaporation deposition approach to make CdS thin films.²⁰⁻²² To get higher power conversion efficiency (PCE) from a material, several factors that control device performance need to be optimized. The ultimate device efficiency for heterojunction thin-film solar cells is depend on both the quality of the absorber material and the interface. Fundamental knowledge of the optoelectronic features, including charge carrier dynamics, and the

presence as well as nature of defect states is extremely important to achieve more efficient Sb_2Se_3 solar cells.

In this chapter, Sb_2Se_3 thin films were deposited on a glass substrate at a substrate temperature of 290 °C followed by deposition of CdS film over Sb_2Se_3 by thermal evaporation deposition technique. The films were characterized using X-ray diffraction (XRD) analysis, field emission scanning electron microscopy (FESEM), optical analysis, and X-ray photoelectron spectroscopy (XPS). FESEM results show the uniform distribution of all elements in the $\text{Sb}_2\text{Se}_3/\text{CdS}$ p-n thin film heterojunction. We have performed TA experiments to investigate the charge transfer, trapping, and relaxation dynamics at the interface of $\text{Sb}_2\text{Se}_3/\text{CdS}$ heterojunction. It is observed that the growth time of CdS bleach increases in the $\text{Sb}_2\text{Se}_3/\text{CdS}$ heterojunction due to the electron transfer from Sb_2Se_3 to CdS. It is important to note that a pronounced TA bleach matching the CdS band edge exciton absorption was still present even when the pump excitation energy was changed to 1.9 eV, which is inadequate to directly excite CdS. This unique finding is only conceivable if there is electron transport from the Sb_2Se_3 domain of the heterojunction to the CdS domain. The fabricated $\text{Sb}_2\text{Se}_3/\text{CdS}$ thin film p-n heterojunction demonstrates a higher photocurrent response as compared to pristine Sb_2Se_3 and CdS films owing to charge separation in the heterojunction system. These findings present a unique method for harvesting solar energy and will open a new path for the development of optoelectronic applications for Sb_2Se_3 -based heterojunctions.

7.2. Results and Discussion

7.2.1. Structural and compositional studies

Sb_2Se_3 thin film was prepared on the glass substrates utilizing a thermal evaporation deposition technique using Sb_2Se_3 powder as precursor material. The substrate temperature was kept at 290° C. The basic thermal deposition process is shown in **Figure 7.1**. For the Sb_2Se_3 film, deposited on the substrate at room temperature, no diffraction peaks were observed, indicating the film is amorphous in nature as reported earlier.²³ However, for Sb_2Se_3 film deposited at the substrate temperature of 290° C, strong diffraction peaks were noticed, and all these peaks agreed well in position with the standard diffraction pattern of the orthorhombic phase of Sb_2Se_3 (JCPDS 00–015–0861), confirming its crystalline nature (**Figure 7.2Aa**).^{23,24} We found no peaks corresponding to Sb_2O_3 or another impurity in the XRD spectrum.

The XRD pattern of the CdS film in **Figure 7.2Ab** shows a sharp peak of $\sim 26.5^\circ$, corresponding to the (002) crystal plane of the hexagonal crystal structure of CdS (JCPDS 96-900-8863).^{25,26}

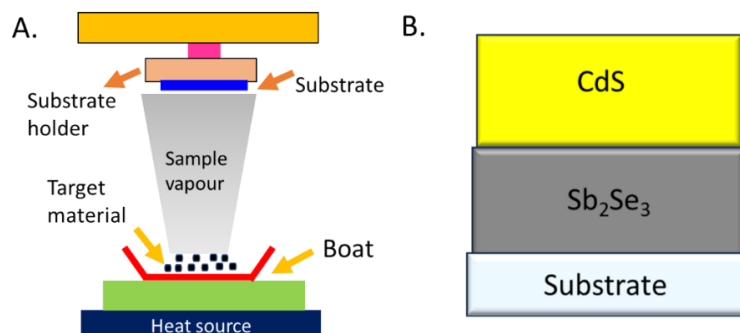


Figure 7.1. Schematic of (A) film deposition by thermal evaporation technique and (B) picture of Sb₂Se₃/CdS thin film heterojunction.

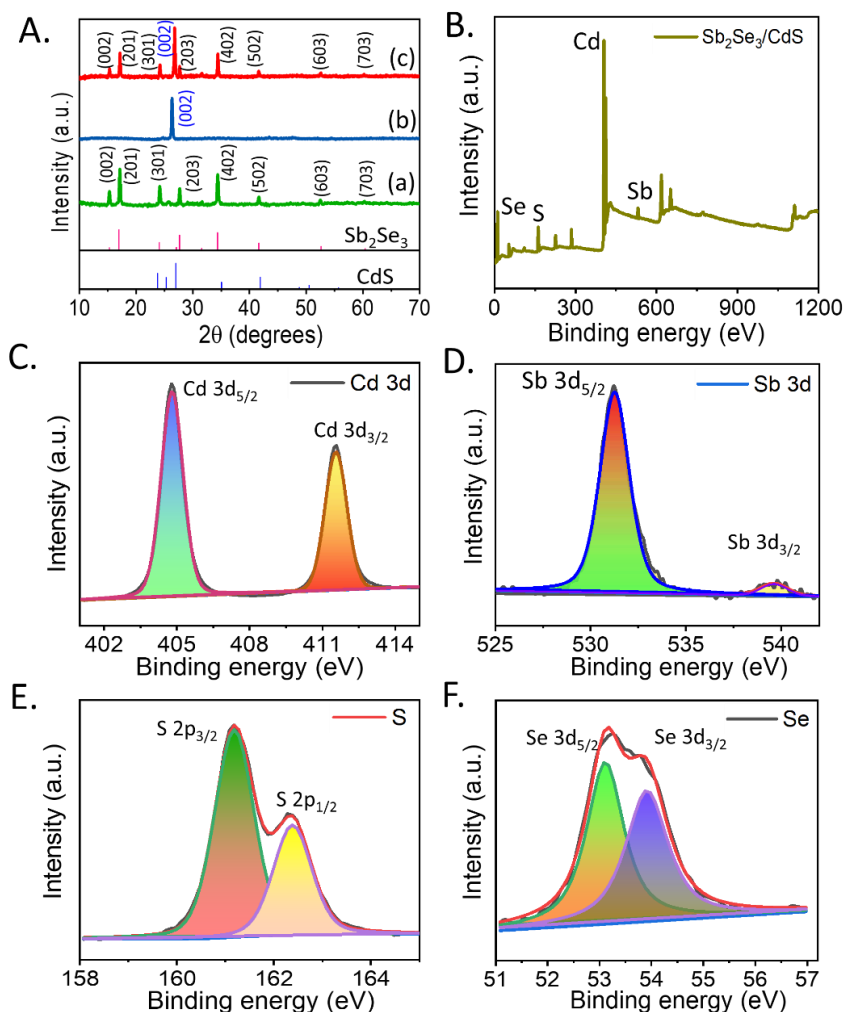


Figure 7.2. (A) XRD pattern of (a) Sb₂Se₃, (b) CdS and (c) Sb₂Se₃/CdS film heterojunction; (B) XPS spectra of Sb₂Se₃/CdS film; High-resolution XPS of (C) Cd, (D) Sb, (E) S, and (F) Se elements.

The XRD pattern of $\text{Sb}_2\text{Se}_3/\text{CdS}$ film shown in **Figure 7.2Ac** consists of peaks from both individual components viz orthorhombic Sb_2Se_3 , as well as hexagonal CdS phases, and no mixed phases were found. This indicates the existence of both materials in the $\text{Sb}_2\text{Se}_3/\text{CdS}$ heterojunction. Further, X-ray photoelectron spectroscopy (XPS) was used to analyze the surface composition and elemental chemical state of the pristine Sb_2Se_3 , CdS films, and $\text{Sb}_2\text{Se}_3/\text{CdS}$ p-n heterojunction film. The XPS survey spectrum in **Figure 7.2(B)** shows the presence of Sb, Se, Cd, and S elements in the $\text{Sb}_2\text{Se}_3/\text{CdS}$ film heterojunction. Further, analysis of the chemical state of the elements was performed by high-resolution XPS spectra. As shown in **Figure 7.2C**, the binding energies of Cd $3d_{5/2}$ and Cd $3d_{3/2}$ of $\text{Sb}_2\text{Se}_3/\text{CdS}$ film are positioned at 401 and 411 eV, respectively, attributed to Cd $3d_{5/2}$ and Cd $3d_{3/2}$ doublets of Cd^{2+} in heterojunction.²⁷ The Sb $3d_{5/2}$ and Sb $3d_{3/2}$ peaks of the $\text{Sb}_2\text{Se}_3/\text{CdS}$ heterojunction are located at binding energies of 531.5 and 539.5 eV, respectively (**Figure 7.2D**). The binding energy of Sb 3d is positively shifted by about 2 eV compared to that of pure Sb_2Se_3 (**Figure 7.3**), but the spacing of the two peaks did not change, indicating that the chemical state of the Sb ion remained unchanged as Sb^{3+} (**Figure 7.2D**). **Figure 7.2F** corresponds to the peaks at 55.1 and 55.9 eV which can be attributed to Se $3d_{5/2}$ and $3d_{3/2}$ of Se^{2-} , respectively, with a positive shift of about 0.85 eV. The S 2p peaks at 161 eV and 162.3 eV correspond to S $2p_{3/2}$ and S $2p_{1/2}$ of S^{2-} in $\text{Sb}_2\text{Se}_3/\text{CdS}$ film heterojunction, respectively.

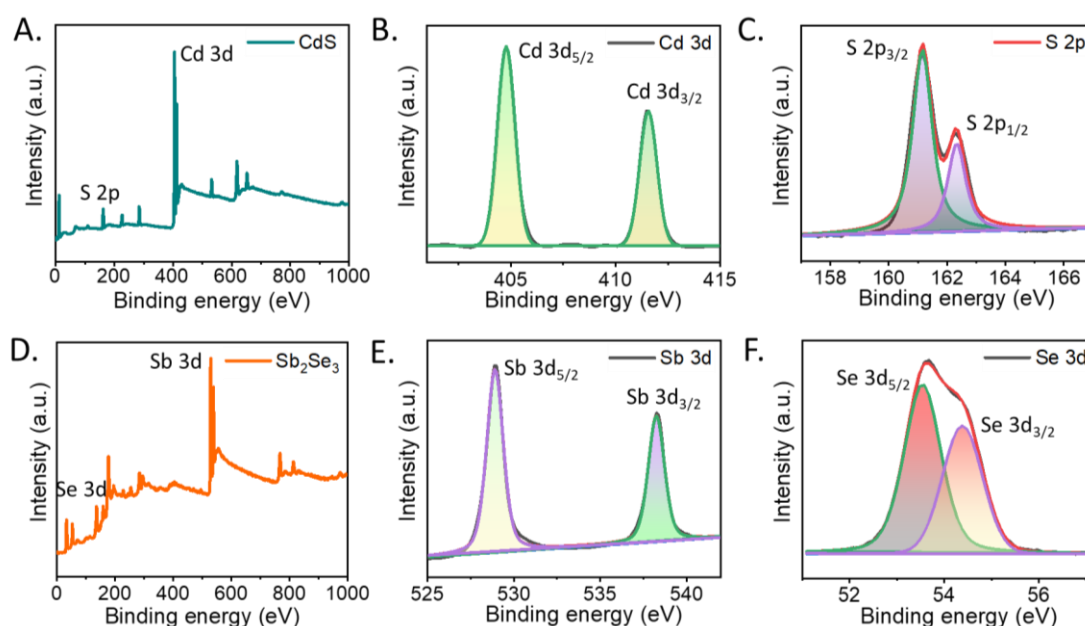


Figure 7.3. XPS of Sb_2Se_3 and CdS films (A) XPS spectrum of CdS film along with high-resolution XPS spectra of (B) Cd 3d, (C) S 2p. (D) XPS spectrum Sb_2Se_3 film along with high-resolution XPS of (E) Sb 3d, (F) Se 3d elements.

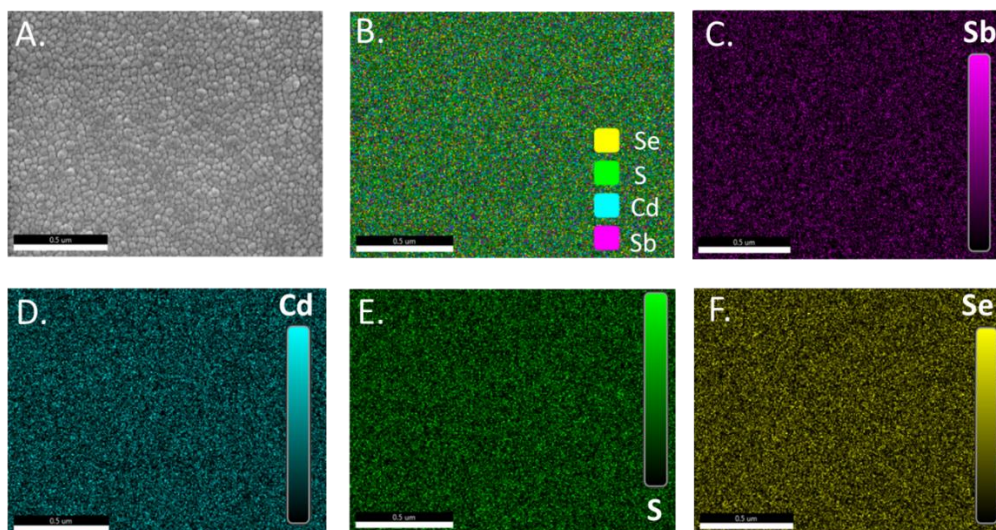


Figure 7.4. (A) FESEM image of $\text{Sb}_2\text{Se}_3@\text{CdS}$ film. (B) EDX Mapping images of $\text{Sb}_2\text{Se}_3@\text{CdS}$ heterojunction, indicating the co-existence and homogenous distribution of (C) Sb, (D) Cd, (E) S, and (F) Se elements.

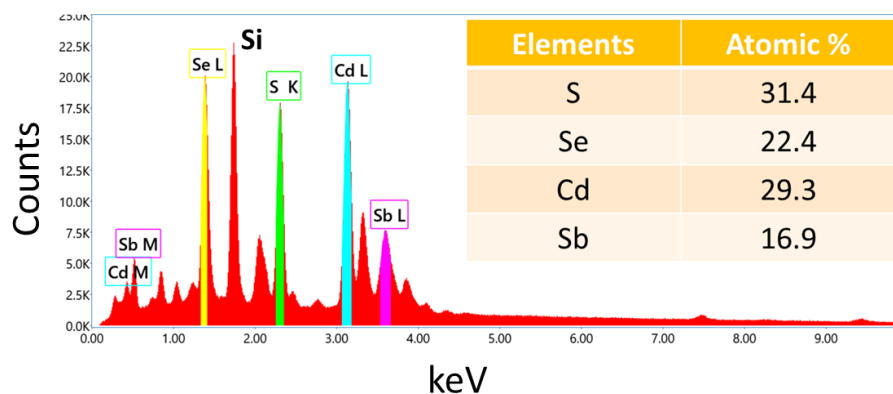


Figure 7.5. Energy dispersive X-ray spectrum of $\text{Sb}_2\text{Se}_3/\text{CdS}$ thin film heterojunction. **Inset:** Observed atomic percentage of Sb, Cd, S, and Se elements.

The XPS studies of pristine Sb_2Se_3 and CdS film are provided in **Figure 7.3**. These results are consistent with the previously reported literature.^{28,29} After the formation of a heterojunction, the charge is transferred between the two semiconductors, eventually leading to a decrease in the electron cloud density of one semiconductor and an increase in the electron cloud density of the other semiconductor, which is manifested in XPS as a shift in the characteristic peaks. The XPS results indicate the successful formation of heterojunction between Sb_2Se_3 and CdS components with a strong interaction. Moreover, the Cd and S elements in $\text{Sb}_2\text{Se}_3/\text{CdS}$ heterojunction are present in the form of Cd^{2+} and S^{2-} further demonstrating the successful deposition of CdS on Sb_2Se_3 .³⁰ The FESEM image of

heterojunction shown in **Figure 7.4A** confirm the uniform growth of the thin film. Further, energy-dispersive X-ray spectroscopy (EDX) elemental mapping was utilized to decipher the composition and elemental distribution of the $\text{Sb}_2\text{Se}_3/\text{CdS}$ p-n heterojunction film. **Figure 7.4 (C-F)** displays the Sb (pink), Cd (blue), S (green), and Se (yellow) EDX colour maps exhibit a homogeneous distribution of all the elements. The EDX elemental analysis confirms the presence of Sb, Cd, S, and Se elements in the as-prepared $\text{Sb}_2\text{Se}_3/\text{CdS}$ heterojunction with the atomic percentage table provided in **Figure 7.5**.

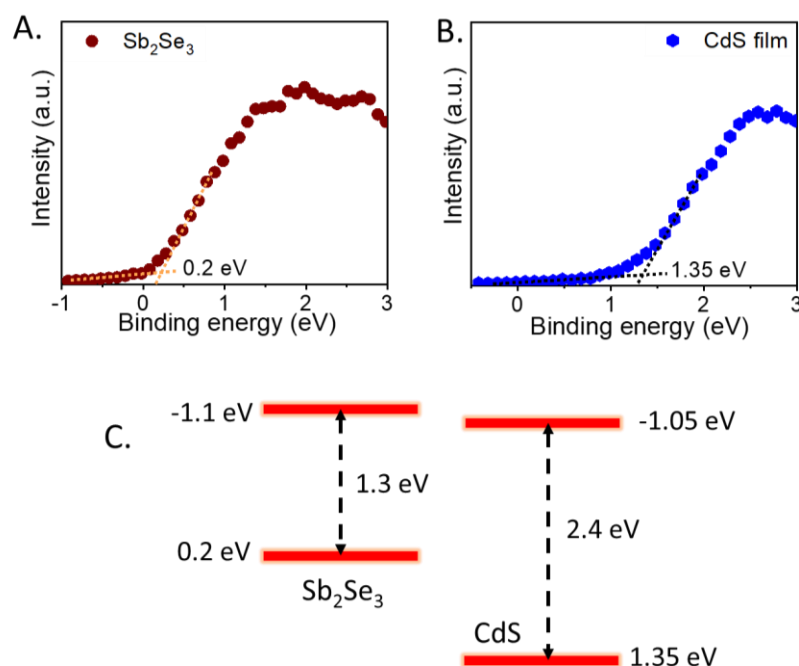


Figure 7.6. Determination of valence band positions of (A) Sb_2Se_3 and (B) CdS films from the XPS valence band spectra. (C) Band alignment of $\text{Sb}_2\text{Se}_3/\text{CdS}$ heterojunction.

In addition, the band gaps and energy levels of CdS and Sb_2Se_3 thin films were determined by UV-vis absorption spectra and X-ray photoelectron spectroscopy (XPS). The bandgap of CdS and Sb_2Se_3 is calculated to be 2.4 and 1.3 eV, respectively. XPS was used to determine the valence band maximum (VBM) of CdS and Sb_2Se_3 thin films. As shown in **Figures 7.6A and 7.6B**, the VBM is estimated to be 0.2 and 1.35 eV, respectively. Therefore, combined with the optical band gap obtained from absorption spectra and XPS data, the positions of the conduction band minimum (CBM) are calculated as -1.1 and -1.05 eV, respectively. Based on the above result, the alignment between Sb_2Se_3 and CdS can be constructed as shown in

Figure 7.6C. Consequently, the conduction band offset (CBO) and valence band offset (VBO) of the $\text{Sb}_2\text{Se}_3/\text{CdS}$ heterojunction are calculated to be +0.05 eV and -1.15 eV, respectively. Therefore, the $\text{Sb}_2\text{Se}_3/\text{CdS}$ interface forms a Type-II heterojunction.³¹

7.2.2. Optical studies

To evaluate material for optoelectronic applications, optical parameters such as optical band gap should be critically analyzed. The steady-state optical absorption spectrum of bare Sb_2Se_3 film shown in **Figure 7.7A** displays a broad absorption in the range of 350–700 nm and the bandgap is calculated to be 1.3 eV (**Figure 7.7B**).³² The absorption spectrum of the CdS film shows the first exciton peak at 480 nm (460-510 nm).³³ Also, from the absorption spectra, the energy bandgap was estimated to be 2.45 eV for CdS film. The measured values closely match the bandgaps reported in the literature.³⁴ Moreover, the absorption of $\text{Sb}_2\text{Se}_3/\text{CdS}$ heterojunction in the visible range is increased as compared to pure CdS film.³⁵

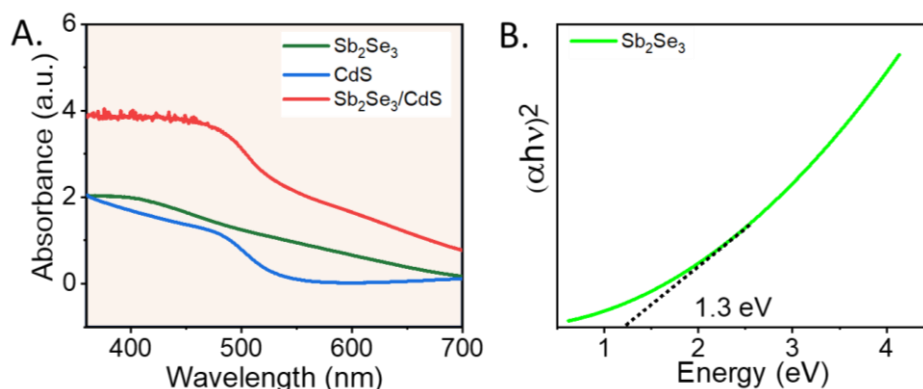


Figure 7.7. (A) Steady-state optical absorption spectrum of pristine Sb_2Se_3 , CdS films, and $\text{Sb}_2\text{Se}_3/\text{CdS}$ heterojunction. (B) Tauc plot for Sb_2Se_3 film.

7.2.3. Transient absorption studies

We have performed TA spectroscopy to probe the charge carrier dynamics in $\text{Sb}_2\text{Se}_3/\text{CdS}$ heterojunction to gain more insight into photophysical processes. TA spectroscopy has proven to be an indispensable tool to monitor charge transfer and recombination dynamics within the $\text{Sb}_2\text{Se}_3/\text{CdS}$ heterojunction system, offering invaluable insights into both single and heterojunction systems.³⁶⁻⁴⁰ The samples were excited with a 410 nm pump pulse and change in the absorbance (ΔA) of the probe

beam in the presence and absence of a pump pulse is monitored. All the experimental conditions were kept similar throughout the experiment. The TA spectrum of Sb_2Se_3 film displayed in **Figure 7.8A** shows a negative photoinduced bleach signal peaking around 579 nm (2.1 eV) which is far from the optical bandgap of Sb_2Se_3 (950 nm), representing excited state bleach and a positive signal with a peak located at 680 nm corresponds to the photo-induced absorption (PIA).⁴¹ The growth of bleach is IRF-limited and it decays very fast (**Figure 7.8B**). The maximum amplitude of the signal decays within 5 ps and the fitting components are provided in **Table 7.1**. Thus, this bleach signal originates from a higher energy band. Previously, Liang et al. also observed a similar negative bleach and PIA signal in Sb_2Se_3 films.⁴¹ The PIA signal can be assigned to the trapping of photo-generated minority carriers.³⁶ The TA kinetics of the PIA signal (**Figure 7.8C**) represent the evolution of charge carrier dynamics. The abrupt rise of the TA signal from the zero-delay position indicates that the ground state electron-hole pairs are excited to a higher energy band to form high energy excitons as the energy of the pump pulse (3 eV) is much larger than the bandgap of Sb_2Se_3 (1.3 eV).

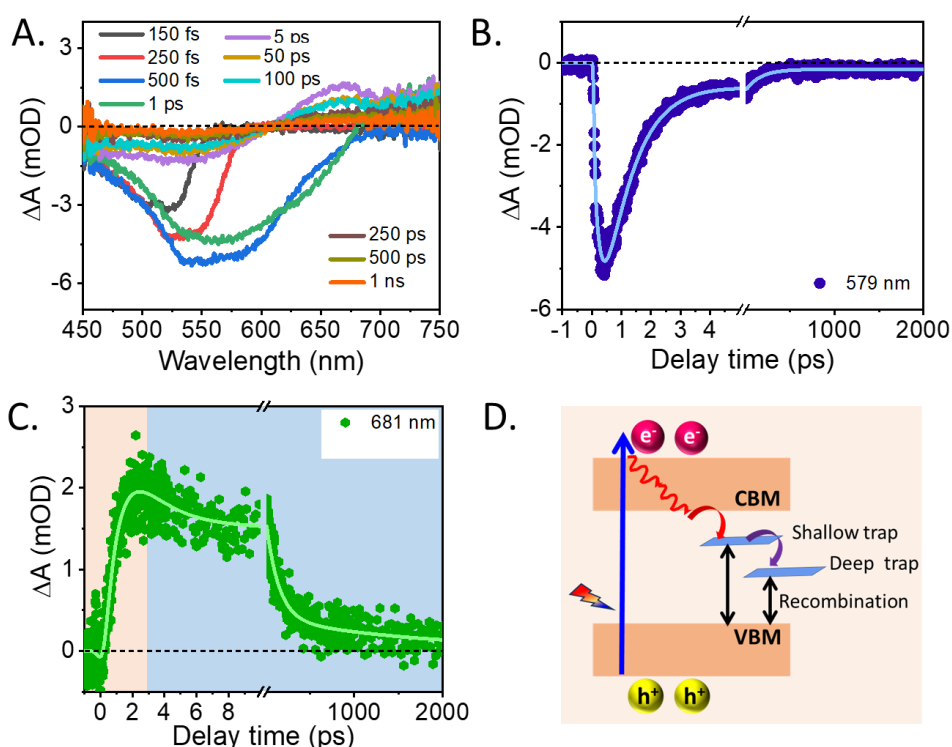


Figure 7.8. TA spectra of (A) Sb_2Se_3 film, (B, C) formation and decay dynamics of Sb_2Se_3 film monitored at 579 and 681 nm probe wavelengths. (D) Schematic diagram showing the different trapping and recombination dynamics of charge carriers in Sb_2Se_3 film after the photoexcitation with a 410 nm laser pulse.

These charge carriers dissipate their excess excitation energy through electron-phonon coupling or electron-electron scattering and then relax to the conduction band minimum and valence band maximum.⁴² After reaching the maximum value, the TA signal decays slowly. The rise in TA indicated in yellow is due to the increased intra-band absorption of the trap states within the bandgap. The blue region shows the decay of excited state carriers which is attributed to trap-assisted recombination which is common in semiconductor materials as reported earlier (**Figure 7.8D**).⁴³ Subsequently, the kinetic decay curves were fitted multi-exponentially (**Figure 7.8B, C**), and the detailed fitting parameters are summarized in **Table 7.1**.

The TA spectra of CdS film as well as the Sb₂Se₃/CdS thin film heterojunction have been recorded and are shown in **Figure 7.9**. **Figure 7.9A** shows the TA spectra of the CdS film after photo excitation with a 410 nm laser pulse as a function of different pump-probe delay times. The TA spectra plots of the photoexcited Sb₂Se₃/CdS heterojunction at different time delay is shown in **Figure 7.9B**. The TA spectrum of Sb₂Se₃/CdS heterojunction looks similar to that of pure CdS film, however, we observed some thought-provoking differences in transient kinetics. The TA spectra of CdS show photobleaching signals with maxima at 500 nm attributed to band edge exciton as discussed in the steady-state absorption spectra, and a positive absorption signal in the red region after 550 nm bleach ascribed to a stark induced biexciton effect. The intensity of bleach and biexciton signal of CdS increases in heterojunction which is possible only if the carriers are migrating to CdS from Sb₂Se₃.

Table 7.1. Fitted parameters for transient kinetic traces of the Sb₂Se₃ film upon photoexcitation with 410 nm pump wavelength.

Sb ₂ Se ₃ film	τ_g	τ_1	τ_2	τ_3
579 nm	< 0.1 ps (100 %)	1 ps (-86.2 %)	67 ps (-9.5 %)	>1 ns (-4.3 %)
681 nm	0.56 ps (-100 %)	4.3 ps (35 %)	40 ps (55 %)	>1 ns (10 %)

To investigate the charge carrier dynamics, cooling, transfer, and recombination dynamics in pristine CdS, Sb₂Se₃, and Sb₂Se₃/CdS heterojunction system, temporal analysis has been carried out at different probe wavelengths.

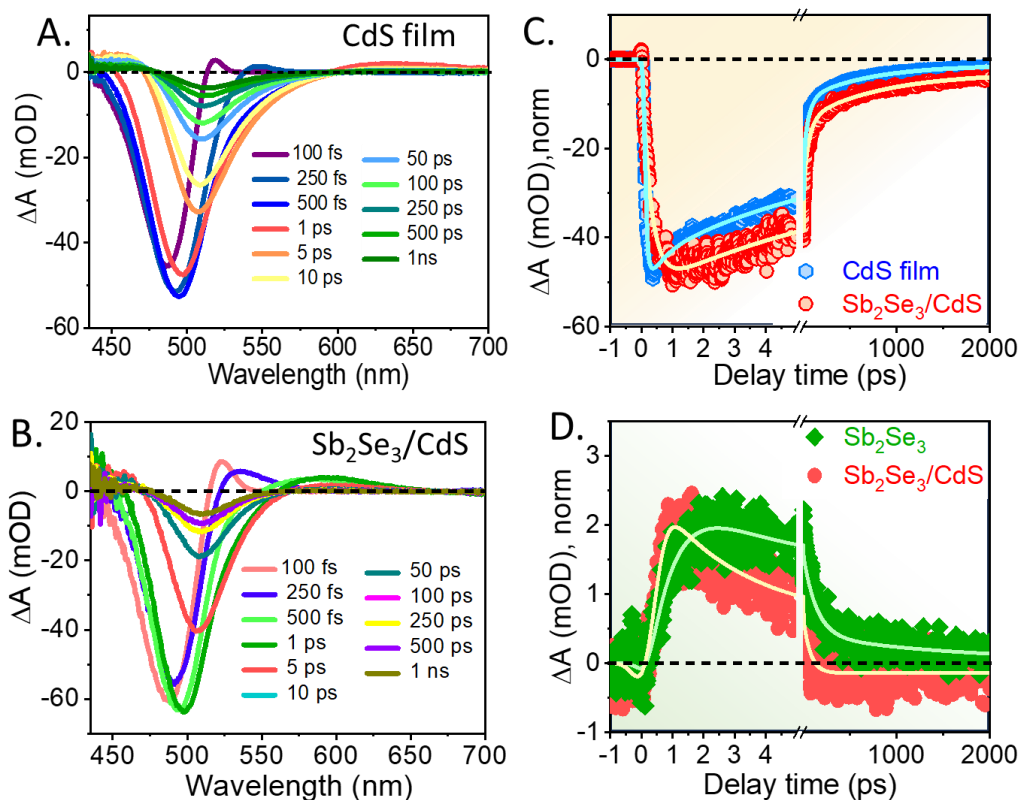
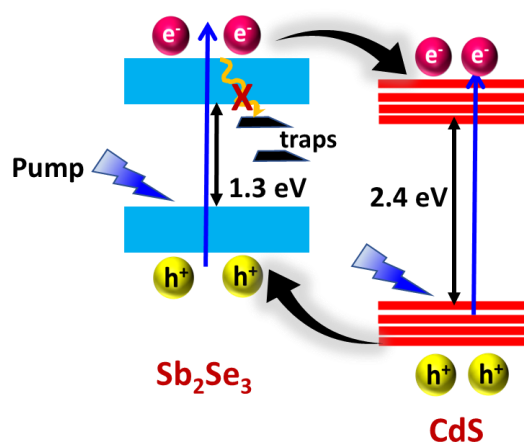


Figure 7.9. TA spectra of (A) CdS film, and (B) Sb₂Se₃/CdS heterojunction at different probe delays following photoexcitation of a 410 nm laser pulse with 200 $\mu\text{J}/\text{cm}^2$ laser fluence. (C) Bleach recovery kinetics of 1S excitonic bleach at 504 and 509 nm for CdS and Sb₂Se₃/CdS heterojunction, respectively. (D) Transient kinetics of the PIA signal of Sb₂Se₃ and Sb₂Se₃/CdS heterojunction monitored at 681 and 650 nm, respectively.

We have monitored the transient decay kinetics of both exciton bleach (1S) and biexciton for bare CdS and Sb₂Se₃/CdS film upon photoexcitation with 410 nm pump pulse and the results are shown in **Figures 7.9C and D**. The transient kinetics at 1S bleach of CdS film is fitted with single-exponential growth with a time constant of <100 fs (IRF limited) and multiexponential decay components listed in **Table 7.2**. Now to understand the carrier dynamics of the photoexcited carriers involved across the p-n junction of the Sb₂Se₃/CdS heterojunction at an ultrafast time scale, we have monitored the kinetics of the bleach and biexciton at 500 nm (1S) and 550 nm in the heterojunction system and compared the results with that of bare CdS film. The decay kinetics of CdS in heterojunction is significantly affected in the presence of Sb₂Se₃. It is found that the growth of the CdS 1S bleach in the Sb₂Se₃/CdS heterojunction is found to be 240 fs, which is slower as compared to the growth of pure CdS film (<100

fs). The growth is assigned to charge carrier cooling from upper excitonic states to the conduction band edge. The slower growth of exciton bleach in the $\text{Sb}_2\text{Se}_3/\text{CdS}$ heterojunction system observed here strongly suggests the dominance of hot electrons transfer from Sb_2Se_3 to CdS over defect-assisted recombination in $\text{Sb}_2\text{Se}_3/\text{CdS}$ heterojunction. This suggests that electrons do not get trapped in the inter-bandgap defect states present in Sb_2Se_3 , but rather get transferred to CdS film which is essential for the fabrication of highly efficient photovoltaic devices. The decay of transient bleach has been fitted multi-exponentially with time constants provided in (Table 2). We have also observed slow recovery of 1S bleach of CdS in the presence of Sb_2Se_3 as compared to that of pure CdS film as indicated in Figure 7.9C.⁴⁴ Recovery of the 1S bleach portrays the depopulation of band edge and excited-state electrons. The slow recovery of the 1S bleach is attributed to the spatial separation of photogenerated charge carriers as a result of the decoupling of electrons and holes in the heterojunction, with electrons being in CdS and holes in Sb_2Se_3 .

Scheme 7.1. Simple scheme representing charge transfer dynamics at the interface of $\text{Sb}_2\text{Se}_3/\text{CdS}$ heterojunction for high-energy (3.0 eV) pump excitation.



As a result, the 1S state of CdS has a longer lifetime in the presence of Sb_2Se_3 ; thus, these carriers can be extracted and are crucial for the improvement of the efficiency of any device, as shown in Scheme 7.1. Furthermore, we monitored the PIA kinetics of Sb_2Se_3 in the absence and presence of CdS. It is found that the growth of the PIA signal of Sb_2Se_3 becomes faster in $\text{Sb}_2\text{Se}_3/\text{CdS}$ heterojunction which further indicates the transfer of hot electrons from Sb_2Se_3 to CdS film. The $\text{Sb}_2\text{Se}_3/\text{CdS}$ heterojunction enhances the ability of charge extraction, which would help in improving the performance of the devices.

Table 7.2. Kinetic fitting parameters at different key wavelengths for Sb_2Se_3 , CdS thin films, and $\text{Sb}_2\text{Se}_3/\text{CdS}$ heterojunction after photoexcitation of the samples with 410 nm pump wavelength.

System	Probe wavelength (nm)	τ_g	τ_1	τ_2	τ_3
CdS film	500	< 0.1 ps	3 ps	52 ps	>1 ns
	(bleach)	(+ 100 %)	(- 57.1%)	(-39 %)	(-3.9 %)
$\text{Sb}_2\text{Se}_3/\text{CdS}$ film	500	0.24 ps	5 ps	80 ps	>1 ns
	(bleach)	(+ 100%)	(-49 %)	(-37.4 %)	(-13.6 %)
CdS film	650	0.2 ps	3.5 ps	28 ps	>1 ns
	(PIA)	(93.3 %)	(-72.2 %)	(-27.8 %)	(6.7 %)

Near Band Edge Excitation: We have further excited the samples on the lower-energy side (pump wavelength, ~ 650 nm; energy, ~ 1.9 eV), maintaining the density of injected carriers similar to that of the 410 nm pump excitation. At this pump energy, CdS film does not get excited as the band gap of CdS film is ~ 2.4 eV, which is higher than the incident pump energy. However, electrons and holes are generated in the Sb_2Se_3 domain as the energy of the pump is higher as compared to the band gap of Sb_2Se_3 ($E_g = 1.3$ eV). **Figures 7.10A and 7.10B** show the TA spectra of the $\text{Sb}_2\text{Se}_3/\text{CdS}$ heterojunction upon 650 nm pump excitation and transient kinetic trace monitored at 500 nm probe wavelength. The appearance of an instantaneous broad bleach (500) confirms the transfer of electrons from the Sb_2Se_3 to the CdS domain in the heterojunction, which is the thermodynamically feasible process according to the band alignment. The bleach at 500 nm appears possible only when the electrons are present at band edge states of CdS. This observation clearly indicates the transfer of electrons from Sb_2Se_3 to CdS film in the $\text{Sb}_2\text{Se}_3/\text{CdS}$ heterojunction system (Scheme 2). The extraction of these charge carriers is substantial for photovoltaic and photocatalytic devices.

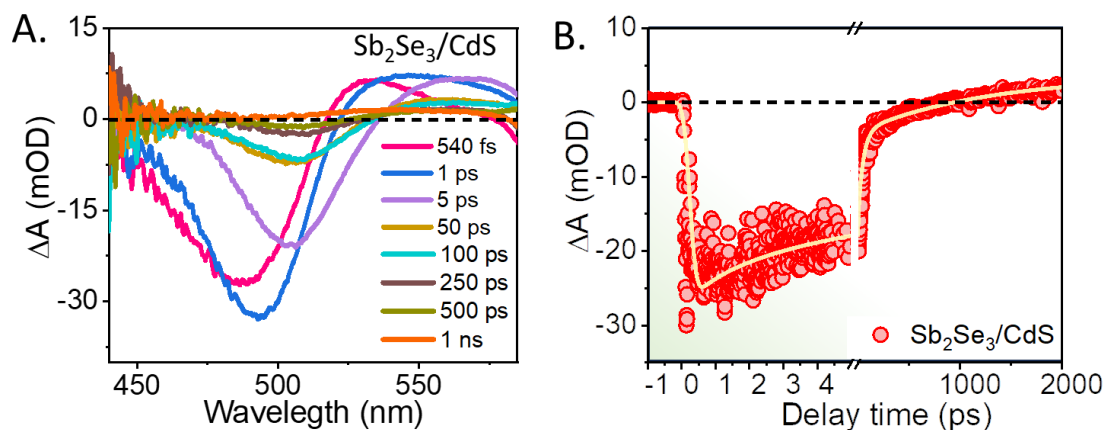
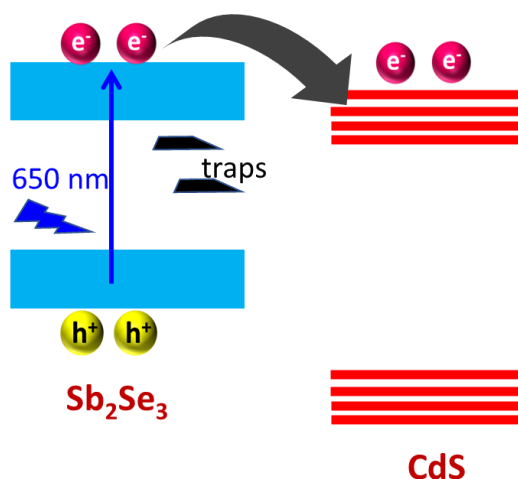


Figure 7.10. (A) TA spectra of the $\text{Sb}_2\text{Se}_3/\text{CdS}$ heterojunction at different probe delays following photoexcitation with 750 nm laser pulse. (B) Transient decay kinetics of bleach signal probed at 503 nm.

Scheme 7.2. Schematic Illustration of charge transfer processes taking place in $\text{Sb}_2\text{Se}_3/\text{CdS}$ heterojunction system upon 650 nm pump excitation.



To investigate the performance of $\text{Sb}_2\text{Se}_3/\text{CdS}$ thin film heterojunction, we have performed time-dependent photoresponse measurements of bare and heterojunction films under solar light illumination. The I-V curves of the $\text{Sb}_2\text{Se}_3/\text{CdS}$ heterojunction film displayed in **Figure 7.11A** showed the diode-like behavior, which gave indirect evidence to demonstrate that p-n heterojunctions were formed between Sb_2Se_3 and CdS. Therefore, the result further supports that the $\text{Sb}_2\text{Se}_3/\text{CdS}$ heterojunction film had been formed between Sb_2Se_3 and CdS. As shown in **Figure 7.11 B**, the time-dependent photoresponse of three different samples including pristine Sb_2Se_3 , CdS, and $\text{Sb}_2\text{Se}_3/\text{CdS}$ heterojunction film are compared. When all the samples are irradiated with the same light source (Xe lamp), the photocurrent

response of $\text{Sb}_2\text{Se}_3/\text{CdS}$ p-n heterojunction film increased substantially as compared to pristine Sb_2Se_3 and CdS films because of higher photogenerated electron-hole separation efficiency at the junction.⁴⁵ These results demonstrate that the formation of the $\text{Sb}_2\text{Se}_3/\text{CdS}$ p-n heterojunction film is advantageous for enhancing the separation of photogenerated carriers.

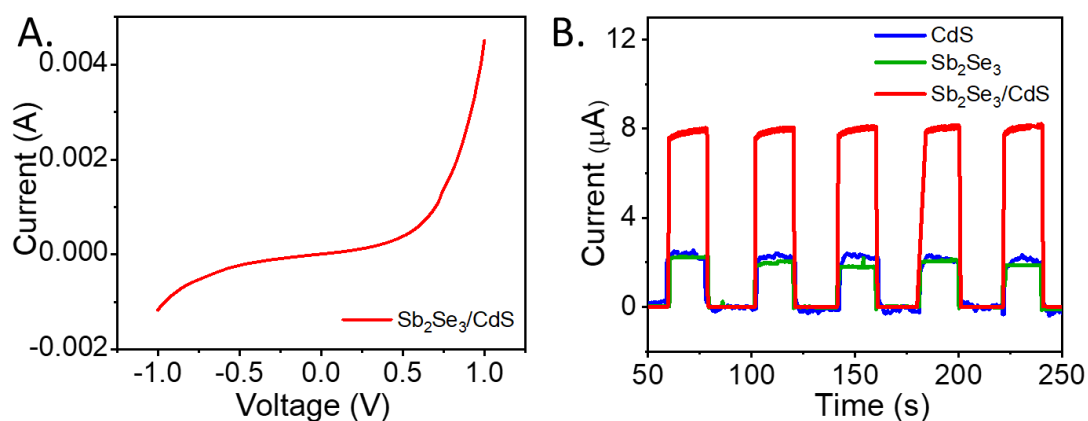


Figure 7.11. (A) I-V characteristics of the $\text{Sb}_2\text{Se}_3/\text{CdS}$ heterojunction. (B) Transient photocurrent response of pristine Sb_2Se_3 , CdS films and $\text{Sb}_2\text{Se}_3/\text{CdS}$ heterojunction film with the periodic (25 s) under solar light illumination of 1 sun power density.

7.3. Conclusion

In summary, we have synthesized $\text{Sb}_2\text{Se}_3/\text{CdS}$ p-n heterojunction film using a two-step thermal evaporation deposition process and performed ultrafast TA studies. XRD, FESEM, and XPS measurements demonstrated the successful formation of $\text{Sb}_2\text{Se}_3/\text{CdS}$ p-n heterojunction. The TA studies reveal the slower bleach growth of CdS bleach in $\text{Sb}_2\text{Se}_3/\text{CdS}$ heterojunction, which indicated the ultrafast electron transfer from Sb_2Se_3 to CdS. The electron transfer was further confirmed by TA results at low-energy pump excitation. Furthermore, the photoresponse of $\text{Sb}_2\text{Se}_3/\text{CdS}$ heterojunction was found to be much higher owing to charge separation in $\text{Sb}_2\text{Se}_3/\text{CdS}$ heterojunction due to the formation of the p-n heterojunction, which creates a depletion region across the junction and promotes charge separation in $\text{Sb}_2\text{Se}_3/\text{CdS}$ heterojunction. Our results emphasize that $\text{Sb}_2\text{Se}_3/\text{CdS}$ heterojunction holds immense potential for extracting charge carriers. This can be used in solar energy harvesting devices such as photodetectors, solar cells, and photocatalyst applications.

7.4. References

- (1) Tang, R.; Zheng, Z. H.; Su, Z. H.; Li, X. J.; Wei, Y. D.; Zhang, X. H.; Fu, Y.Q.; Luo, J. T.; Fan, P.; Liang, G. X. Highly Efficient and Stable Planar Heterojunction Solar Cell Based on Sputtered and Post-Selenized Sb_2Se_3 Thin Film. *Nano Energy* **2019**, *64*, 103929.
- (2) Kaur, A.; Goswami, T.; Babu, K. J.; Shukla, A.; Bhatt, H.; Ghosh, H. N. Efficient Hot Electron Transfer and Extended Separation of Charge Carriers at the 1P Hot State in $\text{Sb}_2\text{Se}_3/\text{CdSe}$ p–n Heterojunction. *J. Phys. Chem. Lett.* **2022**, *13*, 11354–11362.
- (3) Yao, S.; Wang, J.; Cheng, J.; Fu, L.; Xie, F.; Zhang, Y.; Li, L. Improved Performance of Thermally Evaporated Sb_2Se_3 Thin-Film Solar Cells via Substrate-Cooling-Speed Control and Hydrogen-Sulfide Treatment. *ACS Appl. Mater. Interfaces* **2020**, *12*, 24112-24124.
- (4) Ngo, T. T.; Chavhan, S.; Kosta, I.; Miguel, O.; Grande, H. J.; Tena-Zaera, R. Electrodeposition of Antimony Selenide Thin films and application in semiconductor sensitized solar cells. *ACS Appl. Mater. Interfaces* **2014**, *6*, 2836-2841.
- (5) Garcia-Osorio, D. A.; Shalvey, T. P.; Banerji, L.; Saeed, K.; Neri, G.; Phillips, L. J.; Hutter, O. S.; Casadevall, C.; Antón-García, D.; Reisner, E.; Major, J. D. Hybrid Photocathode Based on a Ni Molecular Catalyst and Sb_2Se_3 for solar H_2 production. *ChemComm.* **2023**, *59*, 944-947.
- (6) Singh, Y.; Parmar, R.; Srivastava, A.; Yadav, R.; Kumar, K.; Rani, S.; Shashi, Srivastava, S. K.; Husale, S.; Sharma, M.; Kushvaha, S. S. Highly Responsive Near-Infrared $\text{Si}/\text{Sb}_2\text{Se}_3$ Photodetector via Surface Engineering of Silicon. *ACS Appl. Mater. Interfaces* **2023**, *15*, 25, 30443–30454.
- (7) Li, Z.; Liang, X.; Li, G.; Liu, H.; Zhang, H.; Guo, J.; Chen, J.; Shen, K.; San, X.; Yu, W.; Schropp, R. E. 9.2%-Efficient Core-Shell Structured Antimony Selenide Nanorod Array Solar Cells. *Nat. Commun.* **2019**, *10*, 125.
- (8) Hutter, O. S.; Phillips, L. J.; Durose, K.; Major, J. D. 6.6% Efficient Antimony Selenide Solar Cells using Grain Structure Control and an Organic Contact Layer. *Sol. Energy Mater. Sol. Cells.* **2018**, *188*, 177-181.

-
- (9) Hu, X.; Tao, J.; Weng, G.; Jiang, J.; Chen, S.; Zhu, Z.; Chu, J. Investigation of Electrically-Active Defects in Sb₂Se₃ Thin-Film Solar Cells with up to 5.91% Efficiency via Admittance Spectroscopy. *Sol. Energy Mater. Sol. Cells* **2018**, *186*, 324-329.
- (10) Zhang, Z.; Hu, M.; Jia, T.; Du, J.; Chen, C.; Wang, C.; Liu, Z.; Shi, T.; Tang, J.; Leng, Y. Suppressing the Trapping Process by Interfacial Charge Extraction in Antimony Selenide Heterojunctions. *ACS Energy Lett.* **2021**, *6*, 1740-1748.
- (11) Wen, X.; Chen, C.; Lu, S.; Li, K.; Kondrotas, R.; Zhao, Y.; Chen, W.; Gao, L.; Wang, C.; Zhang, J.; Niu, G. Vapor Transport Deposition of Antimony Selenide Thin Film Solar Cells with 7.6% efficiency. *Nat. Commun.* **2018**, *9*, 2179.
- (12) Liang, G. X.; Zheng, Z. H.; Fan, P.; Luo, J. T.; Hu, J. G.; Zhang, X. H.; Ma, H. L.; Fan, B.; Luo, Z. K.; Zhang, D. P. Thermally Induced Structural Evolution and Performance of Sb₂Se₃ Films and Nanorods Prepared by an Easy Sputtering Method. *Sol. Energy Mater. Sol. Cells* **2018**, *174*, 263-270.
- (13) Ju, T.; Koo, B.; Jo, J. W.; Ko, M. J. Enhanced Photovoltaic Performance of Solution-Processed Sb₂Se₃ Thin Film Solar Cells by Optimizing Device Structure. *Curr. Appl. Phys.* **2020**, *20*, 282-287.
- (14) Li, Z.; Chen, X.; Zhu, H.; Chen, J.; Guo, Y.; Zhang, C.; Zhang, W.; Niu, X.; Mai, Y. Sb₂Se₃ Thin Film Solar Cells in Substrate Configuration and the Back Contact Selenization. *Sol. Energy Mater. Sol. Cells* **2017**, *161*, 190-196.
- (15) Lee, D.; Cho, J. Y.; Heo, J. Improved Efficiency of Sb₂Se₃/CdS Thin-Film Solar Cells: The Effect of Low-Temperature Pre-Annealing of the Absorbers. *Sol. Energy* **2018**, *173*, 1073-1079.
- (16) Chen, S.; Liu, T.; Zheng, Z.; Ishaq, M.; Liang, G.; Fan, P.; Chen, T.; Tang, J. Recent Progress and Perspectives on Sb₂Se₃-Based Photocathodes for Solar Hydrogen Production via Photoelectrochemical Water Splitting. *J. Energy Chem.* **2022**, *67*, 508-523.
- (17) Liu, X.; Xiao, X.; Yang, Y.; Xue, D. J.; Li, D. B.; Chen, C.; Lu, S.; Gao, L.; He, Y.; Beard, M. C.; Wang, G. Enhanced Sb₂Se₃ Solar Cell Performance Through Theory-Guided Defect Control. *Prog. Photovolt.: Res. Appl.* **2017**, *25*, 861-870.
-

- (18) Molli, M.; Pradhan, P.; Dutta, D.; Jayaraman, A.; Bhat Kademane, A.; Muthukumar, V. S.; Kamiseti, V.; Philip, R. Study of Nonlinear Optical Absorption Properties of Sb_2Se_3 Nanoparticles in the Nanosecond and Femtosecond Excitation Regime. *Appl. Phys. A* **2016**, *122*, 1-5.
- (19) Kumar, S. G.; Rao, K. K. Physics and Chemistry of CdTe/CdS Thin Film Heterojunction Photovoltaic Devices: Fundamental and Critical Aspects. *Energy Environ. Sci.* **2014**, *7*, 45-102.
- (20) Isik, M.; Gullu, H. H.; Delice, S.; Parlak, M.; Gasanly, N. M. Structural and Temperature-Dependent Optical Properties of Thermally Evaporated CdS Thin Films. *Mater. Sci. Semicond.* **2019**, *93*, 148-152.
- (21) Sahay, P. P.; Nath, R. K.; Tewari, S.J.C.R.; Optical Properties of Thermally Evaporated CdS Thin Films. *Cryst. Res. Technol.* **2007**, *42*, 275-280.
- (22) Zhang, L.; Ai, Z.; Xu, X.; Shi, D.; Zhang, B.; Hu, H.; Yang, M.; Shao, Y.; Wu, Y.; Hao, X. Research Progress on Synthetic and Modification Strategies of CdS-Based Photocatalysts. *Ionics* **2023**, *29*, 2115–2139.
- (23) Chen, C.; Li, W.; Zhou, Y.; Chen, C.; Luo, M.; Liu, X.; Zeng, K.; Yang, B.; Zhang, C.; Han, J.; Tang, J. Optical Properties of Amorphous and Polycrystalline Sb_2Se_3 Thin Films Prepared by Thermal Evaporation. *Appl. Phys. Lett* **2015**, *107*, 043905.
- (24) Liu, X.; Chen, J.; Luo, M.; Leng, M.; Xia, Z.; Zhou, Y.; Qin, S.; Xue, D. J.; Lv, L.; Huang, H.; Niu, D. Thermal Evaporation and Characterization of Sb_2Se_3 Thin Film for Substrate $\text{Sb}_2\text{Se}_3/\text{CdS}$ solar cells. *ACS Appl. Mater. Interfaces.* **2014**, *6*, 10687-10695.
- (25) Memarian, N.; Rozati, S. M.; Concina, I.; Vomiero, A. Deposition of Nanostructured CdS Thin Films by Thermal Evaporation Method: Effect of Substrate Temperature. *Mater.* **2017**, *10*, 773.
- (26) Dey, M.; Das, N. K.; Gupta, A. S.; Dey, M.; Hossain, M. S.; Matin, M. A.; Amin, N. February. Deposition of CdS Thin Film by Thermal Evaporation. *Int. Conf. Electr. Comput. Commun. Eng.* **2019**, 1-5.

-
- (27) Shao, M.; Wang, A.; Cui, H.; Liu, Z.; Xu, Y.; Li, Z.; Xu, S. Fabrication of ZnFe₂O₄ Decorated CdS Nanosphere Composites with Excellent Visible Light Photocatalytic Activity. *J. Mater. Sci.: Mater. Electron.* **2020**, *31*, 1472-1482.
- (28) Tian, Y.; Sun, Z.; Zhao, Y.; Zhang, Y.; Tan, T.; Yin, F. Facile Spray Drying Approach to Synthesize Sb₂Se₃/rGO Composite Anode for Lithium-Ion Battery. *J. Nanoparticle Res.* **2019**, *21*, 1-11.
- (29) Ju, T.; Koo, B.; Jo, J. W.; Ko, M. J. Enhanced Photovoltaic Performance of Solution-Processed Sb₂Se₃ Thin Film Solar Cells by Optimizing Device Structure. *Curr. Appl. Phys.* **2020**, *20*, 282-287.
- (30) Xin, C.; Cheng, Y.; Wang, J.; Sun, Q.; Liu, E.; Hu, X.; Miao, H. Hole Storage Interfacial Regulation of Sb₂Se₃ Photocathode with Significantly Enhanced Photoelectrochemical Performance. *Langmuir* **2022**, *39*, 627-637.
- (31) Cai, H., Cao, R.; Gao, J.; Qian, C.; Che, B.; Tang, R.; Zhu, C.; Chen, T. Interfacial Engineering Towards Enhanced Photovoltaic Performance of Sb₂Se₃ Solar Cell. *Adv. Funct. Mater.* **2022**, *32*, 2208243.
- (32) Zhang, L.; Li, Y.; Li, C.; Chen, Q.; Zhen, Z.; Jiang, X.; Zhong, M.; Zhang, F.; Zhu, H. Scalable Low-Band-gap Sb₂Se₃ Thin-Film Photocathodes for Efficient Visible–Near-Infrared Solar Hydrogen Evolution. *ACS nano* **2017**, *11*, 12753-12763.
- (33) Cooper, J. K.; Cao, J.; Zhang, J. Z. Exciton dynamics of CdS Thin Films Produced by Chemical Bath Deposition and DC Pulse Sputtering. *ACS Appl. Mater. Interfaces* **2013**, *5*, 7544-7551.
- (34) Kumari, S.; Suthar, D.; Kannan, M. D.; Kumari, N.; Dhaka, M. S. Towards Halide Treatment on CdS Thin Films for Solar Cell Applications: An Evolution to Ion Size Impact on Segregation and Grain Boundaries Passivation. *J. Alloys Compd.* **2023**, *960*, 170593.
- (35) Najm, A. S.; Naeem, H. S.; Majdi, H. S.; Hasbullah, S. A.; Hasan, H. A.; Sopian, K.; Bais, B.; Al-Iessa, H. J.; Dhahad, H. A.; Ali, J. M.; Sultan, A.J. An in-Depth Analysis of Nucleation and Growth Mechanism of CdS Thin Film Synthesized by Chemical Bath Deposition (CBD) Technique. *Sci. Rep.* **2022**, *12*, 15295.
-

-
- (36) Kaur, A.; Goswami, T.; Babu, K. J.; Ghorai, N.; Kaur, G.; Shukla, A.; Rondiya, S. R.; Ghosh, H. N. Probing Ultrafast Charge Separation in CZTS/CdS Heterojunctions through Femtosecond Transient Absorption Spectroscopy. *J. Phys. Chem. C* **2020**, *124*, 19476–19483.
- (37) Kaur, A.; Goswami, T.; Rondiya, S. R.; Jadhav, Y. A.; Babu, K. J.; Shukla, A.; Yadav, D. K.; Ghosh, H. N. Enhanced Charge Carrier Separation and Improved Biexciton Yield at the P-n Junction of SnSe/CdSe Heterostructures: A Detailed Electrochemical and Ultrafast Spectroscopic Investigation. *J. Phys. Chem. Lett.* **2021**, *12*, 10958–10968.
- (38) Justice Babu, K.; Kaur, G.; Shukla, A.; Saha, R.; Kaur, A.; Sachdeva, M.; Yadav, D.K. and Ghosh, H. N. Fast Polaron Formation and Low Carrier Mobility in Defect-Free Polyhedral CsPbBr₃ Perovskite Nanocrystals. *ACS Photonics* **2022**, *9*, 969-978.
- (39) Kaur, A.; Goswami, T.; Babu, K. J.; Ghosh, H. N. Ultrafast Hole Migration at the p–n Heterojunction of One-Dimensional SnS Nanorods and Zero-Dimensional CdS Quantum Dots. *J. Phys. Chem. Lett.* **2023**, *14*, 7483-7489.
- (40) Okuhata, T.; Katayama, T.; Tamai, N. Ultrafast and Hot Electron Transfer in CdSe QD–Au Hybrid Nanostructures. *J. Phys. Chem. Lett. C* **2019**, *124*, 1099-1107.
- (41) Liang, G.; Chen, M.; Ishaq, M.; Li, X.; Tang, R.; Zheng, Z.; Su, Z.; Fan, P.; Zhang, X.; Chen, S. Crystal Growth Promotion and Defects Healing Enable Minimum Open-Circuit Voltage Deficit in Antimony Selenide Solar Cells. *Adv. Sci.* **2022**, *9*, 2105142.
- (42) Sharma, A.; Sharma, C.; Bhattacharyya, B.; Gambhir, K.; Kumar, M.; Chand, S.; Mehrotra, R.; Husale, S. Plasmon Induced Ultrafast Injection of Hot Electrons in Au Nanoislands Grown on a CdS Film. *J. Mater. Chem. C* **2017**, *5*, 618-626.
- (43) Singh, P.; Ghorai, N.; Thakur, A.; Ghosh, H. N. Temperature-Dependent Ultrafast Charge Carrier Dynamics in Amorphous and Crystalline Sb₂Se₃ Thin Films. *J. Phys. Chem. C* **2021**, *125*, 5197-5206.
-

- (44) Tang, R.; Wang, X.; Lian, W.; Huang, J.; Wei, Q.; Huang, M.; Yin, Y.; Jiang, C.; Yang, S.; Xing, G.; Chen, S. Hydrothermal Deposition of Antimony Selenosulfide Thin Films Enables Solar Cells with 10% Efficiency. *Nat. Energy*. **2020**, 5,587-595.
- (45) Choi, D.; Jang, Y.; Lee, J.; Jeong, G. H.; Whang, D.; Hwang, S. W.; Cho, K. S.; Kim, S. W. Diameter-Controlled and Surface-Modified Sb₂Se₃ Nanowires and Their Photodetector Performance. *Sci. Rep.* **2014**, 4, 6714.

CHAPTER 8

Conclusions and Future Perspective

8.1. Conclusions

The major goal of the current thesis is to address certain fundamental photophysical properties of a few well-known metal chalcogenide-based p-n semiconductor heterojunctions that have not yet been fully explored. These characteristics are especially important from the standpoint of photovoltaic and photocatalytic applications. We have utilized femtosecond transient absorption (TA) spectroscopy to investigate the innate photophysical processes in several metal chalcogenide-based semiconductors and their heterojunctions. The first chapter of my dissertation focuses on providing a thorough examination of the "Introduction" to my work. The second chapter covers the synthesis methodologies, and experimental techniques employed throughout my thesis work. The details of the various experimental setups have also been included in this chapter. Beginning with the third chapter, I have talked about several projects that I have worked on using femtosecond TA spectroscopy to analyze the complicated optical behavior at the interface of CZTS/CdS, SnSe/CdSe, Sb₂Se₃/CdSe, SnS/CdS, Sb₂Se₃/CdS p-n heterojunctions.

The third chapter describes the synthesis of Cu₂ZnSnS₄ (CZTS) NPs and CdS QDs and the fabrication of CZTS, CdS, and CZTS/CdS heterojunction thin films using the spin-coating technique. The steady-state and time-resolved photoluminescence studies provide evidence of the hole transfer from photoexcited CdS to CZTS. The hole transfer rate constant was calculated to be $0.366 \times 10^9 \text{ sec}^{-1}$. The charge transfer efficiency in the heterointerface was established by the ultrafast experiments. The results show a drastic increase in the CdS bleach signal intensity in the CZTS/CdS heterojunction which firmly demonstrates the electron transfer from the CZTS domain to the CdS domain with a time constant of 0.14 ps. Our results therefore demonstrate the fast charge separation in CZTS/CdS heterojunction film.

The fourth chapter examines in-depth the underlying hot carrier relaxation and transfer strategies within the SnSe/CdSe p-n heterostructure. The partial cation exchange of Cd²⁺ in CdSe QDs with Sn²⁺ ions result in the synthesis of SnSe/CdSe heterostructure. HRTEM analysis has validated the epitaxial growth of the (400) plane of SnSe along the (111) plane of CdSe. Transient absorption (TA) studies demonstrate a sharp rise in the CdSe biexciton signal, which suggests that the hot carrier transferred from SnSe to CdSe in a short time scale. Following that, these carriers are

returned back to SnSe. The observed delocalization of carriers in these two systems is crucial for an optoelectronic device.

Further, in the fifth chapter, we have looked at the ultrafast excited-state dynamics at the interface of Sb_2Se_3 and CdSe QDs in the $\text{Sb}_2\text{Se}_3/\text{CdSe}$ p-n heterostructure system. The fact that the hot electrons from Sb_2Se_3 migrate to the CdSe system rather than being trapped in the defect states that were present there was demonstrated by the enhanced CdSe hot excitonic (1P) bleach intensity in $\text{Sb}_2\text{Se}_3/\text{CdSe}$ heterostructure. Additionally, the heterostructure's 1S and 1P signals are both dynamically very sluggish when compared to bare CdSe, which supports the charge migration phenomena. Notably, the recovery of the 1P signal takes significantly longer than the recovery of the 1S signal, highlighting the versatility of hot electron transfer in this special heterojunction, which contributes to a longer carrier lifetime in the hot state. This slower decay of high energy excitons offers a unique opportunity to harness these hot charge carriers for the betterment of any solar energy device.

Chapter 6 focuses on the investigation of hole transfer at the 1D/0D SnS@CdS p-n heterojunction. The morphological and structural characteristics demonstrate that CdS QDs are uniformly attached to the surface of SnS NRs and therefore closely bonded to that surface. Transient absorption investigations as well as steady-state and time-resolved photoluminescence research both showed that photoexcited holes were transferred from CdS QDs to SnS NRs. Additionally, the transient investigations revealed the delocalization of electrons between the conduction bands of SnS NRs and CdS QDs in the SnS@CdS heterostructure. Furthermore, pump fluence investigations demonstrated that in SnS@CdS heterostructure, hole migration rather than auger recombination is taking place. These findings will offer a new angle on creating more effective and affordable energy storage devices.

The last and Chapter 7 highlights the charge transfer and recombination mechanisms in the $\text{Sb}_2\text{Se}_3/\text{CdS}$ thin film p-n heterojunction. We used the thermal evaporation technique to fabricate the $\text{Sb}_2\text{Se}_3/\text{CdS}$ film. The ultrafast studies reveal the electron transfer from Sb_2Se_3 to CdS thin film and spatial charge separation at the $\text{Sb}_2\text{Se}_3/\text{CdS}$ p-n junction. Moreover, under light illumination, the photocurrent response of $\text{Sb}_2\text{Se}_3/\text{CdS}$ heterojunction was significantly improved over that of bare Sb_2Se_3 and CdS films. This directly connects to our transient results and shows

enhanced charge separation of photogenerated charge carriers in the heterojunction system. The efficient charge separation in $\text{Sb}_2\text{Se}_3/\text{CdS}$ heterojunction is crucial for the fabrication of photovoltaic and photocatalytic devices.

8.2. Future Perspective

Exploring the electron and hole dynamics within p-n heterojunctions is pivotal for gaining a comprehensive understanding of their optical and material characteristics. The research work presented in this thesis will open a new research paradigm by bringing up in-depth knowledge of ultrafast charge transfer kinetics at heterojunction interfaces. We have looked at the potential use of these materials in various photocatalytic and photovoltaic applications. Despite the high potency of these metal chalcogenide systems, there is still a significant gap between the laboratory-made prototypes and the final, commercially viable products.

The development of semiconductor heterojunctions is an important area of research for practical applications. To date, a variety of approaches have been developed to prepare many kinds of heterojunction systems. It still seems like there is a lot of work to be done in the area of discovering and synthesizing promising materials. Emphasis should be given on synthesis of high quality CZTS NPs, SnS NRs and bare Sb_2Se_3 to improve the quantum yield which would be interesting as we observed a negligible photoluminescence from these samples. It would have a huge effect in reducing the non-radiative channels thereby improving the better charge separation and power conversion efficiency. Furthermore, we need to focus more on synthesizing heterojunction systems. The heterojunctions have already shown their potential in the optoelectronic arena. We should improve the synthesis techniques for making materials. Vacuum-based thermal evaporation deposition method is being implemented in many state-of-the-art optoelectronic devices. To further enhance the transfer of photogenerated electron and hole pairs, double p-n heterojunctions can be designed.

The transition from laboratory to industry places additional constraints on a solar cell material, including its stability and the earth's abundance and nontoxicity of its constituents. The presence of toxic metals such as Cd causes all these materials to fail with respect to one or more of the sustainability criteria. Therefore, the

semiconductor heterojunctions consisting of earth-abundant and non-toxic elements need to be prepared. Keeping in mind of toxicity of cadmium, more and more cadmium-free electron transport layers need to be explored.

Prior knowledge of charge transfer and relaxation dynamics can be truly advantageous for different future applications. Additionally, ultrafast spectroscopic studies at a lower temperature would produce a lot of useful information about the material. To fully comprehend the optical and material features, charge transfer dynamics in semiconductor heterostructures would be beneficial. The research described in this thesis will lead to new discoveries by mentioning an in-depth understanding of ultrafast charge carrier dynamics. In summary, in order to manufacture advanced systems and eventually revolutionize the optoelectronic area, we need to employ the TA spectroscopy approach in a variety of materials.

List of Publications

(Included in the thesis)

- (1) Probing Ultrafast Charge Separation in CZTS/CdS Heterojunctions through Femtosecond Transient Absorption Spectroscopy. **Arshdeep Kaur**, Tanmay Goswami, K. Justice Babu, Nandan Ghorai, Gurpreet Kaur, Ayushi Shukla, Sachin R. Rondiya, and Hirendra N. Ghosh*, *J. Phys. Chem. C* **2020**, *124*, **19476-19483**.
- (2) Enhanced Charge Carrier Separation and Improved Biexciton Yield at the p-n Junction of SnSe/CdSe Heterostructures: A Detailed Electrochemical and Ultrafast Spectroscopic Investigation. **Arshdeep Kaur**, Tanmay Goswami, Sachin R. Rondiya, Yogesh A. Jadhav, K. Justice Babu, Ayushi Shukla, Dharmendra Kumar Yadav, and Hirendra N. Ghosh*, *J. Phys. Chem. Lett.* **2021**, *12*, **10958-10968**.
- (3) Efficient Hot Electron Transfer and Extended Separation of Charge Carriers at the 1P Hot State in Sb₂Se₃/CdSe p-n Heterojunction. **Arshdeep Kaur**, Tanmay Goswami, K. Justice Babu, Ayushi Shukla, Himanshu Bhatt and Hirendra N. Ghosh*, *J. Phys. Chem. Lett.* **2022**, *13*, **11354-11362**.
- (4) Ultrafast Hole Migration at the p-n Heterojunction of One Dimensional (1D) SnS Nanorods and Zero Dimensional (0D) CdS Quantum Dots. **Arshdeep Kaur**, Tanmay Goswami, K. Justice Babu and Hirendra N. Ghosh*, *J. Phys. Chem. Lett.* **2023**, *14*, **7483-7489**.
- (5) Ultrafast Electron Transfer and Efficient Charge Separation in Sb₂Se₃/CdS Thin Film p-n Heterojunction. **Arshdeep Kaur**, Tanmay Goswami, K. Justice Babu and Hirendra N. Ghosh* (**Under revision**)

List of Publications

(Not included in the thesis)

- (1) Concurrent Energy- and Electron-Transfer Dynamics in Photoexcited Mn-Doped CsPbBr₃ Perovskite Nanoplatelet Architecture. K. Justice Babu, Gurpreet Kaur, Ayushi Shukla, **Arshdeep Kaur**, Tanmay Goswami, and Hirendra N. Ghosh^{*} *J. Phys. Chem. Lett.* **2020**, *12*, 302-309.
- (2) Insitu CsPbBr₃ Architecture Engineered in the Electrospun Fibers and Its Ultrafast Charge Transfer Dynamics. K. Justice Babu, Gurpreet Kaur, Ayushi Shukla, **Arshdeep Kaur**, Himanshu Bhatt, Nandan Ghorai, Goutam De and Hirendra N. Ghosh^{*}, *Mater. Adv.* **2022**, *3*, 6566-6576
- (3) Fast Polaron Formation and Low Carrier Mobility in Defect-Free Polyhedral CsPbBr₃ Perovskite Nanocrystals. K. Justice Babu, Gurpreet Kaur, Ayushi Shukla, Ramchandra Saha, **Arshdeep Kaur**, Manvi Sachdeva, Dharmendra Kumar Yadav, and Hirendra N. Ghosh^{*}, *ACS Photonics*, **2022**, *9*, 969-978.
- (4) Defect-Interceded Cascading Energy Transfer and Underlying Charge Transfer in Europium-Doped CsPbCl₃ Nanocrystals. Ayushi Shukla, Gurpreet Kaur, K. Justice Babu, **Arshdeep Kaur**, Dharmendra Kumar Yadav, and Hirendra N. Ghosh^{*}, *J. Phys. Chem. Lett.* **2022**, *13*, 83-90.
- (5) Ultrafast Hot Electron Transfer and Trap-State Mediated Charge Carrier Separation toward Enhanced Photocatalytic Activity in g-C₃N₄/ZnIn₂S₄ Heterostructure. Himanshu Bhatt, Tanmay Goswami, Dharmendra Kumar Yadav, Nandan Ghorai, Ayushi Shukla, Gurpreet Kaur, **Arshdeep Kaur**, and Hirendra N. Ghosh^{*}, *J. Phys. Chem. Lett.* **2021**, *12*, 11865-11872.
- (6) Effect of Confinement on the Exciton and Biexciton Dynamics in Perovskite 2D Nanosheets and 3D-Nanocrystals. Ayushi Shukla, Gurpreet Kaur, K. Justice Babu, Nandan Ghorai, Tanmay Goswami, **Arshdeep Kaur**, and Hirendra N. Ghosh. *J. Phys. Chem. Lett.* **2020**, *11*, 6344-6352.

- (7) Temperature Driven Charge Transfer Process in Quantum Confined Two-Dimensional Mn-doped CsPbBr₃ Perovskite Nanoplatelets. K. Justice Babu, Ayushi Shukla, Gurpreet Kaur, **Arshdeep Kaur**, Himanshu Bhatt, and Hirendra N. Ghosh*, *ChemComm.* 2022, 58, 13899-13902.
- (8) Unveiling the Ultrafast Electron Transfer Dynamics in Epitaxial Dodecahedron CsPbBr₃/Au Heterostructure. Samaresh Samanta, K. Justice Babu, Ayushi Shukla, Gurpreet Kaur, **Arshdeep Kaur**, and Hirendra N. Ghosh* *ChemPhotoChem.* 2023 doi.org/10.1002/cptc.202300242.

List of Conferences

- (1) Actively participated and attended “the Full Agenda of the DST & ACS Workshop” held at Institute of Nano Science and Technology, Mohali (**20th November, 2019**)
- (2) Presented a Poster entitled “Elucidating Charge Transfer Dynamics in CZTS/CdS Heterojunction System using Pump Probe Transient Absorption Spectroscopy” in Ultrafast Sciences conference (UFS 2021) in the Online Zoom Platform (**12th– 13th November 2021**).
- (3) Presented a Poster entitled “Effective Charge Separation and Improved Biexciton Yield at the p-n Junction of SnSe/CdSe Heterostructure (UFS 2022) held at Indian Institute of Science Education and Research, Thiruvananthapuram (**3rd– 5th November 2022**).
- (4) Presented a Poster entitled “Efficient Hot Electron Transfer and Improved Lifetime of Charge Carriers at the 1P Hot State in Sb₂Se₃/CdSe p-n Heterojunction” in International conference on molecules and materials (MMT-2023) held in *National Institute of Technology, Kurukshetra* via Online Zoom Platform (**21st-22nd April 2023**)
- (5) Actively participated and bagged the **Best Oral Presentation Award** on “Ultrafast Charge Transfer and Relaxation Processes in Metal Chalcogenide Based p-n Heterojunctions at 3rd Research Scholar Day, held at Institute of Nano Science and Technology, Mohali Punjab, India (**22nd May– 1st May 2023**).
- (6) Actively participated in the “International Conference: Advanced Characterization Techniques” Conducted Online by the Indian Institute of Science, Bangalore (**18th August, 2023**).
- (7) Participated in a webinar on “Ultrafast lasers and their ever-growing applications to physics, chemistry, material, and life sciences” organized by Laser Science Services (I) Pvt. Ltd. (**10th August, 2022**).

- (8) Presented a Poster entitled “Ultrafast Hole Migration at the p-n Heterojunction of 1D SnS Nanorods and 0D CdS Quantum Dots” in Ultrafast Sciences (UFS 2023) held at CSIR-National Physical Laboratory, New Delhi (**25th– 27th November 2023**).
- (9) Actively participated and bagged the **Best Poster Presentation Award** on the topic “Ultrafast Hot Electron Transfer and Improved Lifetime of Charge Carriers at the 1P Hot State in Sb₂Se₃/CdSe p-n Heterojunction” in an international e-conference on Recent Advances in Science and Technology (**4th– 5th November 2023**).
- (10) Actively participated in CFQT 2023: Crystal for Quantum Technology conference held at Institute of Nano Science and Technology. (**11th– 12th December 2023**).

Permission from Journals

THE JOURNAL OF
PHYSICAL CHEMISTRY C

pubs.acs.org/JPCCC

Article

Probing Ultrafast Charge Separation in CZTS/CdS Heterojunctions through Femtosecond Transient Absorption Spectroscopy

Arshdeep Kaur,[§] Tanmay Goswami,[§] K. Justice Babu, Nandan Ghorai, Gurpreet Kaur, Ayushi Shukla, Sachin R. Rondiya, and Hirendra N. Ghosh*

Cite This: *J. Phys. Chem. C* 2020, 124, 19476–19483

Read Online

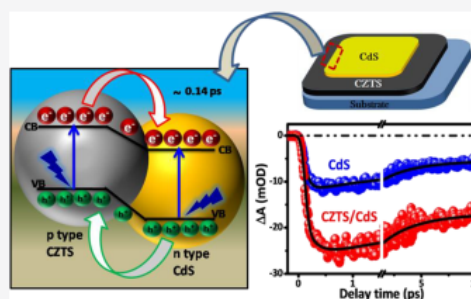
ACCESS |

Metrics & More

Article Recommendations

Supporting Information

ABSTRACT: Chalcogenide-based type II heterojunctions are considered to be a promising candidate for optoelectronic device fabrication such as in solar cells, photodetectors, and light-emitting diodes. Type II heterosystems effectively help in the delocalization of charge carriers owing to facile band arrangements, preventing the recombination of photogenerated carriers resulting in improved photovoltaic efficiency. Herein, we report the synthesis of CZTS nanoparticles and CdS quantum dots using a facile and low-cost hot-injection method followed by fabrication of CZTS, CdS, and CZTS/CdS heterojunction thin films with the help of a spin-coating technique at room temperature. We demonstrated through a combination of steady-state photoluminescence and femtosecond pump–probe spectroscopy experiments that a type-II, staggered band alignment of a CZTS/CdS junction is encouraging for charge carrier transport. We monitored the ultrafast charge carrier dynamics in the junction and confirmed the efficient separation of photoexcited charge carriers in the CZTS/CdS heterojunction. In the CZTS/CdS heterojunction, the photoexcited electrons are transferred from CZTS to CdS, which resulted in a drastic increment of the bleach signal intensity compared to that of bare CdS. Similarly, the photoexcited holes are transferred from CdS to CZTS, monitored by steady-state and time-resolved spectroscopy. A slower bleach recovery confirms the spatial charge separation at the interface of the CZTS/CdS heterojunction, placing electrons and holes at CdS and CZTS, respectively. The controlled introduction of charge carriers and charge separation dynamics in the heterointerface reported here provides a promising approach toward designing CZTS-based solar cells and will open up new avenues for developing more efficient Cu chalcogenide-based photovoltaic and photocatalytic devices.



1. INTRODUCTION

Development of more and more renewable energy sources could be a possible way to overcome the upcoming energy crisis in the world and counter the scarcity of regular nonrenewable (fossil fuel) energy sources in the near future.¹ Among these, solar energy-based optical devices could be the most intriguing option where the sun's energy is directly converted into electricity which could also be used in catalyzing crucial chemical reactions.^{2,3} Photovoltaics and photocatalysis based on heterojunctions have attracted overwhelming attention in recent years, where charge carriers at the heterointerface play a crucial role.^{4–6} The fate of the photoexcited charge carriers dictates the performance of devices, which need to be extracted before they recombine in order to deliver better device efficiency. Various techniques have been adopted to efficiently separate the photogenerated electron–hole pairs in semiconductor materials through doping with metals or forming a heterojunction. Among different other materials, Cu-based chalcogenide systems have been a standout as a potential photocathode due to their

outstanding photovoltaic performances, preferable band positions, and cost efficiency.^{7–9} Also, having a ~30% theoretical upper limit for solar energy conversion efficiency (Shockley–Queisser efficiency) in a p–n junction makes these materials promising for solar cell applications.¹⁰ Currently, copper indium gallium selenide (CIGS) is dominating the thin-film solar cell market, but its prospect is limited due to the low abundance of indium in the Earth's crust. In this scenario, copper zinc tin sulfide (CZTS) emerges as a potential photovoltaic material¹¹ due to its excellent earth abundance,³ nontoxicity, direct band gap (1.5 eV),¹² high absorption coefficient (10^4 cm^{-1}),^{13,14} and high carrier mobility. Among the different heterostructures, CZTS and cadmium sulfide

Received: June 22, 2020
Revised: August 4, 2020
Published: August 4, 2020



ACS Publications

© 2020 American Chemical Society

19476

<https://dx.doi.org/10.1021/acs.jpcc.0c05658>
J. Phys. Chem. C 2020, 124, 19476–19483



RightsLink



Home



Help ▾



Live Chat



Sign in



Create Account

Probing Ultrafast Charge Separation in CZTS/CdS Heterojunctions through Femtosecond Transient Absorption Spectroscopy

**Author:** Arshdeep Kaur, Tanmay Goswami, K. Justice Babu, et al**Publication:** The Journal of Physical Chemistry C**Publisher:** American Chemical Society**Date:** Sep 1, 2020*Copyright © 2020, American Chemical Society*

PERMISSION/LICENSE IS GRANTED FOR YOUR ORDER AT NO CHARGE

This type of permission/license, instead of the standard Terms and Conditions, is sent to you because no fee is being charged for your order. Please note the following:

- Permission is granted for your request in both print and electronic formats, and translations.
- If figures and/or tables were requested, they may be adapted or used in part.
- Please print this page for your records and send a copy of it to your publisher/graduate school.
- Appropriate credit for the requested material should be given as follows: "Reprinted (adapted) with permission from {COMPLETE REFERENCE CITATION}. Copyright {YEAR} American Chemical Society." Insert appropriate information in place of the capitalized words.
- One-time permission is granted only for the use specified in your RightsLink request. No additional uses are granted (such as derivative works or other editions). For any uses, please submit a new request.

If credit is given to another source for the material you requested from RightsLink, permission must be obtained from that source.

[BACK](#)[CLOSE WINDOW](#)

Enhanced Charge Carrier Separation and Improved Biexciton Yield at the p–n Junction of SnSe/CdSe Heterostructures: A Detailed Electrochemical and Ultrafast Spectroscopic Investigation

Arshdeep Kaur, Tanmay Goswami, Sachin R. Rondiya, Yogesh A. Jadhav, K. Justice Babu, Ayushi Shukla, Dharmendra Kumar Yadav, and Hirendra N. Ghosh*

Cite This: *J. Phys. Chem. Lett.* 2021, 12, 10958–10968

Read Online

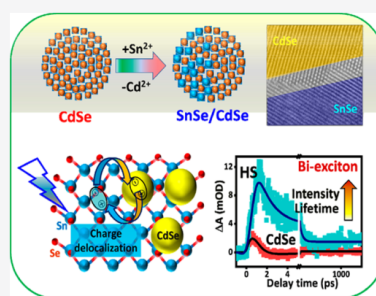
ACCESS |

Metrics & More

Article Recommendations

Supporting Information

ABSTRACT: Tin chalcogenides (SnX, X = S, Se)-based heterostructures (HSs) are promising materials for the construction of low-cost optoelectronic devices. Here, we report the synthesis of a SnSe/CdSe HS using the controlled cation exchange reaction. The (400) plane of SnSe and the (111) plane of CdSe confirm the formation of an interface between SnSe and CdSe. The Type I band alignment is estimated for the SnSe/CdSe HS with a small conduction band offset (CBO) of 0.72 eV through cyclic voltammetry measurements. Transient absorption (TA) studies demonstrate a drastic enhancement of the CdSe biexciton signal that points toward the hot carrier transfer from SnSe to CdSe in a short time scale. The fast growth and recovery of CdSe bleach in the presence of SnSe indicate charge transfer back to SnSe. The observed delocalization of carriers in these two systems is crucial for an optoelectronic device. Our findings provide new insights into the fabrication of cost-effective photovoltaic devices based on SnSe-based heterostructures.



The generation of renewable energy is crucial in order to encounter the world's current energy demands. The development of novel materials becomes a key feature for the evolution of technology and to fulfill the world's rising energy requirements.¹ Over the past few years, improved solar cell efficiency has been reported with copper indium gallium selenide (CIGS) and cadmium telluride (CdTe) absorber materials; however, scarcity and toxicity of the constitute elements hamper further development.² Quaternary Cu₂ZnSn(S/Se)₄ (CZTSSe) systems have also captured much attention in the field of photovoltaics due to their direct band gap ($E_g = 1.1$ eV),³ high absorption coefficient (10^4 cm⁻¹),⁴ and stability.² The highest power conversion efficiency (PCE) of 12.6% has been achieved by Se-rich CZTSSe thin film solar cells with a S/(S + Se) compositional ratio of 0.24.⁵ The major obstacles in achieving a high performance for CZTSSe-based photovoltaic and photocatalytic devices are controlling the formation of secondary phases, inherent Cu–Zn antisite defects, and poor band alignment.⁴ Hence, alternative materials which contain lead-free Earth-abundant, as well as nontoxic elements need to be explored for solar cell applications. Nowadays, two-dimensional (2D) metal chalcogenides and their heterostructures have gained incredible interest owing to their diverse range of properties that enable applications in photocatalysis, optoelectronics, and energy conversion and storage.⁶ As compared to their bulk counterparts, 2D materials possess quantum confinement which give

rise to innovative electronic and optical properties like strong Coulombic interactions, strong spin–orbit coupling, efficient light–matter interactions, higher carrier mobility, an increased electronic band gap, etc. Moreover, these materials are abundant and mechanically strong, rendering them very suitable for future-generation photovoltaic cells.^{7,8} Two-dimensional materials can also improve the photocatalytic performance by maximizing the specific surface area which creates additional active sites, which is a crucial factor for improved catalytic processes.⁸ Recently, tin selenide (SnSe) nanosheets (NSs) have shown excellent properties for photovoltaic applications and could be the future energy source due to its Earth abundance, nontoxicity, band gap tunability up to near-infrared (NIR) region,⁹ high absorption coefficient (10^5 cm⁻¹),¹⁰ and a p-type semiconductor with a high concentration of carriers (10^{15} , 10^{18} cm⁻³).¹¹ Moreover, it shows a high stability of formation due to its binary nature, which overcomes the problems associated with structural, stoichiometry, and secondary phase formation commonly

Received: September 7, 2021

Accepted: October 28, 2021

Published: November 5, 2021





RightsLink



Home



Help ▾



Live Chat



Sign in



Create Account

Enhanced Charge Carrier Separation and Improved Biexciton Yield at the p-n Junction of SnSe/CdSe Heterostructures: A Detailed Electrochemical and Ultrafast Spectroscopic Investigation



Author: Arshdeep Kaur, Tanmay Goswami, Sachin R. Rondiya, et al

Publication: Journal of Physical Chemistry Letters

Publisher: American Chemical Society

Date: Nov 1, 2021

Copyright © 2021, American Chemical Society

PERMISSION/LICENSE IS GRANTED FOR YOUR ORDER AT NO CHARGE

This type of permission/license, instead of the standard Terms and Conditions, is sent to you because no fee is being charged for your order. Please note the following:

- Permission is granted for your request in both print and electronic formats, and translations.
- If figures and/or tables were requested, they may be adapted or used in part.
- Please print this page for your records and send a copy of it to your publisher/graduate school.
- Appropriate credit for the requested material should be given as follows: "Reprinted (adapted) with permission from {COMPLETE REFERENCE CITATION}. Copyright {YEAR} American Chemical Society." Insert appropriate information in place of the capitalized words.
- One-time permission is granted only for the use specified in your RightsLink request. No additional uses are granted (such as derivative works or other editions). For any uses, please submit a new request.

If credit is given to another source for the material you requested from RightsLink, permission must be obtained from that source.

[BACK](#)[CLOSE WINDOW](#)

Efficient Hot Electron Transfer and Extended Separation of Charge Carriers at the 1P Hot State in Sb₂Se₃/CdSe p–n Heterojunction

Arshdeep Kaur, Tanmay Goswami, K. Justice Babu, Ayushi Shukla, Himanshu Bhatt, and Hirendra N. Ghosh*



Cite This: *J. Phys. Chem. Lett.* 2022, 13, 11354–11362



Read Online

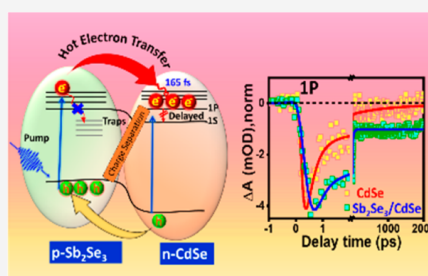
ACCESS |

Metrics & More

Article Recommendations

Supporting Information

ABSTRACT: Utilization of hot carriers is very crucial in improving the efficiency of solar energy devices. In this work, we have fabricated an Sb₂Se₃/CdSe p–n heterojunction via a cation exchange method and investigated the possibility of hot electron transfer and relaxation pathways through ultrafast spectroscopy. The enhanced intensity of the CdSe hot excitonic (1P) bleach in the heterostructure system confirmed the hot electron transfer from Sb₂Se₃ to CdSe. Both the 1S and 1P signals are dynamically very slow in the heterosystem, validating this charge migration phenomenon. Interestingly, recovery of the 1P signal is much slower than that of 1S. This is very unusual as 1S is the lowest-energy state. This observation indicates the strength of hot electron transfer in this unique heterojunction, which helps in increasing the carrier lifetime in the hot state. Extended separation of charge carriers and enhanced hot carrier lifetime would be extremely helpful in extracting carriers and boost the performance of optoelectronic devices.



To address the issue of rising global energy demands, utilization of renewable and clean solar energy is highly required.¹ Recently, quantum dot (QD) heterostructures have emerged as promising candidates for next-generation solar cells as they exhibit unique properties such as broad absorption coefficient, tunable band gap, and multiple exciton generation with single-photon absorption.^{2,3} In addition, quantum dot solar cells (QDSCs) present a theoretically predicted power conversion efficiency (PCE) of 45% in a single-junction QDSC and up to 66% in a multiple-junction QDSC as a result of efficient multiple-exciton generation and hot-electron extraction, with the potential to exceed the Shockley–Queisser limit.^{4–6} Recently, antimony chalcogenides (Sb₂X₃, X = S, Se) QD-based heterostructures have attracted overwhelming attention as light harvesters in the field of photovoltaic and photocatalytic applications.^{7,8} Sb₂Se₃ is a p-type semiconductor having fascinating properties such as low toxicity,⁹ low cost,¹⁰ high abundance, high chemical stability,¹¹ high absorption coefficient (10⁵ cm⁻¹),¹² narrow band gap (1.1–1.3 eV), and considerable carrier mobility (~10 cm² V⁻¹ s⁻¹).¹³ Until now, the highest PCE of Sb₂X₃ (X = S, Se) solar cells has been reported to be 7.5% and 9.2% respectively,^{14,15} which is far below the theoretically predicted efficiency of 32% for Sb₂X₃ (X = S, Se) based solar cells. This is due to the presence of a high concentration of interfacial defect states, which results in faster trapping and recombination of the charge carriers in the Sb₂X₃ materials.¹⁶ Also, the excessive energy of carriers greater than the band gap of the semiconductor is lost to heat due to rapid cooling of hot carriers through emission of phonons.

Extraction of these hot carriers is considered to be a promising way to overcome this loss. To resolve all these issues, fabrication of a heterojunction with type II band alignment of semiconductors has been considered to be a convincing method as it offers broad wavelength tunability, better separation and extraction of charge carriers, and their longer lifetime, thus suppressing the deleterious recombination rate of the photogenerated electron and hole.¹⁷ With this approach, charge carriers can be spatially separated in the heterojunction due to decrease in Coulombic interaction between electrons and holes. It facilitates transport of the charge carriers that can be efficiently extracted and utilized, which is essential for the betterment of device performance.¹⁸ The heterojunction of Sb₂Se₃ with CdSe has attained enormous attention, which we have synthesized via a low-cost cation exchange method. Cation exchange is an effective technique to synthesize heterostructures as it provides proper band alignment and adjustable shape and size by changing the constituents and experimental conditions.^{19–21} CdSe is a wide band gap n-type semiconductor which is widely used for optoelectronic applications. However, owing to the fast recombination of

Received: November 1, 2022
Accepted: November 28, 2022
Published: December 1, 2022



ACS Publications

© 2022 American Chemical Society

11354

<https://doi.org/10.1021/acs.jpclett.2c03308>
J. Phys. Chem. Lett. 2022, 13, 11354–11362



RightsLink



Home



Help ▾



Live Chat



Sign in



Create Account

Efficient Hot Electron Transfer and Extended Separation of Charge Carriers at the 1P Hot State in Sb₂Se₃/CdSe p-n Heterojunction



Author: Arshdeep Kaur, Tanmay Goswami, K. Justice Babu, et al

Publication: Journal of Physical Chemistry Letters

Publisher: American Chemical Society

Date: Dec 1, 2022

Copyright © 2022, American Chemical Society

PERMISSION/LICENSE IS GRANTED FOR YOUR ORDER AT NO CHARGE

This type of permission/license, instead of the standard Terms and Conditions, is sent to you because no fee is being charged for your order. Please note the following:

- Permission is granted for your request in both print and electronic formats, and translations.
- If figures and/or tables were requested, they may be adapted or used in part.
- Please print this page for your records and send a copy of it to your publisher/graduate school.
- Appropriate credit for the requested material should be given as follows: "Reprinted (adapted) with permission from {COMPLETE REFERENCE CITATION}. Copyright {YEAR} American Chemical Society." Insert appropriate information in place of the capitalized words.
- One-time permission is granted only for the use specified in your RightsLink request. No additional uses are granted (such as derivative works or other editions). For any uses, please submit a new request.

If credit is given to another source for the material you requested from RightsLink, permission must be obtained from that source.

[BACK](#)[CLOSE WINDOW](#)

Ultrafast Hole Migration at the p–n Heterojunction of One-Dimensional SnS Nanorods and Zero-Dimensional CdS Quantum Dots

Arshdeep Kaur, Tanmay Goswami, Kaliyamoorthy Justice Babu, and Hirendra N. Ghosh*



Cite This: *J. Phys. Chem. Lett.* 2023, 14, 7483–7489



Read Online

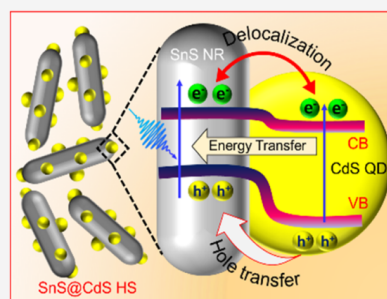
ACCESS |

Metrics & More

Article Recommendations

Supporting Information

ABSTRACT: The p–n heterojunctions fabricated from one-dimensional (1D) p-type tin sulfide nanorods (SnS NRs) decorated with n-type zero-dimensional (0D) cadmium sulfide quantum dots (CdS QDs) have gained significant research attention in energy storage devices. Herein, we have successfully synthesized a 1D/0D SnS@CdS heterostructure (HS) using a hot injection method. Structural and morphological studies clearly suggest that CdS QDs are uniformly anchored on the surface of SnS NRs, resulting in intimate contact between two components. The photoluminescence (PL) study revealed the transfer of photoexcited holes from CdS QDs to SnS NRs, which was further confirmed by transient absorption (TA) studies. TA measurements demonstrate the hole transfer from the valence band of CdS QDs to SnS NRs and delocalization of electrons between the conduction band of SnS NRs and CdS QDs in SnS@CdS HS, resulting in efficient charge separation across the p–n heterojunction. These findings will open up a new paradigm for improving the efficiency of optoelectronic devices.



Semiconductor p–n heterojunctions are a basic building block for any optoelectronic and technological application.^{1–3} It improves the charge separation as well as the carrier transport and hence increases the lifetime of carriers by preventing excitonic recombination, which is highly desirable for device applications. Among them, 1D (IV–VI) p-type tin sulfide (SnS) has emerged as one of the promising candidate for its numerous applications, including photovoltaics,⁴ photocatalysis,⁵ and next-generation energy storage devices,^{6,7} owing to its unique properties such as high stability and tunable band gap,⁴ higher optical absorption coefficient ($>10^4$ cm⁻¹),⁸ and nontoxic and earth abundant elements.^{9,10} Moreover, 1D semiconductor heterostructures demonstrate a large surface-to-volume ratio, which provides a large number of active sites that results in outstanding photocatalytic, optoelectronic, and gas-sensing properties.^{11–14} Recently, SnS has been widely used as an active absorber material in solar cell devices.¹⁵ However, pristine SnS frequently suffers from low charge separation efficiency and trapping of charge carriers, which seriously affect the practical application of photocatalysis. Many efforts have been made to avoid these issues by combining SnS with other nanomaterials to form heterostructures.^{16–19} Hence, in order to achieve efficient performance of devices, the coupling of p-type 1D SnS NRs with n-type 0D CdS QDs has evolved much interest in the field of photovoltaics as the depletion layer at the p–n interfacial region induces an electric field which results in improved separation ability and transport of charge carriers. CdS is a

wide band gap semiconductor with high electronic mobility and excellent thermal stability, exhibiting sharp excitonic peaks and photoluminescence (PL).^{20–22} SnS NRs in a heterojunction with CdS QDs can achieve excellent device performance. Earlier, Wang et al. reported that Sn_{0.38}S–CdS superlattice nanowires display efficient gas-sensing behavior.¹⁴ Cho et al. measured the efficiency of 4.22% for SnS@CdS thin-film solar cells by improving the interface quality of the heterojunction, which is still far below the theoretical Shockley–Queisser limit.²³ In order to improve the fabrication of the junction and enhance the device performance, it is of paramount importance to study the photophysics of generated charge carriers involved at the interface of this SnS NR and CdS QD heterostructure.^{24–26} However, to the best of our knowledge, the charge transfer dynamics in 1D/0D SnS@CdS HS has not been investigated. Femtosecond (fs) transient absorption spectroscopy (TAS) is known to be a powerful technique to monitor the dynamics of photoexcited charge carriers in individual materials as well as heterosystems in the femtosecond-to-nanosecond (ns) time window. The understanding of cooling, transfer, trapping, and

Received: May 21, 2023

Accepted: August 11, 2023

Published: August 14, 2023





RightsLink



Home



Help ▾



Live Chat



Sign in



Create Account

Ultrafast Hole Migration at the p-n Heterojunction of One-Dimensional SnS Nanorods and Zero-Dimensional CdS Quantum Dots



Author: Arshdeep Kaur, Tanmay Goswami, Kaliyamoorthy Justice Babu, et al

Publication: Journal of Physical Chemistry Letters

Publisher: American Chemical Society

Date: Aug 1, 2023

Copyright © 2023, American Chemical Society

PERMISSION/LICENSE IS GRANTED FOR YOUR ORDER AT NO CHARGE

This type of permission/license, instead of the standard Terms and Conditions, is sent to you because no fee is being charged for your order. Please note the following:

- Permission is granted for your request in both print and electronic formats, and translations.
- If figures and/or tables were requested, they may be adapted or used in part.
- Please print this page for your records and send a copy of it to your publisher/graduate school.
- Appropriate credit for the requested material should be given as follows: "Reprinted (adapted) with permission from {COMPLETE REFERENCE CITATION}. Copyright {YEAR} American Chemical Society." Insert appropriate information in place of the capitalized words.
- One-time permission is granted only for the use specified in your RightsLink request. No additional uses are granted (such as derivative works or other editions). For any uses, please submit a new request.

If credit is given to another source for the material you requested from RightsLink, permission must be obtained from that source.

[BACK](#)[CLOSE WINDOW](#)

Conference Certificates



7TH THEME MEETING ON ULTRAFAST SCIENCES - 2021 (UFS-2021)
Dates: November 12 - 13, 2021: Venue: On-line Zoom Platform
Organized by: UM-DAE Centre for Excellence in Basic Sciences,
Mumbai University, Kalina Campus, Santacruz (E), Mumbai-400098

CERTIFICATE OF PARTICIPATION & POSTER PRESENTATION

This certifies that
MS. ARSHDEEP KAUR,

Institute of Nano Science and Technology, Mohali, Punjab, has participated and presented a poster on "Elucidating Charge Transfer Dynamics in CZTS/CdS Heterojunction System using Pump Probe Transient Absorption Spectroscopy" at the 7th Theme Meeting on Ultrafast Sciences 2021 (UFS-2021).

Dipak K. Palit
Convener, UFS-2021

Vimal K. Jain
Chairman, UFS-2021 & Director, CEBS

UFS 2022

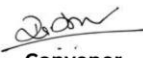
9TH Theme Meeting on Ultrafast Sciences

ORGANIZED BY
Indian Institute of Science Education and Research
Thiruvananthapuram

CERTIFICATE

This is to certify that
Arshdeep Kaur
INST, Mohali

has presented a poster in the UFS 2022 meeting held at
Indian Institute of Science Education and Research, Thiruvananthapuram
during 3-5 November 2022.



Convener
Dr. Rajeev N. Kini



Co-Convener
Prof. Mahesh Hariharan



Secretary
Dr. Adithya Lakshmana



Certificate of Participation

This is to certify that

Arshdeep Kaur

Has participated in webinar on- "Ultrafast lasers and their ever growing applications to physics, chemistry, material, and life sciences" on 10th of August 2022

Speaker- Marco Arrigoni, Director of Segment Marketing – Scientific Instrumentation
Coherent Inc. California.

Organizer- Laser Science Services (I) Pvt. Ltd.

10/08/2022

DATE



Akale

TEAM MARKETING

LASER SCIENCE SERVICES (I) PVT. LTD.



Under Diamond Jubilee Celebration
International Conference

on

Molecules and Materials Technology (MMT-2023)

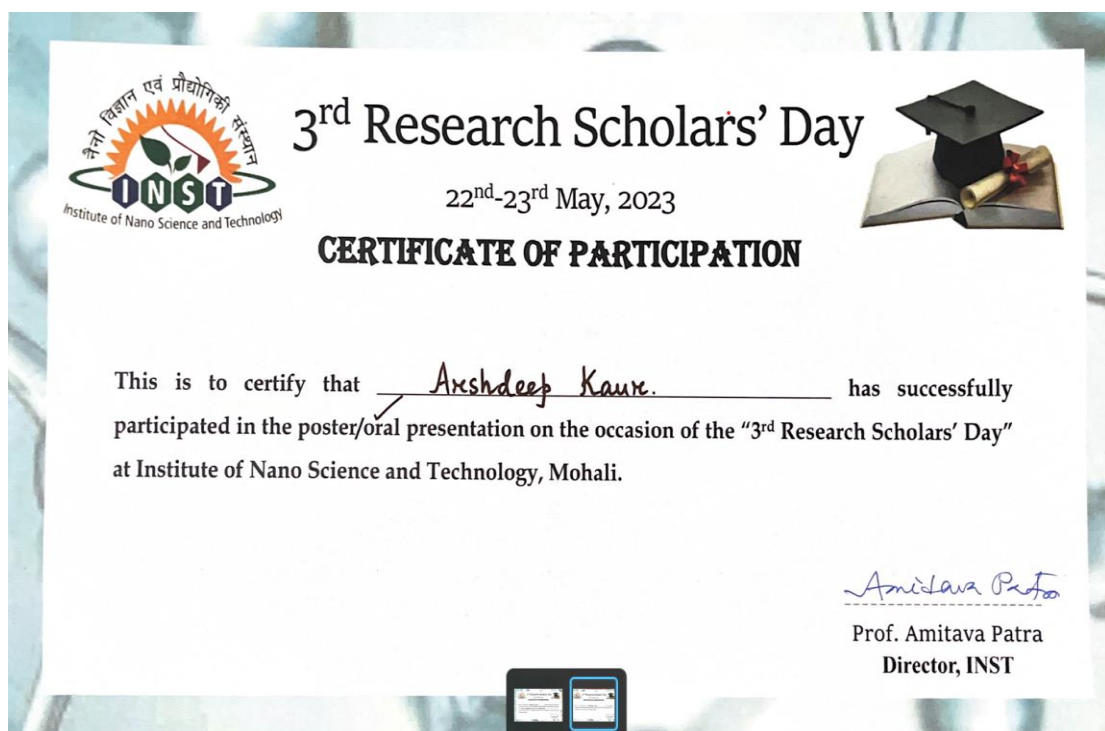
21st - 22nd April, 2023

Certificate of Presentation

This is to certify that Dr./Mr./Ms. Arshdeep Kaur of INST Mohali has presented Poster in International Conference on Molecules and Materials Technology (MMT-2023) organized by, Department of Chemistry National Institute of Technology, Kurukshetra held on 21st -22nd April, 2023.


Conference Secretary
MMT-2023


Chairman
MMT-2023





**International Conference:
Advanced Characterization Techniques
(ACT-2023)**

Certificate of Participation

Arshdeep Kaur

Participated in the
International Conference Conducted Online on 18th August - 2023



Dr. Sachin R. Rondiya
Assistant Professor
Department of Materials Engineering
Indian Institute of Science, Bangalore



Prof. Satyam Suwas
Chair
Department of Materials Engineering
Indian Institute of Science, Bangalore



INTERNATIONAL E-CONFERENCE
RECENT ADVANCES IN SCIENCE & TECHNOLOGY
NOVEMBER 04-05, 2023 | E-PLATFORM | INDIA

BEST POSTER PRESENTATION

On the topic
Ultrafast Hot Electron Transfer and Improved Lifetime of Charge Carriers at the iP Hot State in
Sb₂Se₃/CdSe p-n Heterojunction

By
Arshdeep Kaur

Department of Energy and Envi, Institute of Nano Science and Technology,
Mohali, Punjab, India




Ashish K Upadhyay
Convener


Chetna Verma
Secretary


Shiv K Upadhyay
Conference Chair



Ms. Arshdeep Kaur (Reg. No. PH18206) joined the **Institute of Nano Science and Technology Mohali**, in July 2018 for her doctoral dissertation and **Indian Institute of Science Education and Research (IISER) Mohali** for the award of the degree of Doctor of Philosophy. She completed her B.Sc. and M.Sc. in Physics (Hons.) from the Department of Physics, Panjab University. As a doctoral student, her research is mainly focussed on the investigation of ultrafast charge transfer and relaxation dynamics in metal chalcogenide-based p-n semiconductor heterojunctions.

Arshdeep Kaur

